Structure-based modeling of catalyst layers for proton exchange membrane fuel cells

From the Faculty of Georesources and Materials Engineering of the
RWTH Aachen University

to obtain the academic degree of

Doctor of Natural Science

approved thesis

submitted by

Wolfgang Olbrich, M.Sc.

Advisors: Univ.-Prof. Dr. rer. nat. Michael Eikerling
              Univ.-Prof. Dr.-Ing. habil. Daniela Zander
              Univ.-Prof. Dr.-Ing. Simon Thiele

Date of the oral examination: 19.01.2024

This dissertation includes the following articles:

- W. Olbrich, T. Kadyk, U. Sauter, and M. Eikerling. Review – Wetting Phenomena in Catalyst Layers of PEM Fuel Cells: Novel Approaches for Modeling and Materials Research. *Journal of The Electrochemical Society*, 169(5):054521, May 2022.
  `https://doi.org/10.1149/1945-7111/ac6e8b`

- W. Olbrich, T. Kadyk, U. Sauter, and M. Eikerling. Modeling of wetting phenomena in cathode catalyst layers for PEM fuel cells. *Electrochimica Acta*, 431:140850, Nov. 2022.
  `https://doi.org/10.1016/j.electacta.2022.140850`

- W. Olbrich, T. Kadyk, U. Sauter, M. Eikerling, and J. Gostick. Structure and conductivity of ionomer in PEM fuel cell catalyst layers: a model-based analysis. *Nature Scientific Reports*, 13:14127, Aug 2023.
  `https://doi.org/10.1038/s41598-023-40637-0`

D 82 (Diss. RWTH Aaachen University, 2024)

Danksagung / Acknowledgment

Zu allererst gilt mein besonderer Dank Prof. Michael Eikerling für die Überlassung eines faszinierenden, hochrelevanten Forschungsthemas. Sein großzügiges Fördern wie kompromissloses Fordern exzellenter wissenschaftlicher Arbeit hat mich als Wissenschaftler stets angespornt und über mich hinauswachsen lassen.

Ich danke Dr. Ulrich Sauter für sein Vertrauen in meine eigenwilligen Ideen und die Freiräume, diese zu entwickeln, die guten Diskussionen und die verlässliche Rückendeckung.

Ich danke allen Kolleg*innen der PMD-Gruppe für die spontan-wissenschaftlichen Diskurse jenseits der Brennstoffzelle und die Unterstützung beim Bewältigen des Forschungsalltags von *peer reviews* bis *solver instabilities*. Ich habe mich trotz der Distanz Jülich–Renningen stets als ein integraler Teil des Teams am IEK-13 gefühlt.

I would like to express my heartfelt gratitude to Prof. Jeff Gostick and his research group, who made my stay in Canada a great experience and a fruitful collaboration, despite pandemic times.

Meinen Kolleg*innen in der Abteilung CR/ATC2 danke ich für drei Jahre gelungener Zusammenarbeit. Besonders meine Mit-Doktoranden Chris, Tobi und Michael waren mir treue Weggefährten, auf deren Unterstützung und Humor ich stets zählen konnte.

Saskia, ich bin dir unendlich dankbar, dass du immer ein offenes Ohr hast und mich mit klugen Fragen stets auf den Boden der Tatsachen zurückholst.

Liebe Eltern, ich danke euch für all die Unterstützung, den Halt und den weisen Rat, den ihr mir auf meinen Wegen gegeben habt. Ohne euch wäre ich nicht da, wo ich heute bin.

Meinen Mitbewohner*innen im Kesselhof danke ich für die Abenteuer und die Vertrautheit, die mir diese Gruppe und dieser Ort schenkt. Ganz besonders danke ich Linda für die zahllosen Gespräche im Niemandsland zwischen Kunst und Wissenschaft über Konsens, Kombuchas, Komposte, Kakadus, Korallen und Keramiken.

Yufan, we started as PhD students working on complementary topics and became companions exploring the riddles of life together. It is a heartfelt honor to be your friend.

Maru, danke für all die Jahre und deine generelle Großartigkeit. Friedi, du warst immer da, auch wenn viel zwischendurch passiert ist. Hilke, dein plötzliches Erscheinen in den Rissen des Raumzeitkontinuums ist mir Freude wie Rätsel zugleich. Helena, ich bin froh, dass ich dich hab'. Ich brauch' dich noch! Vera, danke für Tex & Techno. Ich werde meine Schwüre halten. Becky, gemeinsam war das Schreiben viel leichter.

And thank you, all my colleagues and friends who contributed to the proof-reading of this thesis: Christa, Freddy, Larissa, Linda, Matthias, Olga, Oscar, Vera, and Yufan.

Und natürlich, ja vielleicht am allermeisten, danke ich dir, Freddy. Ich würde es alles wieder tun – denn du bist mein *resident derp* und mein Zuhause in der Welt.

Declaration

I certify that the dissertation entitled

Structure-based modeling of catalyst layers for proton exchange membrane fuel cells

is entirely my own work and that I have not used any sources or aids other than those indicated. Passages and content from other sources, and services and works of third parties, have been clearly marked. I have complied with the principles for ensuring good scientific practice at RWTH Aachen University.

I agree to the internal use of this thesis in the libraries of RWTH Aachen University as well as in Forschungszentrum Jülich GmbH and Robert Bosch GmbH.

Erklärung

Ich versichere, dass ich die vorliegende Dissertation mit dem Titel

Strukturbasierte Modellierung von Katalysatorschichten für Protonenaustauschmembran-Brennstoffzellen

selbständig verfasst und keine anderen als die angegebenen Quellen und Hilfsmittel benutzt habe. Passagen und Inhalte aus anderen Quellen, sowie Dienstleistungen und Arbeiten Dritter, sind als solche kenntlich gemacht. Die Grundsätze zur Sicherung guter wissenschaftlicher Praxis der RWTH Aachen habe ich eingehalten.

Mit der internen Verwendung dieser Arbeit in den Bibliotheken der RWTH Aachen sowie im Forschungszentrum Jülich GmbH und der Robert Bosch GmbH bin ich einverstanden.

Wolfgang Olbrich
Stuttgart, 31.05.2023

Declaration on the protection of trade secrets and patents

I hereby declare that my dissertation

Structure-based modeling of catalyst layers for proton exchange membrane fuel cells

does not infringe any trade secrets or patents belonging to Forschungszentrum Jülich GmbH or Robert Bosch GmbH.

Erklärung zur Wahrung von Betriebsgeheimnissen und Patenten

Hiermit erkläre ich, dass durch meine Dissertation

Strukturbasierte Modellierung von Katalysatorschichten für Protonenaustauschmembran-Brennstoffzellen

keine Betriebsgeheimnisse oder Patente der Forschungszentrum Jülich GmbH oder der Robert Bosch GmbH verletzt werden.

Wolfgang Olbrich
Stuttgart, 31.05.2023

Contents

Abstract

**Structure-based modeling of catalyst layers
for proton exchange membrane fuel cells**

Doctoral thesis written by Wolfgang Olbrich

Fuel cells are expected to play an integral role in a future energy system where they act as efficient energy converters generating electricity from renewable hydrogen. Proton exchange membranes fuel cells (PEMFCs) are favored for their robustness, efficiency and compactness and are currently transitioning from prototyping stage and niche applications to large-scale commercial deployment. Ongoing development efforts have to meet ambitious targets in terms of durability, performance and cost effectiveness. Therefore, the overall fuel cell device, and in particular the cathode catalyst layer (CCL), must be further improved and optimized from atomic scale to system level. CCL materials development hinges on comprehensive mathematical models covering the entire causal chain from fabrication parameters during ink stage, over the resulting microstructure, to macroscopic properties, and finally to the operative performance metrics.

The scope of this work covers three major interconnected subjects of research: firstly, structure formation during ink stage is lacking a quantitative approach that rationalizes the cause-effect relations between ink parameters and the resulting agglomerated microstructure; secondly, the crucial relations between molecular-to-mesoscale characteristics of the catalyst microstructure and water-related properties (wetting behavior, water uptake, Platinum utilization, and the CCLs susceptibility to flooding) require a comprehensive, scale-bridging approach to overcome the limitations of a merely empirical consideration, especially with regard to the objective of further lowering the Platinum loading in PEMFCs; and thirdly, experimental literature data indicate a significant impact of ionomer morphology on proton conductivity within the CCL, which is commonly neglected by models available in literature but has gained importance together with efforts to enhance the current density of the cell. Methodologically, these research gaps were addressed by a profoundly structure-based modeling approach that allows to comprehensibly trace the cause-effect-chain from molecular to macroscopic scale.

Starting with the CCL composition model to study structure formation during ink stage, the incremental self-assembly of solvated ionomer and Pt/C particles was analyzed in an analytical-mechanistic approach, from which two key parameters were derived: an ionomer dispersion parameter that captures the tendency of ionomer to self-aggregation or film formation, and the initial ionomer film thickness. The model solution includes pore size distribution and ionomer morphology within the final CCL microstructure and was seamlessly employed as input to the models for wetting behavior and proton transport.

To model the wetting behavior of the CCL composite material, a novel conceptual approach is proposed based on an extensive literature review: the degree of alignment describes the state of molecular ordering of sidechains and backbones in the ionomer thin film and was directly linked to its wetting properties. From this rationalization, macroscopic wetting behavior of the CCL can be deduced. The analysis of the model results supports a crucial hypothesis: lowering the Platinum loading renders the CCL

more prone to flooding, caused by a successive shift of molecular alignment as Platinum particle concentration on the support surface is reduced, which eventually triggers an inversion from hydrophobic to hydrophilic properties.

Extending the wettability model, the common approach of considering water uptake via capillary condensation was refined by including adsorption processes at Platinum nanoparticles, carbon surface, and ionomer. After deconvoluting water uptake, the application of a percolation-based approach could partially reproduce the experimentally observed behavior but also revealed a particular mismatch with the model results for low-Pt-loaded materials. Thus, this works hints, in accordance with a hypothesis from the literature, that connection to the proton supply network might be provided in thin films of adsorbed water, even when the pore space is not fully flooded.

Proton transport properties were calculated from direct numerical simulations for a wide parameter space covering various ionomer morphologies. Based on the statistical information provided from the composition model, a stochastical image generation process was developed. Essential structural features shaping proton conductivity were extracted and coined into an analytical approach based on percolation theory. The model-based analysis of experimental data from the literature attributed deviating trends at identical CCL composition to different regimes of ionomer morphology.

A list of design principles for fuel cell developers was compiled from the results of the different models, thereby proposing concrete levers and measures to tweak and improve fuel cell performance. Additionally, disruptive approaches to overcome limitations regarding Platinum loading, e.g, the chemical modification of carbon support surface, were devised and were found to align with efforts from recent experimental works. With regard to the ongoing extensive efforts in PEMFC research and development, the insights obtained from model-based analysis of experimental data exemplify how structure-based models can guide the interpretation and design of experiments, and ultimately enable acceleration and steering of iterative laborious materials development cycles.

Eventually, the thorough comparison of model results and experimental data revealed emerging gaps in the understanding of structure-property relation in PEMFC catalyst layers, such as an suspected enhanced proton mobility in ionomer thin films and the ambiguous mechanism for Platinum utilization by water in low-Pt-loaded cells, and thereby lays the groundwork for future experimental and theoretical works.

Kurzfassung

Strukturbasierte Modellierung von Katalysatorschichten für Protonenaustauschmembran-Brennstoffzellen

Doktorarbeit verfasst von Wolfgang Olbrich

Brennstoffzellen werden eine wesentliche Rolle in künftigen Energiesystemen einnehmen, wo sie als effiziente Energiewandler fungieren und Strom aus erneuerbarem Wasserstoff erzeugen. Protonenaustauschmembran-Brennstoffzellen (PEMFC) werden wegen ihrer Robustheit, Effizienz und Kompaktheit bevorzugt und vollziehen gerade den Übergang von Prototypen und Nischenanwendungen zum breiten, kommerziellen Einsatz. Die dazu laufende Forschung und Entwicklung muss weitreichende Ziele für Lebensdauer, Leistungsdichte und Kosteneffizienz erfüllen. Dazu muss die gesamte Zelle, insbesonders die Kathodenkatalysatorschicht (CCL), von der Atom- bis zur Systemebene verbessert und optimiert werden. Die Entwicklung von CCL-Materialien benötigt umfassende mathematischen Modelle, welche die gesamte Kausalkette von den Herstellungsparametern der Tinte, über die resultierende Mikrostruktur, bis hin zu den makroskopischen Eigenschaften und schließlich zu den operativen Leistungskennzahlen beschreiben.

Im Rahmen dieser Arbeit wurden die folgenden drei, miteinander verbundenen Forschungsthemen adressiert: Erstens fehlt für die Bildung der agglomerierten CCL-Struktur in der Tinte ein quantitativer Ansatz, der die Ursache-Wirkungs-Beziehungen zwischen den Tintenparametern und der resultierenden Mikrostruktur beschreibt. Zweitens erfordern die Zusammenhänge zwischen molekularen und mesoskaligen Merkmalen der Katalysatormikrostruktur und wasserbezogenen Eigenschaften (Benetzungsverhalten, Wasseraufnahme, Platin-Anbindung und der Anfälligkeit der CCL für Fluten) einen umfassenden, skalenübergreifenden Ansatz, um die Grenzen einer rein empirischen Betrachtung zu überwinden, insbesondere im Hinblick auf das Ziel, die Platinbeladung in PEMFCs weiter zu senken. Drittens deuten experimentelle Literaturdaten auf einen signifikanten Einfluss der Ionomer-Morphologie auf die Protonenleitfähigkeit innerhalb der CCL hin, der von verfügbaren Modellen aus der Literatur in der Regel vernachlässigt wird, aber im Zusammenhang mit Bemühungen zur Erhöhung der Stromdichte der Zelle an Bedeutung gewonnen hat. Methodisch wurden diese Forschungsfragen durch einen grundlegend strukturbasierten Modellierungsansatz angegangen, der es erlaubt, die Kette aus Ursache und Wirkung von der molekularen bis zur makroskopischen Skala nachvollziehbar zu machen.

Ausgehend vom CCL-Zusammensetzungsmodell zur Beschreibung der Strukturbildung in der Katalysatortinte wurde die stückweise, selbsttätige Agglomeration von gelös-tem Ionomer und Pt/C-Partikeln in einem analytisch-mechanistischen Ansatz abgebildet, aus dem zwei Schlüsselparameter abgeleitet wurden: Ein Ionomer-Dispersionsparameter, der die Tendenz des Ionomers zur Selbstaggregation oder Filmbildung erfasst, und die initiale Ionomer-Filmdicke. Die Modelllösung umfasst die Porengrößenverteilung und die Ionomermorphologie der endgültigen CCL-Mikrostruktur und wurde direkt zur Parametrierung der Modelle für Benetzungsverhalten und Protonentransport verwendet.

Zur Modellierung des Benetzungsverhaltens des CCL-Materials wird nach umfassender Analyse der relevanten Literatur ein neuer konzeptioneller Ansatz vorgeschlagen: Der

Ausrichtungsgrad beschreibt den Zustand der molekularen Anordnung der Seiten- und Hauptkette im Ionomer-Film und ist direkt mit den Benetzungseigenschaften verknüpft. Aus dieser Beschreibung lässt sich das makroskopische Benetzungsverhalten der CCL ableiten. Die Analyse der Modellergebnisse stützte dabei eine entscheidende Hypothese: Eine Verringerung der Platinbeladung macht die CCL anfälliger für Fluten, verursacht durch eine sukzessive Verschiebung der molekularen Ausrichtung mit abnehmender Platin-Konzentration auf der Oberfläche des Kohlenstoffträger, wodurch schließlich die Eigenschaften der CCL von hydrophob zu hydrophil umgekehrt werden.

Zur Erweiterung des Benetzbarkeit-Modells wurde der gebräuchliche Ansatz, die Wasseraufnahme als reine Kapillarkondensation zu beschreiben, verfeinert, indem Adsorptionsprozesse an Platin-Nanopartikeln, Kohlenstoffoberfläche und Ionomer einbezogen wurden. Nach erfolgreicher Aufschlüsselung der Wasseraufnahme konnte die Anwendung eines auf Perkolationtheorie basierenden Ansatzes das experimentell beobachtete Verhalten teilweise reproduzieren, zeigte aber auch eine deutliche Diskrepanz zu den Modellergebnissen für niedrig-Pt-beladene Materialien. Somit deutet diese Arbeit in Übereinstimmung mit einer Hypothese aus der Literatur darauf hin, dass eine Anbindung an die Protonenversorgung eventuell durch einen dünnen Wasser-Film hergestellt werden kann, auch wenn der Porenraum selbst nicht vollständig geflutet ist.

Die Protonentransporteigenschaften wurden anhand direkter numerischer Simulationen für einen weiten Parameterraum berechnet, der verschiedene Ionomermorphologien abdeckt. Auf der Grundlage der statistischen Informationen, die sich aus dem Zusammensetzungsmodell ergeben, wurde ein Verfahren zur Erzeugung stochastischer Bilder eingesetzt. Die wesentlichen strukturellen Merkmale, welche die Protonenleitfähigkeit prägen, wurden extrahiert und in einen analytischen Ansatz auf der Grundlage von Perkolationstheorie verarbeitet. Eine modellbasierte Analyse experimenteller Daten aus der Literatur führte voneinander abweichende Trends bei identischer Zusammensetzung der CCL auf verschiedene Regime der Ionomermorphologie zurück.

Aus den gesammelten Modellergebnissen wurde eine Liste von Designregeln für Brennstoffzellenentwickler zusammengestellt, in der konkrete Hebel und Maßnahmen zur Optimierung und Verbesserung der Brennstoffzellenleistung abgeleitet werden. Vorgeschlagene disruptive Ansätze zur Überwindung von Einschränkungen bei der Platin-Beladung, z.B. die chemische Modifikation der Kohlenstoff-Oberfläche, decken sich mit aktuellen experimentellen Arbeiten in der Literatur. Im Hinblick auf die laufenden umfangreichen Bemühungen in der PEMFC-Forschung und -entwicklung unterstreichen die aus der modellbasierten Analyse experimenteller Daten gewonnenen Erkenntnisse, wie strukturbasierte Modelle die Interpretation und Planung von Experimenten anleiten können und letztlich eine Beschleunigung und Steuerung der iterativen, aufwendigen Materialentwicklungszyklen ermöglichen.

Schlussendlich hat der gründliche Vergleich von Modellergebnissen und experimentellen Daten neue Lücken im Verständnis der Struktur-Eigenschafts-Beziehung in PEMFC-Katalysatorschichten aufgedeckt, wie z.B. eine vermutete erhöhte Protonenmobilität in Ionomer-Filmen und das unvollständige Detailverständnis der Platin-Anbindung durch Wasser in Zellen mit niedriger Platin-Beladung, wodurch die Grundlage für zukünftige experimentelle und theoretische Arbeiten gelegt wurde.

Schlüsselwörter: Protonenaustauschmembranen-Brennstoffzellen (PEMFCs), Kathodenkatalysatorschicht (CCL), Katalysatorschichtmikrostruktur, strukturbasierte Modellierung, modellbasierte Materialentwicklung, Katalysatortinte, Platin-Anbindung, Ionomermorphologie, Benetzungsverhalten, Wasseraufnahme, Protonenleitfähigkeit.

List of abbreviations

ACL	anode catalyst layer
AEMFC	anion exchange membrane fuel cells
AFC	alkaline fuel cell
AM	agglomerate model
AIMD	*ab initio* molecular dynamics
CAMMP	Computational and Mathematical Modeling Program
CCL	cathode catalyst layer
CFD	computational fluid dynamics
CHP	coupled heat and power
CL	catalyst layer
CT	computer tomography
DFT	density functional theory
DMFC	direct methanol fuel cell
DNS	direct numerical simulation
DOE	Department of Energy
DMD	direct membrane deposition
ECSA	electrochemically active surface area
FE	flooded electrode
FF	flow field
GDE	gas diffusion electrode
GDL	gas diffusion layer
GHG	greenhouse gas
HSAC	high surface area carbon
IPCC	Intergovernmental Panel on Climate Change
LBM	lattice Boltzmann method
LSAC	low surface area carbon
MCFC	molden carbonate fuel cell
MD	molecular dynamics
MEA	membrane electrode assembly
MHM	macrohomogeneous model
MPL	microporous layer
NASA	National Aeronautics and Space Administration
NIP	Nationales Innovationsprogramm Wasserstoff- und Brennstoffzellentechnologie
NOAA	National Oceanic and Atmospheric Administration
ODE	ordinary differential equation
ORR	oxygen reduction reaction
PAFC	phosphoric acid fuel cell

PEM	proton exchange membrane
PEMFC	proton exchange membrane fuel cell
PFSA	perfluorosulfonic acid
PNM	pore network model
PSD	pore size distribution
PSM	pore scale model
PTFE	polytetrafluoroethylene
QM	quantum mechanics
RWTH	Rheinisch-Westfälische Technische Hochschule
SBM	structure-based model
SEM	scanning electron microscopy
SEM-EDX	scanning electron microscopy combined with energy-dispersive X-ray spectroscopy
SOEC	solid oxide electrolysis cell
SOFC	solid oxide fuel cell
TBD	triple phase boundary
TEM	transmission electron microscopy
UTCL	ultra thin catalyst layer
YSZ	Yttrium stabilized zirconia

1 Introduction

1.1 Climate change – challenge of the 21$^{\text{st}}$ century

Avoiding a critical escalation of climate change is commonly considered the biggest challenge of this century. Compared to the pre-industrial period from 1850–1900, the average global temperature has already risen by 1.1 degree – and keeps rising [1]. Therefore, the ongoing climate change is also referred to as *global warming*. This process is unparalleled in Earth's climate history. Even the fastest changes in earth's climate with similar magnitude were roughly 100 times slower [2]. Without exception, geological findings prove that these past events had disastrous effects for flora and fauna, causing mass extinctions and eradicated whole ecosystems and classes of species. Since all human life, and the societal stability, ultimately depends on intact ecosystems and habitable climate, climate change poses a serious thread to all humanity.

The International Panel for Climate Change (IPCC) collected unequivocal proof that the root cause of global warming are human-caused emissions of green house gases (GHG) [3]. As the most prominent, carbon dioxide (CO_2) from usage and combustion of fossil fuels, e.g., natural gas, coal, and oil, contributes 66% to the total GHG emissions [4]. The recently emerging field of climate attribution science clearly linked the latest global increase in natural disasters, such as droughts, floods, storms and irreversible soil erosion to ongoing global warming [5–7].

The mechanism of global warming is well understood and explained by the green house effect. Sunlight heats the earth surface, which emits infra-red heat radiation back to space. Earth's heat radiation is partially absorbed and reflected by green house gasses in the atmosphere, which are acting like the windows of a green house. The balance of absorbed energy from sunlight and heat loss by infra-red radiation determines the global average temperature. In fact, the naturally occurring green house ensures a habitable climate on earth. However, an increase of GHGs in the atmosphere alters this sensitive balance and shift earth's climate to higher temperatures.

The closer the rise in global temperature gets to 2 degree, an unstoppable climate disaster becomes more likely. Scientific climate system models concordantly predict that the risk of triggering tipping elements in the global climate system (e.g., loss of the tropical rainforests, melting of arctics and alpine ice shields, or collapse of the oceanic streams) sharply increases between 1.5 and 2 degree [8]. These tipping elements are irreversible and their collapse accelerates global warming even further. A chain-reaction can occur, causing the global temperature to rapidly jump by 4 degree or more in second half of the 21$^{\text{st}}$ century – even without further anthropogenic GHG emissions.

Tab. 1.1: CO_2 emissions by sectors, globally and in Germany from the year 2021 [10, 11].

	Germany		Global	
	Mt CO_2	fraction	Mt CO_2	fraction
energy production	235	34.9%	13972	37.7%
mobility and transportation	147	21.8%	7490	20.2%
households and buildings	120	17.8%	3343	9.0%
industrial production and processes	168	24.9%	7954	21.4%
other	4	0.6%	4337	11.7%
total	**673**		**37100**	

In the year 2015 the international community of nations recognized the enormous thread at the United Nations Climate Change Conference in Paris and committed themselves to keep the rise in mean global temperature to well below 2 degree above pre-industrial levels, and pursue efforts to preferably limit the increase to 1.5 degree [9]. The so-called Paris agreement was signed by 184 of the 193 nations and acts as the global guideline for national GHG emission reduction policies. Theses policies typically estimate a remaining budget of GHG emission before the limit of the Paris agreement is reached.

The IPCC estimates the remaining global CO_2 emission budget that would allow holding the 1.5-degree-limit with 50% probability to be 500 Gt [12], counting down from 2019[1]. At present, the annual worldwide emissions of CO_2 already exceed 37 Gt (see Tab. 1.1). Therefore, rapid reduction in CO_2 emissions must be achieved within this decade. Germanys current goal is a 65% reduction of GHG by 2030 (compared to 1990 levels) and full climate neutrality until 2045 [13]. The transformation of the German national economy towards climate friendliness is commonly referred to as *energy transition* (german: Energiewende), and indicates that the change of technological means of energy production and conversion are directly linked with climate protection goals. Some of the necessary technological transformations in the energy system, especially the role of hydrogen and fuel cells, are subject to the following section.

---

[1] In April 2023, during the finalization of this thesis, the according estimate of remaining CO_2 budget was less than 270 Gt – or 6 years and 2 months remaining at current GHG emission rate. A most recent estimate can be tracked online: `https://www.mcc-berlin.net/forschung/co2-budget.html`

1.2 Energy transition and fuel cells

Politically set emission goals ultimately have to be turned into actions. Tracking down emissions to sectors, i.e., mobility, industry, heating, food production, etc., allows to estimate the urge for technological and societal changes in different areas of production energy and goods. The majority of CO_2 emission originates from energy generation, industrial production and processes, and mobility and transportation (see Tab. 1.1). At present, energy generation and mobility rely on combustion technologies. Power plants burn coal, natural gas or other fossil energy carriers to provide electricity, whereas mobility is driven by combustion engines running on oil-based fuels, like Diesel, Gasoline, and Kerosene. Transforming the existing energy system towards climate-friendly energy sources and converters, calls for alternative technologies that do not rely on fossil fuels. So-called renewable energy sources, mainly wind and solar power, which are abundant in nature, can be harvested in form of electricity. In 2022, electricity from such sources already provided 46.2% in the German grid [14]. The sectors heat and mobility obtained 17.3% and 6.8% of their energy demand from renewable sources. In total, 20.4% of the German energy demand was renewable-based. Further action is required from Germany to achieve climate neutrality, especially in the latter sectors. Direct electrification, e.g., replacing combustion engines with electrical drives or replacing a gas heater with a heat pump, has the potential to resolve a major part of CO_2 emission [15, 16]. As sector coupling is favored due to efficiency gains and the versatility of electricity, the classical sector barriers will become more permeable in the future. However, a physical energy carrier is without alternative in numerous applications that can be classified into three main fields of demand [17, 18]:

1. **Chemical agents**: The majority of highly CO_2-intense chemical conversion processes forming the backbone of modern industry cannot be replaced with mere electrical processes, and, therefore, demand hydrogen with prime priority over other applications. For instance, reduction agents are inevitable in steel production or chemical processes, such as the Haber-Bosch process for ammonia synthesis [19, 20].

2. **Matching asynchronous supply and demand**: As the production of electricity from wind and solar power naturally fluctuates daily and seasonally but the electricity demand is not fully flexible, a significant amount of energy must be stored and over-capacities installed as back-up. Conventional storage capacities for electricity, like in batteries or pumped hydroelectric energy storage, are tightly limited. Depending on the availability of electrical storage, excess electricity might be transferred in the form of hydrogen to others sectors (e.g., industry, heat, mobility) [18, 21], rendering installed over-capacities for renewable electricity generation economically more viable. For the rather extreme conditions of electricity demand exceeding the supply capacities and electric storage is exhausted, back-conversion of cavern-stored hydrogen might be an option to ensure ultimate energy grid stability.

3. **Long-haul and heavy-duty mobility**: As batteries have limited specific energy density, they are unsuitable for transport of goods over long distances, e.g., by trucks, trains or ships. Also numerous heavy duty applications in mobile industrial machinery must be provided with a high-energy storage medium [17]. Thus, for such applications, fuel-cell driven vehicles are the rather feasible option.
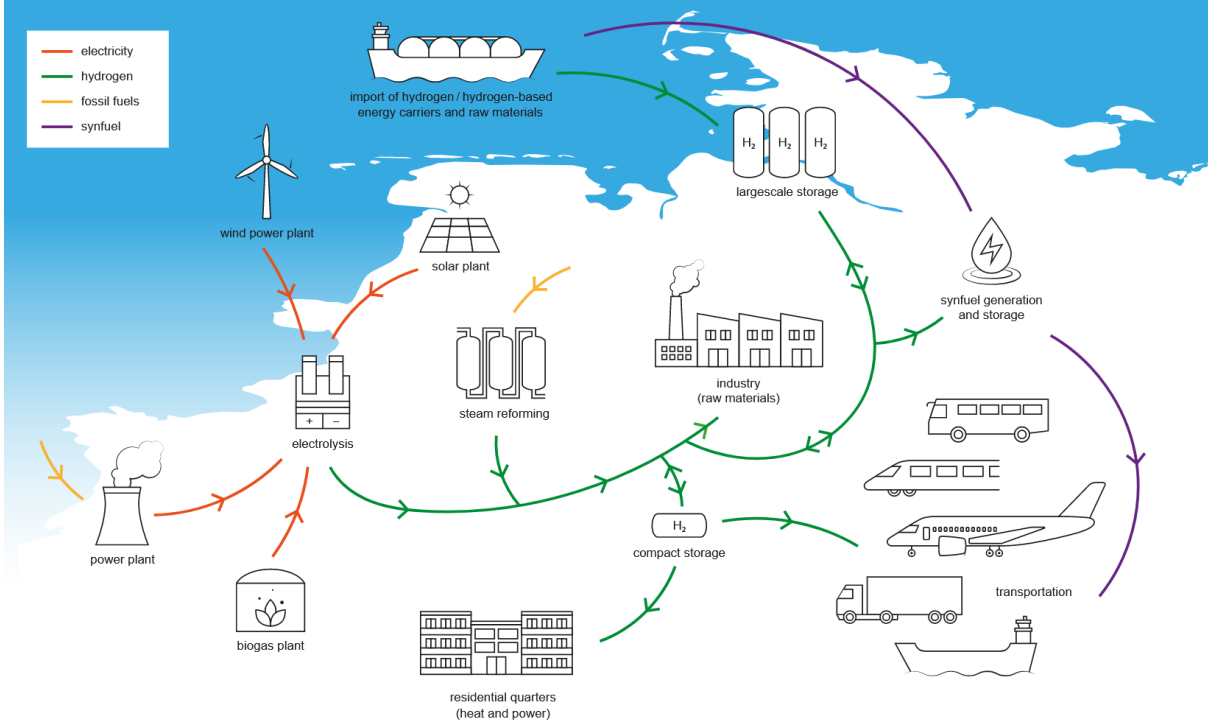
Fig. 1.1: Cross-sectoral network of hydrogen production, storage and usage in a future hydrogen economy, as projected by the German government [22]. The national hydrogen strategy foresees a common hydrogen infrastructure mainly relying on imported hydrogen or hydrogen carriers – but also features locally produced hydrogen from wind and solar power.

The primary molecule of choice to meet these demands will be hydrogen (chem. H_2). It can be produced from electricity via electrolysis of water and can be used directly in chemical processes, can be stored in gas caverns, and be used as a fuel for mobility [18]. In 2020 the German government released it's national hydrogen strategy [22], projecting a roadmap for deployment of an H_2 economy in Germany. By 2030, annual hydrogen demand is estimated to reach 56 to 93 TWh [23], i.e., approximately the double of the current demand for fossil-generated hydrogen. During the 2030s this number might even double again. Current research and development address this strategy, covering all elements of the future hydrogen economy and renewable energy system (depicted in Fig. 1.1), from electricity production, over electrolysis and hydrogen storage, to back-conversion of hydrogen to electricity, which is subject of research in this thesis.

The device of choice to turn hydrogen to electricity is the fuel cell since it acts as an energy converter transforming the chemical energy stored in hydrogen back to electricity. The history of fuel cells, their physical and technological fundamentals and current challenges in research will be discussed in the following sections.

1.3 Fuel cells – a historic technology for new challenges

Research and development of fuel cells spans over more than 200 years of history. They are not a recent invention of the 21st century but as old as the fundamentals of electrochemistry. This section reviews the evolution from first discovery to high performing nowadays fuel cells.

Fuel cells are a direct application of the fundamentals of electrochemistry, a field of science dating back to 1791 when Luigi Galvani described the link between chemical reactions and electricity on his essay *De Viribus Electricitatis in Motu Musculari Commentarius* (transl.: Commentary on the Effect of Electricity on Muscular Motion) [24]. He derived his conclusion from observing that the muscular contraction in organisms[2] can be triggered by electricity provided from a Copper-Zinc battery, the so-called galvanic cell. As the first, he postulated that the energy from chemical reactions can be harvested as electricity, which is the fundamental insight behind all applications of batteries and fuel cells.

During the 19th century the scientific method matured, research professionalized, and physics, chemistry and mathematics advanced rapidly. In this fruitful period the theoretical basis of classical electrochemistry emerged. Three scientists of this time are certainly to name here since they provided the essential set of theory for all research and development of electrochemical devises. In 1833 Michael Faraday described the quantitative relationship of charge and matter during electrochemical reactions [25], turning Galvani's qualitative observations into solid mathematical theory. The most fundamental contribution to the theory of electrochemistry was made by Walther Nernst in 1889 [26]. The Nernst-equation, named in his honor, links concentration of different reactants with cell voltage and describes the energetic equilibrium of the electrochemical reaction based on the laws of thermodynamics. The first kinetic theory of electrochemical reactions, which is still in use today, was proposed by Julius Tafel in 1905 [27], who introduced the overvoltage as the driving force of the reaction rate. Thenceforth, not only the equilibrium state of any electrochemical reaction could be described mathematically but also actual power-generating cells operating in non-equilibrium conditions.

The development of electrochemical theory was paralleled by experimental approaches to develop batteries and fuel cells. The idea to use hydrogen and oxygen to fuel an electrochemical cell was discussed for the first time by Sir William Grove in his publication *On voltaic series and the combination of gases by platinum* [30]. The publication is dated December 1838 but the original manuscript already appeared in October 1838. In a letter to the same journal, dated December 1838, too, Christian Friedrich Schönbein proposes the same idea and reports that he did preliminary experiments with platinum wire electrodes and hydrogen and oxygen dissolved in water to generate electricity [31]. He closed his letter with the correct prediction that the combination of fuels is the source of electric current, and that platinum will be the catalyst of choice for hydrogen/oxygen fuel cells:

---

[2] In fact, the concrete specimen in Galvani's research were the muscles of dead frogs' legs.

(a)

(b)
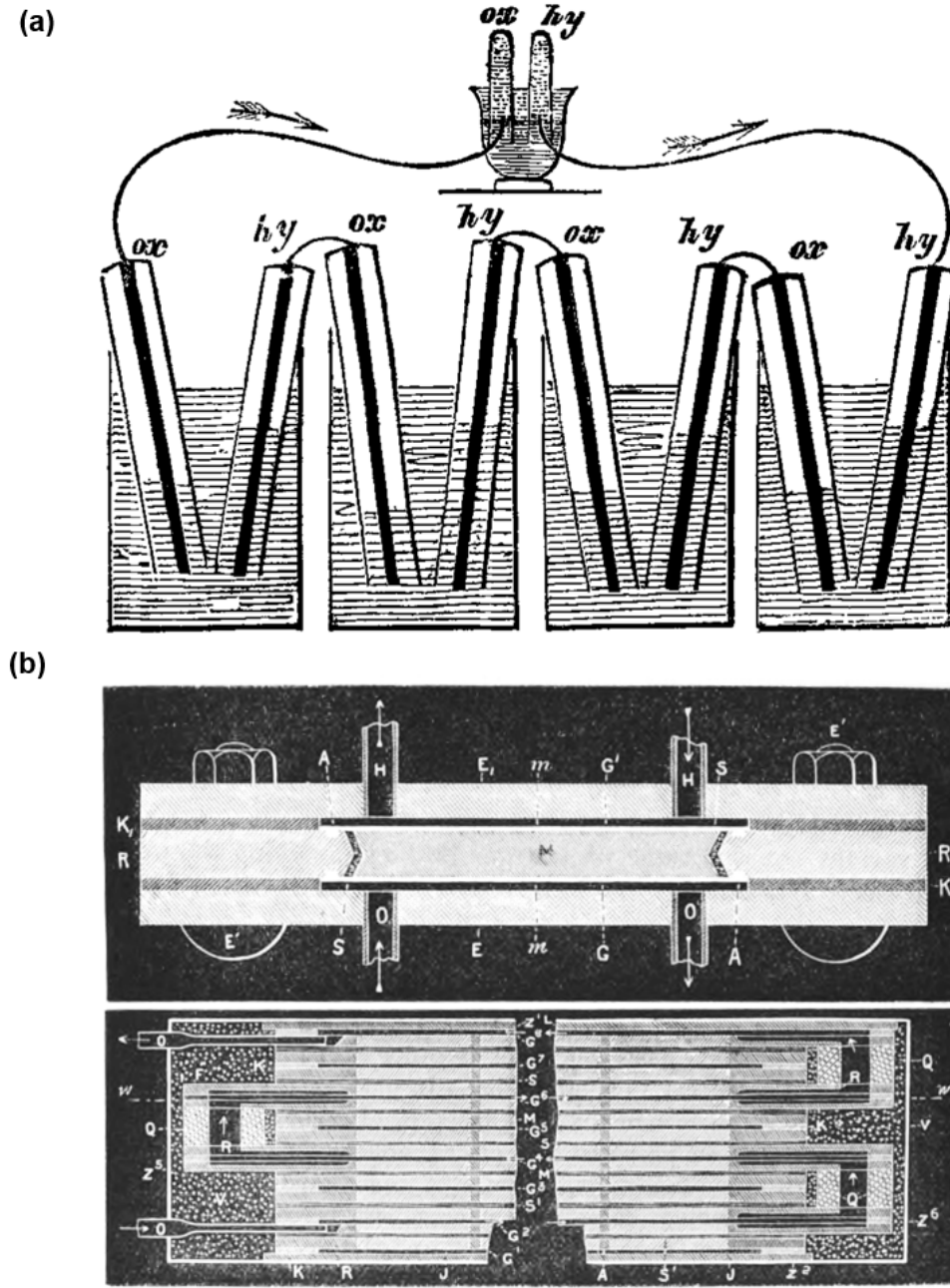
Fig. 1.2: **(a)** The first documented set-up of an hydrogen fuel cell, published by William Grove in 1842. The experiment includes a series of electrically connected gas cylinders filled alternately with oxygen or hydrogen. Each cylinder features a Platinum wire, and both gas and the wire were in direct contact with an sulfuric acid bath. The generated over-voltage of four such double-cells was sufficient to run a water electrolyzer connected to the set-up, demonstrating the electrochemical reversibility of water formation and splitting reactions. Illustration reproduced from Ref. [28], with permission from Elsevier.
(b) Blue prints of the fuel cell designed by Mond and Langer intended for power generation. The stacked, planar design of electrodes, separator and gas supply is clearly visible and still in place in state-of-are fuel cells. Reproduced from Ref. [29], with permission from The Royal Society.

> *"If the mere contact of the two different fluids mentioned there were the real cause of the current obtained, it is obvious that the same current ought to be produced whether the fluid be connected with the galvanometer by means of gold, or if they be connected with the instrument by that of platina wires; but the result being determined by the nature of the connecting wires, and platina being known to favour the union of hydrogen and oxygen."*

Shortly after, in 1842, it was again William Grove who delivered experimental proof of the first complete hydrogen/oxygen fuel cell using platinum electrodes as proposed by Schönbein and himself [28] (see Fig. 1.2 (a)). Grove used the term *gaseous voltaic battery*, indicating that the development of a cell being continuously fueled and operated as an energy converter was not in the scope of his research.

A major leap was made in 1889 (the same year Walther Nernst published the equation named after him), when Ludwig Mond and Carl Langer presented *"a new form of gas battery"* [29]. Taking up the work of Grove and Schönbein, they engineered a stacked cell layout, depicted in Fig. 1.2 (b), and, thereby, introduced vital design principles encountered in modern fuel cells. Perforated platinum sheets acted as combined current collectors and catalyst, and were separated by an acid-soaked diaphragm. Hydrogen and oxygen were fed continuously into the cell, which provided several amperes at 0.73 V. Mond and Langer calculated the corresponding efficiency to be 50%, outperforming any steam or combustion engine available at that time by far. Interestingly, classical challenges in fuel cell engineering that are still relevant in today's research were identified, e.g., the ionic conductivity of the electrolyte, sufficient electrical contacting and severe mass transport resistances. Seeking practical application, Mond and Langer demonstrated the use of coal gas and air as abundant fuels. In addition to their pioneering experiments, they coined the term *fuel cell*.

By the end of the 19th century, individual members of the scientific community were euphoric that electrochemical technology, i.e., batteries and fuel cells, would soon overcome steam engines. Some focused on turning coal to electricity directly, like Mond and Langer. The most prominent advocate of fuel cells was Nobel price laurate Wilhelm Ostwald. He merged the experimental and theoretical insights on fuel cells collected in the 19th century and developed the first holistic explanation of electrochemical processes in side an operational fuel cell, i.e., formulated a theory accounting for anode and cathode side reactions, ion migration, and potential drop. Furthermore, Ostwald developed a vision about the future of electrochemistry, which he described in 1894 as followed [32]:

> *"Haben wir ein galvanisches Element, welches aus Kohle und dem Sauerstoff der Luft unmittelbar elektrische Energie liefert, dann stehen wir vor einer technischen Umwälzung, gegen welche die Erfindung der Dampfmaschine verschwinden muss. Denken wir nur, wie sich das Aussehen unserer Industrieorte ändern wird! Kein Rauch, kein Ruß, keine Dampfmaschine, ja kein Feuer mehr."*

> Transl.: *"If we have a galvanic element which directly supplies electrical energy from coal and the oxygen in the air, then we are facing a technical revolution against which the invention of the steam engine must vanish. Just think how the appearance of our industrial towns will change! No more smoke, no more soot, no more steam engine, no more fire."*

Reducing CO_2 emissions was certainly not the intention of Ostwald's vision. However, his concepts of efficiency and cleanliness of energy conversion kept their outstanding relevance until today – especially since the lines cited above were paralleled by two events that led humanity on a different path of energy production. On 27th August 1859, the first major oil reservoir was discovered at Oil Creek in Titusville, Pennsylvania. The American oil rush had begun. In 1893, one year before Ostwald wrote his vison of *"no more fire"*, inventor and engineer Rudolf Diesel published his invention of a robust and improved combustion engine, which featured reciprocating pistons driven by burning oil-based fuel in a cylindric chambers – a technology that became omnipresent in the 20th century.

During the first half of the 20th century, fuel cells remained in the shadow for a while. Anyway, in 1924, Alfred Schmid published an article on gas-diffusion electrodes, i.e., catalyst layers with a large internal surface, which facilitates high current densities [33]. Further, he was the first to identify the necessity of a triple-phase boundary of gas, electrolyte and current collector, which is the vital spot where the electrochemical reaction occurs. This vital design principle still drives improvements in modern fuel cell development. In the same period, in 1932, the alkaline fuel cell was developed by inventor and engineer Francis Thomas Bacon [34]. This novel type of fuel cell used a concentrated base instead of an acid for electrolyte, featured low-cost nickel catalysts, and enabled high-power fuel cells. With these improvements, Bacon's fuel cell reached 5 kW of power output – roughly 2000 times more then the cell of Mond and Langer.

In 1955, a similar break-through followed for acidic fuel cells. Thomas Grubb, researcher at General Electric, used a sulphonated polystyrene ion-exchange membrane as electrolyte. This modification massively improved ionic transport and allowed to run pressurized cells. In 1958, Grubb's colleague, Leonard Niedrach, invented a way of depositing platinum directly onto the polymer membrane. The so-called Grubb-Niedrach cell was highly robust and even accepted to take hydrocarbons and air as fuels [35, 36].

The improvements made by Bacon, Grubb and Niedrach suddenly rendered fuel cells a vital technology for one of humanity's cutting edge endeavors: manned spaceflight[3]. Pratt & Whitney licensed Bacon's U.S. patents for use in the U.S. space program to supply electricity and drinking water during space missions. The high power output, low weight, and the convenience of hydrogen and oxygen being readily available from the spacecraft tanks made fuel cells the perfect energy converters in the Gemini program (1965–1966) and the Apollo missions (1961–1972). The Gemini program used the Grubb-Niedrach design, the Apollo program used Bacon's alkaline fuel cells. Each of the fuel cell power plants, exemplary depicted in Fig. 1.3 (a), used in the service modules of the Apollo missions contained 31 separate cells connected in series and delivered a maximum of 2.3 kW [38].

---

[3] In a historical anecdote, honoring the merits of Francis Bacon and the crucial role of fuel cells for manned space flight, U.S. President Richard Nixon welcomed Bacon to the White House, and said to him: *"Without you Tom, we wouldn't have gotten to the moon."* [37]
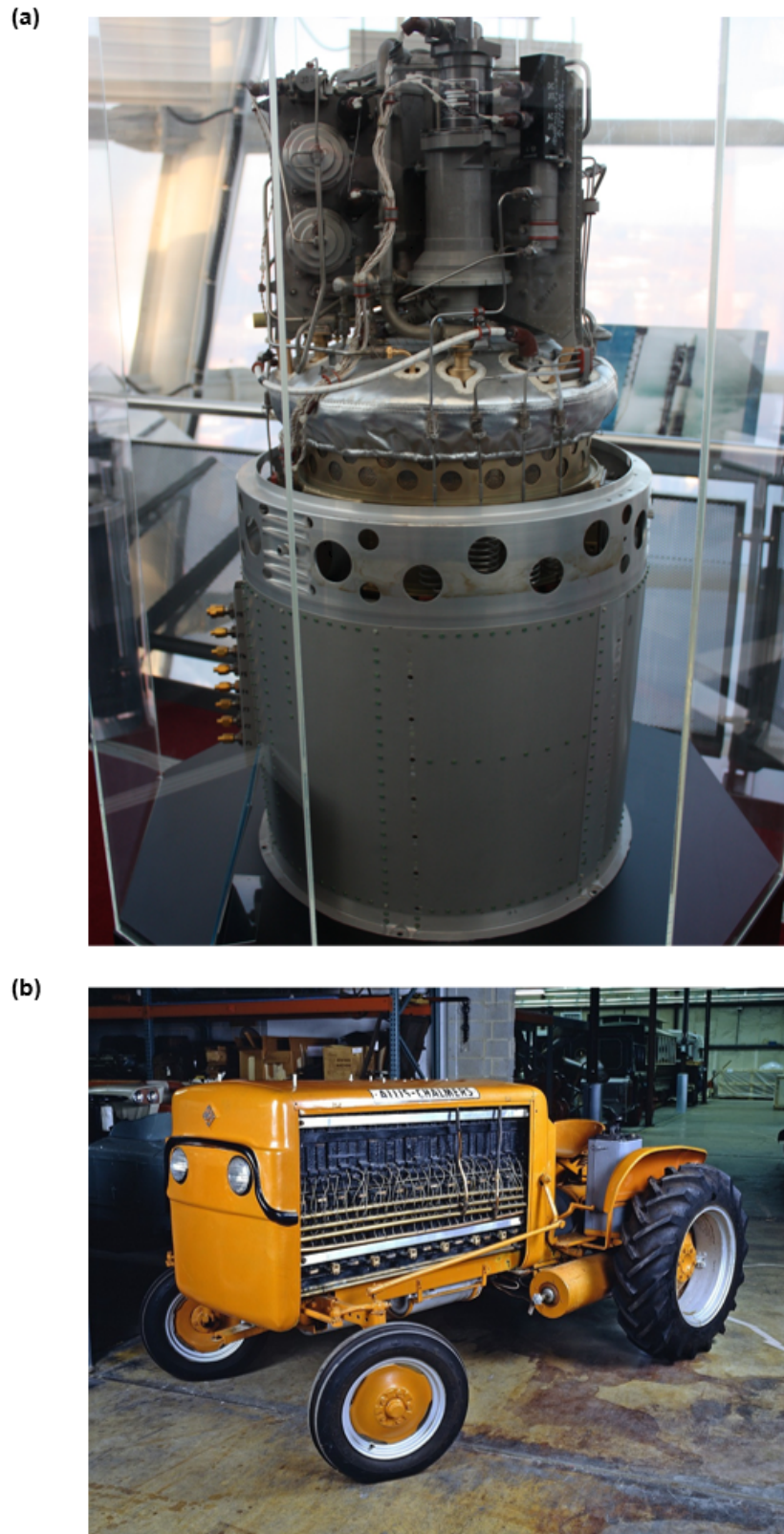
Fig. 1.3: **(a)** Single fuel cell unit as used in the NASA Apollo missions' service modules. Image reproduced under creative commons licence CC BY-SA 3.0 from Ref. [39].
(b) The first vehicle equipped with a fuel cell was the D12 tractor build by Harry Ihrig at Allis Chalmer company. Image provided by the National Museum of American History [40].

In the 1960s, inventors also engineered multiple earth-bound applications of fuel cells. Here, the company Allis-Chalmer and the team around Harry Ihrig took a leading role and demonstrated the first fuel cell driven vehicle in 1959 [41]: the D12, a 15 kW fuel cell tractor (see Fig. 1.3 (b)). Other vehicles followed: a forklift (1960), a one-man underwater research vessel (1964), and a golf cart (1965). However, General Motors build the Electrovan, the world's first fuel cell automobile intended for individual transport, in 1966.

At the second half of the 20$^{\text{th}}$ the path finally cleared for modern fuel cells suitable for broad commercialization. Novel materials, preparation techniques, and improved cell design led to significant increase in current density and power output. Especially polymer electrolyte cells advanced as DuPont invented perfluorosulfonic acid (PFSA) polymers in the 1960s – well known under the brand name Nafion$^{\text{®}}$. PFSA materials finally allowed to manufacture thin and stable membranes. Two researchers at Los Alamos National Laboratories, Ian Raistick and Thomas Zawodzinski, eventually established today's state-of-the-art for polymer electrolyte fuel cells. Raistick merit lays in the invention of gas diffusion electrodes impregnated with PFSA polymer in 1989, which resolved the issue of poor ionic contact between catalyst and membrane [42, 43]. During the 1990s Zawodzinski and coworkers developed numerous characterization techniques of fuel cell components and materials, contributed to theory and modeling, and recognized the crucial role of water management in polymer electrolyte cells [44, 45].

Around the year 2000, a sharp raise in publications numbers of fuel cells related research could be noticed [46] and fuel cell research diversified and specified widely. This novel interest in fuel cells is driven by the raising awareness for climate change and the urge for alternatives to combustion engines and triggered also first major commercial interest. For instance, in 2007, Honda started the first commercial series production Honda Clarity, a fuel cell car.

At present, over 180 years after their first discovery, fuel cells finally get attention by major national research programs. Germany has been specifically supporting fuel cell research (and other hydrogen related technology) since 2007 with the *National Hydrogen and Fuel Cell Technology Innovation Programme* (NIP) [47]. Until 2016, the German Federal Government and industry provided a total of 1.4 billion euros for technology promotion and demonstration projects. This path will be continued with the follow-up program 2016-2026 (NIP II) and aims to bring fuel cell mobility to market maturity in the next few years. Finally, after almost 130 years, Ostwald's vision of a cleaner energy system that builds on electrochemical devices, such as fuel cells, seems closer than ever. To eventually turn *"no more fire"* reality, mission and goal of engineers and scientists remain to advance the state-of-the-art of fuel cells, which is presented in the following sections together with the fundamental working principles of fuel cells.

1.4 Working principles of fuel cell technology

The key idea of fuel cells is that the combustion of a fuel with oxygen consists of two half-reactions, called oxidation and reduction. Oxidation refers to the process that one reactant releases electrons (here, hydrogen, the fuel),

$$H_2 \longrightarrow 2 \; H^+ + 2 \; e^-, \tag{1.1}$$

which are consumed by the other reactant (here, oxygen) in the other half-reaction called reduction,

$$^1\!/_2 \; O_2 + 2 \; H^+ + 2 \; e^- \longrightarrow H_2O. \tag{1.2}$$
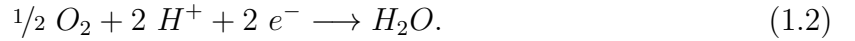
The combination of the half-reactions gives the complete reaction of the combustion,

$$H_2 + {}^1\!/_2 \; O_2 \longrightarrow H_2O. \tag{1.3}$$

In an electrochemical cell the half-reactions can be spatially separated into two half-cells that are allowed to exchange electrons and ions but not fuel or oxygen. By convention, the one half-cell facilitating the oxidation is called *anode*, the other one for reduction is called *cathode*.

Before the technical details of reaction and transport of electrons, ions, fuel and oxygen are explained further, the overall thermodynamics shall be outlined at this point as they manifest one primary particularity of fuel cells: their excellent efficiency. The maximum efficiency of conventional power generators that convert heat to mechanical work, and subsequently electricity, is limited by the fundamental laws of thermodynamics. This limitation was discovered in 1824 by Nicolas Léonard Sadi Carnot [48]. The Carnot-efficiency, named after him, is the ultimate limit for any thermal power generator and is defined as

$$\eta_{Carnot} = 1 - \frac{T_{cool}}{T_{heat}}, \tag{1.4}$$

where T_{hot} and T_{cold} refer to the temperature of the source of heat and the coolant temperature, respectively. State-of-the-art combustion engines typically reach an efficiency of 40-50%, corresponding to a heat source of approximately 600 °C and cooling with ambient heat. Since mechanical stability and corrosion become much harder to handle at increasing temperature, and the maximum combustion temperature is intrinsically limited for any fuel, conventional combustion might never significantly exceed this limit. This brief excursus demonstrates the superior feature of fuel cells that they obey a different limitation. Since no Carnot-type heat-to-power conversion takes place in a fuel cell and, instead, the energy released from the reaction is harvested directly as electricity, the theoretical electrochemical efficiency depends only on the Gibbs free energy reaction and the reaction enthalpy,

$$\eta_{elec} = \frac{\Delta_{\mathrm{R}}G}{\Delta_{\mathrm{R}}H}. \tag{1.5}$$

Applying the numbers for the formation of water from H_2 and O_2 ($\Delta_R H^0 = -285.8\,kJ\,mol^{-1}$ and $\Delta_R G^0 = -237.2\,kJ\,mol^{-1}$, values for liquid water formed at $T = 295\,K$) reveals a maximum efficiency of 83%. This is the fraction of energy released from the chemical reaction that can be turned into work in an ideal cell, the rest will be released as heat. Thus, hydrogen fuel cells are potentially twice as efficient as conventional combustion engines, rendering them the superior energy converter from a thermodynamical viewpoint.

The Nernst equation translates the energetic quantities of thermodynamics to the equilibrium (or *reversible*) cell voltage, a fundamental quantity in electrochemistry,

$$\Delta E = \Delta E^0 - \frac{RT}{z_e F} \ln \prod_{i=1}^{k} a_i^{\nu_i}. \tag{1.6}$$

The superscript ^{0} indicates values at standard conditions, i.e., $298\,K$, $1\,bar$, $1\,M$ of each reactant and product, unmixed reactants and products. Applying the reactants from hydrogen combustion, and assuming ideal gases and the activity of water not affected by pressure, yields

$$\Delta E = \Delta E^0 + \frac{RT}{z_e F} \ln \left(\frac{p_{H_2} p_{O_2}^{0.5}}{(1\,\mathrm{bar})^{1.5}} \right), \tag{1.7}$$

where $\Delta E^0 = 1.229\,V$ and is called standard cell potential, which is a constant for a given pair of half-reactions and is directly related to the standard Gibbs free energy of the reaction,

$$\Delta E^0 = -z_e F \Delta_R G^0. \tag{1.8}$$

Equation (1.8) is derived by considering the work accomplished by a set of z_e electrons transferred at given voltage. The Nernst equation and its link to the free energy reveals a crucial insight: any irreversibility in the process of electrochemical energy conversion, i.e., work being dissipated to heat, results in a voltage drop of the cell. Therefore, all fuel cell development opting for maximized efficiency intends to reduce resistances since current times resistance results in a voltage drop. The main contributors originate from distinct processes that naturally have to occur in an electrochemical cell:

1. **Chemical reactions:** activation resistance depending on the kinetics of the electrochemical reactions on a given catalyst.

2. **Ionic transport:** resistances caused by limited mobility and concentration of ions in the electrolyte.

3. **Electron transport**: ohmic resistances in the electron pathway,

4. **Fuel supply:** mass transport resistances.

Actually type (4) resistances are not directly part of the electrochemical cell processes. However, if transport limitation in the fuel or oxygen supply pathway occurs, the local concentration drops dramatically at the catalyst's reactions sites, leading to an increased activation resistance, i.e., increasing (1). These four processes listed above find their physical counterpart in the different essential components of any fuel cell, each being described further in the following section.

1.5   Fuel cell design and essential components

The set of essential functional elements can be derived from fundamental processes occurring in every fuel cell device, namely the half-cell reactions, ionic connection via an electrolyte, and electronic contacting and transfer of electrons over a closed circuit (see Fig. 1.4). A continuous fuel supply, water removal and mechanical integration must also be ensured in technical fuel cells by their auxiliary components. Generally, fuel cell design in practically relevant devises is planar, i.e., the components described in the following have a flat and thin geometry that can be stacked to larger high-power devices, which, therefore, are being called *stacks*, containing numerous single fuel cells.

1.5.1   Catalyst layer

The half-cell reactions always need a catalyst that tears down the activation energy barrier, thereby enabling reaction rates sufficient to ensure high current densities. As an illustrative example, the activation energy barrier of the direct reaction of H_2 and O_2 molecule (approx. $250\,kJ\,mol^{-1}$ [49]), is roughly 5 times higher than the activation energy for the Pt-catalyzed reaction ($40...70\,kJ\,mol^{-1}$ [50]). Typically, solid catalyst are used to obtain a mechanically stable layer.
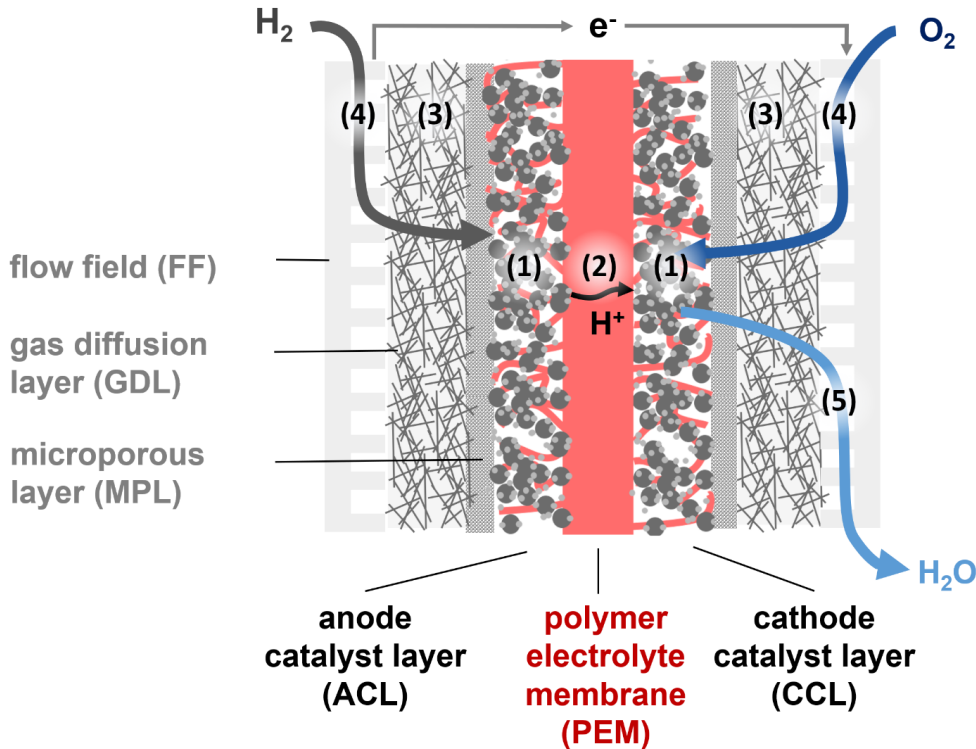

Fig. 1.4: Basic layout of a state-of-the-art PEM fuel cell. Essential processes include **(1)** electrochemical conversion reactions at the catalyst layers, **(2)** proton migration across the membrane, **(3)** electron conduction between reaction sites and the outside of the cell, **(4)** gas supply of fuel and oxygen, and **(5)** removal of water as reaction product.

13

At the catalyst surface the three reactants (molecules, electrons, ions) involved in the half-cell reaction must come to the same spot to react. However, the electrons, ions and molecules travel on different pathways, i.e., physically separated phases. Therefore, the concept of a the triple phase boundary (TPB) was developed, which implies to maximize the triple-phase contact in the catalyst layer to increase the effective reaction rate. Since the catalyst layers is of finite thickness, the electronically conductive phase (typically the catalyst support or the catalyst itself), the ion-transporting phase (the electrolyte), and the void space for fuel and oxygen supply must interpenetrate to come into contact, be well dispersed to ensure high TPB, and be well connected at the same time to feature continuous pathways. If a liquid electrolyte is involved, fuel or oxygen can dissolve in the electrolyte. Such a liquid electrolyte carrying the reactants can wet the catalyst over a large continuous surface domain, thereby turning the *triple* phase boundary into a *binary* phase boundary, which exceeds the TBD by multiple orders of magnitude regarding the number active reactions sites [51]. However, because diffusion of molecules in liquids is limited, macroscopically the concept of a TPB still applies. As discussed later, these features render the catalyst layer the most challenging component in the fuel cell.

1.5.2   Separator and electrolyte

To obtain two separated half-cells, a medium that blocks gas and liquid molecules but allows ions to cross easily must be inserted between the anode and cathode catalyst layers. To reduce the voltage drop caused by ion transport through the separator (typically a flexible film-like membrane or thin solid layer), it should be as thin as possible. Further, ion concentration and mobility should be high in the separator material to render a suitable electrolyte. However, if these requirements are followed, the permeability for gasses and liquids also increases as no material is ideally blocking diffusion of molecules. Two approaches are conceivable designing the separator: the functionality of physical separation and ion transport are facilized by distinct phases, i.e., an electrolyte is embedded in an inert solid matrix (e.g., encountered in alkaline fuel cells); or a bi-functional material, i.e., a solid electrolyte is used.

The unwanted transfer of oxygen or fuel to the other half-cell is called *cross-over* and imposes the risk of severe efficiency loss if the half-cell reactions are not electrochemically separated anymore, i.e., they cannot contribute to the generation of electric power. The design of membranes or electrolyte layers as thin as possible whilst ensuring mechanical stability and durability remains a major challenge in fuel cell development [52].

1.5.3   Gas diffusion layer, bipolar plate and flow field

Since the energy released in the fuel cell shall be harvested as electricity, the reaction sites in anode and cathode catalyst layers must be well connected to a continuous electrical network that collects the electric current. Typically, a multiscale design is applied to create a pathway from the reaction site to the outside of the devise. On the material level of the catalyst layer, an electronically conductive support is required if the electronic conductivity of catalyst material is insufficient.

The outer mechanical support structure holding the fuel cell in place serves as electrical lead-out of the total current generated by the cell and is manufactured from conductive

materials, such as steel or graphite. In fuel cell stacks, this component separates neighboring cells and transfers voltage and current from one cell to the next. Since this inserted sheet or plate faces the anode side of one cell and the cathode side of the neighboring one, it is commonly referred to as *bipolar plate*.

The exposure of bipolar plates to over-voltage triggers corrosion processes, which are electrochemical reactions, too. Thus, an ongoing challenge is to coat or treat current collector materials to prevent corrosion. However, such measures come typically to the price of increased contact resistances within in the electrical pathway and are subject to ongoing efforts in fuel cell development [53].

Similar to the electronic pathway, fuel and oxygen molecules must be transferred continuously from the outside of the cell to the reaction site inside the catalyst layers. Again, a multiscale design is typically applied. On the outside gas manifolds are needed that direct fuel and oxygen into channel-like structures integrated into the bipolar plates, which are called *flow fields*. Here, distinct flow field designs exist: co- or counter-flow, referring to relative direction of fuel and oxygen on cathode and anode side. Typically, flow channels are straight and parallel, distributing the fuel and oxidant media across the cell area. Serpentine, wave-form, or circular channel geometries are also in use.

Even more challenging is the reverse pathway that water has to take when leaving the cell. In low temperature cells, liquid water condenses in large amounts. If accumulated in the porous layers of the cell, oxygen supply can be cut. Such *flooding* of the cell can cause severe voltage drops and is intensively addressed in current research and development.

1.5.4 Auxiliary components and fuel cell system

To obtain a practical and robust device, additional stack components are needed that are not directly related to the electrochemical processes inside the cell, such as a mechanism of screws and springs for upholding clamping pressure, a sealing concept, a robust casing, and thermal insulation. On system level a fuel tank system, fuel recirculation, power electronics, and cooling sub-system for thermal management are needed integrate the stack into its technological environment and render it eventually a usable device.

1.6 Current state-of-the-art fuel cell technologies

Each of the previously introduced fundamental components must be realized in any fuel cell. However, fuel cells can differ widely in their design of these components, the materials used and their operation conditions. Therefore, the state-of-the-art in fuel cell technology features a variety of distinct fuel cell technologies, which will be discussed in the following.

Fuel cells can be categorized as distinct types by the material used as electrolyte, which determines mainly the catalysts used and the operating temperature. Thus, the alternative common classification by operating temperature distinguishes between low temperature cells, operating below or little above 100 °C, whereas high temperature cells require several hundreds degree Celsius (typically > 500 °C) to function.

Each type and class of fuel cell has distinct advantages and unresolved challenges. Therefore, the different types of fuel cells currently available are reviewed and analyzed with regard to their technological maturity and most advantageous applications. Table 1.2 provides an overview on fuel cell technologies discussed here; listing the chemistry of anode, cathode and electrolyte; operating temperature; efficiency; costs; and typical stack power output.

1.6.1 Proton exchange membrane fuel cells

Proton exchange membrane fuel cells (PEMFCs) are a type of fuel cell technology that uses a perfluorosulfonic acid (PFSA) polymer membrane as an electrolyte. They are known for their fast response time, robustness and high power density. Due to these unique characteristics, PEMFCs are the first choice in applications that require high-power output, a compact design and quick start-up time, such as in fuel cell vehicles and portable power devices. The massive development efforts during recent decades established PEMFCs as a mature and commercialized technology. By now, mass produced devices are available, resulting in a significant advance in the price per nominal output power. Fuel cells developed for the space program in the 1960s had came with to the price of 600,000 $/kW. At present, commercial PEMFC stacks with nominal costs below 100 €/kW are released to market.

Commonly, PEMFCs are operated at around 80 °C to ensure fast reaction kinetics and low ionic transport resistance. Since the membrane must be well hydrated to uphold its ability to conduct protons, increasing the temperature further leads to successive dry-out and performance loss. Further, the electrodes and the polymer material suffer from accelerated degradation at higher temperatures.

In PEMFCs, water management is crucial. The cell requires liquid water, which provides active reaction sites in the catalyst layer and is the essential medium for proton transport in both membrane and catalyst layer. However, liquid water is generated as the inevitable reaction product from the combination of hydrogen and oxygen. An excessive accumulation of liquid water can lead to flooding of the cell, especially at high current densities, cutting the fuel supply at the electrodes. Managing the balance of water generation and removal poses an ongoing field of research and development, where multiple distinct approaches are sought, such as improved thermal management, optimized fluid dynamics, or tailored wetting properties of the electrode materials.

Tab. 1.2: Comparison of available fuel cell technologies by type, catalyst material and half-cell reactions, electrolyte material, thermoelectrical efficiency, nominal cost per power output, and typical devise power, classified in low and high temperature cells. Data collected from Refs. [54–57].

Type	Half-cell reactions and catalyst	Exchanged ion and electrolyte material	Operating temperature	Thermoelectric efficiency at operational conditions	Cost per nominal power output	Typical power output per device
Low temperature cells						
Proton exchange membrane fuel cell (**PEMFC**)	Catalyst: Platinum nanoparticles on carbon support. Anode: $H_2 \rightarrow 2H^+ + 2e^-$ Cathode: $1/2\,O_2 + 2\,H^+ + 2\,e^- \rightarrow H_2O$	H^+ in hydrated PFSA membranes, e.g., Nafion®	Typical: 80°C. Operational from freeze start to 120°C	>60%, prototypes in development striving to reach 65...70%	Stack: < 100 $/kW, striving to reach <40 $/kW	1...100 kW
Phosphoric acid fuel cell (**PAFC**)	Catalyst material and half-cell reaction as in PEMFC	H^+ from molten phosphoric acid in SiC matrix	100...210°C	40...45%	3000...4500 $/kW	5...400 kW, 100 kW module size
Alkaline fuel cell (**AFC**)	Catalyst: Pt/C catalysts, also Nickel/Nickel oxide can be used. Cathode: $1/2\,O_2 + H_2O + 2e^- \rightarrow 2OH^-$ Anode: $+2OH^- \rightarrow 2H_2O + 2e^-$	OH^- in porous diaphragms soaked with concentrated KOH solution.	Typical: 40...75°C Apollo missions: 200...230°C	Up to 60%	104...170 $/kW	1...100 kW
Anion Exchange Membrane Fuel Cell (**AEMFC**)	like AFC	OH^- in anion-conductive polymer membranes, used with or without concentrated alkaline electrolyte solution	50...90°C	Up to 60%	approx. 400 $/kW	1...100 kW
Direct methanol fuel vell (**DMFC**)	Anode with Pt/Ru catalyst: $CH_3OH + H_2O \rightarrow CO_2 + 6H^+ + 6e^-$ Cathode with Pt catalyst: $1.5\,O_2 + 6H^+ + 6e^- \rightarrow 3_H2O$	H^+ in hydrated PFSA membranes, e.g., Nafion®	50...120°C	approx. 30...40%	Not available	0.01...10 kW
High temperature cells						
Solid Oxide Fuel Cell (**SOFC**)	Cathode, using conductive Peroskite-type oxides: $H_2 + O^{2-} \rightarrow H_2O + 2e^-$ Anode (Porous Ni/YSZ electrode): $1/2\,O_2 + 2e^- \rightarrow O^{2-}$	O^{2-} in solid state oxygen ion conductor: Yttrium stabilised zirconia (YSZ) with typically 8...9 mol% Y_2O_3 in ZrO_2	500...1000°C	Cell level: 60-65% System running on natural gas: 55...60%	Stack: 300-1200 $/kW System: 1000-4000 $/kW	up to 2 MW plants using multi-100 kW modules
Molten Carbonate Fuel Cell (**MCFC**)	Supported Nickel catalysts, as used for syngas processing or steam reforming. Anode: $H_2 + 2CO_3^{2-} \rightarrow 3CO_2 + H_2O + 4e^-$ Cathode: $CO_2 + O_2 + 4e^- \rightarrow 2CO_3^{2-}$	CO_3^{2-} in binary molten mixture of Li_2CO_3 and K_2CO_3, embedded $LiAlO_2$ matrix	650...1000°C	Cell approx. 55% System: close to 50%	3000...4000$/kW	300 kW...3 MW, realized by approx. 300 kW modules

1.6.2 Phosphoric acid fuel cells

The straightforward approach to increase temperature beyond 100 °C, thus, turning all water to vapor, which resolves the issue of flooding, requires a change in materials for the electrolyte. The hydrated PFSA can be replaced by liquid phosphoric acid. Such phosphoric acid fuel cells (PAFCs) share with PEMFCs the high power density but operate at temperatures around 100...210 °C. However, their efficiency and dynamic operation behavior lags behind PEMFC technology. Still, PAFCs are a mature fuel cell technology and have well-established niche application in stationary power generation in remote locations, often as combined heat and power (CHP) systems. Their increased operation temperature brings benefits regarding tolerances of fuel contamination, such as carbon monoxide and carbon dioxide, a more robust and compact heat removal systems, lower maintenance and higher reliability.

The costs of PAFCs are still relatively high. As in PEMFCs, the rare noble metal Platinum used as catalyst complicates further cost reduction. At present, Platinum is without foreseeable alternative in acidic cells. Other experimental and cheaper catalyst are not stable in the aggressive acidic environment or do not exhibit sufficient catalytic activity. Current efforts in fundamental research try to find novel catalyst but with no major break-through so far. The most promising approach is to maximize Pt utilization and reduce Platinum loading. Thus, commercially available acidic low temperature fuel cells will rely on Platinum for at least another decade.

1.6.3 Alkaline fuel cells and anion exchange membrane fuel cells

To sidestep the use of Platinum, alkaline fuel cells (AFC) can be used. This type of fuel cell uses an alkaline electrolyte, typically a concentrated potassium hydroxide solution. Under the alkaline conditions in AFCs, Nickel catalysts are stable and provide an excellent activity. AFCs are known for their high energy conversion efficiency, moderate-to-good power density, and ability to operate at a wide range of temperatures. Therefore, they are mainly used in industrial applications, or in niche applications, such as remote sensing and monitoring, where their long life and high efficiency is beneficial. As described in the section 1.3, AFCs have a long history of use, including space flight. As a drawback they are not as compact as PEMFCs since they require a rather heavy, electrolyte-soaked separator. Since the electrolyte is not spatially fixed, careful management of pressures on anode and cathode side is mandatory for AFC devices, complicating their application in compact and portable devices. However, they continue to be a promising fuel cell technology as abundant and cheap catalyst materials can be used. This potential cost reduction in commercial applications, particularly in industrial and niche applications, renders AFCs a compelling technology in the fuel cell technology landscape.

The recent development of anion exchange membrane fuel cells (AEMFCs) seeks to combine the compactness and robustness of PEMFCs with the cost advantages of AFCs. An electrode design known from PEMFCs is used, featuring a polymer membrane and polymer-bound gas diffusion catalyst layers, where instead of an acidic PFSA polymer an anion-conductive polymer is used. A plethora of chemical structures based on positively charged nitrogen-containing functional groups is conceivable, with first promising results

proving the concept to be feasible [58]. At present, these novel electrolyte materials suffer from rapid degradation [59]. Futher, AEMFCs are notoriously inactivated by carbonate forming from CO_2 entering the cell with the air intake. Nonetheless, over the last decade, AEMFCs advanced substantially through the development of new materials and the optimization of system design and operation conditions. With further fundamental research, AEMFC might stay an interesting concept for possible future fuel cells.

1.6.4   Direct methanol fuel cells

Among low temperature fuel cells, direct methanol fuel cells (DMFCs) gained a certain popularity. The compact handling of a liquid fuel that does not require complex gas circulation systems lead to some applications in small portable devises and also industrial mobile applications. In contrast to hydrogen, methanol, a broadly established platform chemical, is easy to produce, transport and store. Materials used and cell design of DMFCs widely resemble PEMFCs. Additional to Platinum, Ruthenium, which is even more expensive and rare, must be used as a catalyst to facilitate the bond cleavage between Carbon and Hydrogen in the methanol molecule. Indeed, the total loading with Platinum and Ruthenium exceeds PEMFCs by one order of magnitude. Another drawback is the intense methanol crossover, requiring a dilution of the fuel down to 3%wt in water, preventing feasible upscaling of DMFC technology to high-power or mobile applications. For a power output of more than 0.3 kW the indirect methanol fuel cell, i.e., externally converting methanol to hydrogen, reaches a higher efficiency and is more cost-efficient[60]. Despite these limitations, some DMFC application where commercialized in portable electronic devices, such as laptops and mobile phones or backup power solutions. Overall, DMFCs are a relatively novel and developing fuel cell technology. Nonetheless, they have a certain potential for use in portable and mobile applications, where their small size, high energy density, and low operating temperature are advantageous.

1.6.5   High temperature fuel cells

Solide oxide fuel cells (SOFCs) and molten carbonate fuel cells (MCFCs) are fundamentally different from low temperature fuel cells since they thermally mobilize ions (oxygen ions and carbonate ions, respectively) from solid ceramic electrolytes or molten salt. The elevated temperature level of several hundreds degree Celsius is difficult to facilitate in mobile or portable devises but is feasible in industrial scale applications and backbone energy systems. The valuable high-temperature waste heat allows for excellent integration into industrial processes where a combined heat and power demand must be met. Research and development of both technologies dates back almost a century, with first commercial applications appearing around the year 2000, whereas MFCFs were always roughly one-to-two decades ahead of SOFCs since MFCFs components are cheaper, easier to manufacture and more robust.

MCFCs use a molten mixture of lithium, sodium, and potassium carbonates fixed in an alumina matrix as electrolyte, thus require operating temperatures around 600-800 ℃. Carbonate is formed from CO_2, which has to be added to the air stream, and is released on the anode side again. Therefore, MCFCs requires some auxiliary heavy machinery,

such as a CO_2 cycling system and are not as compact and modular as SOFC systems. Nevertheless, MCFCs are a mature fuel cell technology with a long history of use, offering a good balance of performance and efficiency for certain power generation applications. However, the costs of MCFCs are still relatively high compared to other forms of power generation.

SOFCs typically use Yttria-stabilized zirconia electrolyte that conducts oxygen ions above 600 °C. The cell design is significantly more compact than in MCFCs as no matrix-liquid separator is used. Key feature of SOFCs is the high energy conversion efficiency, especially in combined heat and power use. The estimated cost per kilowatt for SOFCs is still relatively high. Therefore, current efforts in research and development focus on reducing the cost of SOFCs and improving their performance and efficiency, and increasing their commercial viability. By making these improvements, SOFCs already surpassed MCFCs regarding cost effectiveness and have the potential to become a major contributor to the transition to a clean and sustainable energy system. The ability to run both on both renewable hydrogen and natural gas renders them highly suitable for the transition phase from fossil to renewable energy carriers.

Nickel catalysts used in SOFCs and MCFCs were adapted from hydrocarbon processing, such as steam reforming, and profit from very fast reaction kinetics at elevated temperatures, effortlessly cracking hydrogen-carbon and oxygen-carbon bonds with fast kinetics. Therefore, high temperature fuel cells can be fueled with hydrocarbons, natural gas, biogas, flue gas, or CO rich gas, and have excellent tolerance against contamination in hydrogen fuel. On the downside, degradation issues are faced, especially during temperature cycling and interrupted operation due to the thermal stress imposed on the materials, leading to mechanical disintegration and delamination of the electrodes. Nevertheless, commercially available SOFC and MCFC systems are proven to run reliable and will find their applications as stationary mid-to-large scale energy converters.

1.7 Proton exchange membrane fuel cells: current challenges in research and development

Since all fuel cell technologies have advantages in certain fields and niches of application, it is likely that not a singular technology will cover all demands in a future energy system. At present, for mobile, flexible and mid-size fuel cells devices, as in trucks or trains, PEMFCs are the technology of choice. PEMFCs feature a superior efficiency and the lowest price of all fuel cell technologies, and have their path cleared to broad commercial application. SOFCs might follow shortly after, mainly covering industrial scale heat and power generation. Other technologies, such as PAFCs, AFCs or DMFCs might cover niche markets, as the energy transition progresses during the next decade.

Despite the relatively high maturity of PEMFCs, challenges for science and engineering remain, e.g., further reduction of Platinum loading, performance enhancement and improvements of durability and liftetime. In the last years, research efforts for PEMFC technology were widely oriented along national programs and targets. The most prominent one, the United States' Department of Energy (DOE) fuel cell program for transport applications, has set several ultimate targets for PEMFC technology [61], explicitly aiming on a broad commercial adaption of fuel cell technology in the mobility sector. By the year 2030 an 80-kW-PEMFC system for mobile application should meet the following key requirements:

1. **Cost per net output power**: <30 $/kW (2015 status: 60 $/kW)

2. **Fuel conversion efficiency**: >70% system efficiency (2015 status: 60%)

3. **Durability and lifetime**: Uphold efficiency for >8000 automotive drive cycles (2015 status: 3900 cycles).

Further, the DOE program defines targets to increase power density per weight and volume, i.e., enhancing the compactness and portability of the system, and extended cold start ability.

The targets listed above all intersect in one key component: the cathode catalyst layer (CCL). Since the CCL carries the major fraction of Platinum loading, it is the primary cost driver of the electrode membrane electrode assembly (MEA). According to cost estimates in the literature [62, 63], the ultimate DOE target can be reached when the MEA's costs are reduced by 45%. Some cost efficiency gains can be expected from scaling to mass production. However, the catalyst cost is predominantly a material cost and does not fall with the number of cells produced per year. In contrary, an increased demand for Platinum might trigger a raise of Platinum price, thus even partially rebound the gains from reduced production costs. Therefore, the search for alternative catalyst material to eliminate Pt usage is ongoing. However, even the most promising candidates still contain Pt as the catalytic base material [64, 65].

To overcome this hurdle, one lever to cut down the costs per kilowatt is to use less of expensive catalyst materials, another is to increase power density per catalyst material used, i.e., catalyst utilization should be maximized, the voltage drop in the cell should be minimized, and current density increased. Minimizing the voltage drop also contributes to

the efficiency target. However, these two levers often counteract each other. In particular, reducing the Platinum loading in the catalyst layer can lead to severe unexpected performance losses and poor durability. Approaches to explain and resolve the over-proportional performance losses will be discussed in chapter 2.

Polymer electrolyte fuel cell catalyst layers are complex high-tech materials (see section 2.1) and, despite recent advances, it remains a major challenge for researchers to reveal, disentangle and rationalize the numerous interactions residing in the CCL microstructure. A comprehensive understanding of structure-property relations of the CCL material might enable fuel cell developers to further advance catalyst layer properties, contributing to the targets for cost, performance and lifetime.

With a plethora of CCL material variations tested over the decades, a large empiric database on experimental results is available in the literature [57, 66]. Thus, it is a key task for fuel cell developers to derive universal correlations and design rules for state-of-the-art CCL materials from this rich database. Adequate mathematical models are required to formulate insights from experimental data [67, 68]. Once such models reliably capture the essential structure-property relations of the CCL material, analytical models can become powerful tools to accelerate and guide materials development.

State-of-the-art methods and capabilities of modeling fuel cell performance and catalyst layer properties will be surveyed in following chapter. The necessity of correlating the CCL microstructure with its properties will be carved out and discussed with regard to holistic fuel cell design. Based on this analysis, research gaps currently present in the realm of microstructure models for PEMFC catalyst layers will be identified.

2 Modeling of PEM fuel cell catalyst layers

This chapter introduces the catalyst layer (CL) microstructure as the subject matter of this work in section 2.1, including the interwoven functionalities and properties provided by the microstructure. The historic evolution and origins of CL microstructure modeling approaches are reviewed in section 2.2 and state-of-the-art methods across the different size scales of elements of CL microstructure are evaluated in section 2.3.

2.1 Structural and functional features of catalyst layers for PEM fuel cells

The multi-faceted features of CL microstructure serve as the basis for fundamental assumptions in structure-based models. In the following, a thorough description of the catalyst layer microstructure is provided, including its composition and the properties and intervoven functionalities of each component and phase constituting the CL.

Common state-of-the-art PEM fuel cells employ gas diffusion electrodes (GDEs) as the prevailing catalyst layer design. GDE-type catalyst layers have a thickness range of 2 to $10\,\mu m$ and are composed of a porous solid catalyst material impregnated with a proton-conductive polymer, commonly referred to as *ionomer*. The term *gas diffusion electrode* originates from the essential feature of providing a porous structure that allows gases to diffuse deep into the layer, where they are consumed by the electrochemical half-cell reactions. In contrast, flooded electrodes (FEs) are ionomer-free and have a thickness range of $\leq 200\,nm$ and are therefore also referred to as ultrathin CLs (UTCLs). This second class of catalyst layers operates under different concentration and transport regimes, as the pore space of UTCLs is fully saturated with liquid water, causing oxygen to diffuse as a dissolved species, and proton transport is regulated by the wall charge density of pores [69, 70]. Since GDE-type catalyst layers can vaporize liquid water in the porous structure, they have superior robustness regarding the highly sensitive water balance of UTCLs, which may never dry out and simultaneously fail to effectively remove liquid water generated during operation. Because of this major drawback, FE-type catalyst layers were not a viable approach for further PEM catalyst layer development, whereas GDE-type catalyst layers represent the state-of-the-art in PEM fuel cell technology and will be focused on in the following.

2.1.1 Base materials, ink process and structure formation

GDE-type catalyst layers for PEM fuel cells are commonly fabricated from three distinct base materials: Platinum catalyst, carbon support, and PFSA ionomer. Anode and cathode typically vary in thickness and composition. Apart from that macroscopic differences, they contain the same principle components:

1. **Platinum** serves the active catalyst for the electrochemical conversion reactions, thus is the pivotal component. It is deployed to the catalyst layer in the form of nanoparticles with radii of 1 to 5 nm. Depending on the synthesis approach, Platinum nanoparticles can be deposited predominantly inside the primary pores or on the outer surface of carbon particles [71].

   Metallic Platinum is the outstanding catalyst of choice. Since the invention of fuel cells it is known to exhibit an exceptional electrocatalytic activity for the oyxgen reduction reaction [30, 72] (and even higher for the hydrogen oxidation reaction). Among all catalyst materials being considered for PEM fuel cells, Platinum has remained superior in terms of stability and lifetime requirements [73]. Additionally, Platinum is able to withstand harsh oxidizing conditions and various microscopic degradation mechanisms encountered in the chemical environment of PEM fuel cells [74–77]. However, proper adjustments in Platinum particle sizes and close control of operating conditions, monitoring especially the electrode potential in the cathode, are a necessity to meet lifetime requirements for commercial applications.

   The usage of nanoparticles is motivated two-fold. First of all, the volumetric density of reactions sites, i.e., Platinum surface, in the GDE should be maximized. A planar Platinum electrode would allow a current density, in the order of $\approx 10 \ mA \ cm^{-2}$, referred to the geometric cell area. In a GDE-type catalyst layer, the available catalyst surface is typically a factor in the order of 100 higher, and proportionally bringing up the current density to values $> 1 \ A \ cm^{-2}$. Secondly, Platinum utilization should be maxized, i.e., as little as possible Platinum should be hidden inside massive Platinum structures. Using nanoparticles and providing a different mechanical support (see carbon support below), allows to trim Platinum loading to economically feasible levels. Indeed, the Platinum mass loading of catalyst layers is a crucial factor in determining the economic viability of proton exchange membrane fuel cells and is defined as the mass of Platinum per unit area of the cell (units of $mg \ cm^{-2}$).

2. **Carbon support** carries the catalyst particles, acts as the electronically conductive medium, and provides mechanical support. It features particle radii of 5 to 20 nm and a varying amount of microscopic pores inside the carbon particles with a diameter range of 2 to 10 nm [78]. Various types of carbon materials can be distinguished in terms of particle size, morphology, internal structure and surface properties [79, 80]. These structural properties determine the electronic conductivity, durability and performance of the CL material [79, 81]. Two classes of carbon can be distinguished: high surface area carbons (HSAC) with large internal surface are of several hundreds cm^2 per g provided by a large number of micropores; and low surface area carbons, which are rather compact. Ketjen black and Vulcan carbon are the most common choice for HSAC and LASC, respectively.

3. **Ionomer** is used with the primarily intention to boost proton conductivity. Furthermore, it also supports agglomeration of the Pt/C particles and porous structure formation, and alters wetting behavior of the layer. The chemical structure of proton-conductive PFSA ionomers is based on a polytetrafluoroethylene (PTFE) backbone, which is then substituted with perfluorinated-polyether sidechains that carry sulfonic acid group (-SO$_3$H) on their tail-end [82]. The sufonic acid groups are highly hydrophilic, thus water aggregates around them, resulting in the ability for significant water uptake, i.e., the ionomer material can swell when wetted. The hydrophobic backbones adhere to each other, forming stable interweaved bundels, which provide mechanical integrity of the material [83, 84]. This balance of stability against complete solvation in water (i.e., minimal amount of PTFE backbone required) and maximized proton conductivity (i.e., maximal concentration of -SO$_3$H desired) sets the typical equivalent weight (EW) of ionomer used in PEM fuel cells to 900...1100 $^g/_{mol_{SO_3H}}$. The most commonly used PFSA polymer is Nafion$^{\circledR}$, which is known for its high proton conductivity, good mechanical properties, and excellent chemical stability.

The state-of-the-art manufacturing process for PEMFC electrodes employs mixing an ink that contains all base material dispersed in a solvent, and a subsequent step of layer fabrication. The catalyst material is provided as Pt/C pre-synthesized powder, and ionomer is provided by suppliers as a dispersion in various solvents. Typical ink solvents are water, ethanol, isopropyl-alcohol, butyl-acetate and glycerine [85]. Ink processing is highly sensitive to thermal conditions, and method and duration of mixing. However, critical details of CL fabrication processes are rarely disclosed by manufacturers.

Large-scale production of fuel cell electrodes applies a decal-transfer process in which the catalyst layer is formed on carrier films and then transferred to the membrane by heat and pressure [86]. Rolls and band-conveyors facilitate a continuous mode of operation of the fabrication process. At lab scale and for low volume production, batch processes like doctor blade coating are used for ink deposition and static presses are used for hot-lamination. For larger production volumes, roll-to-roll processes are used. Recent developments employ direct deposition of electrodes onto GDL substrates via 3D printing [87] or ink-jet printing [88]. The latter process can also involve the deposition of the membrane onto the electrode via ink jet printing and is then called direct membrane deposition (DMD) [88]. Gravure printing and screen printing are also promising processes for cost effective mass production of catalyst layers [86]. A comprehensive review of deposition methods including novel experimental stage approaches can be found in Ref. [89].

During ink stage, the Pt/C catalyst particles aggregate and are partially encapsulated by ionomer, which does not enter the primary pores. Instead, it forms a skin-like thin ionomer film with $\approx$ 5...15 nm thickness [91–93]. The described structure can be recognized in Fig. 2.1 (a), which shows a SEM-EDX image of a CL provided in Ref. [90]. Figure 2.1 (b) illustrates the abstract picture of the agglomerated structure.

The porous network in the CL exhibits a bimodal pore size distribution with primary pores, which are provided by the carbon support and some intra-agglomerate pore space (size range from 5 to 20 nm), and inter-agglomerate (or secondary) pores (size range from 20 to 100 nm) between them [94–97]. Although the fractions and sizes of primary and secondary pores may vary depending on the carbon support used and the process param-
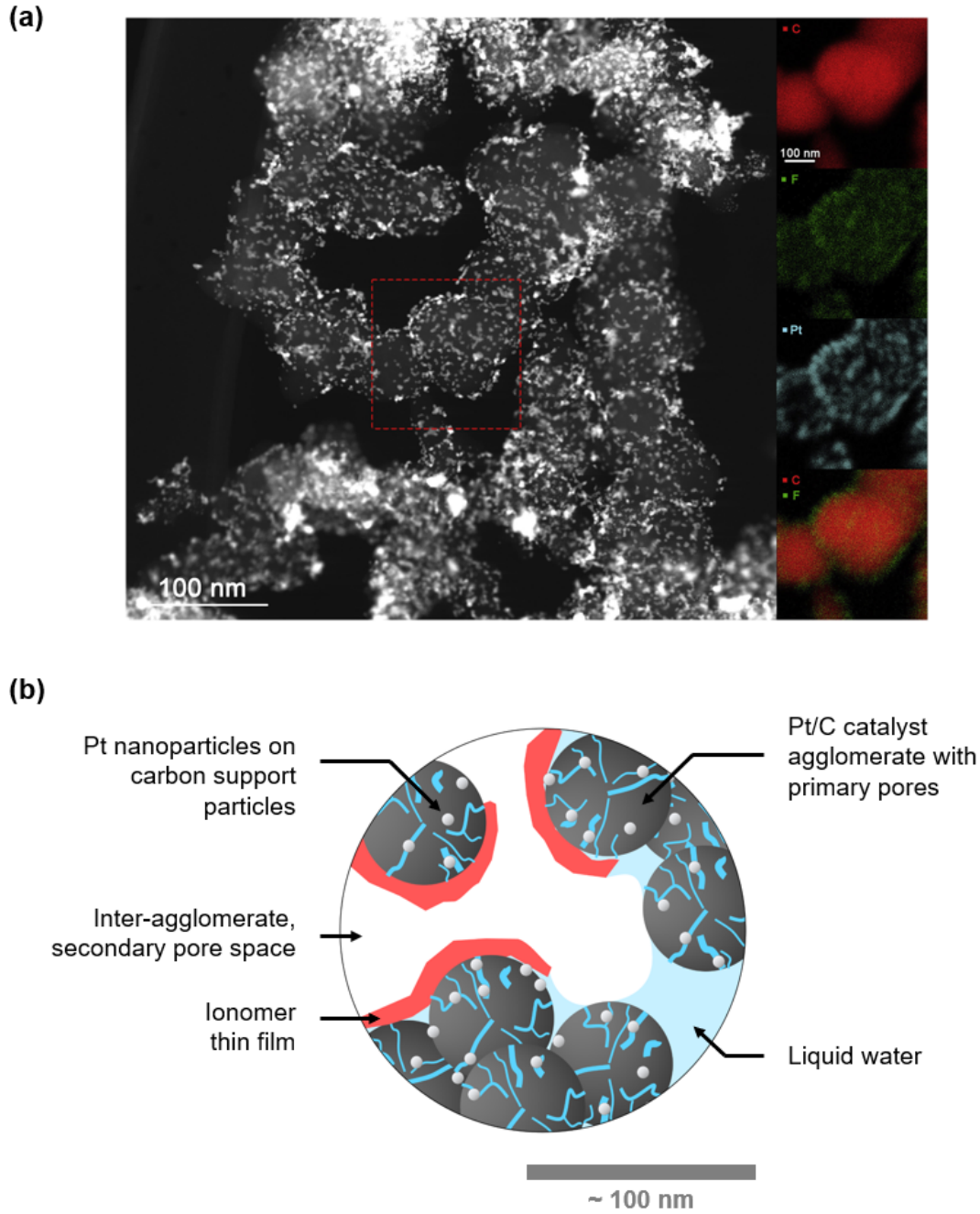
Fig. 2.1: Structure of a PEM fuel cell cathode catalyst layer: **(a)** experimental SEM-EDX image provided in Ref. [90] (with permission from Elsevier), resolving the spatial distribution of Carbon (from ionomer and carbon support), Platinum nanoparticles (also visible as spots of high contrast), and Florine (part of the ionomer); and **(b)** illustration of the according micro-structural picture featuring agglomerated Pt/C catalyst particles, ionomer film, and condensed water in the porous network.

eters employed during ink stage, the bimodal nature of the pore structure is considered a generic and vital feature of GDE-type CLs. A strong indication that agglomeration processes shape the CL microstructure was first observed in porosimetry studies that revealed a bimodal pore size distribution (PSD) [95, 96, 98, 99] and seen also in molecular dynamics simulations [100]. The structure of PEMFC catalyst layers is difficult to observe *ex situ* and to keep intact in microsections prepared from CL material. Thus, agglomerates are difficult to discern in microscopy studies or using other structural characterization methods. Moreover, their impact on performance remains controversial or at least difficult to quantify [101].

Closer investigation of the agglomerate structure and ionomer morphology revealed that the ionomer film is typically distributed unevenly across the agglomerated structure [93, 96, 102–104], with significant variations in both coverage and thickness. Additionally, there have been reports of large ionomer aggregates that are not part of the thin film [104–106]. This composite picture of aggregated and dispersed ionomer is supported by experimental works indicating that, on the one hand, the volume fraction of secondary pores decreases as more ionomer is used in the catalyst layer ink composition [107], which explains the dispersion in the secondary pores. On the other hand, there is no strict anti-correlation between porosity and ionomer content, hinting that not all of the ionomer is used to fill the secondary pore space. Such variations in ionomer morphology can have a significant impact on the percolation behavior of the ionomer network or on the volume fraction and network properties of gas-filled pores [108–110]. The ionomer morphology in the CL is not only determined by the composition of the ink but further affected by Platinum loading, type of carbon support, type of ionomer, ink solvent, and processing parameters, such as processing times and thermal treatments [111–113]. Ongoing experimental efforts aim to better understand how the agglomerated base-structure and the inter-agglomerate ionomer morphology can be tuned and which structures yield optimal cell performance [104, 114–117].

2.1.2 Phase interactions and catalyst layer functionality

In the following, the phenomena and processes inside the cathode catalyst layer (CCL) are primarily addressed. Water is generated on the cathode side of the cell by the oxygen reduction reaction (ORR), rendering the CCL's functionality more complex than for the anode catalyst layer (ACL). Furthermore, the ORR features significantly slower kinetics than the hydrogen oxidation reaction in the ACL, thus is rather performance limiting.

The essential functionalities and peculiar properties of PEM catalyst layers can be disentangled describing the microstructure as four mixed and interpenetrating phases [72], which partially enable functionalities but simultaneously can impose side effects that impair the desired functionality of the layer:

1. The **solid phase (S)** comprises the Platinum catalyst and carbon support. Phase S determines basic electronic, electrostatic and electrocatalytic properties.

2. The liquid **water phase (W)** acts as the reaction medium and renders the catalyst active in the first place. Condensed water is abundantly present at the cathode CL since water is a half cell reaction product of the ORR. Water can condensate inside the pores or adsorb at surfaces of carbon, Platinum, and ionomer [94].

3. The **ionomer phase (I)** incorporates some water and forms its own percolating network with a high proton concentration across the catalyst layer. Furthermore, it strongly interacts with the water-wetted Platinum surface and determines the proton density at the microscale, and other properties, such as wetting behavior.

4. The **gas pore network (G)** that enables facile diffusion of oxygen gas and water vapour but can be replaced with phase W when the cell floods.

Phases S and W are indispensable for CL operation. At the interface of S and W, which includes the active reaction sites at Platinum nanoparticles and the electrochemical double layer, electrochemical activity, which is the key feature of the electrode, is provided. Therefore, a sufficient amount of W that wets the surface of S is a necessity. In contrast, a perfectly dry cell is not operational. The extent of Platinum utilization by phase W is a function of overall water uptake and the distribution of water in the pore space [78, 94, 95]. Here, a crucial distinction to be made is between the water-filling of primary and secondary pores. Water-filled pores bounded on all sides by Platinum or carbon, i.e, *all-metallic* walls, differ significantly from those bounded on one side by Pt/C and on the other side by an ionomer film, i.e, *mixed* walls [70, 118]. This difference leads to a wide range of interfacial reaction conditions at the pore scale in terms of local electrolyte phase potential and pH, resulting in spatial variations in the ORR rate and Pt dissolution rate. Therefore, how water distributes and triggers electrochemical activity remains subject to recent works in the literature [94, 119].

As seen for ultrathin ionomer-free CLs, a CL can function without phase I [120–122]. Thus, phase I is not pivotal for enabling electrochemical reaction in the first place. It rather acts as a booster which enhances the local proton density and thus local activity significantly. The effect can reach up to an order of magnitude [118, 123]. However, other studies have suggested an adverse impact of phase I on catalyst activity via adsorption of sulfonate anions, i.e., the head groups of the ionomer sidechains [124–126]. Effective interactions between S and I phases, which must be separated by an interfacial water layer,

control the local interfacial proton density and the catalyst activity. Surface modification of catalyst and support modulate these interactions and thus the interface structure and activity [117]. Furthermore, this local interface structure has an impact on the overall wetting behavior of the CCL [127], as discussed later on in this section. Despite the significance of the catalyst-ionomer interface at the microscopic level, several questions concerning its structure and properties remain unresolved. This includes the water layer's thickness between the Pt/C surface and ionomer film, the local ordering in the confined water layer's molecular structure, its dielectric properties, the ionomer sidechain's preferential orientation and interfacial density, the spatial distributions of electrical potential and ion density in the water region, and the effect of the oxide coverage at Pt/C on the electrostatic properties of the interface [118, 128].

Not only contact with phase W is pivotal for phase S to become active. Also, a percolating pathways for protons from the PEM to the reactions sites must be provided. Here, phase I and W act symbiotically: phase I has a high acid content. Upon contact with water, the acid groups dissociate, resulting in a high concentration of mobile extra protons or hydronium ions. With water as solvent, the protons acquire a high mobility. The combination of high hydronium ion density and excellent proton mobility results in a high proton conductivity, both in membranes and ionomer-impregnated CCLs. Nonetheless, even without ionomer, water is able to sustain sufficient rates of proton transport. Indeed, the current understanding in the literature assigns macroscopic proton transport to phase I. This assumption only holds macroscopically since over significant distances ohmic loses are mitigated by the high proton conductivity, whereas on the microscale phase W well-connects reaction sites with the proton-transport network [119, 129].

To extend mere electrochemical activity to actual high performance in power-generating applications, i.e., high current density and according transport rates per geometric cell, phase G is required as an effective transport path. The macroscale gas pore network that exists in secondary pores is crucial for the oxygen supply and water removal in the CCL. However, phase G is not desired at the microscale, where it might replace W, thus would disconnect reaction sites from the proton-supplying network and cut them from contribution to electrochemical activity. In a well-designed CL, active catalyst nanoparticles are located at spots that are simultaneously connected to the percolating proton transport network provided by I and W, phase S for electronic contact, and phase G. This concept of a so-called triple phase boundary (TPB) served as a useful concept to rationalize CCL operation for many decades since its postulation in 1924 [33]. However, as an idealized geometrical construction the TPB is of limited value for understanding GDE-type CCLs in PEM fuel cells, and even evidently non-existent for FE-type CCLs. Electrochemical conversion does not occur on a narrow TPB, but in the whole contact plane of S and W. This contradiction with the TPB is resolved by the fact that oxygen is soluble in water in sufficient amounts to enable a high ORR rate. Oxygen molecules are able to diffuse a certain distance or depth in water-filled pores and provide a sufficient supply for the ORR. Consequently, the active zone for the ORR extends away from the ideal geometric intersection of the TPB, typically to a reaction penetration depth of $\approx 100\,nm$ [72, 130, 131].

Given this length scale, primary pores can be allowed to be flooded during PEM fuel cell operation. Flooding of secondary pores however would markedly increase the oxygen diffusion resistance and render oxygen transport the dominating cause of voltage loss.

If the secondary pore space is mainly hydrophobic, it can withstands being flooded by the liquid pressure [132], which raises as more liquid water is generated with increasing current density. To keep the cell in an optimal wetting state, a mixed wetting behavior might be favorable to uphold free phase G and simultaneously retain enough water to keep the catalyst well-wetted and active.

Interestingly, CCLs actually exhibit mixed wetting behavior with both hydrophilic and hydrophobic pore walls. The wetting properties were found to be tightly coupled to the ionomer content, the Platinum loading, and type of carbon used, i.e., phase I, phase S and the I-S interaction [133, 134]. Hydrophilic surfaces can be attributed to metallic Platinum, carbon, and the ion-lined surfaces of the ionomer. For carbons, even graphitized carbon approaches contact angles of only 90° from below but does not exceed this threshold. The origin of hydrophobic wetting behavior can be attributed to surface patches of ionomer that consist of densely aggregated hydrophobic ionomer backbones [100, 135]. This aligned molecular structure is formed due to attractive interactions of the sulfonate anions with the Pt/C surface, which induces the preferential orientation of sidechains toward the agglomerate surface. The strongly hydrophobic PTFE backbones are left oriented towards inter-agglomerate spaces. However, understanding how modification of CCL materials, e.g., carbon support or ionomer, and the composition of CCL inks affect the wetting properties has not been addressed systematically in the literature.

The crucial water balance managed by the CCL extends over the entire cell. An optimal amount must be retained in the CCL while removing any excess water to neighboring layers, such as the cathode outlet via the MPL and the GDL, or the anode side via the PEM. The water balance becomes more challenging when the Platinum loading is significantly reduced. Unexpectedly high voltage losses occur when the Platinum loading is reduced, even surpassing losses anticipated based on the proportional decrease of the ECSA. In Ref. [136], a tipping water balance was identified as the cause of the detrimental performance effect, although there is no unanimous agreement on this interpretation. The search for the source of the significant Platinum loading effect has become a major focus in the field. One popular hypothesis suggests that a thin ionomer layer covers the Platinum catalyst sites, resulting in an additional local transport loss [137–142]. However, water phenomena cannot be neglected when discussing transport resistances. Moreover, it is questionable that the ionomer thin film can even exert a significant transport barrier. Hence, the thin-film hypothesis can be considered flawed, leaving the unexpected losses subject to ongoing research that focus on deciphering the role of water in this peculiar phenomenon.

The last example underlines once again the importance of comprehensibly understanding the intricate correlations between composition and performance outcome of CCLs and the need for modeling approaches that can disentangle its multifaceted structure-property relations. Therefore, the following section will delve into the history and development of key ideas for models of the PEM fuel cell catalyst layer microstructure.

2.2 Evolution of microstructure models for PEM fuel cell catalyst layers

The historic origins and developments of modeling the microstructure of PEM fuel cell catalyst layers can be overviewed in two major periods that partially overlap but can be distinguished by their focus on certain features of the microstructure, by leaps in understanding the functionality of PEMFC catalyst layers, and by methodological differences and modeling approaches. The first generation of agglomerate models was developed mainly during the second half of the 20th century and was derived from conventional models for reactive transport, as commonly applied in heterogeneous catalysis and process engineering. Here, first attempts to add complexity and account for specific structural features of ionomer-bound GDEs were made. During the 2000s and 2010s, CL microstructure models experienced diversification, specialization and refinement in a novel generation.

In 1939, Ernst W. Thiele presented a dimensionless number, later named after him, to describe simultaneous diffusion and reaction in porous catalyst pellets [143]. The Thiele-number allowed catalyst developers and process engineers to predict and optimize catalyst utilization and is still in use today in chemical engineering. Agglomerate models for PEMFC catalyst layers proposed later kept referring to the Thiele-number and the similarities in the approach of creating a balance between transport and reaction rate, and solving for the spatial distribution of conversion rates inside the porous catalyst particle or agglomerate. The first attempt in this context was undertaken in 1969 by Giner and Hunter from MIT. They assumed cylindrical geometry to describe agglomerates in an alkaline fuel cell catalyst layer flooded with KOH electrolyte [144]. In 1980, Iczkowski and Cutlip transfered a similar approach to an acidic cell and introduced the first electrolyte film model around the agglomerate [145], which later inspired researchers to use similar models to explain the mass transfer limitation inside agglomerates. So did Björnbom in 1987 by futher refining this approach. His work discussed Tafel-slope doubling to originate from oxygen depletion inside the agglomerates, and brought the cell model to agreement with experimental results for limiting current density [146]. In 1997, Broka and Ekdunge later published a consistent parametrization using SEM and other experiments to determine and fit parameters of the CL microstructure [147]. Shortly after, Bultel, Ozil, and Durand discussed the possible local oxygen depletion effect around platinum nanoparticles and introduced a model to describe mass transfer limitations in low-loaded catalysts [148]. Perry and Newman refined the agglomerate model in 1998 by combining oxygen and proton transport inside the agglomerate [149], thereby explaining not only Tafel-slope doubling, but also quadrupling. This first generation of models was marked by the development of analytical Thiele-based approaches and the introduction of agglomerate modeling. They focused mainly on oxygen transport, employed analytical solutions of coupled ODEs for reaction and transport inside flooded agglomerates, and laid the foundation for more complex agglomerate models used in PEM fuel cell research today.

The 1990s marked a significant step forward in the development of CL microstructure modeling, with the introduction of new models and techniques. Published 1991, the work of Springer *et al.* [150] layed the foundation to modern macroscopic cell performance models – and also foreshadowed a methodological shift from mere analytical mathematics

31

to numerical methods[1]. When computational power became more and more accessible to a broader community, numerical multi-physics simulations enabled researchers to perform more complex and accurate calculation. This cleared the path to diversify away from analytical solution for planar, spherical and cylindrical model geometries.

Around the year 2000, the methodological paradigm shift was met by a novel interest in fuel cell technology, driven by the demand for commercially available fuel cells to support fossil-free mobility (see section 1.3). Publication numbers increased exponentially during this period [46] and entire research groups dedicated their work on PEM fuel cells. In the realm of catalyst layer modeling, leading concepts and novel approaches can be attributed to the work of several research groups. Michael Eikerling and Alexei Kornyshev [151] pioneered structure-based modeling of the CL microstructure in the late 1990s – an approach pursued and extended by research on fuel cell-related electrochemical phenomena, including agglomerate models, from 2003 in the Eikerling research group located in Vancouver, Canada. Another group around Adam Weber was founded 2008 at the Research Lab for Energy Conversion in Berkeley, California, and focused on exploring the physical properties and performance of experimental MEAs and CLs. The group also dedicated some work to agglomerate and CL microstructure modeling. The group around Marc Secanell followed shortly at the Energy Systems Design Laboratory at the University of Alberta, Canada, in 2009 and contributed significantly to the modeling of PEMFC components and systems, including the CL. Their work focused on the detailed investigation of transport phenomena and how they affect the performance of PEMFCs.

During the 2010s further advances in CL microstructure modeling were fostered by the general evolution of understanding of the CL microstructure from experimental works. Focussing on some representative works from this period includes the work of Tatyana Soboleva, who confirmed experimentally the bimodal pore size distribution of catalyst layers. Her approach of correlating water uptake and double layer capacitance allowed to scrutinize that condensed water utilizes Pt nanoparticles inside the primary pores [95, 107, 152] and provided indications in which pores Platinum and ionomer deposit. New methods in sample preparation and micro-tomography gave deeper insight into the in-situ structure of agglomerates, e.g., the spatial distribution of ionomer [91, 93]. Also imaging with high magnification (e.g., TEM, STEM) was more and more applied to fuel cell catalysts to identify agglomerate structures. The group around Makoto Uchida at University of Yamanashi, Japan, correlated structural pictures observed *ex situ* in microscopy with performance of the catalyst material *in operando* conditions [96]. Profound explanations were given how the distribution of Platinum inside agglomerates, carbon support type, and morphology of ionomer covering it determine the performance of the CL [81].

Within the community of fuel cell researchers, two distinct approaches towards the governing physics inside the CL microstructure were pursued. The first approach assumed that the pore-filling medium inside the agglomerates is water. Thus, the theoretical fundamentals from aqueous bulk- and interface-physics were employed, such as the Poisson-Nernst-Planck equation coupling proton density, ionic migration and potential. The second approach postulated that the pore-filling medium inside the agglomerates is

---

[1] In fact, as an anecdotal remark, Springer *et al.* wrote in their publication, without further explanation: *"Although these equations can be integrated analytically, we chose to integrate them numerically."*

ionomer, or, at least behaves like a classical homogeneous solid medium, thus applied ohmic ion-conduction for proton transport and rather focused on oxygen diffusion.

Water-filled agglomerate models evolved over two decades with various publications shedding light on different aspects of the approach. In 2004, a first publication on understanding flooded agglomerates replaced the traditional Thiele-based approach by considering water as the filling medium of agglomerates micropores [153]. Discarding the previous assumption of isoprotonic and isopotential conditions inside the agglomerate cleared the path to shed light on the local reaction environment at the catalyst/water interface, including electric potential, electrostatics, and pH value related effects. The Eikerling group went on to explore the relationship between transport properties, evaporation rate, and platinum utilization with the flooding behavior of micro- and mesopores in a 2006 publication [132]. The results highlighted the crucial structure-performance relation that is conveyed by the agglomerated structure and vital to water management of the cell. Refining and resolving the inner geometries of agglomerates became the focus of more recent research. In 2014, a 3D geometry model that included conic pores, partial ionomer coverage, and a theory for metal surface charge was presented [154]. In 2016, the degree of detail could be increased further by a metal-walled nanopore model [70]. The subsequently developed double layer model that merged PtO formation, non-monotic surface charging, and pH dependency [155] became a key component in understanding the performance and effects related to water-filled pores. The double layer model was applied to discrete Pt particles to explain the experimentally observed proximity effect, which boosts the electrochemical activity of close Platinum nanoparticles [156]. A similar boost was derived to occur from Nafion®-Platinum interaction in an aqueous environment [118]. The interface revealed a favorable interplay of pH value, surface charge, and Platinum utilization in the proton distribution in a gap between Nafion® and Platinum. Another work from 2018 extended the approach to an ionomer-connected water-filled nanopore and showed that proton concentration is massively controlled by electrostatics and double layers [157]. Even alkaline pH values were found to play a role and are suspected to determine the ORR mechanism. Overall, the models assuming pores as water-filled and employ according physics have significantly advanced the understanding of performance of PEMFC catalyst layer and provided insights into key components such as water management, sub-agglomerate structures, proton transport, and Nafion®-Pt interactions.

The timeline of modeling works seeking an all-solid-state approach closely follows the development of simulations of the MEA or whole cell, in which the layers of the cell were represented by macro-homogeneous domains [158, 159]. The proposed model frameworks aimed to account for the CL microstructue by extending the expression of the ORR rate with Thiele-like agglomerate models. In the 2010s, the community of fuel cell researchers debated the role of ionomer films, which were hypothesized to cause significant transport resistances in low-Pt-loaded PEM fuel cells. Therefore, some agglomerate models featured an ionomer film to account for this conjectured additional mass transport resistance [68]. Despite experimental and theoretical efforts, no widely accepted theory could explain why ionomer thin films around Platinum particles could have a lower oxygen permeability. In 2011, a pseudo-discrete approach was proposed to explain the increased ionomer film resistance for oxygen around the agglomerates in low loaded CLs [160]. The approach involved modeling discrete reaction domains (not particles) to prove the hypothesis. However, the authors discussed that the ionomer film may also actually be water film or a combination of

the two. In 2014, the Secanell group suggested a dissolution kinetic for oxygen to explain the experimentally measured transport resistance, which could not be explained by the observed ionomer film thickness and agglomerate size [161]. Despite using measured parameters, the model still did not fit the observed behavior. Another numerical study from the same period resolved single Platinum nanoparticles that were randomly distributed inside a spherical agglomerate [162]. The work discussed a locally amplified flux of oxygen around small particles as origin of unexplained mass transport resistances. The comparison of such distinct approaches demonstrates that pseudo-homogeneous all-solid models could not trace down the cause for the observed mass transport resistances. Trapped in a dead-end, Thiele-like agglomerate models stopped evolving. Nonetheless, they kept being employed in macroscopic homogeneous models. However, the parametrization of agglomerates in the CL microstructure was contradictory to experimental findings but the model results were adequate on macroscopic level, i.e., simulations results of cells and even whole stacks agreed with experimental data [163].

Overall, modeling of the CL microstructure in PEM fuel cells has greatly evolved over time, with different approaches proposed and tested. Advancing experimental insights fostered refinement of existing models, so did modeling works contribute to the analysis and guidance of experiments, especially in the debate around a conjectured mass transport resistance of ionomer thin films. Some progress has been made in modeling sub-structures of agglomerates in the context of water-based theories. However, although discussed in the literature [164], a comprehensive framework for agglomerate modeling has not yet been established. The challenge lies in the high degree of complexity on the pore level, requiring a sound basis in physics to accurately capture the underlying mechanisms – together with a method to handle and reduce complexity when coupling to other modeling domains.

How microstructure models available today settle among other approaches covering the multiple scales encountered in PEMFC modeling, and how they might be integrated into this realm, is subject to the next section.

2.3 Methods for multiscale modeling of PEM catalyst layers

Unraveling CL structure and function in comprehensive modeling approaches is a hierarchical challenge. Both their connection to larger scales on cell and device level and down to elemental origins of material properties come into play if a holistic understanding of PEMFCs shall be reached. The topic of multiscale modeling of PEMFCs was extensively reviewed in recent literature [165, 166] and collected in textbooks [72, 167, 168]. In this section, the established methods for each modeling scale are reviewed and discussed with special focus on bridging of scales between CL microstructure models and cell or device level.

2.3.1 Structural levels of hierarchy and length scales

Figure 2.2 illustrates the hierarchy of structures of PEMFC catalyst layers and the methodological approaches to address each level. In the following, this work slightly relaxes the tight definition by length scales. What is considered rather decisive is the mere order of magnitude, and more importantly, the structural feature of interest and its location in the hierarchy. The following structural level (or scales) can be discerned:

1. The term **atomistic scale** refers to a level of detail where individual atoms and molecules are the fundamental building blocks. At this scale around $10^0\,nm$, the behavior of matter is governed by the laws of quantum mechanics, and phenomena such as chemical reactions and molecular interactions can be analyzed in detail.

2. At **pore scale**, physics of individual pores encountered at $\approx 10^1\,nm$, such as the local distribution of potential, ions, or dissolved gases in the electrolyte phase are of interest. Atomistic effects can play a role but are lumped in effective properties of homogeneous phases and interfaces.

3. At **agglomerate scale**, Pt/C particles and intra-agglomerate pores and interfaces are not resolved. Transport and reaction processes that occur within the agglomerated structure are of primary interest. Also, the origins of effective properties impacting performance of the layer on cell lever, such as wetting properties of the secondary pore network, must be addressed on this scale of around $10^2\,nm$. In particular, ionomer film thickness and coverage can be resolved and be subject to mesoscale models.

4. At **macroscopic scale** the entire CL is considered to be a homogeneous domain. The macroscopic gradients of potential and concentration of protons, gases and liquid observable at length scale $> 10^3\,nm$ constitute cell performance at this level.

5. On the **device level** the fuel cell catalyst layer must be integrated into MEAs and stacks, which themselves are interconnected to auxiliary devices that constitute the complete fuel cell system and the operation conditions applied to the fuel cell.
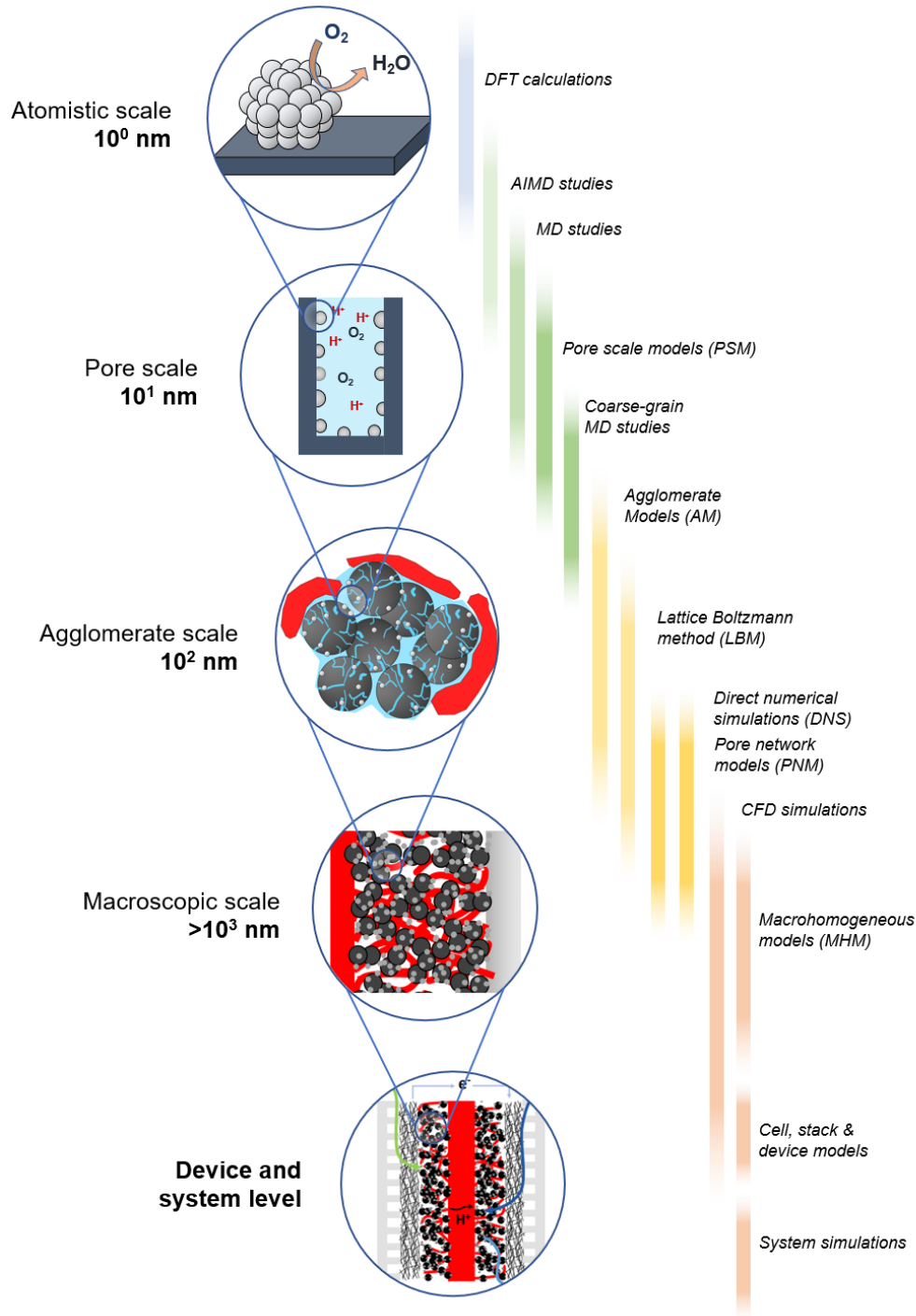
Fig. 2.2: Multiscale structure in a catalyst layer and according modeling techniques: on atomistic scale Platinum nanoparticles facilitate the oxygen reduction reaction; at the next level, water filled pores provided by the carbon support are decorated with catalyst nanoparticles; at agglomerate scale, Pt/C catalyst particles aggregate and are covered by an ionomer film; on macroscopic cell level materials are considered homogeneous; ultimately, the cell must be integrated into a device and complete fuel cell system.

The terms nanoscale, microscale, mesoscale, and macroscale (the according adjectives *nanao-*, *micro-*, *meso-*, *macro*scopic) are commonly encountered in the literature when multiscale modeling is discussed and therefore shall be clarified here how they match the definitions above. The term *nano*scale refers to structures on the order of magnitude of several *nano*meters, thus covers the atomistic and pore scale from the definition above. Accordingly, the *micro*scale can refer to structures of several micrometers. Alternatively, the term microstructure is commonly used to refer to intrinsic material structures that are independent of the dimensions of the piece of matter on the macroscale. For many materials the length scale of such microstructures is indeed the in the range of a few micrometers. However, in PEMFC catalyst layers the essential microstructural dimensions rather fall in the range of $1...100\,nm$, i.e., atomistic, pore and agglomerate scale are covered by this term. More obviously, macroscale refers to what is big enough to be perceived by the naked eye as homogenized bulk properties. Finally, the mesoscale refers to all that lays in between microscale and macroscale (from ancient greek $\mu\acute{\epsilon}\sigma o\varsigma$, mésos, "middle"), thus represents all larger structures that integrate microstructural elements into the macroscale. In the context of PEMFC catalyst layers, this covers the secondary pore network (or mesopores) together with the agglomerates, i.e., there is a certain ambiguity at the transition between microscale and mesoscale.

2.3.2 Methodological toolbox for different scales

At the atomic scale, individual atoms and molecules are resolved, including their positions within a three-dimensional lattice, and their interactions are described by force fields and the principles of quantum mechanics (QM). In this realm, density functional theory (DFT) is the method of choice to understand the electronic structure of molecules, materials, and solids. It is based on the concept that the total energy of a system can be determined by the electron density rather than the wave functions of individual electrons, which is a more efficient computational approach compared to traditional quantum mechanical methods [169]. Regarding, PEMFC catalyst layers, the Platinum nanoparticle size, shape, surface atom arrangement, and interactions with support material, are crucial in determining reaction mechanisms and pathways [170–173]. DFT allows to calculate the free energy changes along reaction pathways. Additional computational studies that combine interface theory and microkinetic modelling can decipher the multistep ORR mechanism and provide kinetic parameters, such as the intrinsic exchange current density and Tafel slope, as a function of electrode potential [174, 175].

To study the free movement and self-organization of molecules and atoms, molecular dynamics (MD) studies are applied. Each atom is modeled separately as a solid sphere with its motions, interactions and collisions being simulated [176]. The required force fields can be parameterized empirically or, alternatively, be derived from first principles QM calculations (referred to as *ab initio* molecular dynamics (AIMD) studies). For PEMFC catalyst layers, MD is employed to gain insights on structure formation, molecular alignment of ionomer, mobility of water, protons and oxygen in the ink or final microstructure [127, 177–179]. MD can be extended in its length and timescale by lumping building blocks of macromolecules or particles of homogeneous composition. So called coarse-grained MD reaches the length scale of agglomerates and has been applied to simulate structure formation in the ink stage [97, 100, 180].

Increasing in scale, pore scale models (PSM) focus on specific types of reoccurring interfaces and building block inside the CLs agglomerated structure, such as slab-like water-filled pores that are confined by the ionomer film and Pt/C [118], or micropores inside the Pt/C catalyst [69]. The confining walls of these models are described as electronically conducting solid materials, such as graphitized carbon black, which supports the Pt nanoparticles. Physics of conservation of mass equation and motion of charged chemical species in fluid media apply, commonly expressed by the Nernst–Planck equation. The charging properties of these walls regulate the density distribution of hydronium ions, or the local pH, in the pore, which is a key variable for the ORR activity and Pt dissolution rate [69, 70, 74, 118, 155]. Model boundaries are clearly defined in a way that potential-dependent charging conditions at pore walls and the corresponding local reaction environment can be accounted for.

Agglomerate models (AM) were the initial approach employed to comprehend the impacts of intrinsic catalyst activity, internal porosity, and real catalyst surface area on reaction rate distributions and the overall electrochemical performance of porous electrodes (see section 2.2). The primary contribution of AMs to PEMFC research is their ability to rationalize local reaction conditions and effectiveness factors [154]. These models consider the agglomerate to be a pseudo-homogeneous sphere (or similar simplified geometry), lumping heterogeneities at the microscale. Together with PSM, AM are powerful tools for parameter studies that analyze how specific structural modifications or material integration alter local reaction environments and the associated transport and reaction rates. These models have broad applications in various scientific fields, and numerous studies have investigated their significance and applications [161, 181–183].

On the mesoscale, pore network models (PNM) are able to replicate the characteristics of the porous CL microstructure, i.e., the connectedness of pores, network morphology, specific transport resistances of individual pores, wetting behavior and pore size distributions. PNM are highly developed in the literature and have a long history in modeling in geo-materials [184]. At present, broadly available software toolboxes exist to simulate materials of various kinds [185, 186]. PNM are closely related to graph theory. The nodes of the graph characterize the pores of the material, the edges represent the throats linking the pores. To extract the network topology from an 3D image (e.g., obtained from micro-CT data), supportive segmentation algorithms are needed [184]. Differential equations that describe transport and conservation laws are numerically solved for the nodes and throats to evaluate the effective properties and behavior of the porous material. In the literature, multiple works applied PNM to the PEMFC catalyst layer microstructure, mainly focusing on water management, wetting behavior and effective transport properties [187–190].

Acting on the same scale as PNM, direct numerical simulations (DNS) are a powerful tool for simulating material microstructures. Differential equations for reactive transport in different phases, and even two-phase flow, can be solved numerically on a simulation domain, using finite difference or finite volume methods. In PEMFC context, DNS can be used to assign physical properties to each voxel in a statistically equivalent geometry of the CL microstructure. Such frameworks can even mimic the structure formation process and thereby allow to study the impact of morphology on effective properties, such as percolating thresholds [102, 191–198]. The higher resolution compared to PNM can

impair computational speed of DNS approaches. In a benchmark comparison from the literature, computation time for a voxel-based DNS was found to be 60 times higher than a PNM to calculate transport properties of a GDL [188]. Although DNSs have higher computational demands, their results are more accurate and reliable due to their ability to resolve small details of the material's microstructure.

When using grid-based geometries to resolve both primary and secondary pores, the computational complexity can become very high, requiring a large and fine grid. At such small scale, the lattice Boltzmann method (LBM) is a viable numerical approach [199], which is also used for simulating fluid flow and other transport phenomena in PEMFC catalyst layers at the pore and molecular level [200, 201]. The approach is based on the Boltzmann equation and describes the behavior of a gas or fluid at the molecular level. Here, sets of particles move along a lattice, with the behavior of the particles being described by probability distributions.

PNM, DNS and LBM approaches commonly rely on 3D tomography data of the CL microstructure to parametrize the resolved geometry of the pore network. In the literature, scanning and transmission electron microscopy (SEM/TEM) tomography [78, 91, 93, 198, 202] and nano-X-ray tomography [203] were employed for this purpose. Such experimentally and computationally demanding methods allow to analyze and calculate a material property for a given instance of a material class but it would require enormous effort to generalize the structure-property correlations, i.e., mapping the full parameter space of conceivable structural data. Therefore, a more viable approach will be discussed in later on in section 2.3.3.

In general, mesoscale models feature a high diversity of approaches compared to other scales and are highly specialized. No single approach can be found in the literature to account for all structural effects at the mesoscale. Whereas PNM and DNS focus on transport phenomena via the mesopore network, AM and PSM are specialized on rationalizing the local reaction environment. Few works in the literature included both aspects. Sadeghi *et al.* [164] accounted for local heterogeneities of proton and oxygen concentration using a PSM that has been combined with a MHM to resolve local effectiveness factors on the levels of agglomerates and across the CL. Centinbas *et al.* [204] presented a complex, highly resolved model which coupled AM and PSM with a DNS.

Macroscopic homogeneous models (MHM) typically treat the CL (and other layers and domains of the MEA, cell or stack) as a continuum and represent larger sections of the CL that are greater than >1 μm by applying volume averaging. In numerical approaches, the simulation domain is discretized into finite elements to solve the ordinary differential equations for heat and mass transport, electrical current and potential, including source and sinks terms from electrochemical conversion and phase transitions of water. Analytical solutions for MHM have also been proposed in the literature [205]. State-of-the-art MHM from the literature reach a high degree of coupling of different physical processes that interact across the different layers of the cell [158, 163, 206].

On the ultimate stage in the modeling hierarchy, entire stacks or even complete FC systems are simulated. Device models are typical engineering tools to optimize design and operation of the FC system and its components, improve their efficiency, and reduce their

cost. They must account for complex electrochemical, transport and thermal processes that occur within the cell, and how they are affected by the device operation conditions, including temperature, humidity, and reactant flow rates. Methods commonly used in device modeling include computational fluid dynamics (CFD), often combined with local MHM domains [165]. Complete fuel cell system engineering and development requires specialized software tools handling the energy and mass streams transferred and converted by the interconnected fuel cell device components.

2.3.3 Bridging modeling scales

In the development of commercial fuel cell devices, parametrization of MHM is of particular interest. The required transport coefficients and kinetic parameters are largely determined by mesoscale structural features of the material. Thus, material properties on the macroscale and structure on the mesoscale are directly coupled. To bridge between the classes of models, i.e., to integrate multiple scales into a single model, remains a reoccurring challenge since models on all scales keep evolving in degree of detail and computational complexity [165]. A three-fold, viable approach to accomplish the bridging from mesoscale to macroscale effects can be carved out from the literature:

1. The **identification of essential features** should become the primary focus of DNS, PNM, AM and PSM, i.e., the addition of more details is not the ultimate target – but finding the decisive relevant structural descriptors of CL microstructure. Building on such insights, model complexity can be subsequently reduced without neglecting crucial relations of structure and properties. In the literature, besides the pore size distribution, quantities such as ionomer coverage of Pt/C surface [207] and interior/exterior fraction at agglomerate scale of Platinum particles [208] have already been found to be such features.

2. **Statistical descriptors** for structural parameters can account for mesoscopic heterogeneity of microstructure without resolving it explicitly, including pore-level transport, local reaction conditions and pore-space connectivity. For instance, bimodal pore size distributions conveying the information to quantify fractions of micropores and mesopores in the CCL material have become an established descriptor [94, 95, 132]. Other statistical or averaged descriptors, e.g., for ionomer coverage or wetting properties, might establish in future CL modeling research. To reliably parameterize the CL microstructure in such terms, the material has to be characterized once by their statistical descriptors, e.g., measure a pore size distribution, requiring a reasonable effort compared to explicit 3D tomography. Eventually, such descriptors could provide the basis for a scale-bridging framework to describe the CL microstructure.

3. Finally, a **generalization of correlations** is conceivable. As the understanding of relations between CL composition and microstructure morphology grows, universal approaches might be distilled. In contrast to mere empirical interpolation over an exhaustive database, mechanistic insights from item (1) in this list contribute here to setting up physical sound theories and employ them in CL models. Therefore,

wherever possible, mesoscale models should be scrutinized for potential generalizations to reliable structure-property relations. Classical random heterogeneous media theories [209, 210], which employ semi-empirical power-law relations such as the Bruggeman relation or are derived from percolation theory, hold enormous potential in the PEMFC context. Various works in the literature already proposed Bruggeman-like relations [163, 211–213] or percolation-type [51, 214] relations to express the correlation of CL composition and microstructure, and properties and performance, thereby proving the viability of this approach for meso-to-macroscale bridging.

The previous discussion signifies a reoccurring methodological theme in multiscale modeling research, e.g., in computational chemistry [215] or multiscale mechanical models [216]: firstly, numerical complexity must be reduced; and secondly, simulation tools to keep the full chain of modeling scale computationally manageable are employed. In recent years, the demand has risen for such solutions to handle multiscale effects in PEMFC catalyst modeling [165]. As outlined in the next chapter, this trend is driven by the increasing interest in comprehensive models suitable for holistic PEM fuel cell design – and shall be met by the research objectives of this work.

3 Research objectives, method of choice and scope of this work

Based on the literature reviewed in the previous chapter, emerging recent trends and current challenges in the realm of modeling of PEM fuel cell catalyst layers are discussed in section 3.1. Here, this work lays special focus on novel ambitions towards holistic fuel cell design and tailored catalyst layer materials. Therefore, this chapter develops a set of methods in section 3.2 to contribute to this overarching objective, and to cover the scope of research of this work outlined in section 3.3.

3.1 Purposefully tailored materials and holistic fuel cell design

In recent years, fuel cell research has been directing increased attention to industrial scale production and broad commercialization of fuel cells, striving to meet the developments goals for fuel cell development introduced in section 1.7. These multi-objective and ambitious, yet clear-cut targets are met by extensive efforts and systematic studies in the experimental literature [66, 111–113]. Here, overarching trends focus on purposefully tailored materials and holistic cell design – two concepts which are also of vital importance in the this work. In fuel cell development, the central role of the cathode catalyst layer (CCL) and its microstructure is commonly acknowledged, as the CCL is the key functional component of the cell and the most critical cost factor [63].

The term *purposefully tailored materials* refers to intentional modifications of the material, i.e., modifications that seek a particular tweak in CCL performance by altering the known root cause in the material microstructure. The aspect of tailoring further refers to customization of the material to suit a particular purpose within the fuel cell device. Here, the close link to *holistic cell design* can be drawn, which strives to co-optimize not only the CCL, but all cell components (including the PEM, GDL, MPL, flow-field, and other auxiliary components) and the overall device design, together with operation conditions and strategies with regard to enhanced performance, durability, and cost-effectiveness. Thus, purposefully tailoring individual components forms the basis for intentional and directed improvements of the fuel cell device, whereas holistic cell design rather steers, integrates and frames the optimization processes for each single material.

As illustrated in Fig. 3.1, development and implementation of novel materials commonly follow an iterative design cycle. In a solely experimental approach, materials are synthesized following a selected recipe and subsequently characterized and tested with regard to their desired performance. Building on this feedback, the material recipe is adjusted in the next iteration. As understanding of the cause-effect relations between materials choice and resulting performance grows with every iteration, the desired outcome is eventually achieved. However, in practice, this can be a time-consuming and
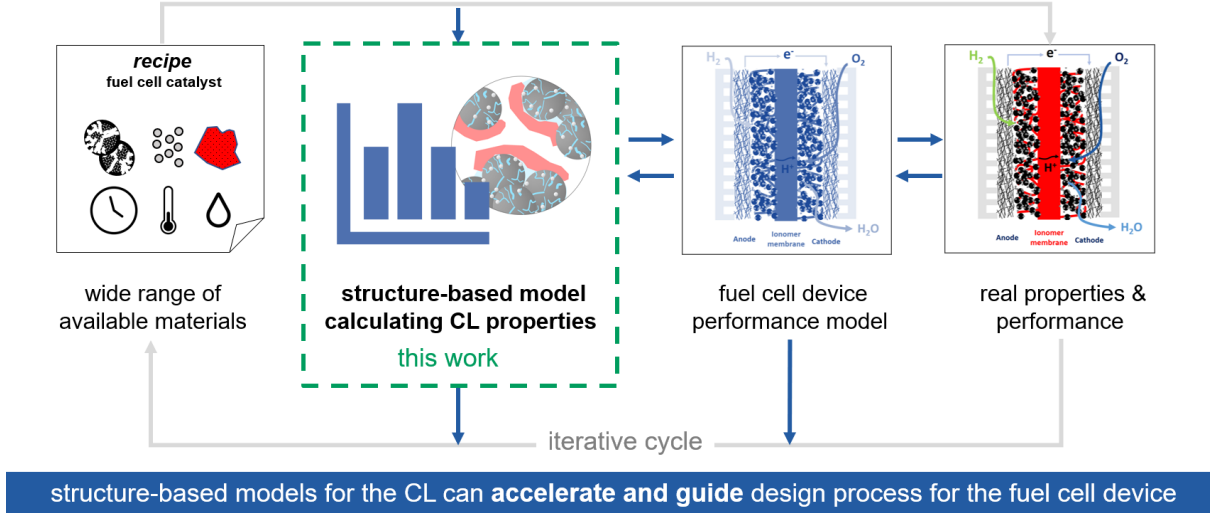
Fig. 3.1: Iterative design cycle of novel materials for PEMFC catalyst layers: CL materials are synthesized, characterized, and tested in an experimental approach. Feedback from these tests is used to adjust the material recipe in each iteration. Models for the CL microstructure and the cell performance on the device level can be integrated in order to guide and accelerate the process.

cumbersome process. Modeling approaches can synergistically blend into this cycle and provide guidance and acceleration [51, 68, 165]. In this context, structure-based models that cover the causal chain of ink-to-structure-to-property play a central role. On a material level, the decision on recipe adjustment can be tremendously supported and purposefully planned if a model is available that predicts likely material properties before any experimental effort is undertaken. An even higher level of integration can be reached if the calculated material properties are fed into a macroscopic device model to assess expected performance if the material is integrated into the device. Here, the interaction with experiments is two-fold: the model results are used to plan and direct future experimental efforts; and the model can be applied to past experiments to interpret and analyze experimental results. The more comprehensive the scope of the used models becomes, the bigger the resulting advantages of acceleration and guidance of the development processes.

Acknowledging the shared challenges across the scientific community, this works strives to enable and foster tailored CL materials and holistic PEMFC design as its overarching research objectives. It will focus on contributing to the completion of the iterative approach discussed above by deploying CL microstructure models. Hereby, it will address gaps in the landscape of available microstructure models of the PEMFC catalyst layer (see the following section 3.3). To deepen the understanding of how CL materials can be brought to enhanced performance and lower costs, the focus of this work is directed towards modeling approaches that incorporate cause-effect relations which propagate from microstructure to macroscale. To assemble a suitable methodology, this work will select from the broad toolbox introduced in section 2.3.2 and adapt novel approaches suitable for multiscale bridging discussed in section 2.3.3. The derived set of guidelines providing the methodological frame of this work, here referred to as *structure-based modeling*, are subject to the next section.

3.2 Structure-based modeling with analytical approaches

The method of analytical modeling was chosen for the objective of this work, i.e., this work will employ and derive mathematical expressions that represent concrete relations and physically sound theories applicable to phenomena in the realm of structure-property relations of PEMFC catalyst layers. A closed-form model brings certain advantages compared to mere empirical or statistical approaches: the model can explain and trace cause-effect relations and complex interactions (also referred to as *white box model*); it can handle even sparse and incomplete data; and its results can achieve high accuracy if the underlying assumptions are correct and complete and the model is properly designed and calibrated. Also, analytical models are generally less computationally expensive, allowing an effective integration into optimization routines. However, it is important to consider that analytical models require a solid theoretical basis, which shall be developed in this work.

In order to account for the supposed role of this work in the iterative design cycle and with regard to the objectives discussed previously, the following guideline principles apply for this work:

1. The model architecture is topologically closely related to real structures in order to represent inter-dependencies, i.e., real structures find their clear equivalent in the model and their respective relationships and interactions are captured.

2. A functionality in the model, e.g., conducting protons, must be fully traceable to concrete, captured structural elements, e.g., the ionomer phase.

3. The descriptors for the microstructure of existing and exploratory materials can be unambiguously captured, as well as their essential properties. The parametrization routines of the model are designed to harmonize with data from common experimental structural analysis.

4. The reversal of any structure-property relation, i.e., property $\mapsto$ structure, should be possible – either explicitly, i.e., by analytical reversal of the calculation, or at least implicitly or numerically via iterative adjustment of model parameters to obtain the pursued solution.

5. Input parameters are used for the individual materials and not for a composite material, allowing to recombine materials and adjust compositions of the CL.

6. Output parameters, i.e., the model's solution should be of a form that can be directly fed as parameters to existing macrohomogeneous models. Also, the intermediate results, i.e, the structure's mesoscale descriptors, are not to be neglected, as they can be utilized to trace the propagation of ink-structure-properties relations from microscale to macroscale.

3.3 Structure-property relations subject to this work

At present, a large experimental database is available from decades of intense fuel cell research. However, not all insights from experimental literature have been included into physical models of the CL microstructure. Therefore, this work will intensively review the available empirical correlations on structure-property relations in experimental works, develop novel modeling approaches where needed, and extend and refine existing models where required – in alignment with the primary objectives of tailored materials and holistic cell design.

In the context of PEMFC catalyst layer modeling, numerous phenomena in the realm of reactive transport are in the potential scope of this work, e.g., diffusion, convection and permeation of fluid through the porous CL structure; heat transfer and conduction; coupled heat-mass transfer via vaporization and condensation; migration and conductivity for electrons electrons; or kinetic parameters and effective reactions rates. From the literature survey undertaken in this work, four primary subjects of research have been carved out and selected, which are presented in Fig. 3.2. Taking up recent trends in the literature, this work focuses on comprehensive understanding of structure formation during ink stage [111, 112], i.e, aggregation and self-assembly controlled by the ionomer-Pt/C-solvent interplay focus, as illustrated in Fig. 3.2 (a). As a direct result of the structure formation process, ionomer morphology, both on molecular and agglomerate scale, is covered by the scope of this work, mainly affecting proton conductivity (Fig. 3.2 (b)) and origins of the CL's complex wetting behavior (Fig. 3.2 (c)). In fact, water management and the proper adjustment of wetting properties of the CCL is still a reoccurring challenge and central motive in PEMFC research [66, 165]. Since flooding phenomena are conjectured to be a major hurdle for future high-performance cells with a lowered Pt loading, structural cause-effect relation of wetting behavior and reduced Platinum loading are jointly discussed in this work. Furthermore, effective water uptake and catalyst utilization by water inside the CL microstructure are also closely linked to the CL's wetting properties. The mechanism and decisive structural features for Platinum utilization in low-loaded cells (see Fig. 3.2 (d)) are not fully ascertained in the literature and will be addressed in this work.

To render the distinct structure-property relations discussed above into a viable approach for multiscale modeling and iterative fuel cell design, a common framework employing statistical descriptors of the CL microstructure is established as the basis for the models developed in the scope of this work. The following subsections further elaborate on the chosen subjects of research outlined above, the methodological resources and approaches to address emerging research gaps, and delineate the scope of each subject.
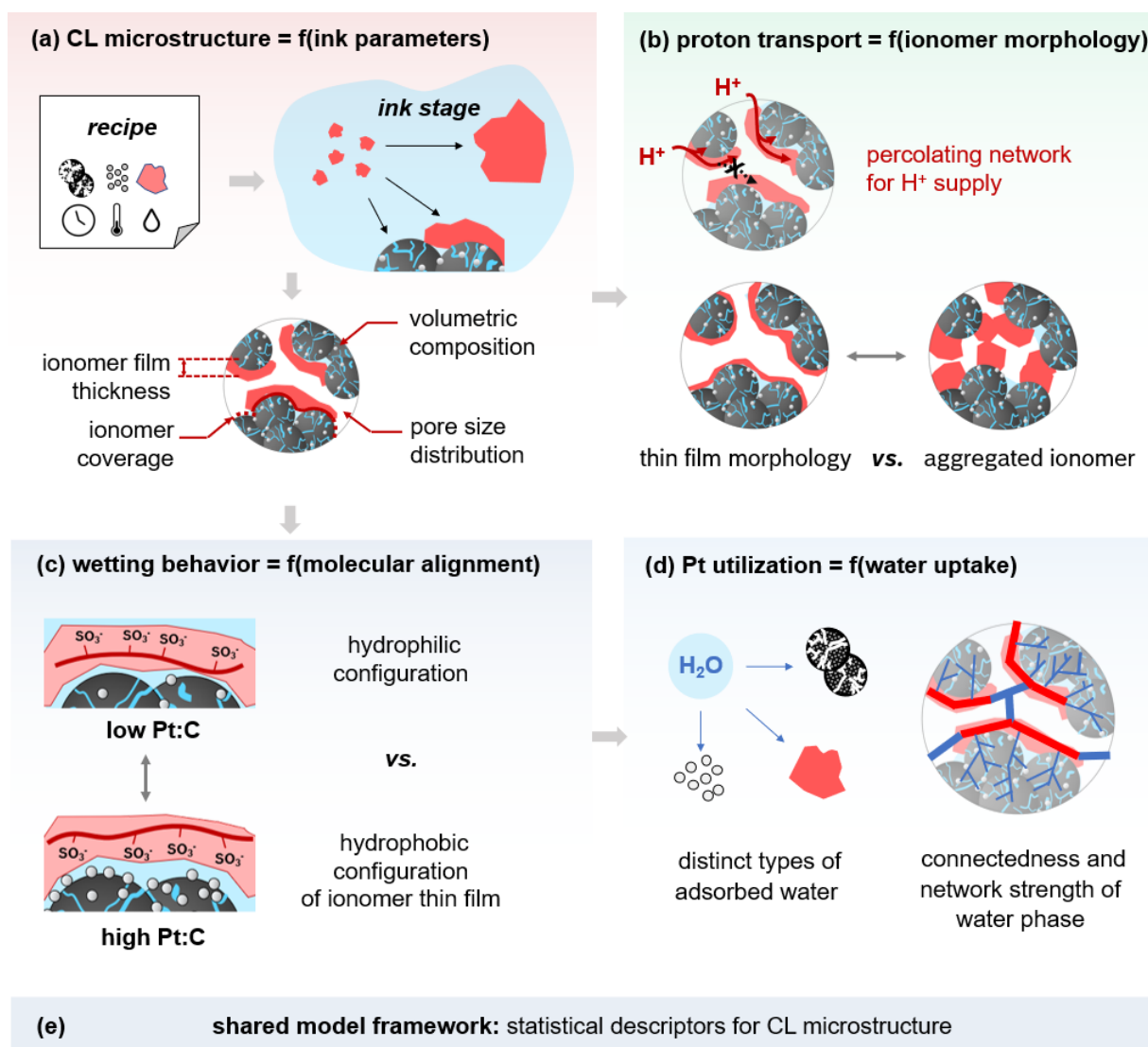
Fig. 3.2: Scope of this work and aspects of microstructure modeled: **(a)** structure formation during ink stage, **(b)** proton transport and how it is affected by ionomer morphology, **(c)** the molecular origin of mixed wetting behavior, and **(d)** catalyst utilization by liquid and adsorbed water inside the catalyst layer microstructure.

3.3.1 CL composition model and shared framework for descriptors of the microstructure

The starting point of this work was to formulate a correlation between ink parameters, the CCLs volumetric composition, and the structure of the ionomer. Thereby, literature insights on structure formation during ink stage will be accounted for. This includes the quantification of volume fractions of dispersed and aggregated ionomer, ionomer coverage in the secondary pores and ionomer film thickness. This work follows the objective to understand the formation of ionomer aggregates, which have been repeatedly observed in the experimental literature [104, 105, 204, 217] as a result of the self-assembly process. Both experimental [95, 106, 116] and computational studies [97, 195, 218] lay the groundwork for modeling the formation of the agglomerated CCL microstructure. In the scope of this work, a mechanistic analytical approach is pursued to describe the incremental self-assembly from the solvated CL ingredients to the final structure.

Addressing the overarching goal of holistic fuel cell design, the developed model is designed to be suitable for multiscale bridging and seamless integration into a common frameworks of statistical descriptors applying the microstructure. The common metrics of pore size distribution and ionomer coverage from previous works [94, 132] are adapted and are extended with additional descriptors of ionomer morphology.

3.3.2 Water uptake and Platinum utilization

During fabrication, the CL structure is formed, later assembled into a fuel cell device, and initially infused with water during first operation, which marks the actual operative state of the material that is of interest for CL developers. Thus, this works aims to transfer the material properties from *de novo* to *in operando* state by accounting for water uptake and the resulting catalyst utilization by water.

The Platinum utilization, i.e., the ratio of active catalyst particles connected to the proton supply network to the total amount of platinum in the CL, correlates with the amount of water taken up by the catalyst layer when exposed to a water-containing atmosphere [78, 152]. Here, the Platinum content seems to be a crucial parameter, determining the observable trend of Pt utilization over increasing relative humidity (RH). Especially low-Pt-loaded CLs are taken into focus in this work, as catalyst utilization drops significantly at moderate RH for such CLs. This phenomenon cannot be brought in agreement with condensation-type models from the literature, thus, an extended approach has to be developed. In the literature, distinct types of water are proposed [94] to explain the observed trends: adsorbed water on Pt/C surfaces; absorbed water in the ionomer phase; and condensed water in the porous network. This work aims to extends and refine existing water uptake models by these additional types of water.

Furthermore, modeling approaches in the literature exclude network effects of water added to the microstructure, i.e., Platinum is considered utilized if it is wetted. A recent work suggested that a continuous connection to the proton conductive network is not always guaranteed [119]. Therefore, this work further refines the picture of free secondary pores and flooded agglomerates, aiming to resolve the distribution of water over the domains of the CL microstructure with a higher degree of detail. Based on this approach,

water uptake data can be deconvoluted and novel insights on Platinum utilization be carved out by the model.

The description of network strength and connectivity of water phase can be accomplished by adapting approaches from percolation theory. Eikerling and Kornyshev already introduced percolation theory to correlate the composition of a CL with its properties in the late 1990s [51, 151]. In past literature works, the ionomer inside the CL was commonly considered the only percolating agent. However, recent experimental works indicate that water as a percolating agent, too. [94, 129] – both on the pore and agglomerate scale. In the scope of this work, this idea is followed up with a novel model approach.

3.3.3 Origins of mixed wetting behavior and water management in low-Pt-loaded cells

A closely controlled water balance is of crucial importance for the operation of PEM fuel cells since liquid water is needed for efficient proton transport and high activity of the oxygen reduction reaction. Conversely, excess water accumulation in the porous layers, i.e., flooding of the cell, can block the porous pathways pivotal for effective oxygen supply. A bi-functional, mixed wetting behavior, i.e, a combination of hydrophilicity and hydrophobicity, was taken into consideration already in the early stages of fuel cell development [66, 219]. However, only scarce datasets are available in the literature and experimental characterization techniques remains laborious [220, 221]. Therefore, a model-support understanding of wetting phenomena gains foremost importance, especially with regard to iterative design cycles.

In the literature, heterogeneous wetting behavior has been observed in experiments with CL composite materials [133, 220, 222]. The mixed wetting behavior can be partially attributed to the wetting properties of the Pt/C catalyst. The carbon support is moderately hydrophilic, whereas metallic Platinum is strongly hydrophilic. More important, being an amphiphilic material, ionomer plays a key role in shaping the wetting properties of the CL. Thin ionomer films exhibit hydrophilic or hydrophobic wetting properties depending on the interaction with the underlying substrate, i.e., the heterogeneous Pt/C surface. According to findings in the literature, the origin of this peculiar behavior lays in the molecular alignment of ionomer sidechains and backbones relative to the pore space [100, 135, 223].

Regarding the peculiar performance breakdown encountered with low-Pt-loaded CLs, a correlation between the susceptibility for flooding and the Platinum loading was conjectured before [136] but cannot coherently be explained, yet. Considering molecular alignment effects in the ionomer film, lowering the Platinum loading could cause inevitably changes the wetting properties of the CL. Therefore, this work strives to identify and understand possible cause-effect relations between details of the CL microstructure and effective wetting behavior.

Available models in the literature phenomenologically accounted for the mixed, heterogeneous wettability of the pore network by dividing pores into to a hydrophilic and hydrophobic fraction [94, 224–227], or entirely rely on measured water retention curves (WRCs) [163, 206]. Meanwhile, a structure-based approach can close the gap of cause-effect relations and trace down the microstructural origin of the heterogeneous wetting behavior on the molecular and agglomerate level. Therefore, this work collects insights

on molecular structure formation from both computational and experimental work in the literature. A model must be developed that accounts for molecular origins of wetting behavior and integrates them in the form of effective descriptors, such as WRCs, into the macroscale behavior of the CL. The common separation of the two distinct pore types used in the literature might be oversimplified, i.e., CCL materials could exhibit continuous distributions of contact angles. Therefore, this works adapts the idea of Weber *et al.* [228], who calculated the water retention curve (WRC) of a gas diffusion layer (GDL) by superposition of a Gaussian distribution of contact angles and a log-normal distribution of pore size. This approach seamlessly fits into the proposed modeling framework, where the calculation of wetting properties and the WRC will employ statistical descriptors provided by the composition model. Ultimately, this work aims to derive the WRC of the CL composite material based on microstructure descriptors, starting from an input parametrization only requiring single materials properties and ink parameters.

3.3.4 Proton conductivity and ionomer morphology

The ionomer content in the catalyst layer is a key optimization parameter: on the one hand, increasing the ionomer content increases the proton conductivity; on the other hand, excessive amounts of ionomer will block the pore space and thus impair gas transport [229]. Optimizing ionomer content of CCL has been the subject of several modeling studies [51, 151, 211, 212, 214] and experimental works [90, 230, 231]. An optimal ionomer volume fraction of $\approx 30...40\%$ has been reported [51, 90, 211, 214, 231, 232], though the exact value can vary significantly, with a range from 13% to 40% found in commercially available catalyst layers [232, 233]. These differences might have their origin in the varying microstructure of the CCL [111]. The understanding of how the ionomer morphology can be tuned and which structures enhance or impair performance is still emerging in recent literature [104, 114–117].

Available relations between ionomer content and proton conductivity in the catalyst layer are adapted from random media theory, such as the Bruggeman relation [163, 211–213] or percolation theory [151, 214]. However, models in the literature commonly neglect essential structural features of the ionomer morphology within the CCL microstructure, such as the existence ot thin films or dense aggregates. From reviewing experimental studies that correlated ionomer content and resulting proton conductivity [90, 234–239] an evident research gap emerges. Comparing the available datasets, no universal trend is recognizable with regard to mere ionomer volume fraction. Therefore, this work attributes the different behavior to variations of the ionomer morphology. To test this conjecture, direct numerical simulations are a viable approach to study a wide range of structural parameters of conceivable ionomer morphologies. Past works have demonstrated that generating synthetic 3D images provides an alternative pathway to experimentally obtained images [193, 194, 240, 241].

A systematic study on the relation between ionomer structure and proton transport could not be found in the literature and is therefore conducted in the scope of this work. The results serve to scrutinize the essential features and to subsequently reduce the model complexity, i.e., develop analytical relations between ionomer morphology and proton transport properties in CCLs.

4 Published work

The peer-reviewed articles that constitute this cumulative thesis are presented in chronological order of publication. Additionally, further results communicated to the scientific community are documented. All methods and models developed in this work and all obtained results are covered in full by the following publications:

- Publication I, titled *Review – Wetting Phenomena in Catalyst Layers of PEM Fuel Cells: Novel Approaches for Modeling and Materials Research*, addresses the molecular origins of mixed wetting behavior in an extensive literature review and proposes a novel descriptor-based approach to translate molecular alignment effects in the ionomer films to effective wetting properties.

- Publication II, titled *Modeling of wetting phenomena in cathode catalyst layers for PEM fuel cells*, includes the developed composition model to calculate metrics of the catalyst layer microstructure from basic ink parameters. Furthermore, it features the complete wettability model to calculate water retention curves based on the composition of the catalyst layer.

- Publication III, titled *Structure and Conductivity of Ionomer in PEM Fuel Cell Catalyst Layers: A Model-Based Analysis*, employs a direct numerical simulation and a stochastical image generation algorithm to study the correlation between details of ionomer morphology and proton conductivity. Applying percolation theory to interpret the simulation results, an analytical model to directly calculate proton conductivity from ionomer morphology parameters is developed.

- Section 4.4 documents further published results on *Structure-Based Modeling to Rationalize the Pt Utilization in Catalyst Layers of PEM Fuel Cells*, including an analytical model to calculate and deconvolute water uptake by PEMFC catalyst layers from a partially saturated atmosphere. Percolation theory is applied to calculate the Platinum utilization by adsorbed water.

4.1 Publication I
Review – Wetting Phenomena in Catalyst Layers of PEM Fuel Cells: Novel Approaches for Modeling and Materials Research

Authors: Wolfgang Olbrich[1,2,3], Thomas Kadyk[1,4], Ulrich Sauter[2], Michael Eikerling[1,3,4]

[1] Theory and Computation of Energy Materials (IEK-13), Institute of Energy and Climate Research, Forschungszentrum Jülich GmbH, 52425 Jülich, Germany
[2] Robert Bosch GmbH, Corporate Research, 71272 Renningen, Germany
[3] Chair of Theory and Computation of Energy Materials, Faculty of Georesources and Materials Engineering, RWTH Aachen University, 52062 Aachen, Germany
[4] Jülich Aachen Research Alliance, JARA Energy, 52425 Jülich, Germany

Author contributions: Conceptualization: WO, TK, US, ME; Methodology: WO Software: WO; Formal analysis: WO; Resources: US; Writing - Original Draft: WO; Writing - Review & Editing: US, TK, ME; Supervision: ME, US, TK; Project administration: US, ME.

Document history: First draft: 14.08.2020, Submitted: 18.02.2022, Received peer review: 18.02.2022, Revised: 22.04.2022, Published: 23.05.2022.

Review—Wetting Phenomena in Catalyst Layers of PEM Fuel Cells: Novel Approaches for Modeling and Materials Research

W. Olbrich,[1,2,3,z] **T. Kadyk,**[1,4] **U. Sauter,**[2] **and M. Eikerling**[1,3,4]

[1]*Theory and Computation of Energy Materials (IEK-13), Institute of Energy and Climate Research, Forschungszentrum Jülich GmbH, 52425 Jülich, Germany*
[2]*Robert Bosch GmbH, Corporate Research, 71272 Renningen, Germany*
[3]*Chair of Theory and Computation of Energy Materials, Faculty of Georesources and Materials Engineering, RWTH Aachen University, 52062 Aachen, Germany*
[4]*Jülich Aachen Research Alliance, JARA Energy, 52425 Jülich, Germany*

The development of high performance polymer electrolyte fuel cells increasingly relies on modeling to optimally tune cathode catalyst layers (CCL) to desired properties. This includes models to rationalize the role of water as promoter and asphyxiant to the oxygen reduction reaction. Existing models are able to reproduce or predict, using assumed parameters, the performance of the cell. However, consideration of the wetting properties of the composite has remained elusive. Experiments to characterize these properties are difficult to perform. There is thus a gap in theory for relating material choices with wetting properties. This article elaborates on this gap and presents a novel conceptual approach to close it. Fundamental modeling approaches, molecular dynamics studies and experimental works have shown that the interaction of ionomer with the Pt/C surface exerts a major impact on wetting behavior and water sorption properties of the porous CCL composite. In our approach, the state of molecular alignment of ionomer sidechains and backbones is linked to the structural characteristics of the Pt/C catalyst. From this rationalization, wetting properties of the CCL can be deduced. An analysis of these correlations supports a crucial hypothesis: lowering the platinum loading leaves the CCL more prone to flooding.

Polymer electrolyte fuel cells (PEFC) are approaching commercialization on a broader scale, with one major roadblock in the way: pairing low platinum loading with high performance and durability.[1,2] Many approaches to meet the targets for power-specific price and platinum loading are based on replacing platinum with cheap non-noble elements, or increasing the platinum utilization. Upon drastic reduction of the platinum loading a hitherto unexplained oxygen transport resistance occurs. This hindrance of oxygen supply results in significant voltage losses, markedly affecting the power performance and efficiency of the fuel cell.

It has been known to fuel cell developers for decades that deficient water management causes flooding of the cell upon increasing the current density.[3] At a critical current density water blocks gas supply via the porous network. Structure-based modeling has elucidated vital mechanistic aspects of cathode catalyst layer (CCL) flooding: the evaporation rate drastically declines as the liquid saturation of the pore space rises over a critical threshold.[4–6] This (in-)stability condition is considered the root cause for the limitations in maximum current density and specific power output.

Water is a mediator of numerous processes during CCL operation. For instance, platinum utilization inside the primary pores of the carbon support hinges on liquid water to render the CCL electrochemically active in the first place.[7,8] Furthermore, the proton conductivity in the CCL depends on the liquid saturation.[9] Liquid water saturation has to be well balanced: not only is a sufficient saturation critical for achieving high performance, but the CCL must also not dry up.[10]

A correlation between the susceptibility for flooding and the platinum loading was conjectured before, but not coherently explained. In order to understand this correlation, Muzaffar et al. extensively reviewed experimental performance data in Ref. 11, which monitored the impact of reducing the platinum loading to ultralow levels. In that work, a well-established macrohomogeneous performance model[4,5,12–15] was fitted to various sets of polarization curves and the parameters for the effective exchange current density and the proton conductivity in the CCL as well as the oxygen diffusion coefficients in CCL and Gas Diffusion Layer (GDL) were extracted from the fits. Plotting these parameters as functions of the platinum loading revealed insightful correlations. A physically consistent explanation of these correlations could be given on the basis of the following hypothesis: curtailing platinum loading by reducing the CCLs thickness, while keeping the the composition of the CCL constant, causes a decline of the vaporization capability, thereby inducing a shift of the water balance toward the tipping point for flooding. A second pathway for reducing the platinum loading is a *dilution* of platinum while keeping the CCL thickness constant. The modeling-based analysis conducted in Ref. 11 revealed how lowering the platinum loading inevitably changes the water-related properties of the CCL. As it is of high interest to clarify the cause and predict the implications of this materials behavior, the underlying causality will be scrutinized further in this article.

With the wide-ranging impact of liquid water inside the CCL in mind, an obvious need emerges to model the wetting-behavior in relation to materials selection and design. With regard to cost reduction efforts two questions arise: how is the platinum loading reduction linked with water management? Could a poorly managed water balance be responsible for the reduced performance of low-platinum-loaded CCLs? As of today, no comprehensive attempt has been made to determine the quantitative relations that link catalyst recipe and fabrication parameters to water management and fuel cell performance.

Reviewing the genealogy of models for water management, hydrophilicity and hydrophobicity were taken into consideration already in the early stages of fuel cell development.[3,16] Heterogeneous wetting behavior had been observed in experiments.[17–19] It was accounted for in CCL models by distinguishing certain proportions of both hydrophobic and hydrophilic pores. Treating wetting properties from this phenomenological perspective requires that macroscopic experimental wetting data, i.e., the wetting behavior of the different CCLs, are measured at continuum scale and used to parametrize the CCL model. Recent efforts rely on measured water retention curves (WRCs).[6,20] On this

[z]E-mail: wolfgang.olbrich@de.bosch.com

basis, neither a prediction of properties nor an optimization of CL composition and structure could be performed, because the microstructural origin of the heterogeneous wetting behavior had remained obscure. To date, no approach exists for correlating wetting properties on the continuum scale to the intrinsic properties of the CCL materials, the CCL recipe and synthesis parameters and the operation conditions of the fuel cell.

In following, we will review basic concepts and existing approaches of modeling CCL wettability. From preceding works in both theory and experiment, we derive a structure-based descriptor for the microscopic wetting properties that connects material selection and intrisic properties with the propensity for flooding of the CCL composite porous medium. We aim to bring a fresh perspective to application-driven materials research on PEM fuel cell with a focus on water management and flooding prevention.

Composite Wettability in CCL Models

Typically, the porous network in the CCL exhibits a bimodal pore size distribution with primary pores (size range from 5 to 20 nm) inside the carbon particles, and secondary pores (size range from 20 to 100 nm) between them (see Fig. 1).[9,21,22] Although the fractions and sizes of primary and secondary pores may vary, the bimodal nature of the pore structure is considered a generic and vital feature of CCL. The greatest ambiguity concerns the wetting properties and resulting functionality of the various pore types.

The evolution of model-based understanding of CCL wettability started with the assumption of a uniform effective contact angle for all pores. From the beginning, this simplification was seen as the minimal assumption. Based on the fact that at least three different materials (platinum, carbon, ionomer) influence surface properties inside the CCL's porous network and that the primary pores are ionomer-free, already principal works discussed a differentiation of wetting properties between primary and secondary pores.[12,23,24] Starting with the assumption of a uniform contact angle, the impact of CCL wetting properties on water management was assessed by Liu and Eikerling.[4,5] To keep the CCL stable against water accumulation, thus enabling high evaporation rates and efficient gas transport, a contact angle of just below 90° for all pores was assumed. Later works accounted for heterogeneous wetting properties by assuming fractions of hydrophilic and hydrophobic pores. However, the distributions of hydrophilic and hydrophobic pores were considered to be uniform over all pore sizes.[25–27] This uniformity assumption was refined by attributing different wetting properties to primary and secondary pores.[9] The parameters for the proportion and distribution of hydrophobic pores in both micro- and mesopores were varied[28,29] and the impact for water management

evaluated. Major conclusions drawn from the development of water management models to date are:

1. To capture wetting behavior correctly, contact angles of pore walls can neither be considered equal for all pores, nor will their distribution be the same for all pore sizes; distributions of pore sizes and wetting angles must be considered independently.
2. Primary ionomer-free pores can be considered hydrophilic, an aspect that is considered to be beneficial by multiple models[9,29] since liquid water renders the catalyst active.
3. Secondary pores might exhibit a heterogeneous wetting behavior with both hydrophilic and hydrophobic surfaces. A dominant fraction of hydrophobic pores is probably favorable for the flooding resistance.[29,30] Nonetheless, a certain amount of hydrophilic secondary pores might help to establish a network for continuous pathways of liquid water transport,[28] contributing to facile efficient removal of water from the CCL at high current densities. This requirement will depend on the vaporization capability and the transport properties of the adjacent gas diffusion layer.

To this point, efforts to account for wettability effects in CCL modeling were made by logical deduction from structural pictures. This kind of approach is sufficient for a cursory impact assessment based on qualitative parametric trends. However, a deep quantitative understanding of the impact of contact angle distributions on performance has not been achieved. With no coherent set of data nor a physically consistent theory available, parametrization was adjusted to fit experimental performance data.[9] Parameter studies of the contact angles and their distribution revealed the importance of CCL wettability and allowed to propose how the wetting properties of a best-performing material should be tailored.[29,30]

As discussed in the introductory section, another approach emerged in CCL modelling that builds on the macroscopic wetting behavior. Because it is still a formidable challenge to measure or even predict contact angles on the microscale, the macroscopic wetting behavior was measured for single CCL materials and used to parametrize macrohomogeneous CCL models.[6,20,31] The water-retention curve (WRC) which links capillary pressure and liquid saturation provides the most suitable representation of the macroscopic wetting properties. Albeit WRCs currently available are based on only a handful of measurements.[32–34] Due to the small number of CCL materials characterized by their WRC, the dataset is too sparse to explore correlations between CCL composition and fuel cell performance. If one wants to follows this phenomenological approach, many more WRCs of different CCL materials must be generated and analyzed. Due to the high experimental effort this
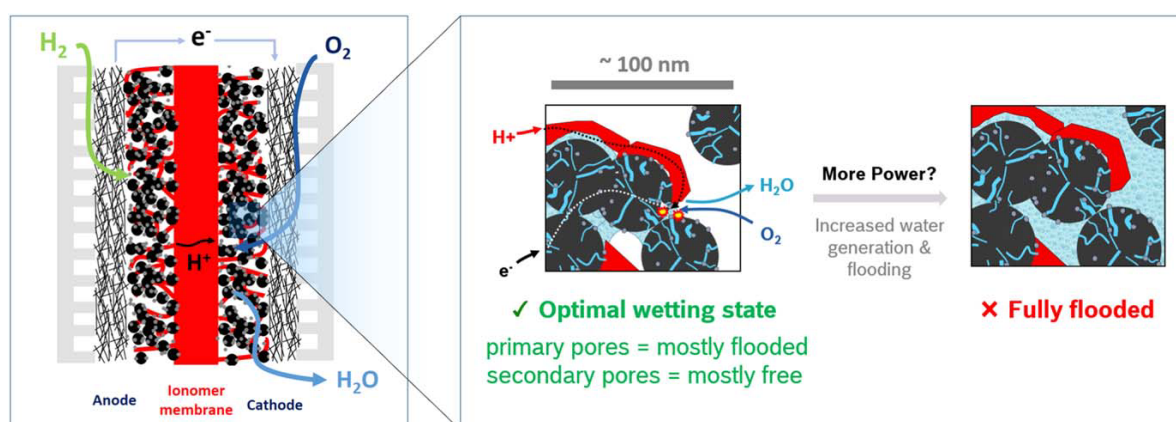

Figure 1. Schematic depiction of a polymer electrolyte fuel cell and the CCL microstructure. Water and flooding play a crucial role for the optimal function, in particular for high performance fuel cells.

approach is currently not a feasible option for fuel cell developers. In the following, we will pursue a complementary theoretical approach and present a basic modeling concept to close this gap in correlating the CCL structure with its wetting behavior.

Origin of Heterogeneous Wettability

In this section, we will explore the relationships between materials choices, structure and composition of the CCL, and heterogeneous wetting behavior by reviewing experimental measurements of contact angles on CCL composite materials. We will also review molecular dynamics studies for additional insights into the impact of interactions among platinum, carbon and ionomer constituents on the structures formed at micro- and mesoscales.

Quantifying Wettability: Experimental Findings.— Rationalizing wettability effects in composite media starts with an understanding of the wetting properties of the different ingredients. The ingredients of state-of-the-art CCLs are the catalyst (i.e., platinum), the support (i.e., carbon), and the ionomer (typically, Nafion or a similar perforluorosulfonic acid-type ionomer).

Carbon acts as the electronically conductive medium and mechanical support. Various types of carbon materials can be distinguished in terms of particle size, morphology, internal structure and surface properties.[35,36] These structural properties determine the electronic conductivity as well as durability and performance.[35,37] They also determine the wetting behavior of the CCL. The two types of carbon that are most commonly used in PEM fuel cells are Vulcan XC72 and Ketjen Black. Vulcan XC72 is a more compact carbon, with a low number of primary pores and low internal surface area (approx. $250 \, \text{m}^2 \, \text{g}^{-1}$). On the other hand, Ketjen Black is the benchmark for a high surface carbon with a high number of primary pores and large inner surface ($>800 \, \text{m}^2 \, \text{g}^{-1}$). Both types of carbin are handled as powders with particle sizes of approx. 50 nm. The carbon surface properties depend on the crystallinity, the surface facets that prevail at graphitic crystallites,[38] and specific surface groups by which wettability can be tuned,[39,40] which are present in most carbon supports and can be removed or added at will to activate or functionalize the material.[41,42]

To compare all involved materials in the composite, we visualize their wetting properties as a contact angle spectrum in Fig. 2. The reference point for all carbon based materials is graphite; its basal plane has a wetting angle of $90°–95°$[39,40,a]. With increasing number of edges, defects and amorphous sections involved, the contact angle

decreases to $60°–70°$.[38–40] Further customization of the contact angle of carbon is possible by introducing functional groups. This allows tuning the contact angle in the range of $5–167°$.[43] Functionalized carbon materials were already studied in the context of fuel cell catalyst development. Golikand et al.[44] and Andersen et al.[45] introduced oxygen-containing acidic groups at the carbon support, tuning both the carbon's wettability as well as carbon-ionomer interactions. Orfanidi et al.[46] doped the carbon with nitrogen, resulting in functional imide, lactam and amid surface groups. In contrast to Golikand et al. and Andersen et al., the work of Orfanidi et al. was dedicated to tuning the ionomer dispersion by controlling the ionomer-carbon interactions, aiming to adjust the thickness and coverage of ionomer films, which are quantities strongly connected to the wetting behavior.

Another key material in the CCL is platinum. It forms nanoparticles with radii of 1–5 nm that adhere to the carbon support. Depending on the synthesis approach, platinum nanoparticles could be deposited predominantly inside the primary pores or on the outer surface of carbon particles[47] where they affect the wetting properties of the respective pores. Metallic platinum surfaces are strongly hydrophilic with contact angles $<10°$.[48] The contact angle is rather insensitive to the particle size[b] and surface structure.[50] Results of Volfkovich et al.,[51] Gunterman et al.,[33] and Mashio et al.[9] confirmed that adding platinum nanoparticles to the carbon support turns the resulting Pt/C catalyst material hydrophilic. Tuning the surface charge density at the platinum surface by changing the electrode potential, as is the case in an operating fuel cell, will change its wetting behavior due to electrowetting or oxide formation. However, to date no studies on these phenomena have been reported in the literature. Therefore, we will take the hydrophilic character as given in further discussion in this article.

The combination of platinum with ionomer exhibits an increased hydrophobicity of the resulting composite in comparison to the average of the two materials involved. In order to understand the interaction of ionomer with the Pt/C catalyst, Volfkovich et al.[17,51] studied the wetting behavior of several carbon support materials, both pure and combined with platinum and/or ionomer. The authors applied their peculiar method of standard porosimetry to reveal the wettability inversion phenomenon: covering a hydrophilic surface, like hydrophilic or platinum covered carbon, with ionomer results in a hydrophobic outer surface of the ionomer layer. Also the opposite inversion effect was observed: hydrophobic carbons resulted in a hydrophilic outer surface when covered with ionomer. The proposed
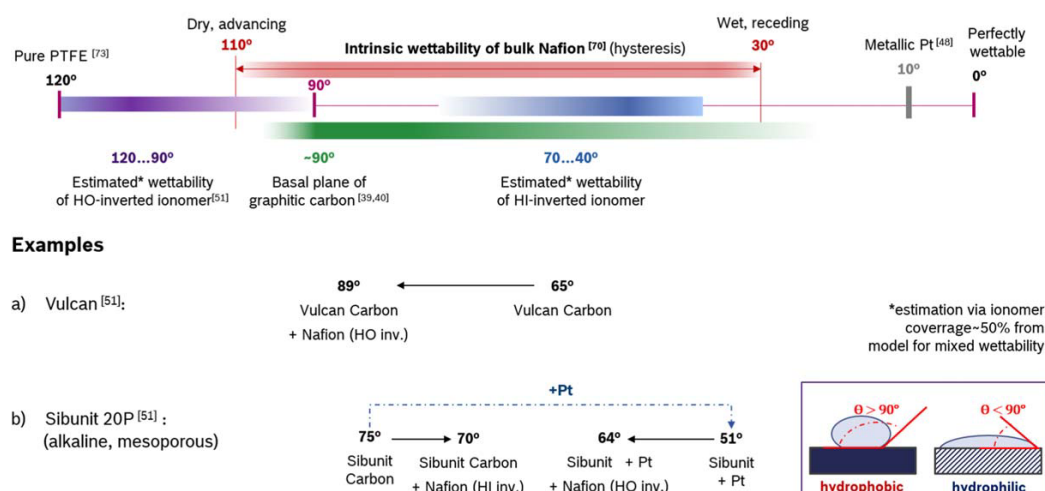
Contact angles in PEFC catalyst layer materials

Figure 2. Spectra of contact angles of materials used in PEFC catalyst layers. Values for contact angles taken from 39, 40, 48, 51, 70, 73.

explanation of this inversion phenomenon is a local structural alignment of the ionomer. In contact with a hydrophilic surface of platinum, on carbon ionomer sidechains will be preferentially oriented toward the Pt/C surface, while the hydrophobic ionomer backbones will point away from this surface, resulting in a hydrophobic effective contact angle on the outer surface. The interplay of effective wettability in the CCL composite material and ionomer orientation is illustrated schematically in Fig. 3. The NMR spectra and wetting behavior of Vulcan carbon covered by Nafion measured by Andersen et al.[45] support this hypothesis.[c] The authors emphasized the importance of well-adjusted wetting properties for the water management and the reduction of mass transport resistances.

Despite these findings of Volfkovich et al. and Andersen et al., almost all research related to the morphology and properties of ionomer films in CCLs focused on transport of oxygen and protons in order to explain performance issues in low-platinum-loaded CCLs.[53] Only few works picked up the alignment hypothesis and related it to the flooding issue discussed in the introductory section.[11]

In order to check for a correlation between ionomer content and its significance of the inversion phenomenon, Li et al.[54] conducted a follow-up study, referring to Volfkovich et al. and supporting their results with another method. They observed the evolution of a small water droplet with a high speed camera on composite films of Vulcan carbon and Nafion ionomer. Vulcan carbon is a slightly hydrophilic carbon with a contact angle of $62°$,[51] and a concentration of acidic surface groups $1\,mmol\,g^{-1}$.[9] Upon variation of the ionomer-to-carbon ratio (I:C ratio), they were able to confirm qualitatively the wetting behavior observed by Volfkovich et al. and further determined the quantitative boundaries of the inversion effect. When the I:C ratio is lower than approx. 1:4, the ionomer cannot fully cover the surface of the carbon support, resulting in a hydrophilic composite. Above an I:C ratio of 7:3, the ionomer film becomes so thick that the composite adopts the bulk-like wetting behavior of Nafion. Typically, CCLs feature I:C ratios of 0.5 to 1, situated in the middle between these cases.

In another work, Mazumder et al.[55] adjusted the Pt:C ratio of Pt/C/ionomer composites between 1:4–1:1 and determined the apparent contact angle via a droplet, elucidating the strong correlation of the wetting properties with the Pt:C ratio. The resulting data show a clear trend. More platinum in the composite shifts the contact angle to more hydrophobic values. The trend is monotonic, but appears to asymptotically approach a contact angle of approx. $120°$, the hydrophobic contact angle of a fully exposed flourinated backbone. Having no overlap with the sample set of Volfkovich, the data extend the trend seamlessly (see Fig. 4). From the combined data we conclude that on Vulcan the ionomer inverts the wetting behavior in a moderate manner, but on platinum the inversion is more pronounced because its interaction with the ionomer sidechain is much stronger. This finding indicates the key role of the platinum loading for establishing sufficient amounts of hydrophobic pores.

All of the aforementioned studies were based on experiments with pseudo-CCLs, i.e., preparing the Pt/C/ionomer composite ex situ and not as a functional part of a fuel cell. That fact raises the question, to which extent findings are transferable to in situ and *operando* conditions. Fang et al.[56] reported the contact angle of a functional CCL based on Vulcan carbon. The study focused on the change of wetting behavior in secondary pores during aging and found a slight decay of hydrophobicity. The reported contact angles were in the range of $110°$–$120°$, matching the results of studies with pseudo-CCLs of the same carbon support material. However, only macroscopic droplets were used to determine wetting properties. A promising technique to evaluate contact angles of a functional CCL down to micrometer scale was demonstrated by Yu et al.[19] Using environmental scanning electron microscopy (ESEM) allowed studying the wetting properties on a micrometer scale. Similar to Fang et al., functional CCLs were studied before and after aging.

Furthermore, Fang et al. and Yu et al. discussed the impact of surface roughness that distorts the apparent contact angles. Applying common correction schemes for the macroscopic roughness and porosity of the CCL sample, such as the Cassie-Baxter-rule, Fang et al. obtained true contact angles in good agreement with values reported by Volfkovich et al. From this finding, we conclude that surface roughness must be considered when measuring CCL wettability with macroscopic droplets, but can be neglected for wetting phenomena on the pore scale. Thus, the reported values for individual contact angles of Pt, carbon and ionomer surfaces can be used.

Complementary to the macroscopic surface property measurements of the Pt/C/ionomer composite, a plethora of works experimentally studied the microstructure of thin PFSA films[d], reviewed by Kusoglu and Weber.[52] The key findings related to CCL wettability are:

- The degree of ordering achieved among ionomer sidechains was predominantly determined by the hydrophilicity of the substrate.
- The affinity of the ionomer thin film to water and the films effective surface hydrophilicity were altered by the ionomer's molecular alignment. The inversion phenomenon observed macroscopically by Volfkovic and Li was found in PFSA thin film measurements as well.
- The degree of ordering was found to be stronger closer to the ionomer/substrate interface and disappeared with increasing distance form the substrate. The propagation of alignment reached up to tens of nm. Platinum substrates where found to significantly impact surface properties in films thinner than ≈ 20 nm.

Another fundamental aspect of properties at the outer surface of a Pt/C/ionomer configuration is the dependence of the wettability on electrode potential that controls the charging state of the interface. It had been suggested in an earlier work that anionic headgroups of ionomer sidechains are chemisorbed at the platinum surface for potentials in the range of 0.1–0.8 *V* vs RHE.[57] Above 0.8 *V*, platinum oxide starts to form, inhibiting the anionic groups from adsorbing to the catalyst surface,[52] but nevertheless inducing a strong preferential orientation of surface anions toward the surface.

The stability and formation of ionomer films is another notable aspect of the wetting behavior of CCL composites. Paul and Karan[58] observed immediate reorganization and loss of all structural orientation when the ionomer film was wetted with liquid water. In contrast, the film was stable over 18 h in water vapor. For flooding control in fuel cells this implies that once flooded, the CCL may loose some of its previously tailored properties. On the other hand, Paul and Karan also showed, that the film can be fully restored by thermal annealing around 130 °C. It should be noted that all these results come from 10 nm thin Nafion ionomer films on *silica* substrate. Hence, it is unclear how this applies to Pt/C catalyst substrates. Nevertheless, time-depended effects of ionomer film reorganization, or aging play a role during cell manufacturing and operation, but still require further research. Since the present work aims to elucidate the principle relations between ionomer film structure and wetting behavior of the CCL, such effects are excluded from the modeling approach at this stage.

Molecular Dynamics: Insight to Structure Formation.— Complementary to experimental approaches, molecular dynamics studies (MD) studies address the question how interfacial structures form and how molecular-level interactions shape their properties. In

---

[a]Contact angles are reported for water, if not noted otherwise.
[b]Only for very small nanoparticles (<1.5 nm) surface energies and properties deviate strongly from the slab-like behavior.[49]
[c]A plethora of experimental works that studied the molecular alignment in thin PFSA films observed similar behavior (reviewed in [52]). However, Andersen et al. are the only ones among them using a fuel cell material (Vulcan XC72) as substrate for the ionomer film.

[d]The vast majority of studies reviewed by Kusoglu and Weber[52] did not use substrates (nor conditions) directly comparable to fuel cell materials. Typically, polished silicon forms the base substrate which then can be coated with platinum, glassy carbon or silica.
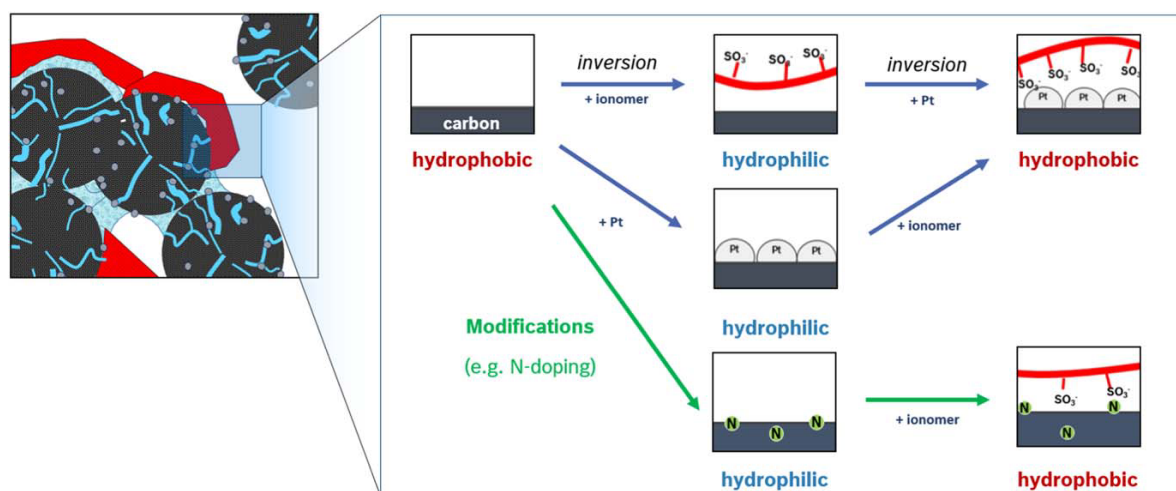
Figure 3. Visualization of the inversion mechanism proposed by Volfkovich, and the impact of modifications as conducted by Ott et al.[51,75]
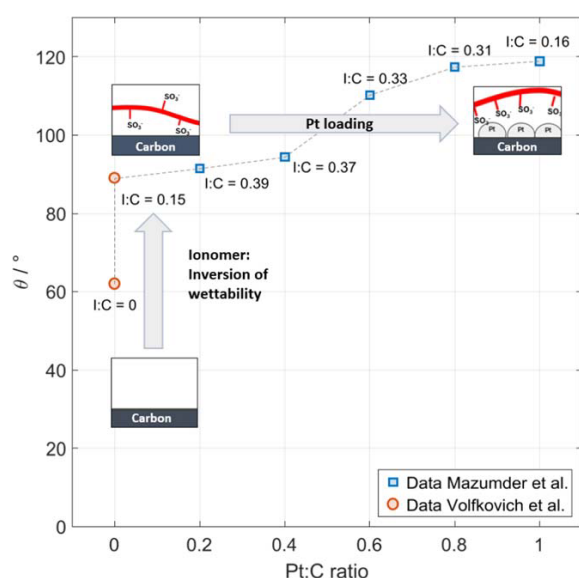

Figure 4. Hydrophobization of Pt/C/ionomer composite with increasing Pt:C ratio, data extracted from Volfkovich[51] and Mazumder.[55]

the following, we will review the MD studies of self-organization or structure formation in CCLs that have been aiming to rationalize the impact of materials modifications, e.g., varying the ion exchange capacity (IEC) of the ionomer, considering different surface groups at the carbon or modifying the composition and thus the dielectric properties of the ink solvent.

Studies to elucidate molecular self-organization inside the CCL focused on the structure and properties of the hydrated Pt/ionomer interface.[59,60] These works recognized a key feature for the inversion phenomenon described in the previous section. The ionomer side-chains interact preferentially with the platinum nanoparticles through the sulfonic groups. However, computed cell sizes were only a few nanometers, which is too small to study organizational effects over several carbon particles or to account for the heterogeneous surface of the Pt/C catalyst.

The perspective on self-organization was extended to the length scale of agglomerates by choosing a coarse-grained (CG-MD)

simulation approach.[23,24] The focus of such studies lies on structure formation in the ink stage of CCL fabrication. As was demonstrated, simulated structures reproduced several features that could also be identified in experimental works, especially pertaining to the structure and morphology of the ionomer.[61,62] The formation of a skin-type ionomer film was observed that corroborated the wettability inversion hypothesis, described above. In case of a hydrophobic carbon surface, the ionomer film assumed a structure in CG-MD simulations with preferential orientation of hydrophobic ionomer backbones toward the hydrophobic carbon surface, while the layer of sidechains with charged head groups is found at the opposite side of the skin layer, oriented away from the carbon surface. Around platinum nanoparticles the sidechains with their charged head groups were oriented toward the platinum surface.

Varying the solvent's dielectric constant, i.e., considering $\epsilon = 2$, 20, 80 to implicitly represent apolar, polar and water-like solvent, showed that solvents with larger dielectric constant lead to the formation of a well-packed, uniform ionomer film.[23] In a follow-up work[24] the inversion mechanism proposed by Volfkovich et al.[51] was corroborated further and implications of this inversion phenomenon were elucidated. Introducing platinum to secondary pores will render the composite more hydrophobic in terms of its overall water sorption behavior. The other case, an effectively hydrophilic composite, will result from drastically reducing the platinum loading or depositing the platinum predominantly inside the primary pores of the carbon that remain inaccessible for the ionomer.

Furthermore, MD simulations confirmed the significant role of functional groups on the carbon's surface. Carboxylic acid groups in both protonated ($-$COOH) and ionic form ($-$COO$^-$) were studied as a practically relevant materials modification.[63] The thus functionalized carbon surface became hydrophilic and therefore attracted the charged headgroups at ionomer sidechains, forcing the backbones to the outer surface of the film configuration and rendering this outer surface more hydrophobic; in effect, the composite medium will effectively appear more hydrophobic.

Mashio et al.[64] further evaluated the role of material modifications, e.g., ionomer IEC, type of carbon, dielectric constant of the ink solvent and surface functionalization of carbon. The quantitative descriptors, namely ionomer coverage and molar percentage of the backbones attached to the carbon, were correlated with a range of material and fabrication parameters. The authors concluded that the proportion of alcohol in the solvent mixture must be thoroughly tuned in terms of ionomer IEC and carbon surface properties in order to foster formation of well-packed ionomer film. The approach of Mashio et al. to evaluate dimensionless quantities of backbone

orientation and ionomer coverage to describe the self-assembled composite was extended by a dimensionless descriptor of wettability by Damasceno Borges et al.[65] Their work focused on understanding the correlation between the strength of the ionomer interaction with the Pt/C substrate and substrate hydrophilicity. The force field was adjusted to the surface wettability of the Pt/C substrate and could not only represent pure carbon or platinum substrates, but also mixed surfaces. The study featured an ionomer film with 3.0–4.5 nm thickness and rated the resulting hydrophilicity at the pore/ionomer interface on a dimensionless scale by accounting for the local concentration of sidechains and backbone.

The Pt/ionomer interface shows some resemblance with biological and colloidal systems studied by Kanduc et al.[66–69] Their MD simulations explored asymmetric water-filled interfaces of hydrophilic and hydrophobic surfaces. The model system used soft walls made of long apolar chains carrying polar hydroxyl headgroups. The interface was studied with regard to its stability. The adhesion/repulsion behavior and width of the water-filed gap region in the simulation were evaluated. As a result, three regimes could be identified for interface stability: hydration repulsion for very polar surfaces, dry adhesion for intermediate polarities, and cavitation-induced long-range attraction for low surface polarities. The transitions among these regimes can be expressed in terms of the surfaces' hydrophilicity as well as their mutual binding strength.[66,67]

Transferred to the Pt/C/ionomer system, these findings imply stability of the interface for carbon-backbone interaction (HO–HO, dry adhesion regime), while a Pt/sidechain combination (HI–HI, hydration repulsion) would not be stable. Water is the essential reaction medium. Together with a sufficient proton concentration it is needed to uphold high reaction rates during fuel cell operation. The stability regimes described by Kanduc et al. might impose additional design boundaries on the wettability of the Pt/C substrate. If the substrate surface is too hydrophobic, as for bare carbon or low platinum particle density, ionomer backbones will be collapsed onto the substrate surface. Consequently, water is expulsed from the interface, thereby causing electrocatalytic inactivation. On the other hand, if the hydrophilicity is too high, as could be the case for high platinum particle density, the unlimited growth of the water-filled gap dilutes proton concentration provided by the ionomer, thus negatively impacting the reaction conditions and electrocatalytic rates at the catalyst surface. An intermediate case with well-attuned carbon wettability and platinum particle density is expected, for which a water water film with stable thickness in the nm-range exists that could ensure high electrocatalytic activity. Possibly, the chemisorption of anionic sidechain headgroups at platinum can stabilize the interface in this condition. Further, the water-gap thickness might be tunable by potential, mediated by the potential-dependent variations in platinum oxide coverage and surface charge density.

Schlaich et al.[69] extended the model system of Kanduc et al. by applying charge densities to the interface walls. For weakly charged surfaces the contributions of hydration and Poisson-Boltzmann repulsion are additive, but for a surface charge density of $\sigma = -0.77\,e\,\mathrm{nm}^2$ this additivity breaks down due to the combination of further effects, such as counterion correlations or the surface charge-induced reorientation of hydration water. Thus, the hydrophilicity of the surfaces alone does not serve as a reliable criterion to predict the stability of an interfacial water film with finite thickness. We will transfer these insights to our model approach in the following section.

Basic Concept to Model CCL Wetting Behaviour.—Based on the review of experimental and theoretical works in previous sections, we have developed a basic concept to capture surface properties and inversion behavior of the Pt/C/ionomer composite that is illustrated in Fig. 5(a).

To quantitatively describe the structural reorganization that causes the observed wettability inversion, we introduce a dimensionless number: *the Degree of Alignment*, Δ_{DA}. It quantifies the inversion state of the ionomer on a scale from 0 to 1. A value of $\Delta_{DA} = 0$ represents a fully hydrophobic inverted ionomer with backbones turned away from the corresponding interface and the sidechains strongly interacting with the support's surface. In the opposite state, sidechains pointing away and backbones attached to the Pt/C surface, is described by $\Delta_{DA} = 1$. Concluding from several works which investigated the wetting behavior together with structural organization effects,[70–72] we assign the following contact angles to the Δ_{DA} scale (see Fig. 5b):

- The state of a fully hydrophobic outer surface ($\Delta_{DA} = 0$) is assumed for $\theta_{HO} = 120°$, which is the value of pure PTFE.[73] Other sources report a value of 119° for a packed CF_3-surface.[74]
- The state of a fully hydrophilic outer surface ($\Delta_{DA} = 1$) is assumed for $\theta_{HI} = 30°$ as the median from literature values[70] for hydrophilic ionomer behavior.

To correlate the dimensionless value of Δ_{DA} with the resulting contact angle of the outer surface, θ_{ion}, we apply a linear interpolation of $\cos(\theta)$,

$$\cos(\theta_{ion}) = \Delta_{DA}(\cos(\theta_{HI}) - \cos(\theta_{HO})) + \cos(\theta_{HO}). \quad [1]$$

The fundamental assumption here is that the contributions to free surface energy from the molecular components of ionomer film, i.e., sidechains and backbone, superimpose linearly. From this assumption, linear superposition of the inherent wetting properties, expressed as $\cos\theta$, follows.[e] The degree of alignment Δ_{DA} acts as a measure for local concentration of either sidechains or backbone and thus directly translates into surface area contributions at the outer surface ionomer film.

The second main idea of our model approach is to assign different surface types a specific value of Δ_{DA} which the ionomer will adapt when interacting with the corresponding surface. To discuss the capabilities of our concept we introduce three scenarios representing different strength of interaction of surface species with the ionomer:

- Since platinum was found to interact strongly with the sidechains it is assigned the minimum value of $\Delta_{DA,Pt} = 0$. Indeed, a contact angle value of around 120° was found experimentally on highly platinum-loaded support materials covered by a thin ionomer film[55] (see Fig. 4).
- A carbon surface interacts moderately with the backbone and weakly with the sulfonic headgroups if it carries only a few functional groups (e.g. Ketjen Black) or is highly graphitized. Therefore $\Delta_{DA,carbon,bare} = 0.75$ was assigned for a conventional carbon. The second main type of carbon, Vulcan XC72, carries more functional groups on its surface, thus will have a lower Δ_{DA} value in the range of 0.2 to 0.4.
- To account for the relatively strong interaction of cationic functional groups with the sidechains[75] a nitrogen-doped functionalized carbon is represented by $\Delta_{DA,carbon,mod} = 0.15$.

The approach of using a Δ_{DA} parameter aims to address the complete picture of interaction and inversion of ionomer on a Pt/C support. The value of Δ_{DA} is not only related to the contact angle of the Pt/C surface, which could be measured experimentally, using one of the techniques discussed above. As revealed by the previously discussed MD studies, surface charges and steric effects are complicating the picture, resulting in a non-trivial correlation between surface properties of the Pt/C catalyst and the resulting degree of alignment in the contacting ionomer film. Since both the ionomer sidechains and the functional groups at carbon carry charges, all effects influencing their interaction like steric hindrance, counterion correlations and surface charge-induced orientational

---

[e]This can be shown by considering the Young-Laplace equation of a triple phase boundary with liquid L on a solid surface S:
$\cos(\theta_{LS}) = \frac{\gamma_S - \gamma_{LS}}{\gamma_L} = \frac{\sum_i a_i \gamma_{S,i} - \sum_i a_i \gamma_{LS,i}}{\gamma_L} = \sum_i a_i \left(\frac{\gamma_{S,i} - \gamma_{LS,i}}{\gamma_L} \right) = \sum_i a_i \cos(\theta_i)$.
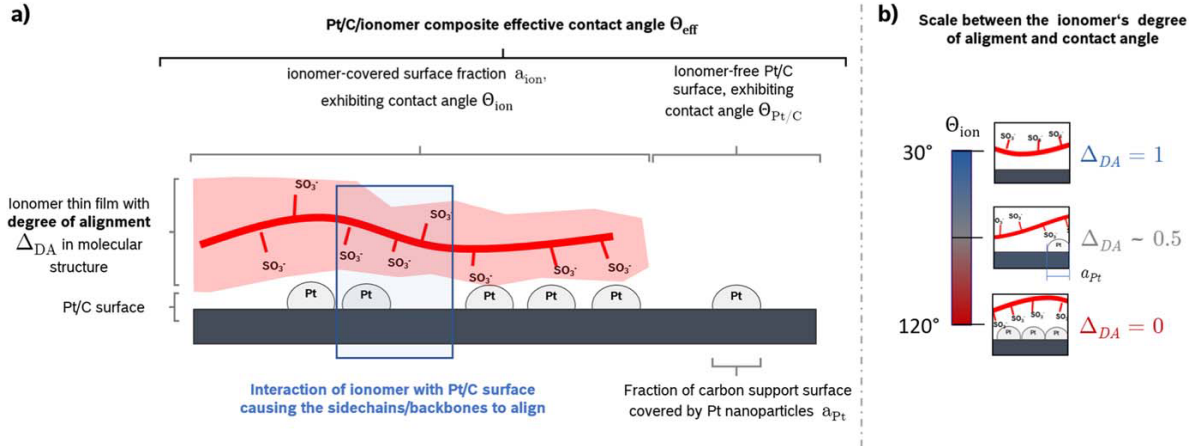
Figure 5. (a) Schematic of the Pt/C/ionomer interface in the secondary pores of the CCL. The heterogeneous wetting properties, described by the model approach, account for the surface fractions of platinum and ionomer and the resulting degree of alignment inside of the ionomer thin film. (b) A linear scale is applied to interpolate contact angles between the two extremes of fully aligned molecular structure of the ionomer thin film.

alignment of dipolar water molecule are lumped in the Δ_{DA} parameter.

The catalyst surface is heterogeneous due to platinum nanoparticles partially covering the carbon surface. Both platinum and carbon will affect the ionomer's molecular alignment. In order to estimate the average degree of alignment imposed to the ionomer thin film, we assume a linear superposition of the quantitative impact according to the surface fraction occupied by platinum, a_{Pt}, and carbon, $a_C = 1 - a_{Pt}$,

$$\Delta_{DA,ion} = \Delta_{DA,Pt}a_{Pt} + \Delta_{DA,carbon}(1 - a_{Pt}). \quad [2]$$

The ionomer covers only a certain fraction of the support surface,[61,62] leaving parts of Pt/C surface bare. The composite's effective contact angle can thus be obtained from a linear superposition via the respective surface area fraction a_i,

$$\cos(\theta_{eff}) = \sum_i \cos(\theta_i)a_i, \quad [3]$$

where the index i denotes the different surfaces involved, $i = \{Pt, C, ionomer\}$. This assumption, also known as Cassie's rule of mixing, is proven to work well in porous systems inside rocks made of minerals with different wetting behavior[76] and is applied here to calculate the contact angle of the bare Pt/C surface ($\theta_{Pt/C}$), and the composite's overall effective contact angle (θ_{eff}) from the ionomer coverage, a_{ion}, and the corresponding contact angles of ionomer and Pt/C surface,

$$\cos(\theta_{Pt/C}) = \cos(\theta_{Pt})a_{Pt} + \cos(\theta_{carbon})(1 - a_{Pt}), \text{ and} \quad [4]$$

$$\cos(\theta_{eff}) = \cos(\theta_{ion})a_{ion} + \cos(\theta_{Pt/C})(1 - a_{ion}). \quad [5]$$

Contact angles assumed for component materials in the base case are listed in Table I. The value for a functionalized carbon had to be estimated. Polar functional groups render the surface moderately hydrophilic, so a contact angle of 60° is reasonable.

Understanding Platinum Loading Reduction and Catalyst Layer Flooding

In order to decipher the wetting behavior at different levels of platinum loading and ionomer dispersion, we conducted a parameter study varying both a_{Pt} and a_{ion} between 0 and 1. The fraction a_{Pt} depends on CCL composition, i.e., Pt:C mass ratio, and other structural details such as platinum particle radius and overall carbon

surface available for platinum deposition. Assuming the latter two to be roughly constant for any Pt:C ratio, a_{Pt} will be taken as a measure for platinum loading of the CCL in the following. The ionomer coverage a_{ion} depends on the dispersion and film thickness of ionomer, which is primarily adjusted by the amount of ionomer, composition of the ink solvent and fabrication route.

Our parameter study yields average contact angles for secondary pores for both conventional and functionalized carbon supports in the CCL composite. The results for the conventional hydrophobic carbon are depicted in Fig. 6a. For low platinum and ionomer coverage, the carbon exhibits properties according to its intrinsic material parametrization. Increasing the platinum loading renders the Pt/C surface more hydrophilic, the contact angle is gradually reduced to 10° at $a_{Pt} = 1$ and $a_{ion} = 0$, representing a pure platinum surface.

Considering addition of ionomer to the composite, accordingly increasing a_{ion}, the impact of the inversion phenomenon becomes clear. Adding ionomer to the Pt-free carbon support, the effective contact angle is shifted toward the hydrophilic range around 60°. In contrast, combining ionomer with a platinum loaded carbon (values of a_{Pt} and a_{ion} approaching 1), results in a highly hydrophobic composite material with a contact angle of up to 120°.

A conventional carbon material with high platinum and ionomer loading exhibits predominantly hydrophobic behavior ($\theta_{eff} > 90°$). As proposed by Villanueva,[29] such a state of the secondary pores is considered beneficial for good water transport and exhibits a large resistance to flooding. When the platinum loading is lowered, as indicated in Fig. 6a, the orientation of sidechains and backbone gradually inverts. Consequently, the wetting behavior of the Pt/C/ionomer composite changes from hydrophobic to hydrophilic and the CCL ends up highly prone to flooding.

This consideration leads us to the main hypothesis that we would like to advocate here: lowering the platinum loading while keeping the CCL thickness constant could trigger the inversion of the wetting behavior of the Pt/C/ionomer composite due to the reorientation of the ionomer. This hypothesis is consistent with the work of Muzaffar et al.[11] where the scenarios of achieving a platinum loading reduction were considered, corresponding to constant composition or constant thickness. For the constant composition scenario, trimming the platinum loading by reducing the CCL thickness, thus keeping the Pt:C ratio constant, will reduce the vaporization capability and thereby shift the tipping point for flooding to lower current densities. Our work here addresses the constant thickness scenario, in which a platinum loading reduction is achieved by lowering the Pt:C ratio while keeping the thickness

Table I. Parametrization of contact angle and degree of inversion for platinum, carbon and ionomer.

Material	θ	Reference	Δ_{DA}
Platinum	10°	[48]	0
Conventional carbon	84°	[41]	0.75
Functionalized carbon	60°	[43]	0.15
Ionomer states			
Hydrophobic-inverted	120°	[73,74]	0
Hydrophilic-inverted	30°	[70]	1

work and it's counterpart from Muzaffar et al. complete the greater picture. As we have found, no matter whether the platinum loading reduction is achieved by reducing the CCL thickness or by diluting the platinum dispersion on the support—in both cases the water balance is expected to shift toward a higher propensity for flooding, which turns out to be the root cause for the increase of oxygen transport losses.

For functionalized carbons (e.g., by nitrogen doping) as indicated in Fig. 6b, the alignment of sidechains toward the Pt/C surface is upheld when lowering the platinum loading. Thus, the effective wetting behavior of secondary pores does not turn hydrophilic as long as the ionomer coverage is high ($a_{ion} > 0.65$). Indeed, for this
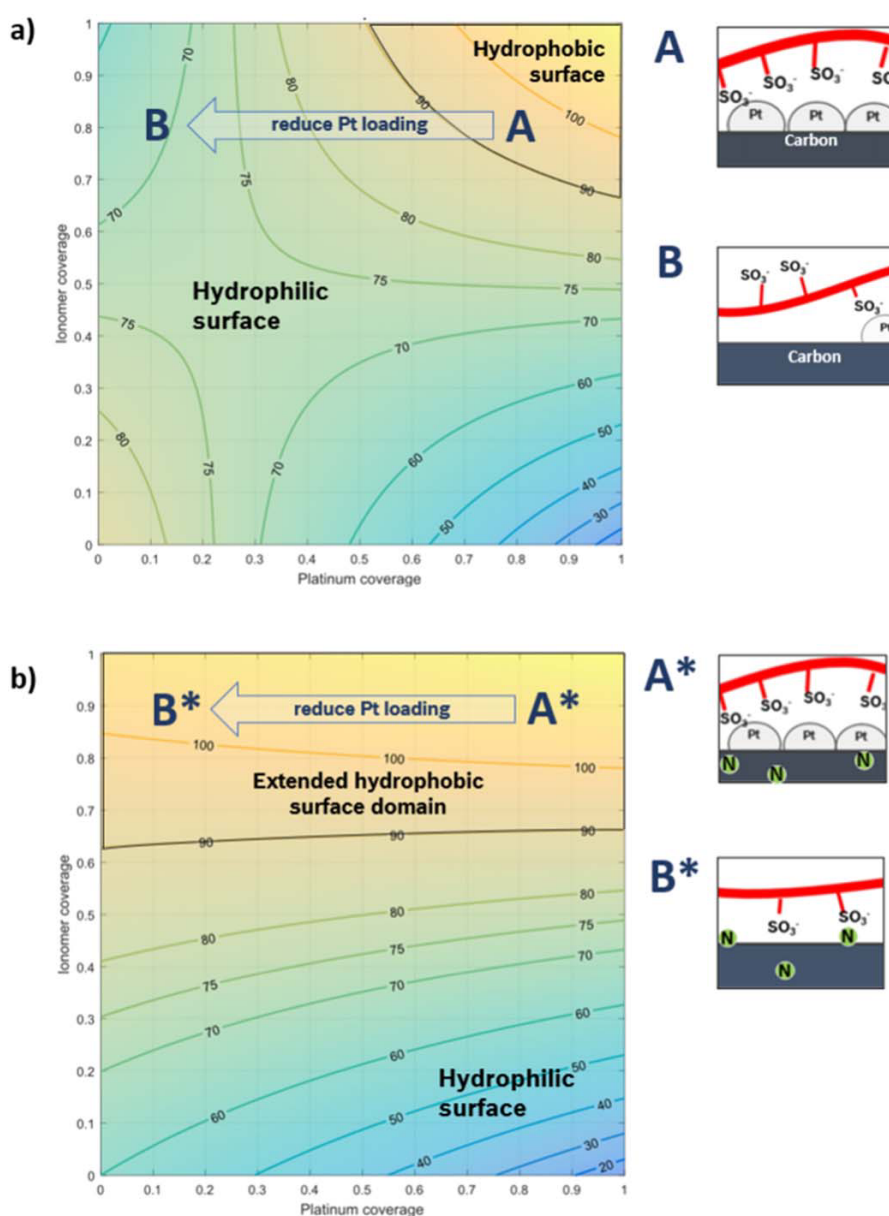
Figure 6. Effective contact angle, θ_{eff}, of Pt/C/ionomer composite over platinum surface fraction a_{Pt} and ionomer coverage a_{ion} for the cases of a (a) conventional carbon support and (b) a functionalized carbon support.

constant, thus diluting the platinum loading. In combination this

case Ott et al.[75] observed a significantly improved performance of

low-platinum-loaded cathodes: the typically observed early onset of mass transport limitations was shifted to higher current densities. The authors interpreted their finding with a more even ionomer distribution, thus a lowered ionomer film resistance. Our hypothesis provides an alternative or additional explanation, based on considering the pivotal role of effective wettability in the space of secondary pores for the water management. Since the functional groups at carbon cause anionic headgroups at ionomer sidechains to orient themselves toward them, the ionomer film's outer surface stays hydrophobic even at much reduced platinum loading.

Towards Tailored Materials for High Performance Fuel Cells.—Structure-based models might be the key to enable fuel cell developers to tailor CCL structure. Deliberately adjusting the structural features via fabrication routes to suit the desired performance offers a more efficient way of developing new materials than the time-consuming empirical screening. Comprehensive models can guide experiments by providing a fundamental understanding of the observed trends and propose steps for the next iteration in experimental optimization of fuel cell materials.

In CCL fabrication, one can choose from a plethora of possible synthesis routes, materials and electrode recipes, all of them affecting the CCL microstructure in a certain way. We see our concept of the degree of inversion as a first attempt to link fabrication, e.g., N-doping, as accomplished by Ott et al.,[75] via a structural impact (ionomer alignment), with properties of key relevance for performance (wetting behavior and susceptibility to flooding). Not only the morphology of carbon can be subject to tailored CCL materials. Also the dispersion and distribution of platinum on the support can be tuned locally to be deposited primarily inside or outside the primary pores of the carbon support.[47] The same applies for ionomer. The choice and composition of the of ink solvent affects the ionomer dispersion and film formation.[77–80] The degree of dispersion can reach from fully lumped ionomer too perfectly dispersed ionomer, with the optimum to be found in-between.[81] The authors will address the resulting heterogeneities in ionomer coverage in a follow-up work, accounting for additional structural parameters, such as component and void fractions, ionomer dispersion and coverage, and the porous network properties. Based on this treatment, a description of mixed wettability will be possible that aligns well with previous works that employed continuous distributions of contact angles.[27,29]

Conclusions

Motivated by the wide-ranging relevance of water in cathode catalyst layers (CCL), this work focused on rationalizing the causal relationship between a reduction of the platinum loading and the presumed changes of the composite's wettability. A reviewing recent relevant works in PEFC performance modeling revealed deficiencies in linking structural features with the wetting behavior of the composite electrode medium. Relevant experimental works in the literature that have explored the wetting behavior of CCL composite media point to an inversion of the wetting behavior: when ionomer covers hydrophilic Pt/C surfaces, an effective hydrophobic behavior of the composite medium has been observed; while interaction of ionomer with a hydrophobic Pt/C surfaces results in effective hydrophilic behavior of the resulting composite medium. Molecular dynamic studies, also reviewed in this article, bolster the mechanistic explanation of this inversion phenomenon, linking the orientation of charged ionomer sidechains and the corresponding wetting behavior to specific interactions of ionomer sidechains and backbones with Pt/C surfaces.

We have shown that the observed mixed wettability can be explained by the different types of surfaces present in secondary pores of the CCL. Ionomer at the interface with the platinum-carrying carbon particles is responsible for the hydrophobic domains of the pore network while bare Pt/C contributes to the hydrophilic portion. Similarly, ionomer-covered domains of hydrophobic carbon

contribute to hydrophilic secondary pores wile bare carbon contributes to hydrophobic secondary pores. The quantitative understanding of the alignment phenomena was rationalized with a novel descriptor, the ionomer's degree of alignment that links surface properties of the Pt/C catalyst with the effective contact angle of the composite medium.

Following the correlations exploited in our model, the observed transport losses when lowering the platinum loading can be plausibly explained: changing the surface properties by lowering the platinum loading—while keeping the CCL thickness constant—will trigger the transition from effective hydrophobic to hydrophilic wetting behavior of the CCL composite. According to these logics, the reduction of the Pt:C ratio (or dilution of Pt in the composite) should leave the cathode more prone to flooding. This hypothesis completes the larger picture of the water balance tipping over when lowering the platinum loading. In any case, regardless of whether a low platinum loading is achieved by thickness reduction or by dilution, the distortion of the water balance will strike by rendering the CCL and GDL more prone to flooding.

In a wider context, our approach of the structure-based modeling of wettability phenomena contributes to bridging the gap between material selection and design, fabrication approach, effective physico-chemical properties of composite CCL media, and fuel cell performance. A comprehensive structure-based model with these added capabilities will be a valuable tool in the hands of fuel cell developers in order to achieve a functionally fine-tuned CCL design.

ORCID

W. Olbrich https://orcid.org/0000-0003-0164-2219
T. Kadyk https://orcid.org/0000-0002-5329-1265
U. Sauter https://orcid.org/0000-0002-0357-5534
M. Eikerling https://orcid.org/0000-0002-0764-8948

References

1. C. Sealy, "The problem with platinum." *Mater. Today*, **11**, 65 (2008).
2. M. M. Whiston, I. L. Azevedo, S. Litster, K. S. Whitefoot, C. Samaras, and J. F. Whitacre, "Expert assessments of the cost and expected future performance of proton exchange membrane fuel cells for vehicles." *Proceedings of the National Academy of Sciences*, **116**, 4899 (2019).
3. H. Li et al., "A review of water flooding issues in the proton exchange membrane fuel cell." *Journal of Power Sources*, **178**, 103 (2008).
4. M. Eikerling, "Water management in cathode catalyst layers of PEM fuel cells." *J. Electrochem. Soc.*, **153**, E58 (2006).
5. J. Liu and M. Eikerling, "Model of cathode catalyst layers for polymer electrolyte fuel cells: the role of porous structure and water accumulation." *Electrochimica Acta*, **53**, 4435 (2008).
6. I. V. Zenyuk, P. K. Das, and A. Z. Weber, "Understanding impacts of catalyst-layer thickness on fuel-cell performance via mathematical modeling." *J. Electrochem. Soc.*, **163**, F691 (2016).
7. T. Soboleva, K. Malek, Z. Xie, T. Navessin, and S. Holdcroft, "PEMFC catalyst layers: the role of micropores and mesopores on water sorption and fuel cell activity." *ACS Applied Materials & Interfaces*, **3**, 1827 (2011).
8. E. Padgett et al., "Connecting fuel cell catalyst nanostructure and accessibility using quantitative Cryo-STEM tomography." *J. Electrochem. Soc.*, **165**, F173 (2018).
9. T. Mashio, K. Sato, and A. Ohma, "Analysis of water adsorption and condensation in catalyst layers for polymer electrolyte fuel cells." *Electrochimica Acta*, **140**, 238 (2014).
10. M. Eikerling, A. A. Kornyshev, and A. R. Kucernak, "Water in polymer electrolyte fuel cells: Friend or foe?" *Phys. Today*, **59**, 38 (2006).
11. T. Muzaffar, T. Kadyk, and M. Eikerling, "Tipping water balance and the Pt loading effect in polymer electrolyte fuel cells: a model-based analysis." *Sustainable Energy & Fuels*, **2**, 1189 (2018).
12. M. Eikerling and A. Kornyshev, "Modelling the performance of the cathode catalyst layer of polymer electrolyte fuel cells." *Journal of Electroanalytical Chemistry*, **453**, 89 (1998).
13. M. Eikerling, A. Ioselevich, and A. Kornyshev, "How good are the Electrodes we use in PEFC?" *Fuel Cells*, **4**, 131 (2004).
14. E. Sadeghi, A. Putz, and M. Eikerling, "Hierarchical model of reaction rate distributions and effectiveness factors in catalyst layers of polymer electrolyte fuel cells." *J. Electrochem. Soc.*, **160**, F1159 (2013).
15. M. Eikerling and A. Kulikovsky, *Polymer Electrolyte Fuel Cells: Physical Principles of Materials and Operation* (CRC Press, Boca Raton, FL) (2014), Google-Books-ID: xUTNBQAAQBAJ.
16. N. Zamel, "The catalyst layer and its dimensionality - A look into its ingredients and how to characterize their effects." *Journal of Power Sources*, **309**, 141 (2016).

17. Y. M. Volfkovich, V. Sosenkin, and V. Bagotsky, "Structural and wetting properties of fuel cell components." *Journal of Power Sources*, **195**, 5429 (2010).
18. H. P. F. Gunterman, "Characterization of fuel-cell diffusion media." *PhD Thesis*, UC Berkeley (2011).
19. H. Yu, C. Ziegler, M. Oszcipok, M. Zobel, and C. Hebling, "Hydrophilicity and hydrophobicity study of catalyst layers in proton exchange membrane fuel cells." *Electrochimica Acta*, **51**, 1199 (2006).
20. L. M. Pant, M. R. Gerhardt, N. Macauley, R. Mukundan, R. L. Borup, and A. Z. Weber, "Along-the-channel modeling and analysis of PEFCs at low stoichiometry: Development of a 1 + 2d model." *Electrochimica Acta*, **326**, 134963 (2019).
21. T. Soboleva, X. Zhao, K. Malek, Z. Xie, T. Navessin, and S. Holdcroft, "On the micro-, meso-, and macroporous structures of polymer electrolyte membrane fuel cell catalyst layers." *ACS Applied Materials & Interfaces*, **2**, 375 (2010).
22. Y.-C. Park, H. Tokiwa, K. Kakinuma, M. Watanabe, and M. Uchida, "Effects of carbon supports on Pt distribution, ionomer coverage and cathode performance for polymer electrolyte fuel cells." *Journal of Power Sources*, **315**, 179 (2016).
23. K. Malek, M. Eikerling, Q. Wang, T. Navessin, and Z. Liu, "Self-organization in catalyst layers of polymer electrolyte fuel cells." *The Journal of Physical Chemistry C*, **111**, 13627 (2007).
24. K. Malek, T. Mashio, and M. Eikerling, "Microstructure of catalyst layers in pem fuel cells redefined: a computational approach." *Electrocatalysis*, **2**, 141 (2011).
25. A. Weber and M. Hickner, "Modeling and high-resolution-imaging studies of water-content profiles in a polymer-electrolyte-fuel-cell membrane-electrode assembly." *Electrochimica Acta*, **53**, 7668 (2008).
26. V. Mulone and K. Karan, "Analysis of capillary flow driven model for water transport in PEFC cathode catalyst layer: Consideration of mixed wettability and pore size distribution." *International Journal of Hydrogen Energy*, **38**, 558 (2013).
27. Z. Zhou, A. Putz, and M. Secanell, "A mixed wettability pore size distribution based mathematical model for analyzing two-phase flow in porous electrodes: i. mathematical model." *J. Electrochem. Soc.*, **164**, F530 (2017).
28. M. El Hannach, M. Prat, and J. Pauchet, "Pore network model of the cathode catalyst layer of proton exchange membrane fuel cells: Analysis of water management and electrical performance." *International Journal of Hydrogen Energy*, **37**, 18996 (2012).
29. P. A. Mateo Villanueva, "A mixed wettability pore size distribution model for the analysis of water transport in PEMFC materials." *PhD Thesis*, University of Alberta (2013).
30. T. Hutzenlaub, J. Becker, R. Zengerle, and S. Thiele, "Modelling the water distribution within a hydrophilic and hydrophobic 3d reconstructed cathode catalyst layer of a proton exchange membrane fuel cell." *Journal of Power Sources*, **227**, 260 (2013).
31. X. Wang and T. V. Nguyen, "Modeling the effects of capillary property of porous media on the performance of the cathode of a PEMFC." *J. Electrochem. Soc.*, **155**, B1085 (2008).
32. T. V. Nguyen, G. Lin, H. Ohn, and X. Wang, "Measurement of capillary pressure property of gas diffusion media used in proton exchange membrane fuel cells." *Electrochem. Solid-State Lett.*, **11**, B127 (2008).
33. H. P. Gunterman, A. Kwong, J. T. Gostick, A. Kusoglu, and A. Z. Weber, "Water uptake in PEMFC catalyst layers." *ECS Trans.*, **41**, 647 (2011).
34. A. Kusoglu, A. Kwong, K. T. Clark, H. P. Gunterman, and A. Z. Weber, "Water uptake of fuel-cell catalyst layers." *J. Electrochem. Soc.*, **159**, F530 (2012).
35. A. L. Dicks, "The role of carbon in fuel cells." *Journal of Power Sources*, **156**, 128 (2006).
36. P. Serp and B. Machado, *Nanostructured carbon materials for catalysis* (Royal Society of Chemistry, Cambridge, UK) (2015).
37. M. Uchida, "PEFC catalyst layers: effect of support microstructure on both distributions of Pt and ionomer and cell performance and durability." *Current Opinion in Electrochemistry*, **21**, 209 (2020).
38. Y. Wei and C. Q. Jia, "Intrinsic wettability of graphitic carbon." *Carbon*, **87**, 10 (2015).
39. Y. J. Shin, Y. Wang, H. Huang, G. Kalon, A. T. S. Wee, Z. Shen, C. S. Bhatia, and H. Yang, "Surface-energy engineering of graphene." *Langmuir*, **26**, 3798 (2010).
40. S. Wang, Y. Zhang, N. Abidi, and L. Cabrales, "Wettability and surface free energy of graphene films." *Langmuir*, **25**, 11078 (2009).
41. K. Kinoshita, *Carbon: Electrochemical and Physicochemical Properties* (Wiley, New York, NY) (1988).
42. J. Tang, J. Liu, N. L. Torad, T. Kimura, and Y. Yamauchi, "Tailored design of functional nanoporous carbon materials toward fuel cell applications." *Nano Today*, **9**, 305 (2014).
43. A. Yan, X. Xiao, I. Külaots, B. W. Sheldon, and R. H. Hurt, "Controlling water contact angle on carbon surfaces from 5° to 167°." *Carbon*, **44**, 3116 (2006).
44. A. N. Golikand, E. Lohrasbi, M. G. Maragheh, and M. Asgari, "Effect of carbon surface oxidation on platinum supported carbon particles on the performance of gas diffusion electrodes for the oxygen reduction reaction." *Journal of Applied Electrochemistry*, **38**, 869 (2008).
45. S. M. Andersen, M. Borghei, R. Dhiman, V. Ruiz, E. Kauppinen, and E. Skou, "Adsorption behavior of perfluorinated sulfonic acid ionomer on highly graphitized carbon nanofibers and their thermal stabilities." *The Journal of Physical Chemistry C*, **118**, 10814 (2014).
46. A. Orfanidi, P. Madkikar, H. A. El-Sayed, G. S. Harzer, T. Kratky, and H. A. Gasteiger, "Key to high performance low pt loaded electrodes." *J. Electrochem. Soc.*, **164**, F418 (2017).
47. G. S. Harzer, A. Orfanidi, H. El-Sayed, P. Madkikar, and H. A. Gasteiger, "Tailoring catalyst morphology towards high performance for low Pt loaded PEMFC cathodes." *J. Electrochem. Soc.*, **165**, F770 (2018).
48. K. Bewig and W. Zisman, "The wetting of gold and platinum by water." *The Journal of Physical Chemistry*, **69**, 4238 (1965).
49. L. Wang, A. Roudgar, and M. Eikerling, "Ab initio study of stability and site-specific oxygen adsorption energies of pt nanoparticles." *The Journal of Physical Chemistry C*, **113**, 17989 (2009).
50. S. G. Kandlikar and T. Kimura, "Molecular dynamics simulation and measurement of contact angle of water droplet on a platinum surface." *Proceedings of the ASME 2001 International Mechanical Engineering Congress and Exposition*Heat Transfer Volume 1 — Fundamentals of Heat Transfer, p.343–348 (2001).
51. Y. M. Vol'fkovich, V. E. Sosenkin, and N. F. Nikol'skaya, "Hydrophilic-hydrophobic and sorption properties of the catalyst layers of electrodes in a proton-exchange membrane fuel cell: a stage-by-stage study." *Russian Journal of Electrochemistry*, **46**, 438 (2010).
52. A. Kusoglu and A. Z. Weber, "New insights into perfluorinated sulfonic-acid ionomers." *Chem. Rev.*, **117**, 987 (2017).
53. A. Kusoglu, "Ionomer thin films in PEM fuel cells." *Encyclopedia of Sustainability Science and Technology*, ed. R. A. Meyers (Springer, New York, NY) pp 1 (2018).
54. X. Li, F. Feng, K. Zhang, S. Ye, D. Y. Kwok, and V. Birss, "Wettability of nafion and nafion/vulcan carbon composite films." *Langmuir*, **28**, 6698 (2012).
55. S. Mazumder, "Carbon-ionomer nanocomposite wetting properties: the role of ionomer composition and surface roughness." *International Journal of Materials Science and Applications*, **4**, 69 (2015).
56. Z. Fang, A. G. Star, and T. F. Fuller, "Effect of carbon corrosion on wettability of PEM fuel cell electrodes." *J. Electrochem. Soc.*, **166**, F709 (2019).
57. T. Masuda, F. Sonsudin, P. R. Singh, H. Naohara, and K. Uosaki, "Potential-dependent adsorption and desorption of perfluorosulfonated ionomer on a platinum electrode surface probed by electrochemical quartz crystal microbalance and atomic force microscopy." *The Journal of Physical Chemistry C*, **117**, 15704 (2013).
58. D. K. Paul and K. Karan, "Conductivity and wettability changes of ultrathin nafion films subjected to thermal annealing and liquid water exposure." *The Journal of Physical Chemistry C*, **118**, 1828 (2014).
59. E. J. Lamas and P. B. Balbuena, "Molecular dynamics studies of a model polymer-catalyst-carbon interface." *Electrochimica Acta*, **51**, 5904 (2006).
60. R. Jinnouchi, K. Kudo, N. Kitano, and Y. Morimoto, "Molecular dynamics simulations on o 2 permeation through nafion ionomer on platinum surface." *Electrochimica Acta*, **188**, 767 (2016).
61. T. Soboleva, "On the microstructure of PEM fuel cell catalyst layers." *PhD Thesis*, Simon Fraser University (2010).
62. M. Lopez-Haro, L. Guétaz, T. Printemps, A. Morin, S. Escribano, P.-H. Jouneau, P. Bayle-Guillemaud, F. Chandezon, and G. Gebel, "Three-dimensional analysis of Nafion layers in fuel cell electrodes." *Nat. Commun.*, **5**, 5229 (2014).
63. T. Mashio, K. Malek, M. Eikerling, A. Ohma, H. Kanesaka, and K. Shinohara, "Molecular dynamics study of ionomer and water adsorption at carbon support materials." *The Journal of Physical Chemistry C*, **114**, 13739 (2010).
64. T. Mashio, A. Ohma, and T. Tokumasu, "Molecular Dynamics Study of Ionomer Adsorption at a Carbon Surface in Catalyst Ink." *Electrochimica Acta*, **202**, 14 (2016).
65. D. Damasceno Borges, G. Gebel, A. A. Franco, K. Malek, and S. Mossa, "Morphology of supported polymer electrolyte ultrathin films: a numerical study." *The Journal of Physical Chemistry C*, **119**, 1201 (2015).
66. M. Kanduč and R. R. Netz, "From hydration repulsion to dry adhesion between asymmetric hydrophilic and hydrophobic surfaces." *Proceedings of the National Academy of Sciences*, **112**, 12338 (2015).
67. M. Kanduč, A. Schlaich, E. Schneck, and R. R. Netz, "Water-mediated interactions between hydrophilic and hydrophobic surfaces." *Langmuir*, **32**, 8767 (2016).
68. M. Kanduč and R. R. Netz, "Atomistic simulations of wetting properties and water films on hydrophilic surfaces." *The Journal of Chemical Physics*, **146**, 164705 (2017).
69. A. Schlaich, A. P. dos Santos, and R. R. Netz, "Simulations of nanoseparated charged surfaces reveal charge-induced water reorientation and nonadditivity of hydration and mean-field electrostatic repulsion." *Langmuir*, **35**, 551 (2019).
70. S. Goswami, S. Klaus, and J. Benziger, "Wetting and absorption of water drops on nafion films." *Langmuir*, **24**, 8627 (2008).
71. T. A. Zawodzinski, S. Gottesfeld, S. Shoichet, and T. J. McCarthy, "The contact angle between water and the surface of perfluorosulphonic acid membranes." *Journal of Applied Electrochemistry*, **23**, 86 (1993).
72. M. Bass, A. Berman, A. Singh, O. Konovalov, and V. Freger, "Surface structure of nafion in vapor and liquid." *The Journal of Physical Chemistry B*, **114**, 3784 (2010).
73. W. A. Zisman, "Contact angle, wettability, and adhesion,." *Advances in Chemistry Series*, **43**, 1 (1964).
74. T. Nishino, M. Meguro, K. Nakamae, M. Matsushita, and Y. Ueda, "The lowest surface free energy based on -CF 3 Alignment." *Langmuir*, **15**, 4321 (1999).
75. S. Ott, A. Orfanidi, H. Schmies, B. Anke, H. N. Nong, J. Hübner, U. Gernert, M. Gliech, M. Lerch, and P. Strasser, "Ionomer distribution control in porous carbon-supported catalyst layers for high-power and low Pt-loaded proton exchange membrane fuel cells." *Nat. Mater.*, **19**, 77 (2020).
76. J. Wang, L. Xiao, G. Liao, Y. Zhang, L. Guo, C. H. Arns, and Z. Sun, "Theoretical investigation of heterogeneous wettability in porous media using NMR." *Sci. Rep.*, **8**, 13450 (2018).
77. A. Orfanidi, P. J. Rheinländer, N. Schulte, and H. A. Gasteiger, "Ink solvent dependence of the ionomer distribution in the catalyst layer of a PEMFC." *J. Electrochem. Soc.*, **165**, F1254 (2018).
78. G. Doo, J. H. Lee, S. Yuk, S. Choi, D.-H. Lee, D. W. Lee, H. G. Kim, S. H. Kwon, S. G. Lee, and H.-T. Kim, "Tuning the ionomer distribution in the fuel cell catalyst layer with scaling the ionomer aggregate size in dispersion." *ACS Applied Materials & Interfaces*, **10**, 17835 (2018).

79. T. Van Cleve et al., "Dictating Pt-based electrocatalyst performance in polymer electrolyte fuel cells, from formulation to application." *ACS Applied Materials & Interfaces*, **11**, 46953 (2019).

80. S. Takahashi, T. Mashio, N. Horibe, K. Akizuki, and A. Ohma, "Analysis of the microstructure formation process and its influence on the performance of polymer electrolyte fuel-cell catalyst layers." *ChemElectroChem*, **2**, 1560 (2015).

81. R. Zeng, H. Y. Zhang, S. Z. Liang, L. G. Wang, L. J. Jiang, and X. P. Liu, "Possible scenario of forming a catalyst layer for proton exchange membrane fuel cells." *RSC Adv.*, **10**, 5502 (2020).

4.2 <u>Publication II</u>
Modeling of wetting phenomena in cathode catalyst layers for PEM fuel cells

Authors: Wolfgang Olbrich[1,2,3], Thomas Kadyk[1,4], Ulrich Sauter[2], Michael Eikerling[1,3,4]

[1] Theory and Computation of Energy Materials (IEK-13), Institute of Energy and Climate Research, Forschungszentrum Jülich GmbH, 52425 Jülich, Germany
[2] Robert Bosch GmbH, Corporate Research, 71272 Renningen, Germany
[3] Chair of Theory and Computation of Energy Materials, Faculty of Georesources and Materials Engineering, RWTH Aachen University, 52062 Aachen, Germany
[4] Jülich Aachen Research Alliance, JARA Energy, 52425 Jülich, Germany

Author contributions: Conceptualization: WO, TK, US, ME; Methodology: WO; Software: WO; Formal analysis: WO; Resources: US; Writing - Original Draft: WO; Writing - Review & Editing: US, TK, ME; Supervision: ME, US, TK; Project administration: US, ME.

Document history: First draft: 18.06.2021, Submitted: 14.05.2022, Received peer review: 20.06.2022, Revised: 22.06.2022, Published: 17.07.2022.

Methods and results covered by this article were presented to the scientific community at the following conferences:

- *InterPore Conference*, held online 31.04.–04.05.2021, poster titled *Heterogeneous Wettability in Porous Catalyst Layers of PEM Fuel Cells: Model-based Analysis and Design.*

- *17th Symposium on Modeling and Experimental Validation of Electrochemical Energy Technologies*, held online 20.–22.04.2021, presentation titled *Understanding heterogeneous wettability in PEFC catalyst layers using a structure-based model.*

Modeling of wetting phenomena in cathode catalyst layers for PEM fuel cells

W. Olbrich [a,b,c,1,*], T. Kadyk [a,d,2], U. Sauter [b,3], M. Eikerling [a,c,d,4]

[a] *Theory and Computation of Energy Materials (IEK-13), Institute of Energy and Climate Research, Forschungszentrum Jülich GmbH, Jülich 52425, Germany*
[b] *Robert Bosch GmbH, Corporate Research, Renningen 71272, Germany*
[c] *Chair of Theory and Computation of Energy Materials, Faculty of Georesources and Materials Engineering, RWTH Aachen University, Aachen 52062, Germany*
[d] *Jülich Aachen Research Alliance, JARA Energy, Jülich 52425, Germany*

ARTICLE INFO

ABSTRACT

Optimal water management in polymer electrolyte fuel cells hinges on understanding wetting phenomena inside the porous network of the cathode catalyst layer. Macrohomogeneous models have evolved to take into account water-related phenomena. However, existing modeling approaches implement a phenomenological description that employs a mixed wettability, thus neglecting vital structural features that constitute the wetting behavior. Other approaches exploit experimentally measured water retention curves to derive descriptors for the wetting properties of the catalyst material. Albeit, such measurements are scarce in the literature, elaborate and expensive, making a materials screening focused on wettability unfeasible. Our approach extends these efforts by providing a structure-based model that predicts water retention curves from catalyst layer ink parameters. The model accounts for structural formation at the ink stage and it captures the statistical distribution of wetting properties. Design trends derived on the basis of this model are in agreement with experimental findings in the literature. Furthermore, the model is analyzed for its implications on fuel cell degradation. Finally, we discuss its capabilities with regard to model-supported fuel cell design and optimization.

1. Introduction

Polymer electrolyte fuel cells (PEFCs) are about to take the leap from prototyping stage and niche applications to commercial deployment. To achieve this step, targets in terms of durability, performance, and cost reduction need to be met. On all scales, from atomic scale to system level, developers are seeking ways to improve the technology to meet or exceed commercialization target.

The cathode catalyst layer (CCL) is of central importance to this development. It is the pivotal component in terms of performance because of the sluggish oxygen reduction reaction (ORR). Water that is produced in this reaction plays a double-edged role in PEFCs. On the one hand, it is the essential reaction medium, as well as proton solvent and transport medium, rendering the CCL active in the first place. On the other hand, when accumulated in porous gas transport layers at high current densities, liquid water acts as an asphyxiant, i.e., it impedes oxygen supply through the porous network [1]. To keep these two antagonistic effects in check requires profound understanding of wetting properties, pressure distributions and water accumulation in the porous network. The wetting behavior of the pore walls confining the liquid water in the CCL is decisive for the overall performance and the dynamic range of the operating cell. The crucial question to answer is: will the CCL and adjacent porous transport layers flood under high current densities or can water be held back from flooding the gas pore network so that high rates of oxygen supply can be maintained?

In the past, the concept of mixed wettability was developed to describe the wetting properties of CCLs. In an effective way, this concept accounts for the finding that CCLs exhibit partially hydrophobic and hydrophilic behaviour. The partially hydrophilic character stems from the wetting properties of the Pt/C catalyst: the carbon support is moderately hydrophilic and metallic platinum is strongly hydrophilic.

Nomenclature

α_{ex}	Ionomer volume excess factor
α_{free}	Volume reduction factor of secondary pore volume
γ	Surface tension of water at 353 K
Δ_{DA}	Degree of alignment of ionomer in thin films
$\Delta_{DA,HI}$ $\Delta_{DA,HO}$	Degree of alignment for limiting cases, hydrophilic (HI) or hydrophobic (HO)
$\Delta_{DA,Pt}$ $\Delta_{DA,C}$ $\Delta_{DA,Pt/C}$	Degree of alignment induced to the ionomer film by platinum, carbon, or the Pt/C catalyst)
$\Delta_{DA,0}$ $\Delta_{DA,\infty}$	Degree of alignment induced to the ionomer film at the substrate/ionomer interface (0) and at the surface of an film of infinite thickness (∞)
θ_j	Contact angle of platinum, carbon or ionomer film ($j = \{Pt, C, ion\}$)
θ_{HI} θ_{HO}	Contact angle of ionomer in ideally aligned hydrophilic (HI) oder hydrophobic (HO) state
θ_{pore}	Effective contact angle of a given pore
θ_f	Effective contact angle of a given pore wall, on which particles of Pt or ionomer are deposited on, i.e., $f = \{Pt, Pt/C\}$)
$\overline{\theta}_2$	Effective contact angle in secondary pores
λ	Expected number of particles deposited in a single pore in a Poisson process
μ_k	Mean value of particles deposited in a single pore
ϕ_1	Weight factor of pore size domain in the pore size distribution($i = \{1,2\}$)
ρ_j	Mass density of platinum, carbon or ionomer film ($j = \{Pt, C, ion\}$)
σ_i	Standard deviation for pore size distribution for primary or secondary pores ($i = \{1,2\}$)
$\sigma_{\cos\theta}$ σ_k	Standard deviation of the contact angle distribution on the scale of contact angles ($\cos(\theta)$) or number of particles deposited in a given pore (k)
$\sigma_{p,2}$	Spread of the WRC on the pressure scale
A_j	Surface area covered by a particle of a given material ($j = \{Pt, ion\}$)
A_i	Surface area of primary or secondary pores ($i = \{1,2\}$)
A_{pores}	Total surface area of the porous network of the CCL)
A_{pore}	Surface area of a single pore
$A_{Pt,nano}$	Surface area of carbon substrate covered by Pt nanoparticles
a_j	Surface fraction of a substrate covered by a particular material ($j = \{Pt, ion\}$)
$\overline{a}$	Average surface fraction of pore wall covered in a given

	pore by Pt or ionomer
B	Bernoulli distribution
F	Cumulative volume fraction in a range of pore contact angles, index $j = \{Pt, ion\}$ applies according to the particles causing the respective wetting behavior heterogeneity
$f_{C\,loss}$	Loss factor of carbon mass from carbon corrosion
$f_{r\,growth}$	Growth factor of Pt nanoparticles from Pt coarsening
H	Heaviside function
k	Number of particles deposited in a single pore
k_A	Ionomer dispersion parameter
k_V	Ionomer film volume evolution parameter
k_{DA}	Decay constant of degree of alignment in ionomer thin films
L_{pore}	Length of a pore
$m_{Pt:C}$	Platinum to carbon mass ratio
$m_{I:C}$	Ionomer to carbon mass ratio
N	Normal distribution
n	Maximum number of particles in a single pore
P	Poisson distribution
p_C	Capillary pressure
$p_{C,min}$	Minimal capillary pressure to flood a given pore
p_2	Inflection point of water retention curve
r	Pore radius
$r_{\mu,i}$	Mean pore radius for pore size distribution for primary or secondary pores ($i = \{1,2\}$)
r_{ion}	Size of ionomer units building up the film
r_{pore}	Radius of a single pore
S	Cumulative volume fraction in a range of pore radii, index $i = \{1,2\}$ applies if solely primary or secondary pores are of interest
t	Ionomer film thickness
t_0	Initial ionomer film thickness
V_i	Primary or secondary pore volume ($i = \{1,2\}$)
$V_{2,0}$	Secondary pore volume in an ionomer-free CCL
V_{pores}	Total pore volume in the CCL
X_{CCL}	Pore volume fraction of porous network in the CCL
X_i	Pore volume fraction of primary or secondary pores ($i = \{1,2\}$)
$X(p_C)$	Water retention curve
$X_{ana}(p_C)$	Analytical water retention curve
X_{HO}	Pore volume fraction of secondary pores with hydrophilic wetting properties
x	Dimensionless ionomer volume
Y	Young-Laplace criterion function to check if a given pore floods

The ionomer constituents of the CCL play a special ambivalent role. Being an amphiphilic material, ionomer exhibits hydrophilic or hydrophobic wettability depending on its interaction with the Pt/C surface and the corresponding orientation of anionically terminated ionomer sidechains relative to the pore space [2–4].

Structure-based models in the literature accounted for the mixed, heterogeneous wettability of the pore network by dividing pores into hydrophilic and hydrophobic fractions [5–9]. Recently, Zhou et al. [8] and Goshtasbi et al. [9] applied this approach in macrohomogeneous cell models and accounted for the mixed wettability of various cell layers, including the CCL, by using two-point discrete contact angle distributions combined with experimentally obtained pore size distributions. The finding of a mixed wettability in the CCL was rationalized by the distinct wetting properties of carbon and ionomer. However, the parametrization of the wetting properties in these works relied on sparse literature data, as discussed below. This separation of the two distinct

pore types might be oversimplified as CCL materials could exhibit continuous distributions of contact angles. In this work, we take up the idea of Weber [10], who calculated the water retention curve (WRC) of a gas diffusion layer (GDL) by superposition of a Gaussian distribution of contact angles and a log-normal distribution of pore sizes.

Macrohomogeneous models that account for the physics of transport across the diffusion media often include water retention curves to incorporate the wetting behavior. The WRC correlates the capillary pressure with the liquid saturation in the porous network. WRCs can be embedded into the equations for liquid water generation and transport [9,11–13], linking the liquid pressure gradient to other saturation-depended properties, such as the platinum utilization and mass transport coefficients. This way, the WRC of the CCL serves as a descriptor that links the wetting properties to water management during cell operation. Varying the characteristics of the WRC revealed that the wetting properties of a CCL must be well adjusted if flooding shall be

2

Fig. 1. Schematic of the model workflow: **(a)** Firstly, CL composition is predicted based on CCL ink parameters. **(b)** Secondly, wetting properties of the pore walls are estimated accounting for molecular alignment of ionomer sidechains and backbones. **(c)** Finally, the combined statistical distribution of pore radius and contact angle is calculated, accounting for heterogeneity in ionomer coverage.

prevented, especially under cold or wet conditions [9,11].

The critical role of the WRC is in stark contrast to the marginal extend of experimental WRC data in the literature. WRCs of CCLs are difficult to assess for several reasons. Firstly, CCLs need a suitable support due to their low thickness. Furthermore, putting the CCL under conditions resembling the *operando* state of a fuel cell poses a significant challenge. The most extensive work was accomplished by Gunterman [14] who used a hydrophobic PTFE membrane to support an isolated CL. The thickness was increased to enable an accurate determination of liquid volume displacement. The steady state hysteresis of $p_C - S_{liq.}$ data was measured using an apparatus where the capillary pressure could be controlled by either the liquid or gas pressure, allowing to measure the full range of the WRC with high accuracy. This method was previously developed for gas diffusion layers in PEM fuel cells by Gostick et al. [15]. Ye and Nguyen took a different approach to tackle the issue of small catalyst layer thickness. Instead of measuring the volume displacement

directly, neutron radiography was used to assess the liquid saturation as a function of p_C. A third option was demonstrated by LaManna et al. [16] who used the method of standard porosimetry, in which a reference medium with known $p_C - S_{liq.}$ relation is brought to equilibrium with the CL sample. The authors applied octane and water to measure both hydrophobic and hydrophilic pores. A non-porous polyimide film served as support for the CCL. However, details on the composition of the CCL were not disclosed in this study.

With only scarce datasets available in the literature and experimental techniques being laborious, a wide-ranging characterization of the wetting properties of fuel cell materials remains out of reach. In this situation, a model based treatment of wetting phenomena gains foremost importance. In this article, we present a model for the complex wetting phenomena in CCLs. Our model extends the approach of describing properties of the porous network of the CCL by distributions of pore sizes and contact angles [5,8,17]. It accounts for the molecular alignment of the ionomer film covering the Pt/C catalyst via the *degree of alignment*, a descriptor proposed in our previous work [18]. The result is a model that calculates the wetting behavior of the CCL, i.e., the WRC, based on the ink composition, i.e., the Pt:C and I:C mass ratios, and intrinsic material properties. We will demonstrate how this model deepens the understanding of structure-property correlations and their underlying causal relationships. Capabilities of the model will be demonstrated by deriving design guidelines to tailor CCL materials.

2. Model and methodology

This work applies the structural picture of a conventional CCL, in which the primary Pt/C particles aggregate and provide a certain volume fraction of primary pores (1–10 nm radius), encompassing both micropores of the carbon and the inter-particle space inside the agglomerates. Secondary pores (10–100 nm radius) form the space between the agglomerates [19]. The ionomer-phase is dispersed in this structure, forming a thin, skin-like layer that partially covers the surface of Pt/C agglomerates, thus forming part of the pore walls of the secondary pore network. The primary pores remain free of ionomer, as the ionomer molecules are too big to penetrate them. Part of the ionomer forms larger aggregates that do not contribute to the covering of the secondary pore network. This picture of aggregated and dispersed ionomer is derived from the experimental observation that on the one hand, the volume fraction of secondary pores decreases as more ionomer is used in the catalyst layer ink [20], explaining the dispersion in the secondary pores. On the other hand, there is no strict anti-correlation between porosity and ionomer content, hinting that not all of the ionomer fills the secondary pores.

Our model of the wetting behavior of this CL structure consists of three submodels, as depicted in Fig. 1: a composition submodel that describes the volumetric composition of the CCL and the structure of the ionomer film (Fig. 1(a)); an alignment submodel that describes the alignment of the ionomer sidechains and the resulting wetting properties of the ionomer film (Fig. 1(b)); a statistical distribution submodel that describes the distribution of pore sizes and their wetting properties, which are then used to calculate the water retention curve (Fig. 1(c)).

2.1. Catalyst layer composition submodel

In the fist step, we quantify the CCLs volumetric composition and the structure of the ionomer. The latter includes volume fraction of dispersed and aggregated ionomer, ionomer coverage in the secondary pores and ionomer film thickness.

The formation of the ionomer structure can be described as an incremental assembly of the composite. A single ionomer molecule floating in the ink could either attach to uncovered Pt/C surface, or deposit on an existing ionomer film and thereby increase its thickness, but not its coverage. Any ionomer not deposited as part of the ionomer film forms large, dense aggregates embedded in the catalyst layer

structure and is therefore not part of the porous network. Such aggregates were repeatedly observed in microscopic images of CCLs [21–24]. Analogous to first-order adsorption kinetics, we describe the incremental assembly of ionomer films by a set of two differential equations,

$$\frac{da_{ion}}{dx} = (1 - a_{ion})k_A \ , \ \text{and} \tag{1}$$

$$\frac{d\alpha_{free}}{dx} = -\alpha_{free}k_V. \tag{2}$$

Here, we introduce the dimensionless variable x as the ratio of dry ionomer volume, V_{ion}, to the volume of secondary pores in an ionomer-free Pt/C catalyst layer, $V_{2,0}$,

$$x = \frac{V_{ion}}{V_{2,0}} \tag{3}$$

with $V_{ion} = m_{I:C}/\rho_{ion}$. Note that $V_{2,0}$ and V_{ion} are volumes normalized to the carbon loading. The ionomer coverage, a_{ion}, is defined as the ratio of the ionomer covered surface, A_{ion} to the total surface of the secondary pores, A_2,

$$a_{ion} = \frac{A_{ion}}{A_2} \ . \tag{4}$$

The ratio of remaining secondary pore volume, which is not displaced by the ionomer film, to the secondary volume in an ionomer-free CCL is denoted as

$$\alpha_{free} = \frac{V_{2,free}}{V_{2,0}}. \tag{5}$$

The first Eq. (1) describes the growth of ionomer coverage by ionomer molecules adsorbing to free surface of the Pt/C support. The probability of this adsorption process is proportional to the free surface fraction $(1 - a_{ion})$. This introduces the dispersion parameter k_A. Eq. (2) describes ionomer attaching to the existing film. The amount of ionomer incrementally depositing inside the secondary pore network, thus reducing the free volume by $\frac{d\alpha_{free}}{dx}$, is proportional to the volume of pores that is still free. The respective constant of proportionality is labeled k_V. Integration of Eqs. (1) and (2) results in

$$\alpha_{free} = \exp(-k_V x), \ \text{and} \tag{6}$$

$$a_{ion} = 1 - \exp(-k_A x). \tag{7}$$

Assuming uniform thickness of the ionomer film, the film thickness t can be calculated as the ratio of the film volume to the surface area covered. Using Eqs. (6) and (7), t can be calculated from

$$t = \frac{V_{ion,film}}{A_{ion}} = \frac{V_{2,0}\left(1 - \alpha_{free}\right)}{A_2 \, a_{ion}} = \frac{V_{2,0}}{A_2}\frac{1 - \exp(-k_V x)}{1 - \exp(-k_A x)}, \tag{8}$$

where A_2 denotes the surface area of secondary pores provided by the carbon support and is calculated from the pore size distribution (c.f. Eq. (17)). We define the *initial film thickness* t_0 as the limit of t for x tending to zero, i.e., considering the first bits of ionomer involved in structure formation. This property is given by

$$t_0 = \lim_{x \to 0}\left(\frac{V_{2,0}}{A_2}\frac{1 - \exp(-k_V x)}{1 - \exp(-k_A x)}\right) = \frac{V_{2,0}}{A_2}\frac{k_V}{k_A}. \tag{9}$$

Eq. (9) links two process parameters, viz. k_A and k_V. Since ionomer molecules are of finite size, t_0 is considered to be a constant for a given material selection, for instance PFSA films on conventional carbon supports, such as Ketjen Black or Vulcan. Taking t_0 and k_A as input parameters, k_V is determined by Eq. (9). In the following, the initial film thickness t_0 is taken as a measure of the length scale of a single layer of ionomer molecules deposited.

2.2. Alignment submodel

In the second step of model development, the wetting properties of the ionomer film and those of ionomer-free surfaces are calculated. The molecular alignment of sidechains and backbones inside the thin ionomer film determines the contact angle of the film. The alignment is determined by the wetting properties of the substrate, on which the thin film is deposited. If the substrate surface is hydrophilic, a thin water layer and with this the ionomer sidechains are attracted to this surface, leaving the backbones to form a hydrophobic outer surface towards to the secondary pore space. Oppositely, a hydrophobic surface substrate attracts the hydrophobic ionomer backbones, leaving the sidechains to form a hydrophilic surface facing secondary pores [25]. Overall, this ionomer alignment effect leads to an inversion of the substrate's wetting behaviour [2].

In our previous work [18], we developed a numerical descriptor for the molecular structure of the ionomer, the *degree of alignment*, Δ_{DA}. This concept constitutes the basis for the second submodel and is extended to include the impact of ionomer film thickness and Pt:C ratio. The model accounts for three aspects that determine the wetting properties in secondary pores:

1. Molecular alignment of ionomer sidechains and backbone: the value of Δ_{DA} is defined to be in the range of $0 - 1$ with $\Delta_{DA} = 0$ corresponding to ionomer backbones pointing away from the Pt/C surface and thus facing secondary pores, and $\Delta_{DA} = 1$ corresponding to ionomer sidechains that point away from the Pt/C surface and are exposed to secondary pores. Accordingly, $\Delta_{DA} = 0$ corresponds to the contact angle of a hydrophobic ionomer surface, i.e., $\theta_{HO} = 120°$ and $\Delta_{DA} = 1$ corresponds to $\theta_{HI} = 30°$. These contact angle values were reported in the literature [26,27]. Via linear interpolation of $\cos(\theta)$, any dimensionless value of Δ_{DA} can be transformed into a contact angle,

$$\cos(\theta_{ion}) = \Delta_{DA}(\cos(\theta_{HI}) - \cos(\theta_{HO})) + \cos(\theta_{HO}). \tag{10}$$

The linear superposition of partial contributions to the contact angle, adapted in this work, has been in employed in other fields [28] and it is justified by the linear superposition of the surface energies involved at the triple phase boundary.

2. Decay of alignment over film thickness: molecular dynamics studies revealed that the intensity of alignment equilibrates quickly over film thickness t [25]. The initial value ($\Delta_{DA,0}$), imposed by interaction with the solid Pt/C, converges exponentially to the value for a random mixture of sidechains/backbones, given by $\Delta_{DA,\infty}$,

$$\Delta_{DA} = \Delta_{DA,\infty} + \left(\Delta_{DA,0} - \Delta_{DA,\infty}\right)\exp(-k_{DA}(t - t_0)). \tag{11}$$

Here, the value for $\Delta_{DA,\infty}$ is derived from the chemical structure of a conventional PFSA ionomer, in which about $\approx 1/3$ of the ionomer molecular volume is occupied by the sidechains (see Section 2.5). Additionally, the shift by t_0 in the argument of the exponential function to accounts for the thickness of the first 'layer' of ionomer formed. Molecular dynamics studies showed that the propagation of alignment weakens over a few such layers [25]. Therefore, the decay constant k_{DA} is expected to lie in the range of $1/t_0$ and will be replaced with that value, to reduce the number of parameters.

3. Linear interpolation between surface area contributions with different chemical nature: Different kind of surface functional groups, bare carbon and platinum can be assigned the surface fraction a_j and the value $\Delta_{DA,0j}$ that the type of surface would induce if it made up the entire surface. Since the real Pt/C surface has a mixed composition, the effective value for $\Delta_{DA,0}$ can be obtained by linear interpolation using the respective surface fractions a_j, $j = \{C,Pt\}$,

$$\Delta_{DA,0} = \sum_i \Delta_{DA,0,i} \ a_i \tag{12}$$

In this work, platinum and carbon support are the only two surface types considered. Furthermore, the model has to account for the varying density of Pt nanoparticles on the Pt/C surface. The sum of the surface fractions of platinum and carbon support equals 1. Thus, the expression can be reduced to

$$\Delta_{DA,0} = \Delta_{DA_C}\left(1 - a_{pt}\right) + \Delta_{DA_{Pt}}a_{pt}. \tag{13}$$

To quantify the platinum coverage a_{Pt}, we assume hemispherical Pt nanoparticles of radius r_{Pt} that are distributed evenly over the available surface in primary and secondary pores. The platinum coverage can then be calculated as follows,

$$a_{Pt} = \frac{A_{Pt,nano}}{A_{pores}} = \frac{1}{A_{pores}}\frac{3m_{Pt:C}}{2\rho_{Pt}r_{Pt}}. \tag{14}$$

2.3. Statistical distribution of pore size and contact angles

Having determined the wetting properties of distinct surface types, i. e., bare Pt/C surface and ionomer film, their statistical distribution inside the CCL microstructure is modeled in the following. Firstly, the pore structure is described using a pore size distribution. Secondly, an analytical expression for the statistical distribution of contact angles is derived for the different pore size domains.

2.3.1. Pore size distribution

To represent the pore size distribution (PSD) of the agglomerated structure of the CCL, a log-normal distribution is written for each pore domain (1 = primary, 2 = secondary),

$$\frac{\partial S_i}{\partial r} = \frac{1}{\sqrt{2\pi}\sigma_i r}\exp\left(-\frac{\left(ln(r) - ln(r_{\mu,i})\right)^2}{2\sigma_i^2}\right) \text{ with } i \in \{1,2\}. \tag{15}$$

where S_i is the saturation of pore domain i, normalized to the total volume of the domain. The weighted sum of the distributions of the domains yields the bimodal PSD,

$$\frac{\partial S}{\partial r} = \frac{1}{\phi_1 + \alpha_{free}\phi_2}\left(\phi_1\frac{\partial S_1}{\partial r} + \alpha_{free}\phi_2\frac{\partial S_2}{\partial r}\right) \text{ with } \phi_1 + \phi_2 = 1, \tag{16}$$

where the factors ϕ_1 and ϕ_2 refer to the volume fractions of primary or secondary pores relative to the total pore volume in the ionomer-free Pt/C material. To account for the ionomer content successively filling secondary pores, ϕ_2 is multiplied by α_{free} (see composition submodel). The combined pore size distribution expresses a saturation ranging from 0 to 1 and is therefore normalized by the factor $1/(\phi_1 + \alpha_{free}\phi_2)$.

The respective surface areas for each pore size domain are evaluated from the PSD via integration, assuming a cylindrical pore geometry with $L_{pore} = 2r_{pore}$,

$$A_i = \phi_i V_{pores}\int_0^\infty \frac{4}{3r}\frac{\partial S_i}{\partial r}dr. \tag{17}$$

2.3.2. Contact angle distribution

The contact angle distribution (CAD) is derived by accounting for the heterogeneous distribution of Pt nanoparticles and ionomer, and thus local wetting properties, inside the CCL microstructure. In the following, both ionomer and platinum are considered to be randomly distributed as finite sized units over the pore network volume, whereas ionomer is only present in the secondary pores. For platinum, the particle character is obvious. For the ionomer, it can be rationalized by the macromolecular nature and finite size of ionomer molecules. This means that the ionomer film is considered to have uniform thickness but to exhibit a heteroge-

neous coverage in secondary pores. Tomographic images that resolve the spatial distribution of ionomer support this view [29]. Therefore this work introduces a radius r_{ion} to describe finite-size building blocks of ionomer. Different from Pt nanoparticles, ionomer units are of irregular shape. Here, we report a radius corresponding to a circular disk-shaped ionomer patch with the same surface area as the irregular patch. This approach to account for the finite-sized nature of ionomer units is common in modeling works. For instance, coarse-grained molecular dynamics [25] or particle models to computationally generate a CCL microstructure [30] introduced an ionomer radius similar to this work.

To link the presence of platinum or ionomer inside a pore with its wetting properties, we further assume that any particle deposited inside a pore increases the surface coverage a_j of the pore wall accordingly. A single pore can be attributed an effective contact angle θ_{pore} by surface-averaging the respective $cos(\theta_j)$ inside the pore,

$$\cos\left(\theta_{pore}\right) = \sum_j \cos\left(\theta_j\right)a_j. \tag{18}$$

To capture the statistics of the heterogeneous distribution of particles in the pore space, a classical Bernoulli process is considered, using the following definitions:

1. The probability of finding a certain number, k, of particles per pore is given by the binomial distribution $B(n,k,p)$.
2. The number of trials in a Bernoulli process, n, represents the maximal number of particles per pore.
3. The maximal number of particles per pore n is reached when the pore wall is fully covered, i.e., $n = k(a = 1)$.
4. The surface coverage is equivalent to the ratio of k to n,

$$a = \frac{k}{n}. \tag{19}$$

5. The maximal number of particles to fit in the pore is a function of pore radius and particle size. With the previous definition, n is calculated from

$$n = \frac{A_{pore}}{A_j}, \tag{20}$$

where the amount of surface taken by one particle A_j is πr_j^2 and the surface area of a single pore A_{pore} is $4\pi r_{pore}^2$, according to the assumption of cylindrical pores with $L_{pore} = 2r_{pore}$.
6. The probability p of a trial in the Bernoulli process to be successful must be equal to the average surface coverage $\overline{a}$,

$$\overline{a} = \frac{\overline{k}}{n} = \frac{pn}{n} = p. \tag{21}$$

The De Moivre-Laplace theorem states that the binomial distribution converges already at small numbers of trials ($n > 5$) to the normal distribution $N(k, \mu, \sigma)$ [31]. The respective mean value, μ_k, and standard deviation, σ_k, of the number of particles are related to the ones of the binomial distribution,

$$\mu_k = n\overline{a} \text{ and} \tag{22}$$

$$\sigma_k^2 = n\overline{a}(1 - \overline{a}). \tag{23}$$

For small pores the distribution has to collapse into a single peak at $n = 0$, i.e., for a particle-free pore, if k_{max} decreases to 1. The structural image behind is that ionomer or platinum cannot enter pores which are too small. For ionomer this applies for the primary pores of the carbon support, whereas platinum reaches there but is excluded from pores with radius $< 1 \ nm$. According to the Poisson limit theorem [31], the

5

binomial distribution and the Poisson distribution equivalently describe the probability density for large n. However, at small n only the Poisson distribution allows to correctly calculate the probability that no particle ($k = 0$) is deposited into the considered pore. The Poisson distribution $P_\lambda(k)$ exhibits the property that if the expected number of particles in the pore λ equals 0, the probability of the pore to be empty equals 1, which is consistent with the structural image. Since λ is equal to $n\bar{a}$, as introduced for the normal distribution, it is substituted accordingly to calculate the probability of a pore for being empty ($k = 0$),

$$P_{\lambda=n\bar{a}}(k=0) = e^{-n\bar{a}}. \tag{24}$$

The probability defined by Eq. (24) will be denoted as $P(n)$ and is applied to interpolate between the broad normal distribution for large n and the sharp peak of empty pores at $k = 0$ for $n < 1$. A narrow Gaussian peak with width $\sigma_{\min}$. The combined distribution for both small and large n is thus given by

$$\frac{\partial F}{\partial k} = P(n)N(k, 0, \sigma_{min}) + (1 - P(n))N(k, \mu_k(n), \sigma_k(n)), \tag{25}$$

where F denotes a fraction from a subset of pores with a given pore radius, i.e., a given n, since n is only a function of pore radius (Eq. (20)). For any given n, the integral of this distribution over all particle numbers equals 1,

$$\int_0^\infty \frac{\partial F}{\partial k} dk = 1. \tag{26}$$

In order to evaluate wetting properties of the CCL, the distribution of particles per pore k is transformed to an effective value of $\cos(\theta)$. To calculate $\cos(\theta)$ from the surface contributions, we apply Eqs. (18) and (19), denoting the particles considered with j and the free, uncovered surface of the pore with f,

$$\cos(\theta) = \cos(\theta_j)a_j + (1 - a_j)\cos(\theta_f) = \cos(\theta_j)\frac{k}{n} + \left(1 - \frac{k}{n}\right)\cos(\theta_f). \tag{27}$$

Evaluation of the fraction of pores within a range of contact angles is facilitated by integration of Eq. (25) in the boundaries of interest, where Eq. (27) is applied to substitute k with $\cos(\theta)$,

$$\int_{k_1}^{k_2} \frac{\partial F}{\partial k}(k)dk = \int_{\cos(\theta_1)=f(k_1)}^{\cos(\theta_2)=f(k_2)} \frac{\partial F}{\partial \cos(\theta)} d\cos(\theta)$$
$$= \int_{\cos(\theta_1)=f(k_1)}^{\cos(\theta_2)=f(k_2)} \frac{\partial F}{\partial k}(k(\cos(\theta)))k'(\cos(\theta))d\cos(\theta), \tag{28}$$

with

$$k'(\cos(\theta)) = \frac{n}{\cos(\theta_j) - \cos(\theta_f)}. \tag{29}$$

Due to the heterogeneity of wetting properties that will be discussed in the following, the variance of the particle number σ_k is transformed to $\sigma_{\cos(\theta)}$. Substitution of the integral definition of the variance[5] results in

$$\sigma_{\cos(\theta)}^2 = \left|\frac{\cos(\theta_j) - \cos(\theta_f)}{n}\right|\sigma_k^2. \tag{30}$$

2.3.3. Combined distribution of pore size and contact angle

The differential for the combined distributions of pore size and contact angle dX is obtained by multiplication of the differentials dS and dF,

$$dX_{i,j} = dS_i(r_{pore})dF_j(r_{pore}, \theta) \tag{31}$$

---

[5] $\sigma^2 = \int_{-\infty}^\infty (x - \mu)^2 f(x)dx$, given the probability density function $f(x)$ with mean value μ

with $dS_i(r_{pore})$ denoting the differential of the pore volume fraction over pore size and $dF_j(r_{pore}, \theta)$ denoting the differential of the distribution of contact angles in a subset of pores with a given pore radius. The indices refer to pore domain ($i = \{1, 2\}$) and type of distributed material ($j = \{Pt, ion\}$). To describe the complete pore space of the CCL, dX is composed of two contributions, accounting for primary and secondary pores,

$$dX_{CCL} = \frac{1}{\phi_1 + \alpha_{free}\phi_2} \left(\phi_1 dS_1 \ dF_{Pt} + \alpha_{free}\phi_2 dS_2 dF_{ion}\right), \tag{32}$$

where the weighted contributions and normalization analogues to Eq. (16) have been employed. Ionomer is excluded from the primary pores. Therefore, inside primary pores only the modulation of the contact angle distribution caused by platinum has to be considered. In secondary pores, ionomer is the particular species which that the contact angle distribution. Here, the uncovered pore surface is represented by the average Pt/C contact angle. The contact angle for ionomer is obtained from the alignment submodel.

2.4. Evaluation of the water retention curve

The water retention curve correlates the fraction of flooded pore volume $X(p_C)$ at a capillary pressure p_C. Here, it is obtained from

$$X(p_C) = \int_0^\infty \int_{-1}^1 Y(r, \theta, p_C) \frac{\partial X_{CCL}}{\partial \cos(\theta)\partial r} d\cos(\theta)dr, \tag{33}$$

where Y represents the Heaviside function H that determines whether a pore is flooded ($Y = 1$) or stays empty ($Y = 0$),

$$Y(r, \theta, p_C) = H(p_C - p_{C,min}(r, \theta)) \quad \text{with} \tag{34}$$

$$p_{C,\min} = -\frac{2\gamma\cos(\theta)}{r}. \tag{35}$$

It is also possible to evaluate the saturation of the primary or secondary pores seperately,

$$X_1(p_C) = \int_0^\infty \int_{-1}^1 \left(\frac{\partial S_1}{\partial r}\right)\left(\frac{\partial F_{Pt}}{\partial \cos(\theta)}\right)Y(r, \theta, p_C) d\cos(\theta) dr \quad \text{and} \tag{36}$$

$$X_2(p_C) = \int_0^\infty \int_{-1}^1 \left(\frac{\partial S_2}{\partial r}\right)\left(\frac{\partial F_{ion}}{\partial \cos(\theta)}\right)Y(r, \theta, p_C) d\cos(\theta) dr. \tag{37}$$

As a criterion for the resistance to flooding, the volume fraction of secondary pores that are hydrophobic, X_{HO}, will be a useful parameter. It can be obtained by integration over hydrophobic pores in Eq. (37),

$$X_{HO} = \int_0^\infty \int_{-1}^0 \left(\frac{\partial S_2}{\partial r}\right)\left(\frac{\partial F_{ion}}{\partial \cos(\theta)}\right) d\cos(\theta) dr. \tag{38}$$

2.4.1. Analytical approximation for the water retention curve

To sidestep the relatively slow numerical integration necessary to solve Eq. (33), an analytical sigmoid function $X_{ana}(p_C)$ can be used to approximate the WRC,

$$X_{ana}(p_C) = X_1 + X_2 \frac{1}{1 + \exp\left(\frac{-(p_C - p_2)}{\sigma_{p,2}}\right)}. \tag{39}$$

The offset X_1 and the step height X_2 correspond to the fraction of primary and secondary pores, which are directly obtained from the composition submodel,

$$X_1 = \frac{\phi_1}{\phi_1 + \alpha_{free}\phi_2} \quad \text{and} \tag{40}$$
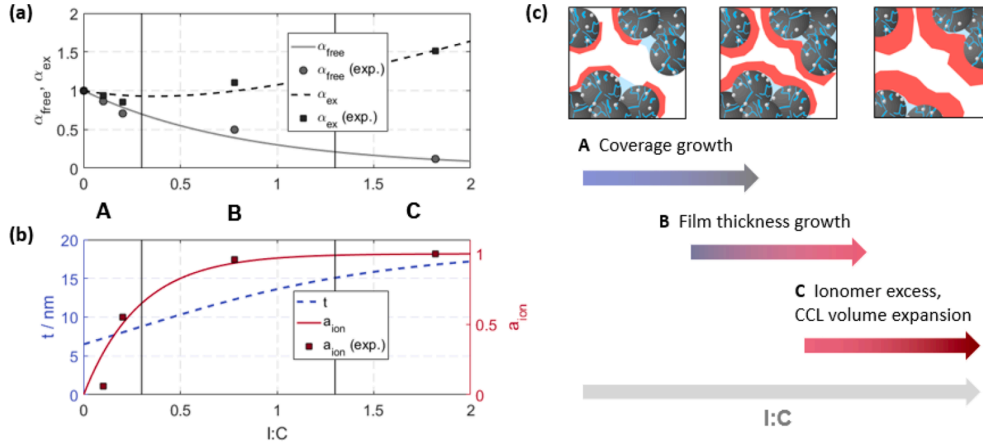
$$X_2 = 1 - X_1. \tag{41}$$

6

Fig. 2. (a) Deposition of ionomer in the secondary pore space of catalyst layer measured by Soboleva [20] and as calculated by the model. **(b)** Ionomer coverage and thickness are also calculated in the latter and in good agreement with data from Ref. [20]. **(c)** Illustration of successive structure evolution of CL with increasing ionomer loading.

The inflection point p_2 of the sigmoid is determined by the maximal propability density, which occurs where both $\partial S / \partial r$ and $\partial F / \partial \cos(\theta)$ exhibit their respective maxima. This is, by definition of the distribution functions, the case at $\theta = \overline{\theta}_2$ and $r = r_2$. The corresponding capillary pressure is calculated by evaluating the Young-Laplace equation,

$$p_2 = -\frac{2\gamma\cos(\overline{\theta}_2)}{r_2}. \tag{42}$$

The mean contact angle of secondary pores, $\overline{\theta}_2$, is calculated from the ionomer surface coverage obtained in the composition submodel,

$$\cos(\overline{\theta}_2) = \cos(\theta_{ion})a_{ion} + (1 - a_{ion})\cos(\theta_{Pt/C}) \quad \text{and} \tag{43}$$

$$\cos(\theta_{Pt/C}) = \cos(\theta_{Pt})a_{Pt} + (1 - a_{Pt})\cos(\theta_C). \tag{44}$$

The width $\sigma_{p,2}$ of the sigmoid increases with greater standard deviation of the contact angle distribution. Taking $\sigma_{\cos(\theta)}$ from the statistical distribution submodel, $\sigma_{p,2}$ can be obtained from the Young-Laplace-Equation,

$$
\begin{aligned}
\sigma_{p,2} &= |p_C(r_2, \cos(\overline{\theta}_2) + \sigma_{\cos(\theta)}) - p_C(r_2, \cos(\overline{\theta}_2) - \sigma_{\cos(\theta)})| \\
&= \left| -\frac{2\gamma(\cos(\overline{\theta}_2) + \sigma_{\cos(\theta)})}{r_2} + \frac{2\gamma(\cos(\overline{\theta}_2) - \sigma_{\cos(\theta)})}{r_2} \right| \\
&= \frac{4\gamma\sigma_{\cos(\theta)}}{r_2}.
\end{aligned} \tag{45}
$$

The standard deviation $\sigma_{\cos(\theta)}$ is a function of pore radius and has to be evaluated for the particular value of r_2. Finally, the descriptor for further discussion, the fraction of hydrophobic secondary pores, X_{HO}, is analytically calculated, using

$$X_{HO} = 1 - \frac{X_{ana}(p_C = 0)}{X_2} = 1 - \frac{1}{1 + \exp\left(\frac{-(p_C - p_2)}{\sigma_{p,2}}\right)}. \tag{46}$$

2.5. Model parameters

A CCL with a low surface area carbon (LSAC), such as Vulcan XC72, will be considered the reference material for our parameter study. The primary set of ink parameters include the Pt:C mass ratio, I:C mass ratio and the dispersion parameter k_A. I:C and Pt:C were set to 0.8 and 0.4, representing a typical CCL ink composition. The value for k_A is 4.5 and was adapted from fitting to the composition dataset provided by Sobo-

leva (see Section 3.1). The parameters ϕ_1 and k_A had to be slightly adapted when describing WRC data for the CCL materials characterized by Gunterman [14] (see Section 3.1). The value of V_{pores} was adapted from Ref. [20] and values for ϕ_i, $r_{\mu,i}$ and $\sigma_{r,i}$ were obtained from fitting the bimodal PSD to experimental data reported in Refs. [6,20].

The parametrization for the degree of alignment Δ_{DA} needs clarification since no comparable set of parameters was reported. The interaction of ionomer sidechains with metallic platinum is very strong, thus $\Delta_{DA,Pt} = 0$ was assumed. A highly graphitized carbon would attract the backbone due to the mild adhesive interaction between the hydrophobic carbon and the hydrophobic backbone. However, functionalized carbons, such as Vulcan XC72, feature a significant amount of oxidic surfcae groups, altering their Δ_{DA} to mildly attracting sidechains [32].

The degree of alignment in a film of infinite thickness, $\Delta_{DA,\infty}$, is estimated by the molecular volume of sidechains and ionomer in a typical PFSA provided by Wescott et al. [33]. Applying the above definition for Δ_{DA}, a value of 0.37 was obtained for $\Delta_{DA,\infty}$. According to the definition of contact angles for the pure sidechain and backbone, this results in a contact angle of 89.7°.

3. Results and discussion

3.1. Model solution

3.1.1. Solution and parametrization of the composition submodel

First, we discuss the solution of the composition submodel and its parametrization by fitting to data from Soboleva [20]. The data extracted from Soboleva (see Appendix, Table 3) include sets of I:C values for two different types of carbon (Ketjen Black, Vulcan XC72). The measured volumes of secondary pores and dry ionomer per mass of carbon as well as the ionomer coverage were used to compare the experimental results with our model. The volumes were normalized with the volume of secondary pores $V_{2,0}$ of a ionomer-free CCL, to compare with the volume reduction factor $\alpha_{free} = \frac{V_2}{V_{2,0}}$ and the dimensionless variable $x = \frac{m_{I:C}}{\rho_{ion}V_{2,0}}$ (see Section 2.1, Eqs. (3) and (6)). The measured ionomer coverage was normalized by its upper limit at high I:C ratios, to obtain a quantity between 0 and 1. Using this normalization, the following model functions were used to fit the model solution to the data,

$$\alpha_{free} = \exp(-k_V x) = \exp\left(-k_A t_0 \frac{A_2}{V_{2,0}} \frac{m_{I:C}}{\rho_{ion}V_{2,0}}\right) \text{and} \tag{47}$$
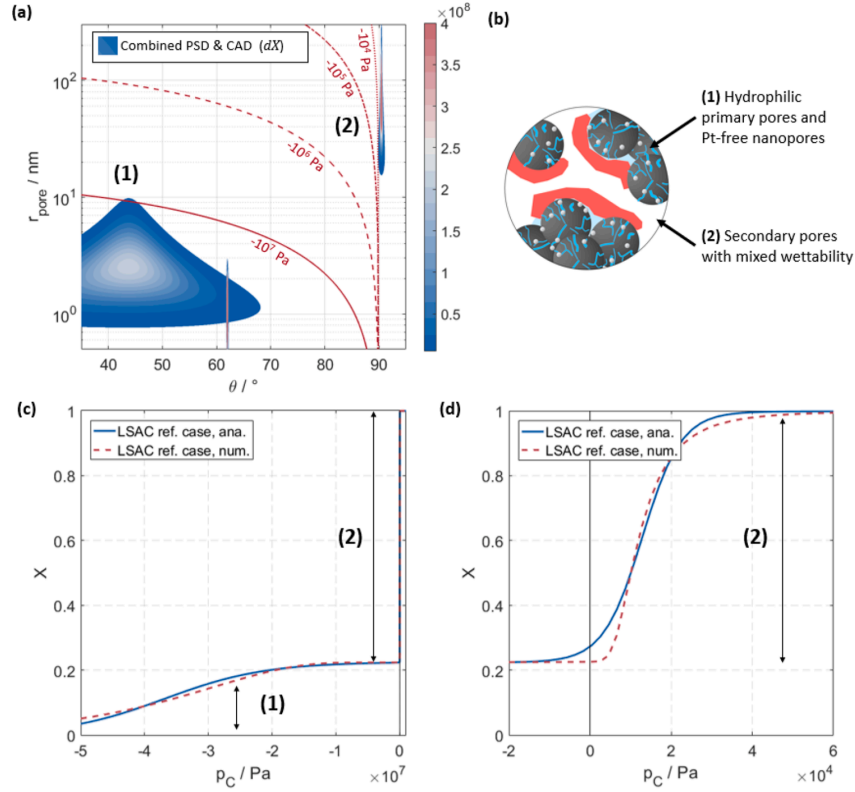
Fig. 3. (a) Combined probability distribution of pores over contact angles and pore radius of LSAC reference case. **(b)** Illustration of pore domains in the CCL microstructure. **(c,d)** Obtained water retention curves of LSAC reference case via analytical and numerical solution, plotted on different pressure scales.

$$a_{ion} = 1 - \exp(-k_A x) = 1 - \exp\left(-k_A \frac{m_{I:C}}{\rho_{ion} V_{2,0}}\right), \tag{48}$$

where k_V was replaced using Eq. (9), leaving t_0 and k_A as free fitting parameters. The initial film thickness t_0 was found to be 6.5 *nm*, which is in good agreement with reported values of dry ionomer films [29,34]. The dispersion parameter k_A was found to have the same value of 4.5 for both carbon materials (Ketjen Black, Vulcan XC72) examined by Soboleva. This demonstrates that k_A is primarily determined by the CCL fabrication process – and not by the materials used. As we will see in the following, this dispersion parameter is of fundamental importance.

The results of the composition submodel are depicted in Fig. 2 (a) and (b), together with the data from Soboleva [20] for Ketjen Black. The model captures the experimentally observed behavior: ionomer fills the secondary pores, but not all ionomer is used to replace pore volume. To describe this behavior, the excess volume factor α_{ex} is used. It evaluates the combined volume of ionomer and free pore space, normalized to $V_{2,0}$,

$$\alpha_{ex} = \frac{V_{ion} + V_{2,free}}{V_{2,0}} \tag{49}$$

$$= x + \alpha_{free}. \tag{50}$$

A value greater 1 expresses an increase in total CL volume, whereas a value between 0 and 1 indicates a contraction of the CL structure. At increasing I:C ratios (> 0.5), additional ionomer volume expands the CCL volume compared to the ionomer-free structure. At small I:C, around I:C ≈ 0.3, the experimentally observed volume contraction is captured by the model. This contraction might be a result of the ionomer

binding the carbon particles closer together. Additionally, data for ionomer coverage in Fig. 2(b) are in good agreement with the model. The calculated ionomer film thickness is found in the experimentally observed range from 7 to 15 nm [29,34,38]

The schematic illustration in Fig. 2(c) rationalizes three growth stages that can be distinguished: at small I:C, the coverage grows quickly, followed by a range for which film thickness growth is dominant. Ultimately, at high I:C, thickness and coverage cannot grow further and excess ionomer expands the total CCL volume.

3.1.2. Contact angle distribution and analytical WRC

The combined distribution of pore size and contact angle of the reference LSAC material is depicted in Fig. 3 (a). The peak of secondary pores (labeled with **(2)**) is located at $\overline{\theta}_2 = 90.5°$ and spreads over $\pm1.5°$. Primary pores exhibit a wider contact angle distribution (peak **(1)**) expanding over the range from 20° to 60° with the maximum located at $\theta_{Pt/C} = 43.7°$. The narrow peak C at pore radii ≤ 1 *nm* with sharply defined contact angle $\theta_C = 62°$ represents primary pores of the carbon support that are to small to take up any platinum nanoparticles.

The isobaric lines indicate the flooding condition based on the Young-Laplace equation for different liquid pressures. All pores to the left of the line will flood, thus are integrated over in the WRC evaluation and contribute to the saturation. While primary pores, labeled with **(1)**, are flooded under all relevant liquid pressures, the secondary pores will start to flood for a certain p_C. With regard to the analysis of water management, primary pores can safely be excluded from further discussion. Given the boundaries of pore scale and contact angles they will never become dry under any relevant operating conditions. This is favorable for platinum utilization. Secondary pores instead might turn

Table 1
Model parametrization, default value applies to reference material if not indicated otherwise.

		LSAC reference case	**Gunterman** commercial	**Gunterman** experimental		Refs.
Base ink parameters	Pt:C	0.4	0.25	0.25		[14]
	I:C	0.7	1	0.3		
	k_A	4.5		4		Fitted, see 3.1
Pore size distribution	V_{pores}	0.39			cm^3/g_C	[20]
	ϕ_1	0.13	0.1	0.25		[6,20]
	ϕ_2	0.87	0.9	0.75		
	$r_{\mu,1}$	3			nm	
	$r_{\mu,2}$	80			nm	
	$\sigma_{r,1}$	0.5				
	$\sigma_{r,2}$	0.5				
Degree of alignment	$\Delta_{DA,C}$	0.25				
	$\Delta_{DA,Pt}$	0				
	$\Delta_{DA,\infty}$	0.37				
Intrinsic contact angles	θ_C	62°				[2]
	θ_{Pt}	10°				[35]
	θ_{HI}	30°				[26,27]
	θ_{HO}	120°				[36]
Particular dimensions	t_0	6.5			nm	Fitted, see 3.1
	r_{ion}	5			nm	[30]
	r_{Pt}	1.5			nm	[37]
Constants	γ at T=353 K	0.0637			J/m^2	
	ρ_{ion}	1.9			g/cm^3	
	ρ_{Pt}	21.45			g/cm^3	
	ρ_C	2.1			g/cm^3	

Table 2
Results.

	Gunterman, experimental			
	LSAC reference case	**Gunterman** commercial	**Gunterman** experimental	
Ionomer dispersion quantities				
V_{ion}	0.42	0.53	0.16	cm^3/g_C
A_2	6.57	6.87	5.67	m^2/g_C
x	1.21	1.45	0.53	
k_V	0.6	0.6	0.5	
a_{ion}	0.996	0.999	0.878	
t	25.9	29.2	13.7	nm
α_{free}	0.51	0.45	0.77	
α_{ex}	1.72	1.90	1.30	
Ionomer alignment				
$\Delta_{DA,0}$	0.127	0.169	0.215	
Δ_{DA}	0.358	0.364	0.319	
Surface wetting properties				
θ_{ion}	90.6°	90.2°	93.7°	
$\theta_{Pt/C}$	43.7°	50.4°	57.2°	
$\bar{\theta}_2$	90.5°	90.1°	89.5°	
X_{HO}	0.94	0.79	0.32	
WRC shape parameters (analytical)				
X_1	0.23	0.18	0.30	
X_2	0.77	0.82	0.70	
p_2	1.3E+04	3.2E+03	-1.5E+04	Pa
$\sigma_{p,2}$	4.8E+03	2.5E+03	2.0E+04	Pa

out hydrophilic or hydrophobic depending on the CCL ink parameters. They require detailed consideration to scrutinize the impact of material choices on water management.

In the total WRC depicted in Fig. 3(c), the two major domains **(1)** and **(2)** in the combined pore size and contact angle distribution result in two steps. The first step marks the flooding of the primary pores and occurs at liquid pressures with an order of magnitude exceeding tens of bars. In contrast, pressures under operation of the fuel cell are $\pm 10^4 \dots 10^5$ *Pa*. In this range, the larger step of the WRC occurs, which lies in the region of secondary pores, as shown with higher resolution in Fig. 3(d). For a higher resolution of the contact angle distribution in secondary pores,

see Fig. A.1 in the appendix.

Fig. 3 (c) and (d) depict the comparison of numerically and analytically obtained WRCs. The numerical solution is not perfectly symmetrical because the variance in contact angle scales with r_{pore}. However, the sigmoid interpolation by the analytical solution captures well the essential features of the curve, such as inflection point, spread and step height. In the following, solely the analytical approximation was used for the model solution and parameter studies.

3.1.3. Comparison with experimental WRC data

To compare the model with measured WRC data, two catalyst layer materials from Gunterman [14], an experimental and a commercial CCL, are used as references. Generally, the data available in literature are very scarce, especially because wetting properties and information on materials and fabrication process are needed. Some works report WRCs, but a sufficient parametrization for the CCL ink parameters could not be extracted [13,39]. The modeling works of Pant et al. [12] and Zenyuk et al. [11] include measured WRCs, but further information on the exact materials used was not provided. The thesis of Gunterman [14] is often cited wherever data for wetting properties of CCL or GDL are of concern and was found to be the only source providing both the required ink parameters and the corresponding WRCs of the CCLs.

Pt:C and I:C ratios of the materials used by Gunterman are listed in Table 1 and model results are reported in Table 2. Experimental WRC data for the commercial and experimental CCL are plotted together with the calculated WRC in Fig. 4. The parametrization was adjusted with regard to ϕ_1, to match the step height in the WRC. It was lowered to 0.09 in the commercial CL and raised to 0.25 for the experimental sample. This might be caused by some compaction or pressing of the CCL during fabrication, or by better agglomeration. Slightly adapting the value of k_A for the experimental material to 4 further improved the quality of the fit. This can be attributed to some deviations in the ink parameters from the commercial case. However, the overall comparison with the dataset of Gunterman resulted in good agreement and demonstrates the ability of the model to calculate WRCs based on the CCL ink parameters in a plausible manner. Deviations and phenomena not captured by the model, such the WRC hysteresis, are mainly attributed to pore network effects, such as trapping or snap-off during injection and withdrawal of
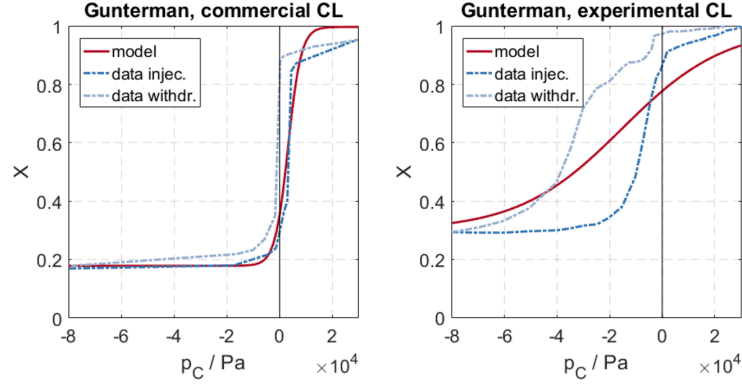
9

Fig. 4. Comparison of model and measured WRC data from Gunterman [14] **(a)** of commercial CCL **(b)** and experimental CL material.
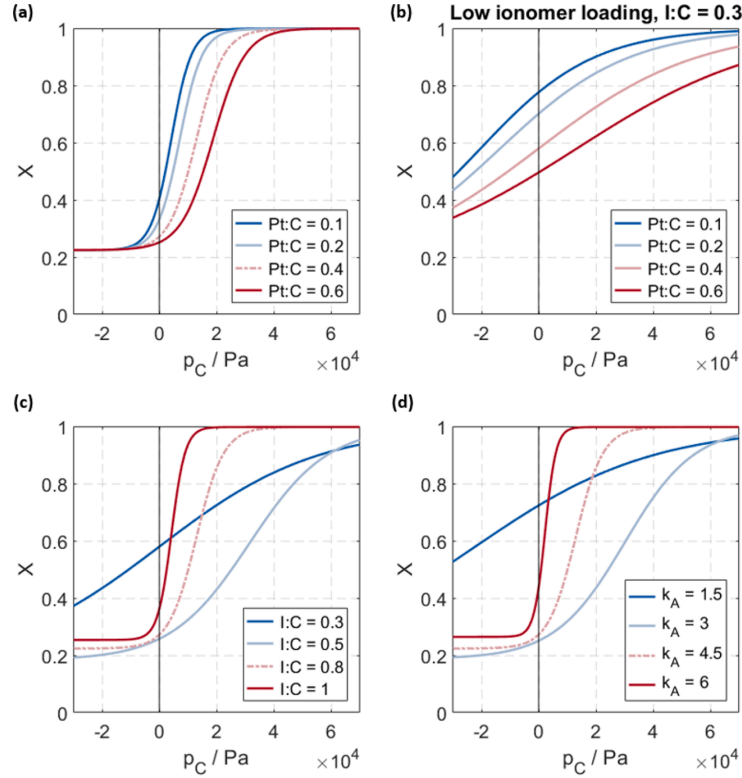

Fig. 5. Single parameter variation of LSAC base case for **(a)** platinum concentration (Pt:C = 0.1, 0.2, 0.4, 0.6), **(b)** platinum concentration (Pt:C = 0.1, 0.2, 0.4, 0.6) at lowered ionomer loading (I:C = 0.3), **(c)** variation of ionomer loading (I:C = 0.3, 0.5, 0.8, 1), **(d)** ionomer dispersion via variation of k_A = 1.5, 3, 4.5, 6. The dashed curves show the base case.

liquid. These effects are beyond the scope of the presented model, as it volume-averages the wetting properties of the CCL. Other methodologies, such as pore network models or direct simulations of liquid water transport, resolve the pore-level effects and, therefore, allow calculating the WRC hysteresis. However, such models often have to assume wetting properties, as only sparse experimental data are available in the literature. Foreseeing possible applications of the presented model, it might be used as a basis to parameterize the WRCs used in other models.

3.2. Impact of catalyst composition on wetting behavior

The model was solved for a series of parameter variations in order to understand how the microstructure of the CCL might be tweaked to meet performance requirements for fuel cells. As a criterion for evaluating the obtained WRCs, an increased hydrophobicity of secondary pores is considered favorable to protect the cell against flooding.

The Pt:C ratio is the first parameter of interest regarding CCL ink composition. In this study, the values for Pt:C represent the cases of low (0.1), moderate (0.2) and high (0.4, 0.6) Pt density. The low Pt density

10
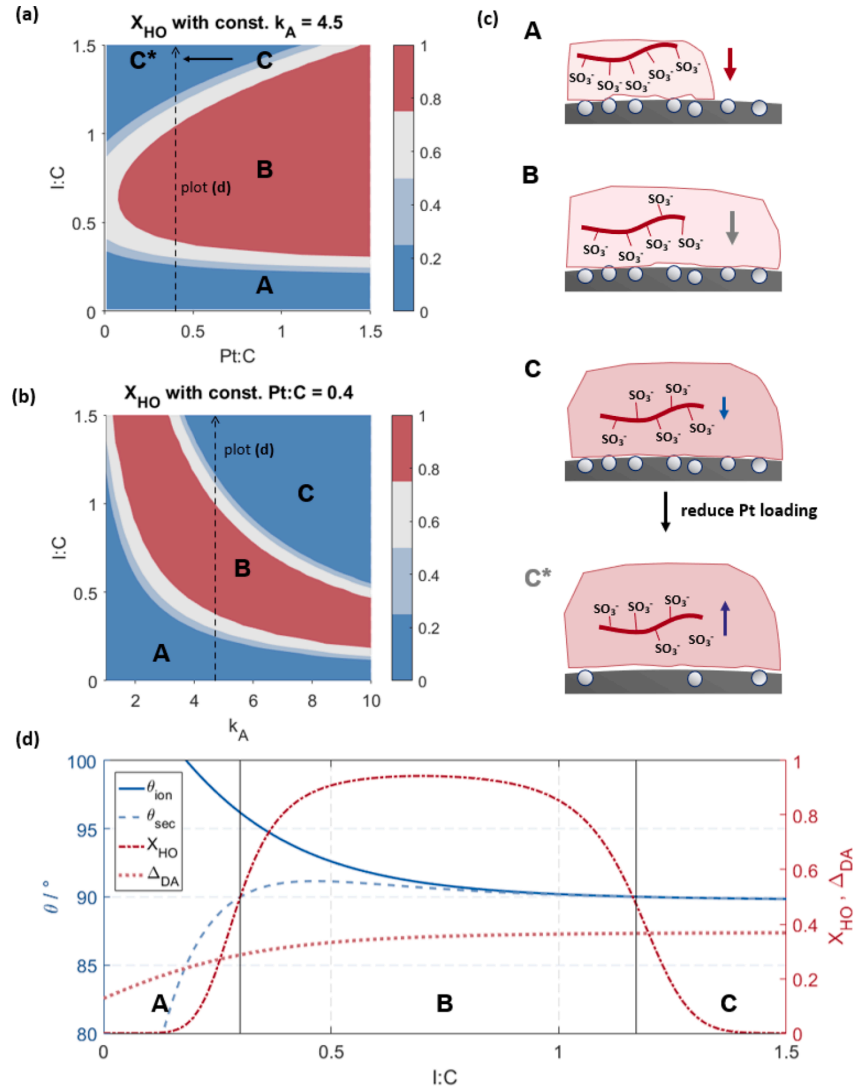
Fig. 6. Mapping of effective hydrophobic fraction as design criterion over **(a)** Pt:C vs. I:C and **(b)** k_A vs. I:C. **(c)** The underlying structural regimes are illustrated. **(d)** Evolution of wetting properties and degree over increasing I:C ratio. The three stages of structure evolution can be distinguished by the hydrophobic fraction of secondary pores X_{HO}.

case in Fig. 5(a) results in a WRC step partially located in the hydrophilic regime, i.e., a significant liquid saturation is reached at $p_c = 0$. Increasing the Pt:C ratio shifts the WRC towards higher p_c, i.e., a more hydrophobic regime. For Pt:C > 0.6 the full WRC step occurs at positive capillary pressures, indicating the hydrophobization of the ionomer film in secondary pores by platinum. The sidechains of ionomer strongly interact with platinum, resulting in an alignment of of the ionomer structure where hydrophobic backbones arefacing secondary pores. This trend is in line with experimental observations of Volfkovich et al. [2].

In order to rationalize the role of ionomer, a second Pt:C variation with a reduced I:C ratio of 0.3 was conducted. The resulting WRCs in Fig. 5(b) reveal that the amount of ionomer is not sufficient to cover significant parts of the pore walls, leaving a significant fraction hydrophilic Pt/C surface exposed. This results in a weak overall hydrophobization of secondary pores. However, the trend towards more hydrophobic wetting behavior of the ionomer film with increasing Pt:C persists. Furthermore, the WRCs spread extends for low I:C ratios (also

to be seen in Fig. 5(c)) due to a much larger heterogeneity of wetting properties at moderate ionomer coverage.

The variation of the I:C ratio spans from moderately low to moderately high ionomer loadings (I:C = 0.3, 0.5, 0.8, 1). The respective WRCs are shown in Fig. 5(c) and exhibit at first an increasing hydrophobization with increasing I:C ratio, shifting the WRC towards higher values of p_c. Around I:C = 0.5, this trend is reversed and higher I:C ratios cause the WRC to exhibit a steeper step. The observed trend can be explained by the ionomer film first growing quickly in coverage, turning wetting properties of secondary pores more hydrophobic. When more ionomer is added, the ionomer film starts growing in thickness, weakening the hydrophobic alignment of backbone towards the secondary pore space. The maximum in hydrophobicity at intermediate I:C ratio was also reported in the experimental literature [40,41].

Varying the dispersion parameter k_A from 1.5 to 6 in Fig. 5(d) results in a very similar picture as seen for the I:C variation: first, an increase in hydrophobicity is observed, followed by a collapse of hydrophobicity to

a steeper step. The underlying picture is similar to the previous variation of I:C, but now only the morphology of the ionomer film is affected, not the I:C ratio. For low values ($k_A \leq 2$) a thin ionomer film with poor coverage forms and a larger amount of ionomer is aggregating inside the CCL without contributing to film formation. Around $k_A \approx 3$ the dispersion of ionomer reaches an optimum with high coverage and the film thickness not too high to impair wetting properties. Above $k_A > 5$ the ionomer is strongly adhering to the Pt/C structure during ink stage, thus resulting in coverage of ≈ 1 and high film thickness. The parameter k_A captures the tendency for the ionomer morphology of a certain ink recipe, but it does not directly imply a specific choice of solvent or material modifications. That makes it suitable to describe a wide range of modification and might help quantify different approaches to tune ionomer dispersion.

3.3. Design guidelines for favorable CCL wetting properties

Both the amount and the dispersion of ionomer are key parameters in the application of ionomer. Whereas the concentration of platinum nanoparticles primarily alters the molecular alignment and renders the ionomer surface in the secondary pore space hydrophobic, an optimal combination of coverage and thickness of the ionomer phase is required to assure an overall hydrophobic secondary pore space. In order to disentangle these dependencies and find design guidelines for the combined adjustment of Pt:C, I:C and k_A, a study exploring the combined impact of these parameters was conducted.

To evaluate the wetting behaviour of CCLs, the hydrophobic fraction of secondary pores X_{HO} was chosen as a scalar metric. In Fig. 6(a), X_{HO} was mapped over a Pt:C and I:C range of 0 to 1.5. For each value of Pt:C a minimal and maximal I:C ratio manifests where a high hydrophobic fraction ($X_{HO} \geq 0.8$) is reached. Below and above the respective I:C range, the wetting properties are mostly hydrophilic ($X_{HO} \leq 0.2$). The window between lowest and highest possible I:C shrinks drastically when lowering the Pt loading. Whereas the I:C window at Pt:C > 1 spans from 0.3 to 1.3, a diluted catalyst (Pt:C < 0.1) cannot uphold $X_{HO} \geq 0.8$ for any I:C.

The underlying structural causalities are illustrated in Fig. 6(c) and (d) and can be categorized into three cases: in Case A, the ionomer film is thin and highly hydrophobic, but does not gain sufficient coverage to effectively render the CL hydrophobic; in Case B, the ionomer film is slightly increased in thickness, but still moderately hydrophobic; ionomer coverage is high, thus the overall wetting properties become hydrophobic; exceeding this optimal condition by applying more ionomer will lead to Case C, in which the film grows further in thickness and the hydrophobic properties fade but are still sufficient to uphold a certain hydrophobicity. A reduction of Pt:C ratio, as illustrated as Case C* in Fig. 6(c), will cause the ionomer alignment to fade and the hydrophobicity to decay. Consequently, the overall wetting properties of the CCL change from mostly hydrophobic to fully hydrophilic.

These insights consolidate an important principle for CCL design: the lower the Pt:C ratio, the less room remains to maneuver with regard to the I:C ratio. This is of particular importance when reducing the platinum loading for cost efficient CCLs. If the morphology of the ionomer film is inadequate, i.e., film coverage and thickness are not well adjusted, hydrophilic wetting behavior and thus proneness to flooding will result.

Following these insights, the two main parameters for tuning the ionomer properties, I:C and k_A, were evaluated in combination in Fig. 6 (b). With larger k_A, a lower I:C ratio is required to obtain hydrophobic wetting behavior. Also, the respective I:C window gets narrower at higher k_A. For a low-dispersed ionomer ($k_A = 3$) any I:C in the range from 0.5 to1.5 will result in a mostly hydrophobic CCL. Both range and absolute values decrease at $k_A = 8$, where the hydrophobic condition occurs in the range of I:C from 0.2 to 0.7. Again, this manifests the importance of balancing ionomer coverage and thickness. The previously discussed cases (A: too low coverage, B: coverage and thickness
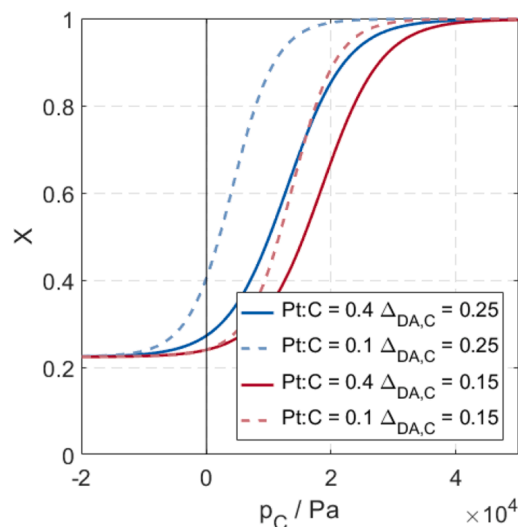

Fig. 7. Impact of modification of the chemical nature of the carbon surface, e.g. by nitrogen incorporation on the wetting properties of the CCL.

balanced, C: to high coverage and/or film thickness) apply accordingly.

The potential to improve the performance of the CCL by adjusting ionomer coverage and thickness was recognized in recent experimental studies. Multiple works discussed the partial formation of highly dispersed ionomer, as opposed to lumped aggregations [42–45]. Different attempts to alter the tendency of ionomer to spread in thin films were tested. A variation of the ink solvent was found to be very effective in several works [22,42,44,46,47]. A recent review on ink parameter variations by Berlinger et al. [48] concluded that the I:C ratio and the ink solvent are the key parameters for tuning catalyst layer properties. The underlying interactions between ionomer & carbon support and ionomer & solvent are critical for structure formation. During the ink, stage the solvent alters the balance between polar and dispersion interactions among ionomer molecules and between ionomer and the Pt/C surface. Consequently the ionomer will exhibit a different likelihood to either adhere to already aggregated ionomer or free Pt/C surface.

Another approach to increase ionomer dispersion introduces nitrogen containing functional groups at the carbon support surface [45,49]. These positively charged aminic groups strengthen the interaction of sidechains with the carbon surface and consequently disperse the ionomer as well as cause the sidechains to align towards the interface of Pt/C surface and ionomer film. Molecular dynamics studies revealed that also oxygen-containing groups, which are also abundant on common carbon support materials such as Vulcan Carbon, significantly alter the sidechain alignment [50].

The impact of the sidechain alignment imposed by the carbon support, $\Delta_{DA,C}$, on the WRCs are depicted in Fig. 7. The reference parametrization with Pt:C = 0.4 and $\Delta_{DA,C} = 0.25$ results in moderately hydrophobic wetting behavior. As discussed above, lowering the Pt:C ratio causes a shift towards the hydrophilic domain, increasing the proneness to flooding. In order to increase the hydrophobicity of the CCL, $\Delta_{DA,C}$ can be lowered to 0.15 through carbon modification. This pushes the WRCs of CCLs with low or moderate platinum density to a more hydrophobic wetting behavior.

3.4. Wettability during CCL lifetime

The parameter study is completed by evaluating the impact of aging of the fuel cell. Two major degradation mechanism contribute to the
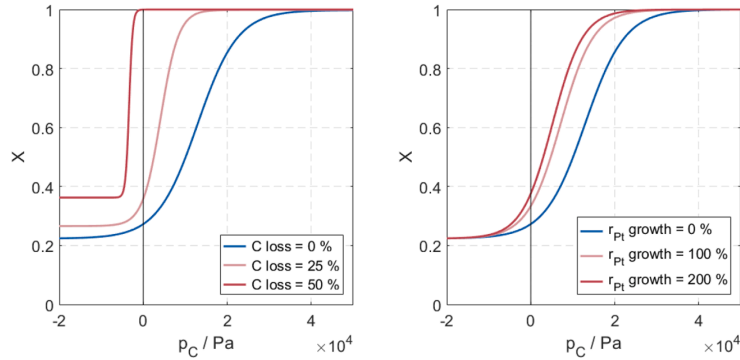
Fig. 8. Changes in wettability during aging caused by **(a)** carbon corrosion, i.e., a loss of carbon support structure and **(b)** platinum particle growth.

decay of performance over the lifetime of the cell: carbon corrosion and platinum coarsening.

Carbon corrosion was incorporated by the assumption that the carbon support shrinks in mass. This results in a shift of the I:C and Pt:C ratios to higher values, according to

$$m_{I:C,aged} = \frac{m_{I:C}}{1 - f_{C\,loss}} \quad \text{and} \tag{51}$$

$$m_{Pt:C,aged} = \frac{m_{Pt:C}}{1 - f_{C\,loss}}, \tag{52}$$

where $f_{C\,loss}$ is the fraction of carbon mass lost. The impact on the wetting behavior caused by a loss of carbon mass by 0%, 25% and 50% is illustrated in Fig. 8. The WRCs show a shift of the WRC towards a steep, moderately hydrophilic step. The step height, i.e., the secondary pore volume, is reduced significantly. This behavior is similar to the scenario where the I:C ratio is increased. Indeed, the underlying structural picture is the same: more ionomer per Pt/C surface results in larger ionomer coverage and thickness, ultimately causing a decay of the hydrophobicity in secondary pores. Measurements by Fang et al. confirm this decay of hydrophobicity [51].

Concurrent to the primary effect of the ionomer, the amount of platinum nanoparticles remained constant, but covers a reduced carbon surface. This increases platinum coverage and consequently intensifies the interaction of ionomer sidechains with the Pt/C surface. The increase in hydrophobicity due to this effect is small and masked by the primary effect of ionomer thickness. This secondary effect on ionomer alignment can be evaluated separately if solely platinum coarsening is considered, as it also occurs in the Pt degradation mechanisms.

In order to simulate coagulation and Ostwald ripening of the Pt catalyst, the radius of the Pt nanoparticles was increased by a growth factor $f_{r\,growth}$, with $r_{Pt,aged} = (1 + f_{r\,growth})r_{Pt}$, while the Pt:C ratio was held constant. The resulting trends for increasing r_{Pt} by $f_{r\,growth} = \{100\%, 200\%\}$ in Fig. 8(b) shows that the WRC is shifted into the hydrophilic regime the larger the Pt particles grow. Similar to lowering the Pt:C ratio (cf. Fig. 5, a reduced platinum coverage due to larger particles results in a weaker ionomer alignment, thus a decay in hydrophobicity.

An experimental study also found the chemical nature of the carbon support to change during accelerated stress test. When carbon corrodes, oxygen containing functional groups form on its surface [52]. This third effect can impact the degree of alignment of the ionomer (as shown in Fig. 7) in a way that it maintains some hydrophobicity. However, the extend of this effect is small and was found to be reversible by recovery protocols [52].

3.5. Towards tailored wetting properties of cathode catalyst layers

The proposed model might be used by material scientists and

engineers to adjust the wetting properties of the CCL to achieve maximal fuel cell performance. For a specific application, the optimal shape of the WRC (i.e., inflection point and spread of the major step) will hinge on the design of other diffusion media and the overall operation strategy of the fuel cell. Especially the function with the adjacent gas diffusion layer has to be tuned carefully: at the CCL/GDL boundary capillary pressure and liquid saturation have be paired in a way that water crosses over the boundary effciently. Our model can possibly be incorporated into existing macro-homogeneous fuel cell models describing water transport and liquid water saturation via a water retention curves [11,12].

A particularly interesting goal for such optimizations is the reduction of the Pt loading. Muzaffar et al. defined two limiting scenarios to reduce the Pt loading: reducing the CCL thickness at fixed composition; or upholding the thickness but reducing the Pt:C ratio [53]. For thickness reduction, they conjectured that since the volumetric water production in the catalyst increases, while at the same time the vaporization capability decreases, more water needs to leave the CCL in liquid form. This leads to a tipping of the water balance, with flooding occuring in both CCL and adjacent porous transport media [11,17,53]. Our work complements these studies by a model-based analysis of the second limit, the lowering the Pt loading via reducing the Pt:C ratio. Here, the tip-over of the water balance is caused by the decreased coverage of the carbon support surface with platinum particles, which results in a more hydrophilic orientation of ionomer towards the secondary pore space.

Considering conventional CCLs only from the perspective of layer thickness and Pt:C ratio restricts the possibilities of further reduction of Pt loading. As our model implies, multiple levers exist to potentially push the limits of Pt loading (see Section 3.3). In accordance with current experimental developments, we see large potential in tweaking the ionomer dispersion during the fabrication process [22,42,44,46,47] or manipulating of the chemical nature of the carbon surface [45,49], to name just two further possibilities.

However, the detailed interaction of ionomer and Pt/C is more complex as implemented in this work. For instance, the role of hydration of the ionomer/Pt interface or the potential dependence of this interaction have been neglected. These aspects certainly contribute to the wetting properties of the ionomer film but the mechanisms and extend of such influences remain speculative. Regarding hydration effects, results from MD simulations indicate that the principal effect of sidechain alignment dominates the molecular structure, but the formation of micelles or layered structures depends on the humidity conditions [54]. Thin film effects were already experimentally studied in the past, but many insights rely on support materials not used in fuel cell technology [55]. Future experimental and theoretical works are necessary to clarify and consolidate the understanding of the complex interactions between the ionomer film and the substrate or catalyst.

Table 3
Data extracted from Soboleva [20] for Ketjen Black based CL material.

I:C	V_2 / $cm^3 g_C^{-1}$	$\alpha_{free} = V_2/V_{2,0}$	$x = V_{ion}/V_{2,0}$	a_{ion}
0.00	0.68	1.00	0.00	0.00
0.10	0.59	0.87	0.07	0.06
0.20	0.48	0.71	0.15	0.55
0.78	0.34	0.50	0.60	0.96
1.82	0.08	0.12	1.40	1.00

4. Summary and conclusion

The wetting properties of the porous network in fuel cell catalyst layers are the key to improving the operation of polymer electrolyte fuel cells. In order to derive quantitative relationships between catalyst composition, structural features and resulting properties, the role of the ionomer thin film covering the Pt/C catalyst needs to be understood. Especially, the experimentally observed inversion phenomenon of ionomer films altering the wetting properties of the Pt/C support needs to be taken into account.

This work provides a quantitative model that bridges the gap between catalyst ink parameters, electrode structure and macroscopic properties. Firstly, a composition model was developed by rationalizing the structure formation during ink stage in catalyst layer fabrication. This introduced a novel dispersion parameter, which captures the tendency of ionomer to form thin films or to aggregate. Secondly, the molecular alignment of ionomer sidechains and backbones was assumed to be decisive for the resulting wetting properties. A novel approach of describing the degree of alignment was proposed, which was then linked to the chemical nature of the underlying Pt/C surface as well as the ionomer film thickness. Thirdly, a statistical distribution of wetting angles over pore sizes was derived and used to calculate water retention curves that can be used as descriptor for the macroscopic wetting behaviour in macrohomogeneous performance models.

From our model-based analyses the following key insights were obtained: lowering the density of platinum in the CCL, i.e., reducing the Pt: C ratio, weakens the hydrophobization of the ionomer film; this decreases the range of ionomer thickness and coverage, in which favorable wetting properties exist. This limitation can be counteracted in two ways: firstly, the ionomer dispersion can be tuned during fabrication, for instance by the choice of the ink solvent; and, secondly, the intrinsic interaction between carbon surface and ionomer can be altered by modifying the carbon support.

Further, the model provides an estimate how wetting properties will change when the catalyst layer degrades by carbon corrosion or platinum coarsening: in both cases, the wetting properties will become more hydrophilic and impair efficient water management towards the end of the fuel cell lifetime.

The identified approaches for optimizing the CCL wetting properties are in line with current developments in the experimental literature, such as solvent variation and carbon modification by functional groups. The trends in these works are in agreement with the insights of the present study regarding the optimized design of the catalyst microstructure. For future development, the model might help to define new directions for both interface and pore level modeling and simulation, and experimental characterization.

Looking at the larger context of fuel cell modeling, this work contributes to bridging composition to microstructure to macroscopic catalyst layer properties. Embedded into holistic optimization routines the proposed structure-based model enables tailored design of catalyst layer properties by devising optimized ink recipes.

CRediT authorship contribution statement

W. Olbrich: Conceptualization, Methodology, Software, Formal analysis, Writing – original draft. **T. Kadyk:** Writing – review & editing, Supervision. **U. Sauter:** Resources, Writing – review & editing, Supervision, Project administration. **M. Eikerling:** Writing – review & editing, Supervision, Project administration.

Declaration of Competing Interest

The authors declare that they have no known competing financial interests or personal relationships that could have appeared to influence the work reported in this paper.

Data availability

No data was used for the research described in the article.

Appendix A

Data used to fit k_A and t_0 parameter

The volume of secondary pores was measured by Soboleva [20] using nitrogen sorption and extracting the pore size distribution. The condensed volume attributed to the secondary pores is reported here. The value of the ionomer-free material was taken as the reference volume $V_{2,0}$. The trends for the Vulcan-based catalyst layers are similar, but did not contain enough data points. Thus only the Ketjen Black data set is used in this work, which is a high surface area carbon and has a different pore size distribution than Vulcan. Ketjen Black features smaller secondary pores ($r_{\mu,2} = 30$ *nm*), a larger fraction of primary pores ($\phi_1 = 0.21$), and a higher total pore volume ($V_{pores} = 0.86$ cm^3/g_C). Evaluating the resulting surface area from the pore size distribution yields $A_2 = 34$ m^2/g_C. This parametrization was used to fit the composition model and create Fig. 2.

To estimate the ionomer coverage, we follow the analysis of Soboleva, which compares the double layer capacitance under dry vs. wet conditions. The ratio is considered a measure for the surface fraction covered by ionomer. At high I:C ratios, this ratio reaches $\approx 60\%$. At such a CL composition all secondary pore surface is covered by ionomer. Thus, the remaining surface is attributed to the primary pores. To match the normalization convention of this work, which discusses ionomer coverage for the secondary pores only, the value for ionomer coverage at I:C = 1.82 was set to be the reference for $a_{ion} = 1$.
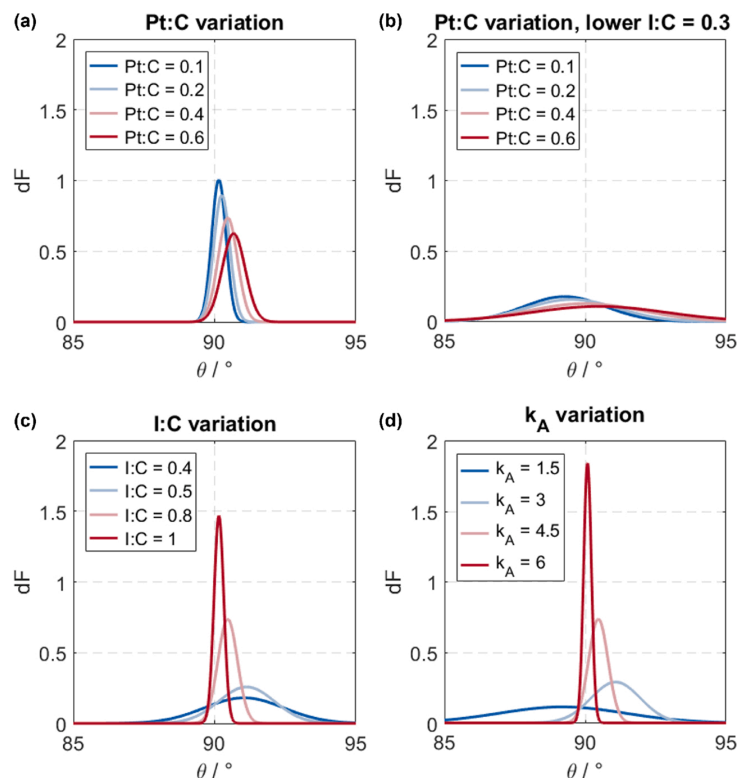
Contact angle distribution at 20 nm

Fig. A.1. Contact angle distribution of the secondary pores, reported for $r_{pore} = 20$ *nm* and variations of **(a)** platinum density (Pt:C = 0.1, 0.2, 0.4, 0.6), **(b)** platinum density (Pt:C = 0.1, 0.2, 0.4, 0.6) and at I:C = 0.3, **(c)** ionomer loading (I:C = 0.3, 0.5, 0.8, 1), and **(d)** ionomer dispersion via $k_A = 1.5, 3, 4.5, 6$.

References

[1] M. Eikerling, A.A. Kornyshev, A.R. Kucernak, Water in polymer electrolyte fuel cells: friend or foe? Phys. Today 59 (10) (2006) 38–44, https://doi.org/10.1063/1.2387087.

[2] Y.M. Vol'fkovich, V.E. Sosenkin, N.F. Nikol'skaya, Hydrophilic-hydrophobic and sorption properties of the catalyst layers of electrodes in a proton-exchange membrane fuel cell: a stage-by-stage study, Russ. J. Electrochem. 46 (4) (2010) 438–449, https://doi.org/10.1134/S1023193510040099.

[3] K. Malek, T. Mashio, M. Eikerling, Microstructure of catalyst layers in PEM fuel cells redefined: a computational approach, Electrocatalysis 2 (2) (2011) 141–157, https://doi.org/10.1007/s12678-011-0047-0.

[4] D.L. Wood, J. Chlistunoff, J. Majewski, R.L. Borup, Nafion structural phenomena at platinum and carbon interfaces, J. Am. Chem. Soc. 131 (50) (2009) 18096–18104, https://doi.org/10.1021/ja9033928.

[5] V. Mulone, K. Karan, Analysis of capillary flow driven model for water transport in PEFC cathode catalyst layer: consideration of mixed wettability and pore size distribution, Int. J. Hydrogen Energy 38 (1) (2013) 558–569, https://doi.org/10.1016/j.ijhydene.2012.07.107.

[6] T. Mashio, K. Sato, A. Ohma, Analysis of water adsorption and condensation in catalyst layers for polymer electrolyte fuel cells, Electrochim. Acta 140 (2014) 238–249, https://doi.org/10.1016/j.electacta.2014.07.058.

[7] P.A. Mateo Villanueva. A mixed wettability pore size distribution model for the analysis of water transport in PEMFC materials, University of Alberta, 2013. PhD Thesis.https://era.library.ualberta.ca/items/e96ae1d9-450e-467b-9f82-4d5fddc7f839

[8] J. Zhou, A. Putz, M. Secanell, A mixed wettability pore size distribution based mathematical model for analyzing two-phase flow in porous electrodes: I. Mathematical model, J. Electrochem. Soc. 164 (6) (2017) F530–F539, https://doi.org/10.1149/2.0381706jes.

[9] A. Goshtasbi, P. García-Salaberri, J. Chen, K. Talukdar, D.G. Sanchez, T. Ersal, Through-the-membrane transient phenomena in PEM fuel cells: a modeling study, J. Electrochem. Soc. 166 (7) (2019) F3154–F3179, https://doi.org/10.1149/2.0181907jes.

[10] A.Z. Weber, Improved modeling and understanding of diffusion-media wettability on polymer-electrolyte-fuel-cell performance, J. Power Sources 195 (16) (2010) 5292–5304, https://doi.org/10.1016/j.jpowsour.2010.03.011.

[11] I.V. Zenyuk, P.K. Das, A.Z. Weber, Understanding impacts of catalyst-layer thickness on fuel-cell performance via mathematical modeling, J. Electrochem.

[12] L.M. Pant, M.R. Gerhardt, N. Macauley, R. Mukundan, R.L. Borup, A.Z. Weber, Along-the-channel modeling and analysis of PEFCs at low stoichiometry: development of a 1+2D model, Electrochim. Acta 326 (2019) 134963, https://doi.org/10.1016/j.electacta.2019.134963.

[13] Q. Ye, T.V. Nguyen, Three-dimensional simulation of liquid water distribution in a PEMFC with experimentally measured capillary functions, J. Electrochem. Soc. 154 (12) (2007) B1242, https://doi.org/10.1149/1.2783775.

[14] H.P.F. Gunterman. Characterization of Fuel-Cell Diffusion Media, UC Berkeley, 2011. Ph.D. thesis.

[15] J.T. Gostick, M.W. Fowler, M.A. Ioannidis, M.D. Pritzker, Y.M. Volfkovich, A. Sakars, Capillary pressure and hydrophilic porosity in gas diffusion layers for polymer electrolyte fuel cells, J. Power Sources 156 (2) (2006) 375–387, https://doi.org/10.1016/j.jpowsour.2005.05.086.

[16] J.M. LaManna, J.V. Bothe, F.Y. Zhang, M.M. Mench, Measurement of capillary pressure in fuel cell diffusion media, micro-porous layers, catalyst layers, and interfaces, J. Power Sources 271 (2014) 180–186, https://doi.org/10.1016/j.jpowsour.2014.07.163.

[17] M. Eikerling, Water management in cathode catalyst layers of PEM fuel cells, J. Electrochem. Soc. 153 (3) (2006) E58, https://doi.org/10.1149/1.2160435.

[18] W. Olbrich, T. Kadyk, U. Sauter, M. Eikerling, Review–Wetting phenomena in catalyst layers of PEM fuel cells: novel approaches for modeling and materials research, J. Electrochem. Soc. (2022), https://doi.org/10.1149/1945-7111/ac6e8b.

[19] T. Soboleva, X. Zhao, K. Malek, Z. Xie, T. Navessin, S. Holdcroft, On the micro-, meso-, and macroporous structures of polymer electrolyte membrane fuel cell catalyst layers, ACS Appl. Mater. Interfaces 2 (2) (2010) 375–384, https://doi.org/10.1021/am900600y.

[20] T. Soboleva. On the microstructure of PEM fuel cell catalyst layers, Simon Fraser University, 2010. Ph.D. thesis.https://summit.sfu.ca/item/11450

[21] D. Susac, V. Berejnov, A.P. Hitchcock, J. Stumper, STXM Study of the ionomer distribution in the PEM fuel cell catalyst layers, ECS Trans. 41 (1) (2011) 629–635, https://doi.org/10.1149/1.3635596.

[22] G. Doo, J.H. Lee, S. Yuk, S. Choi, D.H. Lee, D.W. Lee, H.G. Kim, S.H. Kwon, S. G. Lee, H.T. Kim, Tuning the ionomer distribution in the fuel cell catalyst layer with scaling the ionomer aggregate size in dispersion, ACS Appl. Mater. Interfaces 10 (21) (2018) 17835–17841, https://doi.org/10.1021/acsami.8b01751.

Soc. 163 (7) (2016) F691.https://iopscience.iop.org/article/10.1149/2.1161607jes/meta

[23] L. Guetaz, M. Lopez-Haro, S. Escribano, A. Morin, G. Gebel, D.A. Cullen, K.L. More, R.L. Borup, Catalyst-Layer ionomer imaging of fuel cells, ECS Trans. 69 (17) (2015) 455–464, https://doi.org/10.1149/06917.0455ecst.

[24] F.C. Cetinbas, R.K. Ahluwalia, N.N. Kariuki, V. De Andrade, D.J. Myers, Effects of porous carbon morphology, agglomerate structure and relative humidity on local oxygen transport resistance, J. Electrochem. Soc. 167 (1) (2020) 013508, https://doi.org/10.1149/2.0082001JES.

[25] K. Malek, M. Eikerling, Q. Wang, T. Navessin, Z. Liu, Self-Organization in catalyst layers of polymer electrolyte fuel cells, J. Phys. Chem. C 111 (36) (2007) 13627–13634, https://doi.org/10.1021/jp072692k.

[26] S. Goswami, S. Klaus, J. Benziger, Wetting and absorption of water drops on nafion films, Langmuir 24 (16) (2008) 8627–8633, https://doi.org/10.1021/la800799a.

[27] T.A. Zawodzinski, S. Gottesfeld, S. Shoichet, T.J. McCarthy, The contact angle between water and the surface of perfluorosulphonic acid membranes, J. Appl. Electrochem. 23 (1) (1993) 86–88, https://doi.org/10.1007/BF00241582.

[28] J. Wang, L. Xiao, G. Liao, Y. Zhang, L. Guo, C.H. Arns, Z. Sun, Theoretical investigation of heterogeneous wettability in porous media using NMR, Sci. Rep. 8 (1) (2018), https://doi.org/10.1038/s41598-018-31803-w.

[29] M. Lopez-Haro, L. Guétaz, T. Printemps, A. Morin, S. Escribano, P.-H. Jouneau, P. Bayle-Guillemaud, F. Chandezon, G. Gebel, Three-dimensional analysis of Nafion layers in fuel cell electrodes, Nat. Commun. 5 (1) (2014), https://doi.org/10.1038/ncomms6229.

[30] M. So, K. Park, Y. Tsuge, G. Inoue, A particle based ionomer attachment model for a fuel cell catalyst layer, J. Electrochem. Soc. 167 (1) (2020) 013544.https://iopscience.iop.org/article/10.1149/1945-7111/ab68d4/meta

[31] Papoulis, A., Pillai, S.U., Probability, random variables, and stochastic processes, McGraw-Hill, Boston, Mass., 4. ed., internat. ed., nachdr edition, 2009. OCLC: 255904469.

[32] Y.M. Volfkovich, V.E. Sosenkin, V.S. Bagotsky, Structural and wetting properties of fuel cell components, J. Power Sources 195 (17) (2010) 5429–5441, https://doi.org/10.1016/j.jpowsour.2010.03.002.

[33] J.T. Wescott, Y. Qi, L. Subramanian, T. Weston Capehart, Mesoscale simulation of morphology in hydrated perfluorosulfonic acid membranes, J. Chem. Phys. 124 (13) (2006) 134702, https://doi.org/10.1063/1.2177649.

[34] T. Morawietz, M. Handl, C. Oldani, K.A. Friedrich, R. Hiesgen, Quantitative *in situ* analysis of ionomer structure in fuel cell catalytic layers, ACS Appl. Mater. Interfaces 8 (40) (2016) 27044–27054, https://doi.org/10.1021/acsami.6b07188.

[35] K.W. Bewig, W.A. Zisman, The wetting of gold and platinum by water, J. Phys. Chem. 69 (12) (1965) 4238–4242.

[36] T. Nishino, M. Meguro, K. Nakamae, M. Matsushita, Y. Ueda, The lowest surface free energy based on -CF₃ alignment, Langmuir 15 (13) (1999) 4321–4323, https://doi.org/10.1021/la981727s.

[37] Y.C. Park, H. Tokiwa, K. Kakinuma, M. Watanabe, M. Uchida, et al., Effects of carbon supports on Pt distribution, ionomer coverage and cathode performance for polymer electrolyte fuel cells, J. Power Sources 315 (2016) 179–191, https://doi.org/10.1016/j.jpowsour.2016.02.091.

[38] S. Holdcroft, Fuel cell catalyst layers: a polymer science perspective, Chem. Mater. 26 (1) (2014) 381–393, https://doi.org/10.1021/cm401445h.

[39] T.V. Nguyen, G. Lin, H. Ohn, X. Wang, Measurement of capillary pressure property of gas diffusion media used in proton exchange membrane fuel cells, Electrochem. Solid-State Lett. 11 (8) (2008) B127, https://doi.org/10.1149/1.2929063.

[40] X. Li, F. Feng, K. Zhang, S. Ye, D.Y. Kwok, V. Birss, Wettability of nafion and nafion/vulcan carbon composite films, Langmuir 28 (16) (2012) 6698–6705, https://doi.org/10.1021/la300388x.

[41] S.M. Andersen, L. Grahl-Madsen, Interface contribution to the electrode performance of proton exchange membrane fuel cells - impact of the ionomer, Int. J. Hydrogen Energy 41 (3) (2016) 1892–1901, https://doi.org/10.1016/j.ijhydene.2015.11.101.

[42] S. Takahashi, T. Mashio, N. Horibe, K. Akizuki, A. Ohma, Analysis of the microstructure formation process and its influence on the performance of polymer electrolyte fuel-cell catalyst layers, ChemElectroChem 2 (10) (2015) 1560–1567, https://doi.org/10.1002/celc.201500131.

[43] R. Zeng, H.Y. Zhang, S.Z. Liang, L.G. Wang, L.J. Jiang, X.P. Liu, Possible scenario of forming a catalyst layer for proton exchange membrane fuel cells, RSC Adv. 10 (9) (2020) 5502–5506, https://doi.org/10.1039/C9RA09864J.

[44] T. Van Cleve, S. Khandavalli, A. Chowdhury, S. Medina, S. Pylypenko, M. Wang, K. L. More, N. Kariuki, D.J. Myers, A.Z. Weber, S.A. Mauger, M. Ulsh, K.C. Neyerlin, Dictating Pt-based electrocatalyst performance in polymer electrolyte fuel cells, from formulation to application, ACS Appl. Mater. Interfaces 11 (50) (2019) 46953–46964, https://doi.org/10.1021/acsami.9b17614.

[45] S. Ott, A. Orfanidi, H. Schmies, B. Anke, H.N. Nong, J. Hübner, U. Gernert, M. Gliech, M. Lerch, P. Strasser, Ionomer distribution control in porous carbon-supported catalyst layers for high-power and low Pt-loaded proton exchange membrane fuel cells, Nat. Mater. 19 (1) (2020) 77–85, https://doi.org/10.1038/s41563-019-0487-0.

[46] A. Orfanidi, P.J. Rheinländer, N. Schulte, H.A. Gasteiger, Ink solvent dependence of the ionomer distribution in the catalyst layer of a PEMFC, J. Electrochem. Soc. 165 (14) (2018) F1254.https://iopscience.iop.org/article/10.1149/2.1251814jes/meta

[47] S. So, H. Kang, D. Choi, K.-H. Oh, Tunable aggregation of short-side-chain perfluorinated sulfonic acid ionomers for the catalyst layer in polymer electrolyte membrane fuel cells, Int. J. Hydrogen Energy 45 (38) (2020) 19891–19899, https://doi.org/10.1016/j.ijhydene.2020.05.128.

[48] S.A. Berlinger, S. Garg, A.Z. Weber, Multicomponent, multiphase interactions in fuel-cell inks, Curr. Opin. Electrochem. 29 (2021) 100744, https://doi.org/10.1016/j.coelec.2021.100744.

[49] Z. Fang, M.S. Lee, J.Y. Kim, J.H. Kim, T.F. Fuller, The effect of carbon support surface functionalization on PEM fuel cell performance, durability, and ionomer coverage in the catalyst layer, J. Electrochem. Soc. 167 (6) (2020) 064506, https://doi.org/10.1149/1945-7111/ab7ea3.

[50] T. Mashio, A. Ohma, T. Tokumasu, Molecular dynamics study of ionomer adsorption at a carbon surface in catalyst ink, Electrochim. Acta 202 (2016) 14–23, https://doi.org/10.1016/j.electacta.2016.04.004.

[51] Z. Fang, A.G. Star, T.F. Fuller, Effect of carbon corrosion on wettability of PEM fuel cell electrodes, J. Electrochem. Soc. 166 (12) (2019) F709–F715, https://doi.org/10.1149/2.0231912jes.

[52] X. Zhang, L. Guo, H. Liu, Recovery mechanisms in proton exchange membrane fuel cells after accelerated stress tests, J. Power Sources 296 (2015) 327–334, https://doi.org/10.1016/j.jpowsour.2015.07.063.

[53] T. Muzaffar, T. Kadyk, M. Eikerling, Tipping water balance and the Pt loading effect in polymer electrolyte fuel cells: a model-based analysis, Sustain. Energy Fuels 2 (6) (2018) 1189–1196, https://doi.org/10.1039/C8SE00026C.

[54] D. Damasceno Borges, G. Gebel, A.A. Franco, K. Malek, S. Mossa, Morphology of supported polymer electrolyte ultrathin films: a numerical study, J. Phys. Chem. C 119 (2) (2015) 1201–1216, https://doi.org/10.1021/jp507598h.

[55] A. Kusoglu, Ionomer thin films in PEM fuel cells, in: R.A. Meyers (Ed.), Encyclopedia of Sustainability Science and Technology, Springer New York, New York, NY, 2018, pp. 1–23, https://doi.org/10.1007/978-1-4939-2493-6_1021-2.

4.3   Publication III
Structure and Conductivity of Ionomer in PEM Fuel Cell Catalyst Layers: A Model-Based Analysis

Authors: Wolfgang Olbrich[1,2,3], Thomas Kadyk[1,4], Ulrich Sauter[2], Michael Eikerling[1,3,4], Jeffrey Gostick[5]

[1] Theory and Computation of Energy Materials (IEK-13), Institute of Energy and Climate Research, Forschungszentrum Jülich GmbH, 52425 Jülich, Germany
[2] Robert Bosch GmbH, Corporate Research, 71272 Renningen, Germany
[3] Chair of Theory and Computation of Energy Materials, Faculty of Georesources and Materials Engineering, RWTH Aachen University, 52062 Aachen, Germany
[4] Jülich Aachen Research Alliance, JARA Energy, 52425 Jülich, Germany
[5] Department of Chemical Engineering, University of Waterloo, Waterloo, ON, Canada.

Author contributions: Conceptualization: WO, TK, US, ME, JG; Methodology: WO; Software: WO; Formal analysis: WO; Resources: US, JG; Writing - Original Draft: WO; Writing - Review & Editing: US, TK, JG, ME; Supervision: JG, ME, US, TK; Project administration: US, ME.

Methods and results covered by this article were presented to the scientific community at the *18th Symposium on Modeling and Experimental Validation of Electrochemical Energy Technologies*, held 14.–26.04.2022 in Schloss Hohenkammer, Germany, presentation titled *Proton Conductivity in PEFC Catalyst Layers: Imaging-Supported Modeling* .

Check for updates

OPEN

Structure and conductivity of ionomer in PEM fuel cell catalyst layers: a model-based analysis

W. Olbrich [1,2,3✉], T. Kadyk[1,4], U. Sauter[2], M. Eikerling[1,3,4] & J. Gostick[5]

Efforts in design and optimization of catalyst layers for polymer electrolyte fuel cells hinge on mathematical models that link electrode composition and microstructure with effective physico-chemical properties. A pivotal property of these layers and the focus of this work is the proton conductivity, which is largely determined by the morphology of the ionomer. However, available relations between catalyst layer composition and proton conductivity are often adopted from general theories for random heterogeneous media and ignore specific features of the microstructure, e.g., agglomerates, film-like structures, or the hierarchical porous network. To establish a comprehensive understanding of the peculiar structure-property relations, we generated synthetic volumetric images of the catalyst layer microstructure. In a mesoscopic volume element, we modeled the electrolyte phase and calculated the proton conductivity using numerical tools. Varying the ionomer morphology in terms of ionomer film coverage and thickness revealed two limiting cases: the ionomer can either form a thin film with high coverage on the catalyst agglomerates; or the ionomer exists as voluminous chunks that connect across the inter-agglomerate space. Both cases were modeled analytically, adapting relations from percolation theory. Based on the simulated data, a novel relation is proposed, which links the catalyst layer microstructure to the proton conductivity over a wide range of morphologies. The presented analytical approach is a versatile tool for the interpretation of experimental trends and it provides valuable guidance for catalyst layer design. The proposed model was used to analyze the formation of the catalyst layer microstructure during the ink stage. A parameter study of the initial ionomer film thickness and the ionomer dispersion parameter revealed that the ionomer morphology should be tweaked towards well-defined films with high coverage of catalyst agglomerates. These implications match current efforts in the experimental literature and they may thus provide direction in electrode materials research for polymer electrolyte fuel cells.

Polymer electrolyte fuel cells (PEFCs) will be a key technology of a future sustainable energy ecosystem. At the brink of commercialization, further advances in performance and durability are needed[1]. A major proportion of irreversible performance losses originate in transport processes in the gas diffusion electrodes. This applies to all species involved in the overall fuel conversion, namely oxygen, hydrogen, protons, and electrons as well as water in liquid and vapor state. In earlier stages of fuel cell development, proton conductivity was not as critical as it is in today's high-performing cells. The introduction of perfluorosulfonic acid (PFSA) polymers, such as Nafion, as highly charged electrolytes in the late 1980s[2,3], alleviated the problem of proton supply in the cathode catalyst layer (CCL). However, during the last two decades large improvements of water management, oxygen supply and membrane resistance finally cleared the path to higher current densities and higher specific power output. With this progress, the proton conductivity in the catalyst layer emerged again as a crucial performance bottleneck[4].

The ionomer content in the catalyst layer is a key optimization parameter: on the one hand, increasing the ionomer content increases the proton conductivity; on the other hand, excessive amounts of ionomer will block the pore space and thus impair gas transport[5]. Finding the optimal ionomer content has thus been the subject of several modelling studies[6-10] and experimental efforts[11-13]. An optimal ionomer volume fraction of $\approx$ 30...40% has been reported in the literature[7,8,10,12-14], though the exact value can vary significantly, with a range

[1]Theory and Computation of Energy Materials (IEK-13), Institute of Energy and Climate Research, Forschungszentrum Jülich GmbH, 52425 Jülich, Germany. [2]Robert Bosch GmbH, Corporate Research, 71272 Renningen, Germany. [3]Chair of Theory and Computation of Energy Materials, Faculty of Georesources and Materials Engineering, RWTH Aachen University, 52062 Aachen, Germany. [4]Jülich Aachen Research Alliance, JARA Energy, 52425 Jülich, Germany. [5]Department of Chemical Engineering, University of Waterloo, Waterloo, ON, Canada. ✉email: w.olbrich@fz-juelich.de

1

from 13 to 40% found in commercially available catalyst layers[14,15]. These differences might have their origin in the varying microstructure of the CCL[16]. The optimal ionomer content also depends on operation conditions, catalyst layer thickness and Pt loading[13]. The ionomer content (in relation to Pt/C content) controls the interplay of transport (oxygen, water, and protons) and reaction, and thus can be tuned to optimize this interplay[6,10]. However, the relation between CCL microstructure and proton conductivity is not yet fully understood. Therefore, this work puts a primary focus on ionomer coverage and film thickness in the agglomerated CCL microstructure, which seem to be key parameters shaping proton conductivity. Molecular level structural features matter in this context, as water layer formation and structural ordering could both enhance or impair the proton mobility[17,18].

In conventional CCLs, Pt/C catalyst particles aggregate and are partially covered by a thin ionomer film with $\approx$ 5...15 nm thickness[19,20]. Closer examination of this agglomerate structure and of the ionomer morphology revealed that typically the ionomer film is unevenly distributed[21–24], i.e., its coverage and thickness can vary significantly. Additionally, large ionomer aggregates that are not part of the thin film have been observed[24–26]. These variations in ionomer morphology largely impact the percolation behavior of the ionomer network and thus the proton conductivity of the CCL, as well as the volume fraction and network properties of gas-filled pores needed for oxygen supply[27–29]. The ionomer morphology in the CCL is not only determined by the composition of the ink, but also by Pt loading, type of carbon support, type of ionomer, ink solvent and processing parameters like processing times and thermal treatments[16,30,31].

The understanding of how the ionomer morphology can be tuned and which structures yield an optimal performance remains a subject of ongoing experimental efforts[24,32–35]. At present, fuel cell developers have to optimize the CCL composition and fabrication process individually for every material combination and fuel cell application. Models that correlate the aforementioned variations in microstructure with transport properties and performance could provide much-needed guidance in this process[10,36].

Analytical relations between proton conductivity and CCL composition. Structure- and composition-dependent expressions for the proton conductivity of the CCL often employ semi-empirical power-law relations such as the Bruggeman relation or they are derived from percolation theory. The Bruggeman relation, proposed in 1935[37,38], is widely adopted for transport properties in heterogeneous media and provides a satisfying fit to experimental data in specific applications, e.g., gas diffusion in porous media[39], thermal conductivity of composite materials[40], or magnetic permeability of ferromagnetic composites[41]. It expresses the relative reduction of a transport coefficient in the medium compared to the known bulk value through a simple power law. The semi-empirical relation proposed by Bruggeman implies an exponent of 1.5. This value was also adopted in modeling works for the proton conductivity in PEFC catalyst layers[8,9,42,43]. Other works suggested values of 1.0[44] or 2.0[45,46], leaving the value up to debate and revealing the lack of generality of the approach.

The original approach taken by Bruggeman[37,38] to derive a volume-averaged transport coefficient originally assumed a spherical geometry of primary particles forming the the conductive phase. Hashin and Shtrikman extended Bruggeman's approach to spherical particles covered by a uniform, conductive film[47]. Das et al.[48] applied the coated sphere model of Hashin and Shtrikman to PEFC catalyst layers by introducing a second coating, which represents the pore space between agglomerates, and introduced a dependence on the void fraction in the CL material. Since the approach of Das et al. describes the upper limit of proton conductivity, an additional empiric factor was introduced to account for a potentially lowered conductivity due to effects of ionomer geometry and agglomerate shape, i.e., the proposed correlation could not analytically resolve the dependence on ionomer morphology.

Percolation theory offers another approach to relate the proton conductivity with ionomer content[6,7]. The mathematical fundamentals of percolation theory were originally derived by Broadbent and Hammersley in 1957[49] and form a sound statistical-physical basis to describe transport properties in heterogeneous media[50,51]. Above the percolation threshold, the dependence of proton conductivity on ionomer volume fraction is given by a power-law, with a critical power-law exponent that depends solely on the dimension of the percolating system ($\approx$ 2 in the 3D case), whereas the percolation threshold depends on the the lattice structure or morphology of the continuous phase. In contrast to the Bruggeman relation, percolation theory provides a direct connection between relevant parameters, i.e., critical exponent and percolation threshold, and the microstructure of the material of interest. Eikerling et al.[6] suggested to use an ionomer volume fraction of 0.1...0.2 for the percolation threshold of ionomer in catalyst layers, indicating a high level of connectedness in the ionomer network. Additionally, percolation theory enables the prediction of other structural features, such as the interfacial area of different phases or the relative utilization of a randomly connected phase[10].

A different approach was taken by Liu et al.[52] who derived a relation assuming spherical, cubically packed catalyst particles that are all fully covered by an ionomer film of uniform thickness. To fit the model prediction to their dataset, the authors introduced an adsorbed ionomer volume of I:C = 0.3 and a roughness factor (*rf*) of 1.6. The proposed relation describes the singular dataset considered in their work well, but was of limited applicability to other CCL material combinations. Additionally, the proton conductivity does not converge to the value of bulk ionomer upon increasing the ionomer content. However, as common in the literature, Liu et al.[52] assumed the proton conductivity of the polymer electrolyte membrane to approximate the value of bulk ionomer.

From comparing the experimental findings with available relations for proton conductivity, a clear shortcoming can be identified. Whereas both the Bruggeman relation and percolation theory treat the CCL as an ideal random medium and do not address partial order in the ionomer morphology, the geometry-based relation proposed by Liu et al. cannot fully capture variations in the ionomer morphology. To bridge this gap and reveal essential structural elements in ionomer morphology, the CCL microstructure can be studied using pore-scale simulations.

nature portfolio

2

Image-supported modeling: assisting the analysis of ionomer morphology. The simulation of material microstructures dates back to the 1970s and 1980s when Joshi[53] and Quilibier[54] pioneered the fundamentals of Gaussian processes for stochastic image generation. These early works already outlined the potential of simulations on generated 3D material images to extract transport properties. Stochastic image generation has been applied to PEFC catalyst layers, where multiple works focused on gas and/or vapor transport through the pore space[55–59]. In the following, we will briefly review works that include simulation of proton conductivity of the electrolyte phase.

Sui et al.[60] employed a catalyst layer imitation consisting of spherical carbon particles that were randomly placed and fully coated by an ionomer film of uniform thickness. Since the authors aimed to optimize the CCL composition, the single parameter of interest was the ionomer volume fraction of the CCL. Variations of ionomer morphology were not addressed. Nonetheless, this pioneering work demonstrated how relations derived from pore scale simulations can form the basis for cell optimization with basic electrode models.

In the time between 2008 and 2012, multiple works developed more sophisticated simulation approaches of proton transport properties. Hattori et al.[61] used randomly placed carbon particles and varied the microscopic ionomer thickness and coverage by allowing randomness in the distribution of the ionomer film. They did not evaluate the proton conductivity but calculated the polarisation curve directly through simulation of reactive transport in the 3D model system. From studying variations in ionomer distribution, uniform films with high coverage were found to be most favorable to yield high cell performance. This was rationalized by a favorable connectivity of the electrolyte phase and a high catalyst utilization.

Kim and Pitsch[62] aimed to refine stochastic structure generation and proposed a sphere-based annealing method, which built on a Gaussian field and used two-point correlation functions from experimental CCL images. They found the conductivity to follow a power law with an exponent of 2. Below an ionomer volume fraction of 0.25, simulation results were seen to deviate from the power law. However, the authors did not interpret these results in terms of a percolation threshold.

To describe the incremental self-assembly of the CCL structure during ink stage, Siddique et al.[63] proposed an alternative technique for image generation. At first, random seeds were placed in a volume of 200 nm × 100 nm × 100 nm with 2 nm resolution. Carbon particles agglomerated around the seed points. Subsequently, ionomer was iteratively aggregated around seeds on the carbon particles surfaces. A variation of the I:C ratio revealed a dramatic discrepancy between the Bruggeman relation and simulation results, but the results closely matched the percolation law with percolation threshold of 0.2.

Lange et al.[64] developed an algorithm based on randomly placed spheres and widely varying geometric parameters, such as particle radius and overlap tolerance. Bigger particles and larger overlap, i.e., less tortuous geometries with less curvature of the ionomer film, led to an increased proton conductivity. Thus, the curvature and roughness of agglomerates must be considered as a source of error when running simulations of transport in thin films. In a follow-up work, Lange et al.[65] considered several reconstruction algorithms that did not reveal a significant impact on effective transport properties in most cases. In contrast, the results showed a significant dependence on the assumptions about the ionomer morphology, i.e., whether ionomer uniformly covers catalyst agglomerates or randomly aggregates throughout the catalyst layer.

More recently, Inoue et al.[66] modeled the aggregation of primary carbon particles using an algorithm that emulates particle attraction and repulsion. Two distinct ionomer morphologies were simulated: carbon aggregates coated with ionomer of uniform thickness and partial coverage; and heterogeneously distributed ionomer, where the ionomer resembled a wetting liquid that formed menisci with uniform curvature. Both cases exhibited a power-law behavior at low I:C ratios ≤ 0.5 with an exponent of 1.8. In the case of uniform curvature, a different power-law was observed with an exponent of 3 at I:C > 0.5, which was linked to inter-agglomerate bridging of the ionomer phase. Since ionomer coverage evolved over I:C ratio in a non-linear manner, the impact of different ionomer film thickness, coverage and content could not be fully disentangled.

The question arises whether the ionomer structure can be resolved through reconstruction from experimental tomographic images. Lange et al. demonstrated that a resolution of 2 nm in a cubic volume of $(200 \text{ nm})^3$ gives accurate results for finite-element steady-state proton transport simulations at reasonable computational costs[64,67]. 3D imaging techniques like nano-CT[21,68] and FIB-SEM[55,67,69,70] reach a resolution of 10 to 100 nm, which is sufficient for visualizing the ionomer morphology on the agglomerate level, but cannot reliably resolve finer details, such as ionomer film thickness. Additionally, carbon and ionomer have similar densities, thus only a binary image resolving solid and void space can be obtained. However, exchanging the protons of the sulfonic headgroups with Cs^+ ions creates sufficient contrast to resolve the ionomer within the CCL. Using this technique, Komini Babu et al.[21] reported images from CCLs with three different ionomer loadings (35 wt%, 50 wt%, 60 wt%) and observed changes in ionomer morphology that affected the proton conductivity in simulations and the cell performance in experiments. Images that resolved voxels of 16 nm^3 were used to run simulations of proton transport, partially resolving the fine structure of agglomerates and thin films. At the lowest ionomer content, poorly connected aggregates formed, whereas a thick uniform film on the catalyst aggregates formed with increasing amount of ionomer. In a recent study, Goswami et al.[71] applied a similar approach to PEFC catalyst layers degraded by carbon corrosion, extending the perspective on ionomer morphology to be subject to changes during the cell life-cycle, which consequently might evoke changes in proton conductivity during operation.

Simulations based on experimentally obtained images allow studying only a few points in the parameter space of ionomer morphology. Works discussed above have demonstrated that generating synthetic 3D images provides an alternative pathway to investigating the ionomer morphology since a wide range of structural parameters can be simulated. However, a systematic study on the relation between ionomer structure and proton transport could not be found in the literature.

In this work, we have developed analytical relations between ionomer morphology and proton transport properties in CCLs. To first understand how the CCL microstructure affects proton transport, we have applied

89

stochastic image generation for a wide range of ionomer coverage and film thickness and simulated the effective proton conductivity. Subsequently, the complexity of simulation results has been reduced by resorting to percolation theory to yield analytical relations between decisive structural features in ionomer morphology and the effective proton conductivity of the CCL.

Model and methodology

This work describes the structure of a conventional CCL, in which primary Pt/C particles aggregate and are partially covered by a skin-like ionomer film. The coverage and thickness of the ionomer film can vary significantly, albeit being accessible in experiment[72,73], rendering them suitable parameters for modelling works.

The model distinguishes two pore size domains, following the classification from previous modeling works[6,10,74,75]. The carbon support contains a certain volume fraction of primary pores (1 to 10 nm diameter), whereas secondary pores (10 to 100 nm diameter) form the space between agglomerates[76]. The ionomer is deposited at the agglomerate interface in secondary pores and is assumed to be excluded from primary pores since the ionomer macromolecules are too big to enter.

Correlations between the proton conductivity and the ionomer morphology have been established in two steps (see Fig. 1). First, a 3D image of the CCL structure has been generated based on a synthetic binary image. The phases of ionomer, carbon and pore space have been stochastically reconstructed. The ionomer morphology depends on ionomer coverage and thickness. Next, a steady-state finite-element simulation of proton conductivity within the ionomer phase has been conducted and percolation properties have been evaluated. We have used PoreSpy, an open source software package for Python[77], to run image generation, manipulation, evaluation and conductivity simulation. All functions and routines referred to in the following are included in PoreSpy unless denoted otherwise. To support the analysis of the simulation results, we have used a composition model for the CCL from our previous work[78].

CCL image generation. Image generation begins by creating a binary image that distinguishes between a condensed agglomerate phase, which lumps together carbon, catalyst, primary pores and ionomer, and the secondary pore space. In an operational catalyst layer, water will condense in primary pores. Depending on the operational conditions, the secondary pores can be flooded as well. Water renders the catalyst layer active in the first place, as it serves as reaction medium and proton shuttle. The ionomer also absorbs water, which mobilizes protons provided by the ionomer, thus enabling a high proton conductivity. Therefore, we consider the ionomer phase to include water. Bulk-like liquid water condensed in primary and the secondary pores is not resolved, since it only marginally contributes to the proton conductivity as the proton concentration is several orders of magnitude lower compared to the ionomer electrolyte phase[79].

Cubic volume elements were used with a length conversion factor of $1\,vx = (2\,nm)^3$, adopting the proposed resolution from Lange et al.[64], which was found to give numerically convergent results also in this work (see Fig. S1 in the supplementary material). Binary tomographic images of CCL materials reported in the literature resemble random heterogeneous media in which the local thickness of the solid phase exhibits a Gaussian size distribution[70,80,81], with no additional stochastic features. Therefore, our work has employed as well as simple Gaussian field without further features, such as 2-point-correlations. Further, Lange et al.[64,65,67], demonstrated that the choice of reconstruction algorithm has a limited impact on simulation results, if essential structural features of the CL structure are correctly captured (agglomerated Pt/C particles, ionomer film formation). For this purpose, PoreSpy is the most suitable tool as it allows close control of generated geometries. The reconstruction
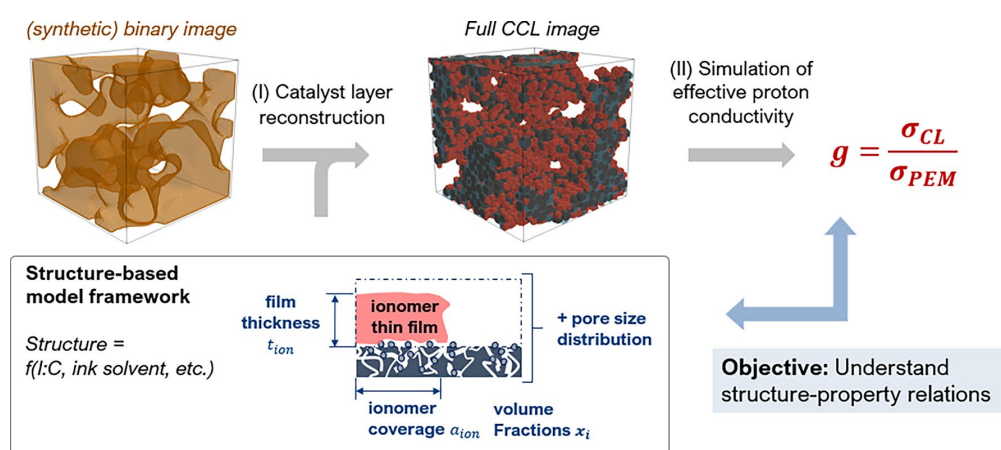

Figure 1. The image generation workflow of the model builds on binary tomografic images, which are combined with information from a structure based model[78]. Calculation of proton conductivity is performed subsequently with the objective to understand underlying structure-property relation of the CCL material.

algorithm presented in the following employs the structural picture of CCL microstructure as supported by the experimental literature[19,76], consisting of the following assumptions:

1. Carbon support and ionomer form an agglomerates structure.
2. Ionomer does not enter the intra-agglomerate pore space.
3. Ionomer forms a thin film of uniform thickness.
4. The spatial distribution of the solid structure is a Gaussian field, i.e., has no local ordering.
5. Ionomer is randomly distributed in finite-sized building blocks (of 'patches') on the agglomerate surface.

Transferring this understanding of CCL microstructure to this work, the `PoreSpy` software has been used to generate images of agglomerated structures by applying a Gaussian blur filter to a random noise field. This step has been followed by applying a direct threshold to obtain a desired volume fraction of agglomerates x_{agg}. The resulting 'agglomerate phase' served as a template for the reconstruction of the agglomerated structure. This procedure has been implemented as the `blobs` function in `PoreSpy`. The standard deviation σ_b for the kernel of the Gaussian filter was adjusted to match the desired average agglomerate size r_{agg}, which is controlled by the input parameter B in the `blobs` function,

$$\sigma_b = \frac{L}{40\,B} \quad \text{and} \tag{1}$$

$$B = \frac{L}{40\,r_{agg}\,(1 - \ln(1 - x_{agg}))}. \tag{2}$$

The obtained images were smoothed using `binary_opening` from the `scipy.ndimage` package and a sphere with with a radius of 3 vx as structural element. An exemplary image is depicted in Fig. 2(1).

To reconstruct the internal structure of agglomerates, spherical carbon particles with radius r_{carbon} have been placed inside the agglomerate phase (see Fig. 2(2)). The routine `pseudo_electrostatic_packing` has been used to fill the agglomerate space with carbon particles. This packing algorithm mimics the effect of an electrostatic field pulling particles to the inside of the agglomerate phase. Running an Euclidean distance transform over the agglomerate phase returns a scalar value for each voxel that is interpreted as a measure for the 'field strength'. Carbon particles have been iteratively placed at the point of maximum field strength that is not occupied by other particles. For further details of the algorithm we refer the reader to the documentation of `PoreSpy`[77]. Carbon particles were allowed to overlap by a third of the carbon particle radius and protrude into the secondary pore space by half of their radius. This procedure of reconstructing the carbon particles was adopted from a preceding work of Sadeghi et al.[82]. To reconstruct the primary pore space, the space between carbon particles was filtered for pore size using `local_thickness` and applying a threshold r_1. Pores below that threshold are defined as primary pores and lie entirely inside the agglomerate phase (see Fig. 2(3)). All remaining void space between the agglomerates is defined as secondary pore space. In the following, the combined phase of carbon particles and primary pores replaces the agglomerate phase, rejecting the template agglomerate phase from the image. This distinction of primary and secondary pores in the phase image serves to identify the deposition spots of ionomer on the interface of agglomerate and secondary pore space.

The deposition of ionomer on the outer surface of agglomerates employs mathematical morphology operations for binary images provided by the `sciPy` package[83]. A binary dilation of one voxel has been applied to the agglomerate phase, defining the agglomerate surface. From the resulting set of voxels, a random position was picked to place a piece of ionomer. An ionomer patch was generated from the binary product of a sphere with radius r_{ion} and the set of voxels identifying the agglomerate surface. An ionomer 'patch' was then created by running another binary dilation on the ionomer film thickness t_{ion} on the picked subset marking the ionomer surface element to be covered with ionomer. The resulting building block of ionomer was added to the ionomer phase. The result is exemplary illustrated in Fig. 2(4). Through summation of the voxels in the intersection of the ionomer phase and the voxels identifying the agglomerate surface, the ionomer coverage a_{ion} has been estimated. It is defined as the ratio of surface area covered by ionomer to the agglomerate surface,

$$a_{ion} = \frac{A_{covered}}{A_{agg}}. \tag{3}$$

The process has been repeated until a predetermined ionomer coverage was reached.

The final image was checked for consistency by evaluating the volume fraction of each phase and the size distribution of pores, agglomerates and ionomer. The volume fractions have been calculated as the ratio of the sum of the voxels in one phase to the total voxel count of the image,

$$x_i = \frac{\sum \mathrm{vx}_i}{L^3}. \tag{4}$$

The size distributions of pores, ionomer and agglomerate were obtained from running the function `local_thickness` on each phase which assigns each voxel the value of the largest sphere that could fit in the local pore that includes the voxel. The function `pore_size_distribution` returns the histogram data for the distribution of pore sizes, ionomer film thicknesses and agglomerate sizes. Finally, the image was saved to a `.vtk` file and visualized in `ParaView`. All parameters used for the image generation workflow are listed in Table 1.
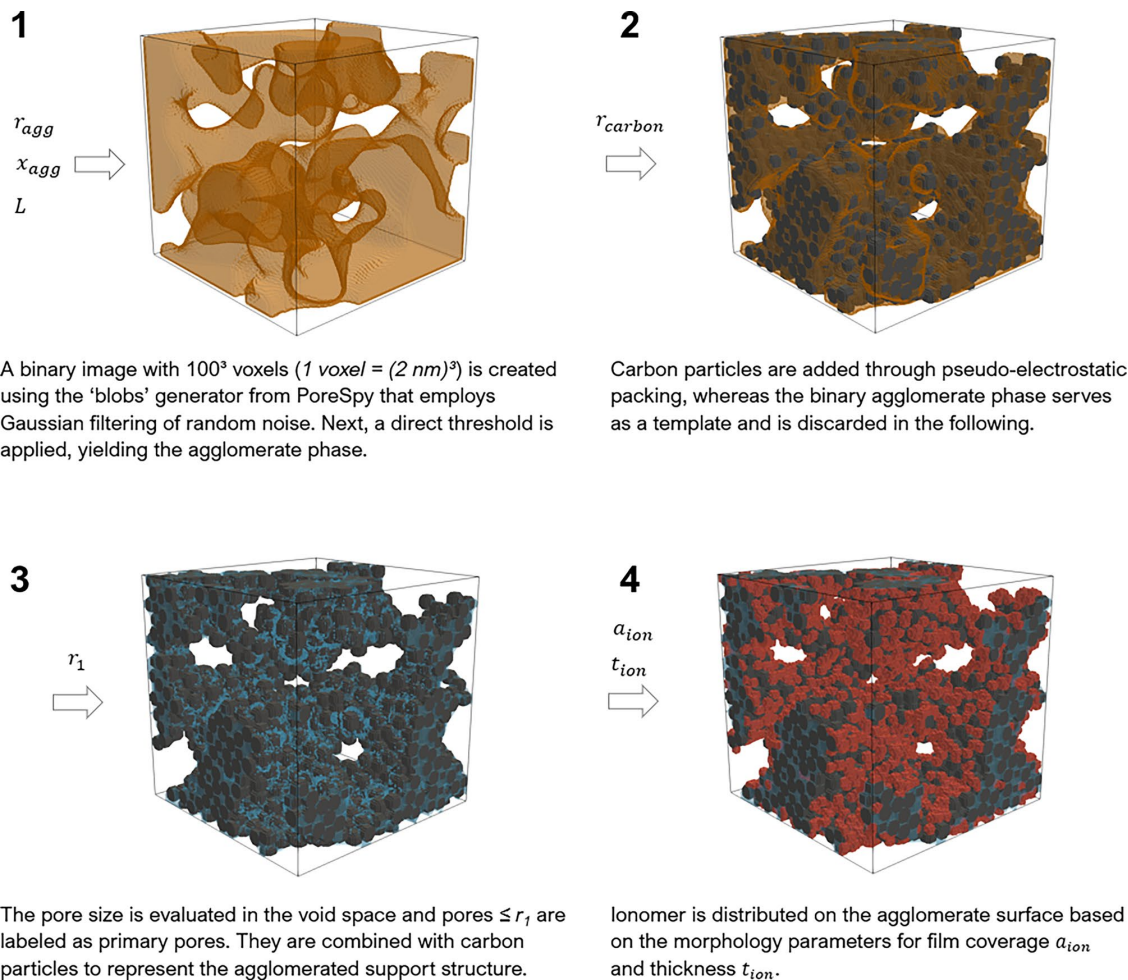
91

1

r_{agg}
x_{agg}
L

A binary image with 100³ voxels (*1 voxel = (2 nm)³*) is created using the 'blobs' generator from PoreSpy that employs Gaussian filtering of random noise. Next, a direct threshold is applied, yielding the agglomerate phase.

2

r_{carbon}

Carbon particles are added through pseudo-electrostatic packing, whereas the binary agglomerate phase serves as a template and is discarded in the following.

3

r_1

The pore size is evaluated in the void space and pores $\leq r_1$ are labeled as primary pores. They are combined with carbon particles to represent the agglomerated support structure.

4

a_{ion}
t_{ion}

Ionomer is distributed on the agglomerate surface based on the morphology parameters for film coverage a_{ion} and thickness t_{ion}.

Figure 2. The workflow for image generation follows four steps: (**1**) generation of a binary image, based on tomographic data, (**2 + 3**) reconstruction of the agglomerate structure, resolving carbon particles and primary pores, and (**4**) deposition of ionomer onto the agglomerate surface.

Ionomer coverage and ionomer film thickness are the most sensitive parameters and are of primary interest in this work. All other parameters were tested for their sensitivity as well, as reported in Fig. S2 in the supplementary material.

Calculation of proton conductivity. The proton conductivity of the obtained CCL images has been evaluated by solving the following steady-state equation in voxel domains occupied by ionomer,

$$\nabla \cdot (-\sigma_{ion} \nabla \phi) = 0. \tag{5}$$

The function `tortuosity_fd` was used to compute the proton conductivity through the ionomer phase using a finite difference approach, similar to the widely used `TauFactor` software[84]. The function operates by applying boundary conditions automatically for a specified direction, i.e., proton flux enters the volume through one face of the cube and leaves through the opposite face. At the inlet and outlet face of the cube a constant potential and all other faces a zero-flux condition was applied,

$$\phi_{in} = const., \quad \phi_{out} = const. \quad \text{with} \quad \phi_{in} > \phi_{out} \quad \text{and} \tag{6}$$

$$n_\perp \cdot \nabla \phi = 0 \text{ at all other faces.} \tag{7}$$

The function returns the relative conductivity *g*,

92

Parameter	Value	Unit
L	200	nm
x_{agg}	0.5	–
r_{agg}	20	nm
r_{carbon}	10	nm
r_1	6	nm
r_{ion}	10	nm
a_{ion}	0.5	–
t_{ion}	10	nm

Table 1. Base case parameters for stochastical CCL image generation.

$$g = \frac{\sigma_{CL}}{\sigma_{PEM}}, \tag{8}$$

which is normalized to the conductivity of the polymer electrolyte membrane, σ_{PEM}, a known property[4,52]. By using a dimensionless proton conductivity, this work aligns with previous works[4,85] and allows comparing different operating conditions and ionomers with different molecular structure, ion exchange capacity or molecular weight.

CCL composition model. To discuss the evolution of ionomer morphology over a range of I:C ratios, we applied the composition model developed previously in Ref.[78]. It accounts for the dependence of ionomer morphology on ink and process parameters via the initial film thickness, t_0, and a dispersion parameter, k_A. The relations for ionomer film coverage and thickness are

$$a_{ion} = 1 - \exp\left(-k_A x\right) \quad \text{and} \tag{9}$$

$$t_{ion} = \frac{V_{2,0}}{A_2} \frac{1 - \exp(-k_V\, x)}{1 - \exp(-k_A\, x)}, \tag{10}$$

where x denotes the dimensionless ionomer volume per secondary pore volume in an ionomer-free reference sample,

$$x = \frac{m_{I:C}}{\rho_{ion} V_{2,0}} \tag{11}$$

and k_V depends on t_0 and the secondary pore space geometry via A_2 and $V_{2,0}$,

$$k_V = t_0 k_A \frac{A_2}{V_{2,0}}. \tag{12}$$

As the ionomer film partially occupies the secondary pore space, the remaining 'free' secondary pore volume is obtained as

$$V_{2,free} = V_{2,0}\left(1 - \exp(-k_V\, x)\right). \tag{13}$$

The volume of the ionomer film is given by

$$V_{ion} = \frac{A_2}{V_{2,0}} a_{ion} t_{ion}. \tag{14}$$

The difference between film volume and total ionomer volume used to fabricate the CL,

$$V_{ex} = \frac{m_{I:C}}{\rho_{ion}} - V_{film}, \tag{15}$$

constitutes 'excess' ionomer, which forms large aggregates. Volume fractions are defined as follows to perform the analysis of the CL composition,

$$x_i = \frac{V_i}{\sum_i V_i} \quad \text{with } i \in \{2,\ agg,\ ion,\ ex\}. \tag{16}$$

Here, the agglomerate volume is a sum over carbon and primary pores,

$$V_{agg} = 1/\rho_{carbon} + V_1. \tag{17}$$

The fraction of total ionomer volume $x_{ion,total}$ is given as the sum of ionomer film volume and excess ionomer volume,

7

$$x_{ion,total} = x_{ion} + x_{ex}. \tag{18}$$

Table 2 lists values used for the parametrization of the composition model are listed.

Extraction of reference data from the literature. We collected literature data for proton conductivity of CLs from various sources listed in Table 3. If reported, the respective value of σ_{PEM} was adopted as the reference value for the dimensionless proton conductivity g. If not reported, the proposed correlation for PEM conductivity from Gerling et al. [4] was applied to obtain the value of σ_{PEM} for the respective operating conditions, i.e., relative humidity and temperature, used in a particular literature source,

$$R_{PEM} = 1.2 \, RH^{-1.44} \exp\left(\frac{7.0 \text{ kJ mol}^{-1}}{RT}\right) [\text{m}\Omega \text{ cm}^2] \quad \text{and}$$

$$\sigma_{PEM} = \frac{18 \, \mu\text{m}}{R_{PEM}}.$$

Liu et al. [52] demonstrated that for a correct description of the dependence of g on x_{ion}, the water uptake and the swelling of ionomer need to be taken into account. Thus, if not already done in the respective source, we calculated the wet ionomer volume fraction x_{ion} from the data for the dry ionomer volume fraction $x_{ion,dry}$, using the correlations proposed by Liu et al.[52],

$$\lambda = \left[1 + 0.2325 \, RH^2 \, \frac{T - 303K}{303K}\right] (14.22 \, RH^3 - 18.92 \, RH^2 + 13.41 \, RH) \tag{19}$$

$$x_{ion} = x_{ion,dry}\left(1 + \frac{\rho_{ion,dry}}{\rho_W} \frac{\lambda M_W}{EW}\right), \tag{20}$$

where ρ_W and $\rho_{ion,dry}$ denote the densities of water ($\approx 1 \text{ g cm}^{-3}$) and dry ionomer ($\approx 2 \text{ g cm}^{-3}$), and M_W is the molecular weight of water ($= 18 \text{ g mol}^{-1}$). For the EW the reported value of the ionomer value was applied. If not reported, $EW = 1000 \text{ g mol}^{-1}$ was assumed.

In some references, only the I:C ratio was reported. In such cases, the ionomer volume fraction was estimated from other CCL data, e.g., CCL thickness, mass loading and densities of ionomer and carbon or the CCL porosity.

Parameter	Value	Unit
$V_{2,0}$	0.8	$\text{cm}^3/\text{g}_{carb}$
V_1	0.2	$\text{cm}^3/\text{g}_{carb}$
A_2	20	$\text{m}^2/\text{g}_{carb}$
t_0	{4, 6, 8}	nm
k_A	{2, 3, 5}	–
ρ_{ion}	2	g/cm^3
ρ_{carbon}	2	g/cm^3

Table 2. Parameters to predict the ionomer morphology as a fuction of ionomer content. The parameters t_0 and k_A allow analyzing the impact of ink processing.

Reference	Method to measure σ_{CCL}	Reference value for σ_{bulk}	Ionomer content information	Relative humidity RH	Temperature T	Ionomer used
Liu et al.[52]	EIS	Provided as g	As x_{ion}	35%, 50%, 75%, 122%	80 °C	Nafion 1050 EW, Nafion 850 EW
Yakovlev et al.[12]	EIS	120 mS cm⁻¹, estimated	As I:C	100%	60 °C	Nafion 1100 EW
Boyer et al.[44]	DC	100 mS cm⁻¹, provided	As x_{ion}	100%	50 °C	Nafion 960 EW
Suzuki et al.[86]	EIS	89 mS cm⁻¹, estimated	As x_{ion}	100%	Room temperature	Nafion, no EW reported
Du et al.[87]	DC	300 mS cm⁻¹, provided	As x_{ion}	100%	80 °C	Nafion, no EW reported
Modestov et al.[79]	EIS	7 mS cm⁻¹, provided	As I:C	100%	Room temperature, 22–25 °C	Nafion, no EW reported
Havránek and Wipperman[88]	EIS	120 mS cm⁻¹, provided	As x_{ion}	Flooded	40 °C	Nafion, no EW reported

Table 3. Sources in literature for experimental data correlating CCL proton conductivity with ionomer content.

94

Typically, the proton conductivity can be determined from electrochemical impedance spectroscopy (EIS) measurements. The CCL proton conductivity is extracted from EIS spectra by fitting a transmission line model or equivalent circuit model. However, some sources obtained the proton conductivity through DC measurements. These different methods can give diverging results under low humidity conditions. Qi et al.[85] proposed that AC measurements, such as EIS, include more tortuous and dead-ended pathways. Under humid conditions, the discrepancy is diminished as condensated water provides bridging pathways that lower the apparent tortuosity. High humidity was considered in all data reported here, thus a divergence between AC and DC methods is not suspected in the dataset.

Results

In the following, firstly, we review various sets of literature data and discuss the observed trends. Secondly, we present a parameter study to understand these trends and identify the essential structural elements that determine the proton conductivity. Thirdly, we derive a modified approach based on percolation theory that accounts for insights from simulations of proton conductivity. In the fourth step, implications of our results for CCL fabrication and the prospects of the approach to guide the design of CCLs with tailored properties will be discussed.

Literature data and classical relations for proton transport. The selected datasets for ionomer content x_{ion} and relative conductivity g are plotted in Fig. 3, together with relations proposed in the literature. The Bruggeman relation with an exponent of $\alpha = 1$ roughly fits the data from Boyer et al.[44], which also sets the limit for the highest reported values of relative conductivity. Assuming that the proton conductivity of the CCL should not be higher than σ_{PEM}, values appearing significantly above this limit should not be possible. Other datasets (Suzuki et al.[86], Yakovlev et al.[12], Havránek and Wipperman[88], Du et al.[87]) scatter around a classical Bruggeman relation with $\alpha = 1.5$.
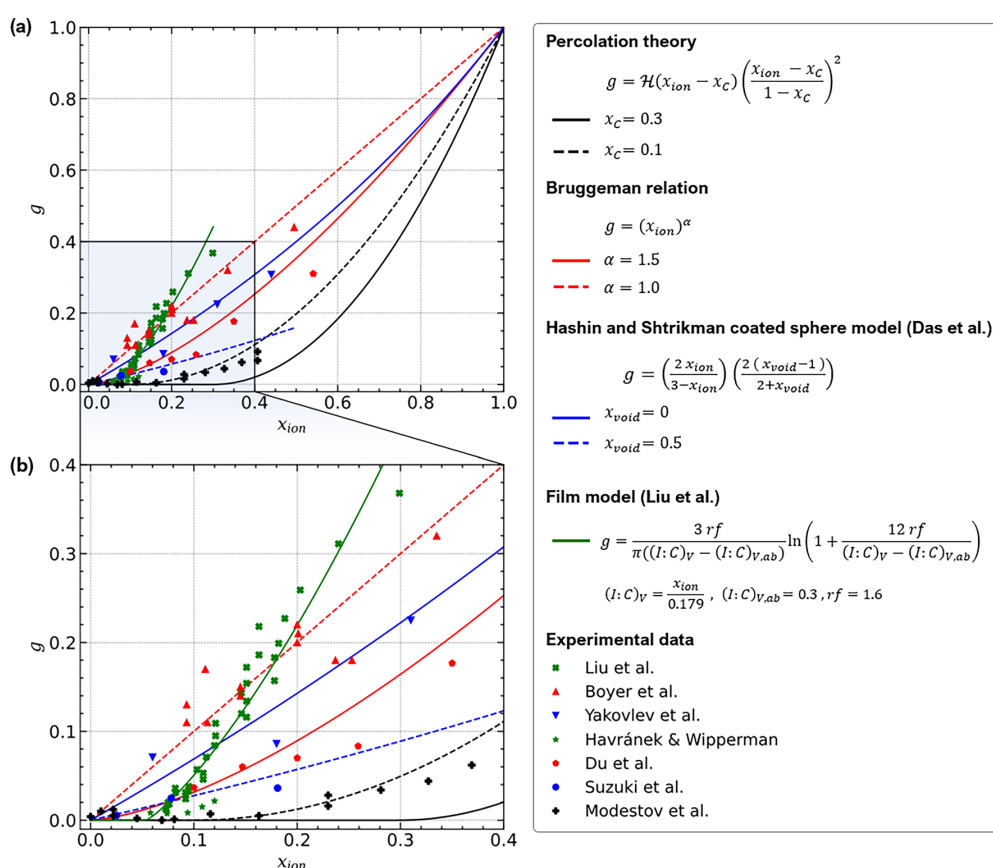
Figure 3. Comparison of literature data[12,44, 52,79,86–88] for proton conductivity and available relations for heterogeneous random media (Bruggeman relation, percolation theory, Hashin and Shtrikman coated sphere model proposed by Das et al.[48] and spherical film model proposed by Liu et al.[52]). Please note that the original equation provided in Ref.[48] has been rearranged for the sake of clarity.

95

Datasets of Liu et al.[52], Havránek and Wipperman[88], and Modestov et al.[79] are compatible with a percolation threshold of $x_c \approx 0.1$. The dataset from Modestov et al.[79] follows a percolation law with this percolation threshold and a critical exponent of 2. The thin-film model of Liu et al.[52] describes their own dataset well. However, the model is physically inconsistent since it predicts relative conductivities $g > 1$ for $x_{ion} \to 1$, where as g must approach 1 from below.

Overall, the cited literature data do not exhibit a unique relation between g and x_{ion}. The reason might be difference in fabrication approaches and conditions that result in different ionomer morphologies.

Simulation results. To unravel the relations between proton conductivity and ionomer content, we have conducted a parameter study for ionomer coverage a_{ion} and film thickness t_{ion}. The results for g are plotted over x_{ion} in Fig. 4a. The highest values for g are obtained for morphologies with large ionomer coverage, $a_{ion} > 0.8$. In this case, g scales almost linearly in both t and x_{ion} for small ionomer contents. Extrapolation towards $x_{ion} = 0$ indicates a vanishing percolation threshold. Please note that our simulations could not cover the range $0\text{ nm} \leq t_{ion} < 4\text{ nm}$ due to the limited resolution of the generated images. A film represented by only one voxel in thickness would disconnect on the curved surface of the agglomerates and would give a non-physical numerical fragment. Additionally, films thinner than 5 nm have been rarely observed in literature. Hence, the resolution chosen in this work (2 vx or 4 nm) can be considered adequate.

A different picture emerges for scenarios where $a_{ion} < 0.5$. A percolation threshold is evident around $x_{ion} \approx 0.15$. Below this threshold, the simulation results indicate very low proton conductivity. Where the threshold is exceeded, the conductivity scales with a power-law behavior with exponent $\alpha \approx 2$. The intermediate cases of moderate ionomer coverage interpolate between the limiting cases of high and low ionomer coverage.

The underlying structural pictures explaining the simulation results are illustrated in Fig. 4b (A)–(D). In the case of a thin film (A), percolation on the agglomerate surface governs proton conductivity. Oppositely, at low coverage and high thickness, randomly placed coarse ionomer pieces connect (B), leading to a situation that resembles 3D continuum percolation. The intermediate cases (C) have a moderate ionomer coverage, thus percolation on the agglomerate surface plays a role, but also some random connectivity of ionomer across the inter-agglomerate space occurs. All three cases converge with increasing amount of ionomer into case (D). If all volume not already occupied by Pt/C agglomerates is filled with ionomer no variation in the morphology is possible, hence g converges into a single value, as observed in the simulation results.

To analyse the impact of the support structure, in Fig. 5a the volume fraction of the agglomerate, x_{agg}, was varied between 0.1 and 0.9, while the ionomer film thickness was held constant at $t_{ion} = 10$ nm. The simulation was repeated for $a_{ion} = \{0.4,\ 0.6,\ 0.7,\ 0.9\}$. For $x_{agg} = 0.3 \dots 0.7$, secondary pore space is mostly open, i.e., pathways reaching through the whole CL exist. In the same range, the agglomerate phase is continuous as well, as illustrated in Fig. 5c. If both phases provide continuous pathways, then the surface of the agglomerate-pore
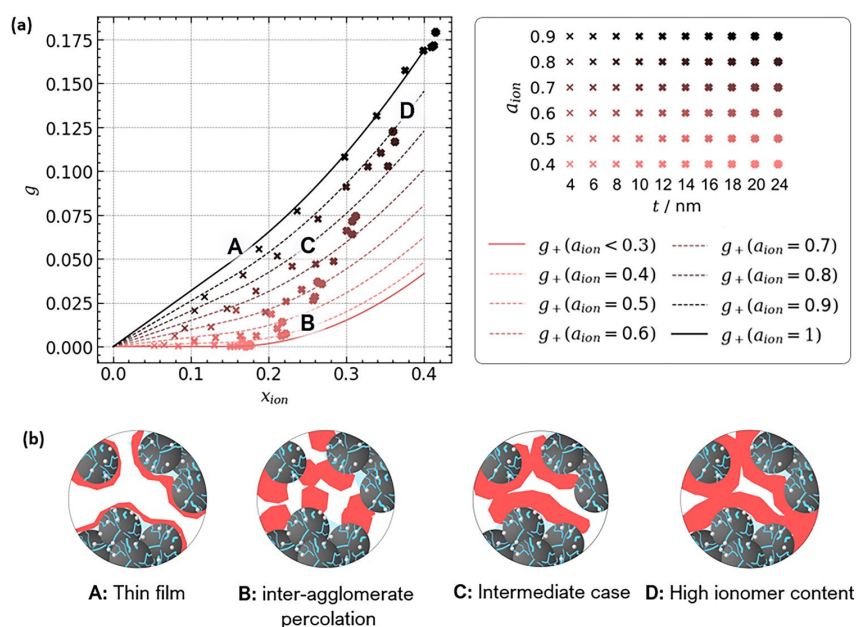
Figure 4. (**a**) Simulation results from variation of ionomer coverage a_{ion} and thickness t. The agglomerate volume fraction was held constant ($x_{agg} = 0.5$). The proposed relation based on percolation theory is plotted as well. (**b**) Four cases of ionomer morphology can be identified and their structural images are illustrated.

96
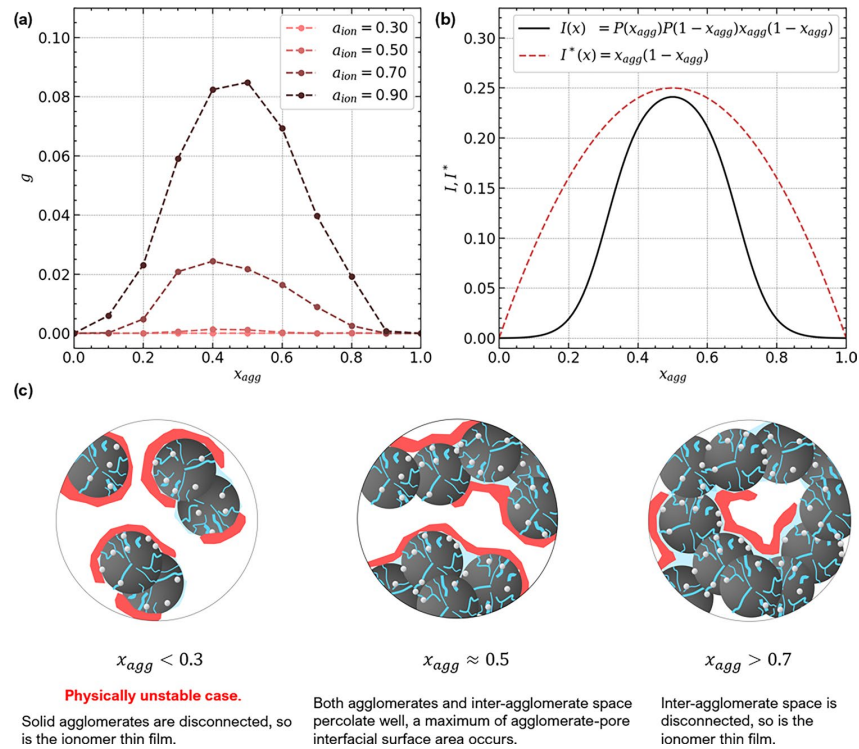
Figure 5. (**a**) Simulation results of proton conductivity for the variation of x_{agg} and ionomer coverage a_{ion}. Ionomer film thickness was held constant ($t = 10$ nm). (**b**) The observed trend can be described using Eq. (23) for the percolation interfacial surface area between agglomerates and secondary pores. (**c**) The underlying structural images are illustrated.

interface is also well-connected and allows pathways for proton conductivity across the CL. Note that a structure with $x_{agg} < 0.3$ would be physically unstable, since agglomerates would be largely disconnected.

When x_{agg} exceeds 0.7, secondary pores become closed and disconnected and the proton conductivity declines steeply. Between these two boundaries, g exhibits a maximum, whose height increases with a_{ion} above ≈ 0.4. Below that value, no closed path for proton transport is formed by the ionomer film deposited on the agglomerate-pore interface. This implies two requirements for high high proton conductivity: not only the agglomerate-pore interface must provide a well-connected network; also the ionomer coverage must be sufficiently high for the ionomer to percolate.

Analytical relations for proton conductivity. The previous discussion has shown that the proton conductivity depends on the surface density of agglomerate/pore interface per CCL volume. This finding allows to derive a first analytical approach to describe the simulation results. The percolation theory approach for the interface density $I(x_A, x_B)$ in a binary mixture can reproduce the trend in x_{agg} (see Fig. 5b),

$$I(x_A, x_B) = x_A P(x_A) x_B P(x_B),\qquad(21)$$

where x_A and x_B denote the percolating phases in an binary continuum and $P(x)$ the percolation probability, represented by a sigmoid function,

$$P(x) = \frac{1}{1 + \exp\left(\frac{-(x-x_c)}{b}\right)}\qquad(22)$$

with $b = 0.01$ and $x_c = 0.3$. As the conductivity scales with the interfacial surface area between agglomerate and the complementary phase of pores and ionomer, we replace x_A with x_{agg}. Thus, x_B becomes $1 - x_{agg}$, yielding

$$g_{film} \sim I(x_{agg}) = x_{agg} P(x_{agg})(1 - x_{agg}) P(1 - x_{agg}).\qquad(23)$$

Further, simulation results indicate that for thin films g scales with a power-law in ionomer coverage. Therefore, a percolation law for conductivity as a function of ionomer coverage a_{ion} is applied,

$$g_{film} \sim \mathcal{H}(a_{ion} - a_c)\left(\frac{a_{ion} - a_c}{1 - a_c}\right)^2. \tag{24}$$

Here, $\mathcal{H}$ represents the Heaviside step function and a_c the percolation threshold. A linear scaling of g with film thickness has been observed in simulations,

$$g_{film} \sim t_{ion}. \tag{25}$$

Combining Eqs. (23), (24) and (25) yields an analytical relation for the proton conductivity in thin films,

$$g_{film} = \tau_{agg} \frac{A_{agg}}{V_{CL}} I(x_{agg}) \mathcal{H}(a_{ion} - a_c)\left(\frac{a_{ion} - a_c}{1 - a_c}\right)^2 t_{ion}, \tag{26}$$

where $\frac{A_{agg}}{V_{CL}}$ is a scaling factor that accounts for the total agglomerate surface per CCL volume. It has the units of an inverse length and depends on agglomerate size. The simulation results for thin films revealed that the surface to volume ratio of a cylindrical geometry can be applied,

$$\frac{A_{agg}}{V_{CL}} = \frac{2}{r_{agg}}. \tag{27}$$

Of course, the agglomerate phase has no cylindrical geometry. However, when the local thickness is evaluated by finding the largest sphere to fit, one could span an approximately circular perimeter and apply a differential cylindrical volume element with $V = \pi r_{agg}^2 dL$ and $A = 2\pi r_{agg} dL$.

If the ionomer film is sufficiently thin, x_{ion} can be calculated from t_{ion} and a_{ion},

$$\begin{aligned} x_{ion} &= I^*(x_{agg}) \frac{A_{agg}}{V_{CL}} a_{ion} t_{ion} \\ &= I^*(x_{agg}) \frac{2}{r_{agg}} a_{ion} t_{ion}. \end{aligned} \tag{28}$$

Here $I^*(x_{agg})$ indicates the same interfacial factor as $I(x_{agg})$ in Eq. (23), but includes the non-percolating interfacial area. Thus, the factors $P(x)$ and $P(1 - x)$ are dropped. Still, $I^* \approx I$ in $x_{agg} = 0.3...0.7$. Anyway, values outside this range are not of relevance. In a CL with $x_{agg} < 0.3$ the mechanical suppport collapses, thus such a CL is unphysical; at $x_{agg} > 0.7$ the pore volume closes and does not provide percolation pathways.

The additional factor τ_{agg} in Eq. (26) accounts for the tortuosity of the curved agglomerate surface. Assuming a spherical curvature of the smoothed Gaussian field used in this work, $\tau_{agg} = \frac{1}{\pi}$ was chosen and matches the simulation results.

When Eqs. (26) and (28) are combined, the factors $I(x)\frac{A_{agg}}{V_{CL}}$ cancel out, yielding an expression for g_{film}, which solely depends on x_{ion} and a_{ion},

$$g_{film} = \frac{1}{\pi}\mathcal{H}(a_{ion} - a_c)\left(\frac{a_{ion} - a_c}{1 - a_c}\right)^2 \frac{x_{ion}}{a_{ion}}. \tag{29}$$

In scenario (C) of Fig. 4, a thin film does not form and connectivity establishes across the inter-agglomerate space. The volume fraction of the inter-agglomerate space is defined as $x_2 = 1 - x_{agg}$. An adapted percolation law can be applied, accounting for the connectivity of ionomer in the secondary pore space,

$$g_2 \sim \mathcal{H}(x_{ion}/x_2 - x_c)\left(\frac{x_{ion}/x_2 - x_c}{1 - x_c}\right)^2. \tag{30}$$

In Eq. (30) the ionomer volume fraction in the inter-agglomerate space is decisive for establishing percolating pathways. Further, g_2 scales with the connectivity of the inter-agglomerate space,

$$g_2 \sim \mathcal{H}(x_2 - x_c)\left(\frac{x_2 - x_c}{1 - x_c}\right)^2, \tag{31}$$

where the inter-agglomerate volume fraction x_2 is used to describe percolation across the catalyst layer volume. Merging Eq. (30) with Eq. (31) yields the analytical expression for g_2 as a function of x_{ion} and x_2,

$$g_2 = \mathcal{H}(x_{ion}/x_2 - x_c)\left(\frac{x_{ion}/x_2 - x_c}{1 - x_c}\right)^2 \mathcal{H}(x_2 - x_c)\left(\frac{x_2 - x_c}{1 - x_c}\right)^2. \tag{32}$$

If $x_{ion} \to x_2$, i.e., all secondary pore volume is replaced by ionomer, Eq. (32) converges to a percolation law for random 3D media.

The expressions for g_{film} and g_2 describe the limiting cases where solely thin films on the agglomerates or inter-agglomerate connections control the conductivity. However, for the majority of ionomer morphologies, an intermediate behavior will occur, i.e., the contributions from the thin film and inter-agglomerate percolation will superpose in a random network type fashion. Thus, the effective conductivity can be anything between a series of resistors and a parallel circuit. The highest proton conductivity conceivable, g_+, is the sum of both contributions, assuming ideal parallel proton transport pathways,

98

$$g_+ = g_{film} + g_2. \tag{33}$$

This expression is plotted in Fig. 4 together with the simulation results. The linear dependence for thin films with high coverage can be clearly distinguished. The threshold behavior at low ionomer coverage is well captured. The extend and slope of the linear range in x_{ion} scale with a_{ion} and provide a transition for the full spectra of ionomer morphologies studied in the simulation.

In Fig. 6, g_+ was plotted for moderate and high ionomer coverage, $a_{ion} = 0.6$ and 1.0, together with datasets from the literature. The proposed analytical solution for g_+ cannot capture the literature data. The deviation is especially large for datasets with high conductivities and a linear trend over x_{ion}, e.g., from Boyer et al., indicating that the conductivity of the ionomer thin film is underestimated by the model. As discussed above, agglomerate roughness largely affects proton conductivity. The roughness and curvature in real catalyst layer materials might be significantly lower than in simulations due to water uptake or ionomer swelling[85] that effectively reduces the tortuosity of the proton conducting pathways. Further, experimental work indicated that the assumption of $g_{ion} \approx g_{bulk}$ might not be true for thin ionomer films. Experimental works reported a lower proton conductivity of PFSA thin films on SiO_2 substrates[89,90] and attributed the impaired proton mobility to the lack of phase-separated water[91]. However, on Pt substrates a well defined water layer at the Pt/ionomer interface forms[92,93], which boosts conductivity by one order of magnitude compared to SiO_2 substrates[94]. Hence, it might be the case that the thin film conductivity in catalyst layers is even higher than the ionomer bulk conductivity. A recent modeling study from the literature evaluated different conceivable molecular structure regimes that might establish on real Pt/C catalyst substrates and found a significant impact on the resulting proton conductivity of the CCL[17]. However, both the effects of tortuosity and distinct ionomer conductivity cannot be quantified reliably. Setting $\tau_{agg} = 1$ in Eq. (26) yields good agreement with the full range of experimental data, hinting that the thin film conductivity in polymer-based catalyst layers is effectively increased by a factor of ≈ 3.

The comparison of the corrected relation $g+$ with literature data illustrates how distinct ionomer morphologies can explain different trends in proton conductivity and their dependence on structural parameters, such as a_{ion}. Single datasets are well captured by the model and can be linked to different scenarios of ionomer morphology. For instance, the dataset of Boyer et al.[44] closely follows $g_+(a_{ion} = 1)$. Thus, the observed linearity of g in x_{ion} can be explained by a thin film morphology present in the CCL material studied. The datasets of Yakovlev et al.[12], Suzuki et al.[86] and Du et al.[87] align along the relation for the intermediate morphology of moderate ionomer coverage. Some data, e.g., from Modestov et al.[79], closely follow the relation for low ionomer coverage. Only the dataset of Liu et al.[52] seems to be difficult to capture by any relation. It is possible that the ionomer morphology largely changes as ionomer content increases, i.e., the ionomer coverage might be a function of x_{ion}.

If the approximation g_+ is applied to structures with high ionomer content, i.e., $x_{ion} > 0.5$, it might overestimate the proton conductivity. The two pathways for proton conductivity (ionomer thin film and inter-agglomerate percolation) are not separated anymore because the ionomer thin film and larger ionomer pieces in the inter-agglomerate space increasingly overlap. This renders the assumption of two parallel pathways for proton transport invalid, thus the effective conductivity will be lower. However, the proposed approximation accurately describes the simulation results over the catalyst layer composition in the range of technical relevance.

Adjusting CCL fabrication parameters to tailor proton conductivity. The question arises how ionomer coverage and film thickness depend on the I:C ratio and how the ionomer structure might be tuned during CCL fabrication. Therefore, we have employed a composition model and aimed at providing various
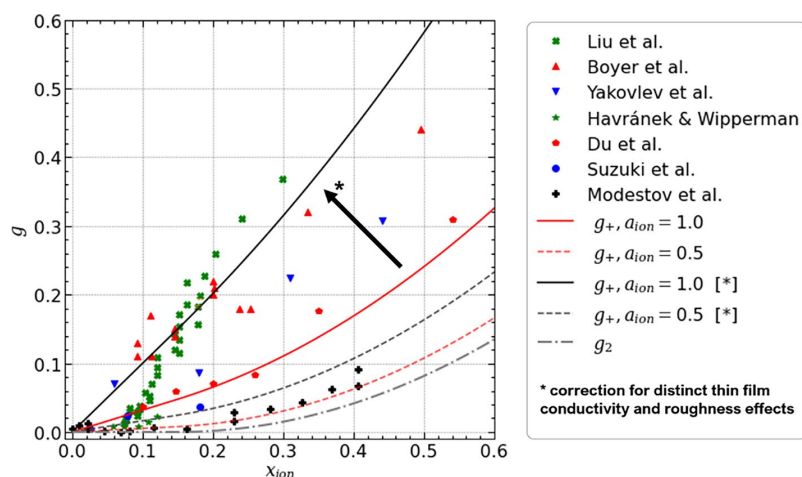
Figure 6. Comparison of literature data for proton conductivity and proposed relations. As a correction for distinct thin film conductivity and roughness effects, the factor $\frac{1}{\pi}$ was dropped in g_{film}.

99

references to practical approaches (ionomer content, ionomer dispersion by solvent, carbon surface modifications), which implement the specific modifications of the CCL microstructure.

Experimental studies varying the ionomer content reported that the ionomer coverage increases sharply upon initially adding of ionomer[76,95]. Subsequently, a growth in film thickness follows[76,95]. At high ionomer contents, excess ionomer aggregates can form that do not contribute to the ionomer film[24–26]. How this resulting ionomer structure can be controlled by ink and process parameters, such as the solvent used, is complex and subject to ongoing research[30,31]. The interactions between Pt/C surface, ionomer and solvent control the self-assembly process during ink stage and largely determine the resulting ionomer morphology. The evolution of a_{ion} and t_{ion} with the I:C ratio can be captured by the composition model developed in Ref.[78] and allows to discuss the impact of basic ink parameters.

To link structure formation during ink stage and proton conductivity in the resulting catalyst layer, in Fig. 7 multiple cases for the ink parameters k_A and t_0 that we have studied over an I:C range from 0 to 1.5. The proton conductivity predicted by the expression for g_+, using the correction discussed above, is plotted together with the literature data from Boyer et al.[44], Du et al.[87], and Modestov et al.[79]. The analysis of the ionomer coverage and film thickness (Fig 7b), and volumetric composition of the catalyst layer (Fig. 7c) reveals how the microstructure evolves over increasing I:C ratio in different scenarios. The dataset from Boyer et al. can be described choosing the values $k_A = 5$ and $t_0 = 8$ nm, i.e., the ionomer adsorbs well on the agglomerate surface and the resulting film is rather thick (>15 nm at I:C >0.6). Two effects contribute to the high proton conductivity in this case: the effective percolation threshold of g is lowered, as ionomer coverage increases sharply at low I:C ratios; and the higher film thickness further enhances conductivity, because the proton conductivity increases proportionally with ionomer film thickness.

Reducing ionomer dispersion and initial film thickness ($k_A = 2$ and $t_0 = 4$ nm) results in a significantly impaired proton conductivity, as reported in the dataset of Modestov et al. Sufficient ionomer coverage is established only at rather high I:C ratios ($a_{ion} > 0.5$ at I:C > 0.5) and the resulting film thickness is low, < 8 nm for the full range of I:C studied. In such a scenario, a major fraction of the ionomer is not dispersed in the ionomer film, but forms larger aggregates, which do not contribute to proton conductivity. As only little ionomer is deposited as part of the thin film in the secondary pore space, more pore volume remains free (see $x_{2,free}$ in Fig 7c).

In intermediate scenarios as for the dataset of Due et al., in which either k_A or t_0 is high, or both parameters are moderate (e.g., $k_A = 3$ and $t_0 = 6$ nm), the volumetric compositions of the catalyst layers are quite similar, because the ionomer film volume is proportional to the product of a_{ion} and t_{ion}. However, the proton conductivity varies significantly. Here, the case of a stronger ionomer-carbon interaction ($k_A = 5$) and low initial film thickness ($t_0 = 4$ nm) results in proton conductivities twice as high as in the opposite case ($k_A = 2$ and $t_0 = 8$ nm). The gain in proton conductivity from higher ionomer coverage clearly exceeds the gain due to increasing film thickness. This implies measures to adjust the ink formulation or interaction of ionomer with the Pt/C catalyst
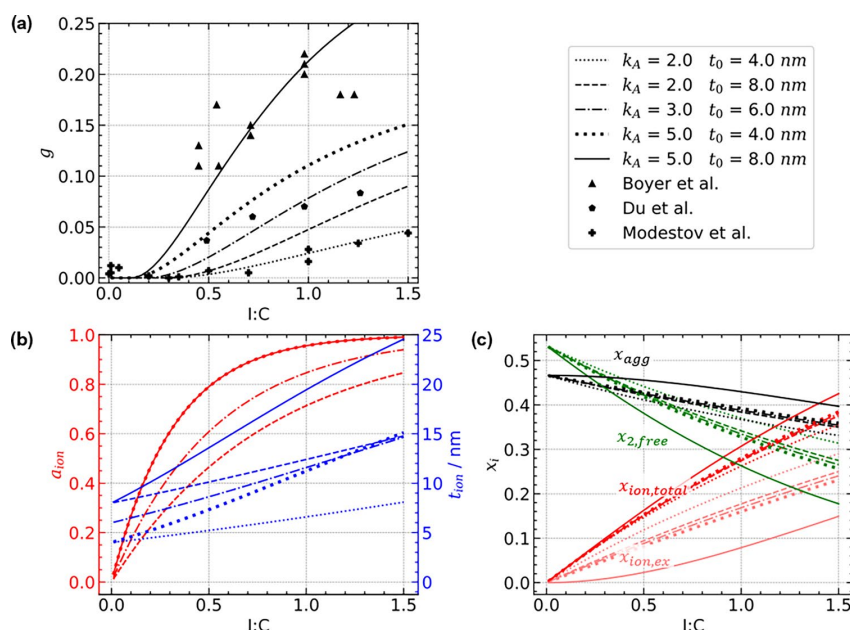
Figure 7. (**a**) Evolution of proton conductivity over I:C ratio, depending on the ink parameters k_A and t_0. (**b**) Ionomer coverage and thickness emerge differently for varying ink parameters. Please note that curves of a_{ion} calculated from equal values of k_A always coincide. (**c**) Depending on the ink parameters, also the trajectory of volumetric composition over I:C ratio, e.g., the volume faction of the pore network or aggregates of excess ionomer, is altered.

100

that foster a thinner film with higher coverage. Efforts in the experimental literature match these findings, such as adjusting solvent composition[24,32–34] or doping the carbon support with nitrogen containing groups[35,96] to achieve a higher dispersion of ionomer.

Conclusion

Polymer electrolyte fuel cells must be designed and optimized to meet the demands of power output and durability. The key to achieving this goal lies in the cathode catalyst layer (CCL) and its microstructure. To this end, we have reviewed modeling approaches for CCL design. We have identified the crucial gap that available relations between composition and proton conductivity in the catalyst layer, such as the Bruggeman relation or percolation theory, neglect specific structural features of the ionomer morphology within the CCL microstructure.

In this work, we have used direct numerical simulations studying the impact of ionomer morphology on proton conductivity. In the past, image-based pore scale simulations focused on gas and liquid transport, but rarely discussed proton conductivity. However, stochastic image generation was found to be a versatile technique to study the impact of different ionomer morphologies. Adopting this approach, we have employed virtual structure generation to generate synthetic binary images that mimic tomographic data, followed by stochastic reconstruction of carbon and ionomer phases. Proton conductivity has been simulated over a wide range of structure parameters in terms of ionomer coverage and film thickness. Two distinct limiting structural regimes could be identified: ionomer can either form a thin film on the catalyst agglomerate surface, where the connectivity of the ionomer coverage dominates the observed trends; or the ionomer forms pieces with substantial thickness that only partially cover the Pt/C agglomerates but connect across the inter-agglomerate space.

Building on these insights from simulation results, a new analytical relation between ionomer morphology and proton conduction was derived from percolation theory. This relation was found to be in close agreement with simulation results and it directly links structural metrics of ionomer coverage and thickness with the proton conductivity. It can capture both limiting cases and reliably interpolates intermediate morphologies. Trends in the literature from multiple sources could be captured. The differences in experimental trends could be linked to variations of ionomer morphology.

To provide guidance for purposeful CCL design and fabrication, structure formation during ink stage has been addressed using a composition model from a previous work. Ionomer morphology and proton transport have been studied over a range of ink parameters, including the I:C ratio, initial ionomer film thickness, and the ionomer dispersion parameter. From this analysis, measures to optimize proton conductivity have been derived and were found in agreement with current experimental literature.

This work demonstrates how profound quantitative modeling and understanding of the relation between CCL microstructure and effective properties can guide the interpretation of experimental data and provide a framework for tailored fuel cell design.

Data availability

The authors declare that the results and data to reproduce the methods and results are reported in full in the article.

References

1. Pollet, B. G., Kocha, S. S. & Staffell, I. Current status of automotive fuel cells for sustainable transport. *Curr. Opin. Electrochem.* **16**, 90–95 (2019).
2. Raistrick, I. D. Modified gas diffusion electrode for proton exchange membrane fuel cells, In *Proceedings of the Symposium on Diaphragms, Separators, and Ion-Exchange Membranes*, Vol. 86, 72, (1986).
3. Wilson, M. S. & Gottesfeld, S. Thin-film catalyst layers for polymer electrolyte fuel cell electrodes. *J. Appl. Electrochem.* **22**, 1–7 (1992).
4. Gerling, C., Hanauer, M., Berner, U. & Andreas Friedrich, K. Full factorial in situ characterization of ionomer properties in differential PEM fuel cells. *J. Electrochem. Soc.* **168**, 084504 (2021).
5. Huang, J., Li, Z. & Zhang, J. Review of characterization and modeling of polymer electrolyte fuel cell catalyst layer: The blessing and curse of ionomer. *Front. Energy* **11**, 334–364 (2017).
6. Eikerling, M. & Kornyshev, A. Modelling the performance of the cathode catalyst layer of polymer electrolyte fuel cells. *J. Electroanal. Chem.* **453**, 89–106 (1998).
7. Wang, Q. *et al.* Functionally graded cathode catalyst layers for polymer electrolyte fuel cells. *J. Electrochem. Soc.* **151**(7), A950 (2004).
8. Song, D. *et al.* A method for optimizing distributions of Nafion and Pt in cathode catalyst layers of PEM fuel cells. *Electrochim. Acta* **50**, 3347–3358 (2005).
9. Secanell, M., Carnes, B., Suleman, A. & Djilali, N. Numerical optimization of proton exchange membrane fuel cell cathodes. *Electrochim. Acta* **52**, 2668–2682 (2007).
10. Eikerling, M., Ioselevich, A. & Kornyshev, A. How good are the electrodes we use in PEFC?. *Fuel Cells* **4**, 131–140 (2004).
11. Kobayashi, A. *et al.* Effect of Pt and ionomer distribution on polymer electrolyte fuel cell performance and durability. *ACS Appl. Energy Mater.* **4**, 2307–2317 (2021).
12. Yakovlev, Y. V. *et al.* Ionomer content effect on charge and gas transport in the cathode catalyst layer of proton-exchange membrane fuel cells. *J. Power Sources* **490**, 229531 (2021).
13. Alink, R. *et al.* Full parametric study of the influence of ionomer content, catalyst loading and catalyst type on oxygen and ion transport in PEM fuel cell catalyst layers. *Molecules* **25**, 1523 (2020).
14. Xing, L. *et al.* Membrane electrode assemblies for PEM fuel cells: A review of functional graded design and optimization. *Energy* **177**, 445–464 (2019).
15. Wang, Y., Ruiz Diaz, D. F., Chen, K. S., Wang, Z. & Adroher, X. C. Materials, technological status, and fundamentals of PEM fuel cells—A review. *Mater. Today* **32**, 178–203 (2020).

101

16. Suter, T. A. M. *et al.* Engineering catalyst layers for next generation polymer electrolyte fuel cells: A review of design, materials, and methods. *Adv. Energy Mater.* **11**, 2101025 (2021).
17. Randall, C. R. & DeCaluwe, S. C. Physically based modeling of PEMFC cathode catalyst layers: Effective microstructure and ionomer structure-property relationship impacts. *J. Electrochem. Energy Convers. Storage* **17**, 041006 (2020).
18. Kusoglu, A. & Weber, A. Z. New insights into perfluorinated sulfonic-acid ionomers. *Chem. Rev.* **117**, 987–1104 (2017).
19. Lopez-Haro, M. *et al.* Three-dimensional analysis of Nafion layers in fuel cell electrodes. *Nat. Commun.* **5**, 5229 (2014).
20. Morawietz, T., Handl, M., Oldani, C., Friedrich, K. A. & Hiesgen, R. Quantitative in situ analysis of ionomer structure in fuel cell catalytic layers. *ACS Appl. Mater. Interfaces* **8**, 27044–27054 (2016).
21. Komini Babu, S., Chung, H. T., Zelenay, P. & Litster, S. Resolving electrode morphology's impact on platinum group metal-free cathode performance using nano-CT of 3d hierarchical pore and ionomer distribution. *ACS Appl. Mater. Interfaces* **8**(48), 32764–32777 (2016).
22. Sun, C.-N., More, K. L. & Zawodzinski, T. A. Investigation of transport properties, microstructure, and thermal behavior of PEFC catalyst layers. *ECS Trans.* **33**, 1207–1215 (2010).
23. Park, Y.-C., Tokiwa, H., Kakinuma, K., Watanabe, M. & Uchida, M. Effects of carbon supports on Pt distribution, ionomer coverage and cathode performance for polymer electrolyte fuel cells. *J. Power Sources* **315**, 179–191 (2016).
24. Doo, G. *et al.* Tuning the ionomer distribution in the fuel cell catalyst layer with scaling the ionomer aggregate size in dispersion. *ACS Appl. Mater. Interfaces* **10**, 17835–17841 (2018).
25. Susac, D., Berejnov, V., Hitchcock, A. P. & Stumper, J. STXM study of the ionomer distribution in the PEM fuel cell catalyst layers. *ECS Trans.* **41**, 629–635 (2011).
26. Zeng, R. *et al.* Possible scenario of forming a catalyst layer for proton exchange membrane fuel cells. *RSC Adv.* **10**(9), 5502–5506 (2020).
27. Xie, Z. *et al.* Fuel cell cathode catalyst layers from "green" catalyst inks. *Energy Environ. Sci.* **1**(1), 184 (2008).
28. Xie, J. *et al.* Influence of ionomer content on the structure and performance of PEFC membrane electrode assemblies. *Electrochim. Acta* **55**, 7404–7412 (2010).
29. Lee, M. *et al.* New evaluation method for the effectiveness of platinum/carbon electrocatalysts under operating conditions. *Electrochim. Acta* **55**, 8504–8512 (2010).
30. Holdcroft, S. Fuel cell catalyst layers: A polymer science perspective. *Chem. Mater.* **26**, 381–393 (2014).
31. Berlinger, S. A., Garg, S. & Weber, A. Z. Multicomponent, multiphase interactions in fuel-cell inks. *Curr. Opin. Electrochem.* **29**, 100744 (2021).
32. Sharma, R. & Andersen, S. M. Zoom in catalyst/ionomer interface in polymer electrolyte membrane fuel cell electrodes: Impact of catalyst/ionomer dispersion media/solvent. *ACS Appl. Mater. Interfaces* **10**, 38125–38133 (2018).
33. Van Cleve, T. *et al.* Dictating Pt-based electrocatalyst performance in polymer electrolyte fuel cells, from formulation to application. *ACS Appl. Mater. Interfaces* **11**, 46953–46964 (2019).
34. Orfanidi, A., Rheinländer, P. J., Schulte, N. & Gasteiger, H. A. Ink solvent dependence of the ionomer distribution in the catalyst layer of a PEMFC. *J. Electrochem. Soc.* **165**(14), F1254 (2018).
35. Ott, S. *et al.* Ionomer distribution control in porous carbon-supported catalyst layers for high-power and low Pt-loaded proton exchange membrane fuel cells. *Nat. Mater.* **19**, 77–85 (2020).
36. Weber, A. Z. *et al.* A critical review of modeling transport phenomena in polymer-electrolyte fuel cells. *J. Electrochem. Soc.* **161**(12), F1254–F1299 (2014).
37. Bruggeman, D. A. G. Berechnung verschiedener physikalischer Konstanten von heterogenen Substanzen. I. Dielektrizitätskonstanten und Leitfähigkeiten der Mischkörper aus isotropen Substanzen. *Annalen der Physik* **416**(7), 636–664 (1935).
38. Tjaden, B., Cooper, S. J., Brett, D. J., Kramer, D. & Shearing, P. R. On the origin and application of the Bruggeman correlation for analysing transport phenomena in electrochemical systems. *Curr. Opin. Chem. Eng.* **12**, 44–51 (2016).
39. Davis, H. T. The effective medium theory of diffusion in composite media. *J. Am. Ceram. Soc.* **60**, 499–501 (1977).
40. Cernuschi, F., Ahmaniemi, S., Vuoristo, P. & Mäntylä, T. Modelling of thermal conductivity of porous materials: Application to thick thermal barrier coatings. *J. Eur. Ceram. Soc.* **24**, 2657–2667 (2004).
41. Chalapat, K. *et al.* Ferromagnetic resonance in ε-Co magnetic composites. *Nanotechnology* **25**, 485707 (2014).
42. Pant, L. M. *et al.* Along-the-channel modeling and analysis of PEFCs at low stoichiometry: Development of a 1+2d model. *Electrochim. Acta* **326**, 134963 (2019).
43. Gloaguen, F. & Durand, R. Simulations of PEFC cathodes: An effectiveness factor approach. *J. Appl. Electrochem.* **27**(9), 1029–1035 (1997).
44. Boyer, C., Gamburzev, S., Velev, O., Srinivasan, S. & Appleby, A. Measurements of proton conductivity in the active layer of PEM fuel cell gas diffusion electrodes. *Electrochim. Acta* **43**, 3703–3709 (1998).
45. Sánchez-Ramos, A., Gostick, J. T. & García-Salaberri, P. A. Modeling the effect of low Pt loading cathode catalyst layer in polymer electrolyte fuel cells: Part I. Model formulation and validation. *J. Electrochem. Soc.* **168**, 124514 (2021).
46. Weisbrod, K. R. Through-the-electrode model of a proton exchange membrane fuel cell. *ECS Proc. Vol.* **1995–23**, 152–166 (1995).
47. Hashin, Z. & Shtrikman, S. A variational approach to the theory of the effective magnetic permeability of multiphase materials. *J. Appl. Phys.* **33**, 3125–3131 (1962).
48. Das, P. K., Li, X. & Liu, Z.-S. Effective transport coefficients in PEM fuel cell catalyst and gas diffusion layers: Beyond Bruggeman approximation. *Appl. Energy* **87**, 2785–2796 (2010).
49. Broadbent, S. R. & Hammersley, J. M. Percolation processes: I. Crystals and mazes. *Math. Proc. Camb. Philos. Soc.* **53**, 629–641 (1957).
50. Hunt, A. G., Ewing, R. P., & Ghanbarian, B. Percolation theory for flow in porous media. No. volume 880 in Lecture notes in physics, 3rd ed. (Springer, 2014). OCLC: ocn871300236.
51. Stauffer, D. & Aharony, A. *Introduction to Percolation Theory* (Taylor & Francis, 2018).
52. Liu, Y., Jorne, J. & Gu, W. Thin shell model for proton conduction in PEM fuel cell cathodes. *J. Electrochem. Soc.* **157**(7), B1068 (2010).
53. Joshi, M. Y. *A Class of Stochastic Models for Porous Media* (University of Kansas, 1974).
54. Quiblier, J. A. A new three-dimensional modeling technique for studying porous media. *J. Colloid Interface Sci.* **98**, 84–102 (1984).
55. Sabharwal, M. *et al.* Analysis of catalyst layer microstructures: From imaging to performance. *Fuel Cells* **16**(6), 734–753 (2016).
56. Khakbazbaboli, M. Development of a Micro-scale Cathode Catalyst Layer Model of Polymer Electrolyte Membrane Fuel Cell. PhD thesis, Queen's University, Kingston, ON, Canada, (2013).
57. Barreiros Salvado, M. *et al.* Towards the understanding of transport limitations in a proton-exchange membrane fuel cell catalyst layer: Performing agglomerate scale direct numerical simulations on electron-microscopy-based geometries. *J. Power Sources* **482**, 228893 (2021).
58. Zheng, W. & Kim, S. H. The effects of catalyst layer microstructure and water saturation on the effective diffusivity in PEMFC. *J. Electrochem. Soc.* **165**(7), F468 (2018).
59. Mukherjee, P. P., Wang, C.-Y. & Kang, Q. Mesoscopic modeling of two-phase behavior and flooding phenomena in polymer electrolyte fuel cells. *Electrochim. Acta* **54**, 6861–6875 (2009).
60. Sui, P.-C., Chen, L.-D., Seaba, J. P., & Wariishi, Y. Modeling and optimization of a PEMFC catalyst layer. *SAE Trans.* 729–737, (1999).

102

61. Hattori, T. *et al.* Development of the overpotential simulator for polymer electrolyte fuel cells and application for optimization of cathode structure. *Appl. Surf. Sci.* **254**, 7929–7932 (2008).
62. Kim, S. H. & Pitsch, H. Reconstruction and effective transport properties of the catalyst layer in PEM fuel cells. *J. Electrochem. Soc.* **156**(6), B673 (2009).
63. Siddique, N. & Liu, F. Process based reconstruction and simulation of a three-dimensional fuel cell catalyst layer. *Electrochim. Acta* **55**, 5357–5366 (2010).
64. Lange, K. J., Sui, P.-C. & Djilali, N. Pore scale simulation of transport and electrochemical reactions in reconstructed PEMFC catalyst layers. *J. Electrochem. Soc.* **157**(10), B1434 (2010).
65. Lange, K. J., Sui, P.-C. & Djilali, N. Determination of effective transport properties in a PEMFC catalyst layer using different reconstruction algorithms. *J. Power Sources* **208**, 354–365 (2012).
66. Inoue, G. *et al.* Simulation of carbon black aggregate and evaluation of ionomer structure on carbon in catalyst layer of polymer electrolyte fuel cell. *J. Power Sources* **439**, 227060 (2019).
67. Lange, K. J. *et al.* PEM fuel cell CL characterization using a standalone FIB and SEM: Experiments and simulation. *Electrochim. Acta* **85**, 322–331 (2012).
68. Epting, W. K., Gelb, J. & Litster, S. Resolving the three-dimensional microstructure of polymer electrolyte fuel cell electrodes using nanometer-scale X-ray computed tomography. *Adv. Funct. Mater.* **22**, 555–560 (2012).
69. Thiele, S. *et al.* Multiscale tomography of nanoporous carbon-supported noble metal catalyst layers. *J. Power Sources* **228**, 185–192 (2013).
70. Zhang, X., Ostadi, H., Jiang, K. & Chen, R. Reliability of the spherical agglomerate models for catalyst layer in polymer electrolyte membrane fuel cells. *Electrochim. Acta* **133**, 475–483 (2014).
71. Goswami, N., Mistry, A. N., Grunewald, J. B., Fuller, T. F. & Mukherjee, P. P. Corrosion-induced microstructural variability affects transport-kinetics interaction in PEM fuel cell catalyst layers. *J. Electrochem. Soc.* **167**, 084519 (2020).
72. Iden, H. & Ohma, A. An in situ technique for analyzing ionomer coverage in catalyst layers. *J. Electroanal. Chem.* **693**, 34–41 (2013).
73. Takeshita, T., Kamitaka, Y., Shinozaki, K., Kodama, K. & Morimoto, Y. Evaluation of ionomer coverage on Pt catalysts in polymer electrolyte membrane fuel cells by CO stripping voltammetry and its effect on oxygen reduction reaction activity. *J. Electroanal. Chem.* **871**, 114250 (2020).
74. Eikerling, M. Water management in cathode catalyst layers of PEM fuel cells. *J. Electrochem. Soc.* **153**(3), E58 (2006).
75. Mashio, T., Sato, K. & Ohma, A. Analysis of water adsorption and condensation in catalyst layers for polymer electrolyte fuel cells. *Electrochim. Acta* **140**, 238–249 (2014).
76. Soboleva, T. *et al.* On the micro-, meso-, and macroporous structures of polymer electrolyte membrane fuel cell catalyst layers. *ACS Appl. Mater. Interfaces* **2**, 375–384 (2010).
77. Gostick, J. *et al.* PoreSpy: A python toolkit for quantitative analysis of porous media images. *J. Open Source Softw.* **4**, 1296 (2019).
78. Olbrich, W., Kadyk, T., Sauter, U. & Eikerling, M. Modeling of wetting phenomena in cathode catalyst layers for PEM fuel cells. *Electrochim. Acta* **431**, 140850 (2022).
79. Modestov, A. D., Kapustin, A. V., Avakov, V. B., Landgraf, I. K. & Tarasevich, M. R. Cathode catalyst layers with ionomer to carbon mass ratios in the range 0–2 studied by electrochemical impedance spectroscopy, cyclic voltammetry, and performance measurements. *J. Power Sources* **272**, 735–742 (2014).
80. Epting, W. K. & Litster, S. Effects of an agglomerate size distribution on the PEFC agglomerate model. *Int. J. Hydrogen Energy* **37**, 8505–8511 (2012).
81. Jankovic, J., Zhang, S., Putz, A., Saha, M. S. & Susac, D. Multiscale imaging and transport modeling for fuel cell electrodes. *J. Mater. Res.* **34**, 579–591 (2019).
82. Sadeghi, M. A. *et al.* Predicting pemfc performance from a volumetric image of catalyst layer structure using pore network modeling, (Under review), (2023).
83. ...Virtanen, P. *et al.* SciPy 1.0: Fundamental algorithms for scientific computing in python. *Nat. Methods* **17**, 261–272 (2020).
84. Cooper, S., Bertei, A., Shearing, P., Kilner, J. & Brandon, N. TauFactor: An open-source application for calculating tortuosity factors from tomographic data. *SoftwareX* **5**, 203–210 (2016).
85. Qi, Y. *et al.* Interpreting ionic conductivity for polymer electrolyte fuel cell catalyst layers with electrochemical impedance spectroscopy and transmission line modeling. *J. Electrochem. Soc.* **168**, 054502 (2021).
86. Suzuki, T., Murata, H., Hatanaka, T. & Morimoto, Y. Analysis of the catalyst layer of polymer electrolyte fuel cells. *R &D Rev. Toyota CRDL* **39**(3), 33–38 (2003).
87. Du, C., Shi, P., Cheng, X. & Yin, G. Effective protonic and electronic conductivity of the catalyst layers in proton exchange membrane fuel cells. *Electrochem. Commun.* **6**, 435–440 (2004).
88. Havránek, A. & Wippermann, K. Determination of proton conductivity in anode catalyst layers of the direct methanol fuel cell (DMFC). *J. Electroanal. Chem.* **567**, 305–315 (2004).
89. Paul, D. K., Fraser, A. & Karan, K. Towards the understanding of proton conduction mechanism in PEMFC catalyst layer: Conductivity of adsorbed Nafion films. *Electrochem. Commun.* **13**, 774–777 (2011).
90. Siroma, Z. *et al.* Depression of proton conductivity in recast Nafion*film measured on flat substrate. *J. Power Sources* **189**, 994–998 (2009).
91. Karan, K. Interesting facets of surface, interfacial, and bulk characteristics of perfluorinated ionomer films. *Langmuir* **35**, 13489–13520 (2019).
92. Shrivastava, U. N., Fritzsche, H. & Karan, K. Interfacial and bulk water in ultrathin films of Nafion, 3m PFSA, and 3m PFIA ionomers on a polycrystalline platinum surface. *Macromolecules* **51**, 9839–9849 (2018).
93. Nagao, Y. Proton-conductivity enhancement in polymer thin films. *Langmuir* **33**, 12547–12558 (2017).
94. Ono, Y. & Nagao, Y. Interfacial structure and proton conductivity of Nafion at the Pt-deposited surface. *Langmuir* **32**, 352–358 (2016).
95. Andersen, S. M. & Grahl-Madsen, L. Interface contribution to the electrode performance of proton exchange membrane fuel cells—Impact of the ionomer. *Int. J. Hydrogen Energy* **41**, 1892–1901 (2016).
96. Orfanidi, A. *et al.* The key to high performance low Pt loaded electrodes. *J. Electrochem. Soc.* **164**(4), F418–F426 (2017).

Acknowledgements

Author contributions

Conceptualization: W.O., T.K., U.S., M.E., J.G.; Methodology: W.O.; Software: W.O.; Formal analysis: W.O.; Resources: U.S., J.G.; Writing—original draft: W.O.; Writing—review and editing: U.S., T.K., J.G., M.E.; Supervision: J.G., M.E., U.S., T.K.; Project administration: U.S., M.E.

103

Additional information
Supplementary Information The online version contains supplementary material available at https://doi.org/10.1038/s41598-023-40637-0.

Correspondence and requests for materials should be addressed to W.O.

Reprints and permissions information is available at www.nature.com/reprints.

Publisher's note Springer Nature remains neutral with regard to jurisdictional claims in published maps and institutional affiliations.

4.4 Further published results
Structure-Based modeling to rationalize the Pt utilization in catalyst layers of PEM fuel cells

Authors: Wolfgang Olbrich[1,2,3,*], Thomas Kadyk[1,4], Ulrich Sauter[2], Michael Eikerling[1,3,4]

[1] Theory and Computation of Energy Materials (IEK-13), Institute of Energy and Climate Research, Forschungszentrum Jülich GmbH, 52425 Jülich, Germany
[2] Robert Bosch GmbH, Corporate Research, 71272 Renningen, Germany
[3] Chair of Theory and Computation of Energy Materials, Faculty of Georesources and Materials Engineering, RWTH Aachen University, 52062 Aachen, Germany
[4] Jülich Aachen Research Alliance, JARA Energy, 52425 Jülich, Germany

Author contributions: Conceptualization: WO, TK, US, ME; Methodology: WO; Software: WO; Formal analysis: WO; Resources: US; Writing - Original Draft: WO; Writing - Review & Editing: US, TK, ME; Supervision: ME, US, TK; Project administration: US, ME.

Document history: Submitted abstract: 11.01.2022, Presented: 18.05.2022.

Cite as: W. Olbrich, T. Kadyk, U. Sauter, and M. Eikerling. Structure-Based Modeling to Rationalize the Pt Utilization in Catalyst Layers of PEM Fuel Cells. *Presented 18 May 2022 at* 31st Topical Meeting of the International Society of Electrochemistry *in Aachen, Germany.*

In the following, methods and results as presented in a talk at the *31st Topical Meeting of the International Society of Electrochemistry*, held 15.–19.05.2022 in Aachen, Germany, are documented as a brief manuscript together with the abstract submitted to the conference.

Structure-Based Modeling to Rationalize the Pt Utilization in Catalyst Layers of PEM Fuel Cells

W. Olbrich[1,2,3,*], T. Kadyk[1,4], U. Sauter[2], M. Eikerling[1,3,4]

[1] *Theory and Computation of Energy Materials (IEK-13), Institute of Energy and Climate Research, Forschungszentrum Jülich GmbH, 52425 Jülich, Germany.*
[2] *Robert Bosch GmbH, Corporate Research, 71272 Renningen, Germany.*
[3] *Chair of Theory and Computation of Energy Materials, Faculty of Georesources and Materials Engineering, RWTH Aachen University, 52062 Aachen, Germany*
[4] *Jülich Aachen Research Alliance, JARA Energy, 52425 Jülich, Germany.*
* *wolfgang.olbrich@de.bosch.com*

Liquid water plays a crucial role in low-temperature polymer electrolyte fuel cells (PEFCs). It serves as electrochemical reaction medium and proton solvent in the cathode catalyst layer (CCL) and is thus crucial for high proton conductivity and optimal Pt utilization [1]. From experimental studies, it is known that the Pt utilization depends strongly on relative humidity, ionomer loading and Pt loading [2,3,4]. To date, structure-based models insufficiently account for these effects [4,5,6]. The basic structural unit of a conventional catalyst layer is the primary carbon particle (50-100 nm diameter) that supports Pt nanoparticles (~2-10 nm diameter) on its outer surface and in its internal nanopores [7]. The ratio of external/internal deposition of the Pt nanoparticles depends on catalyst synthesis route, carbon type, Pt nanoparticle size, and Pt:C mass ratio [4,7]. Primary Pt/C particles assemble into agglomerates, which are partially covered by a skin-type ionomer film (~5-10 nm thickness). Pt utilization is facilitated by contact with liquid water that exists at the ionomer film or in agglomerate pores, as illustrated in Figure 1 [2,3]. The proposed model framework provides structural descriptors to quantitatively capture the CCL microstructure, such as ionomer coverage and pore size distribution. Besides water vapor, the model distinguishes three states of condensed water in the CCL: liquid water in capillaries, water adsorbed at Pt and carbon surfaces, and water absorbed in the ionomer film. Based on the humidity-dependent water uptake of the CCL, the model calculates the probability for the existence of a percolating proton transport pathway in the agglomerated structure. Using the model, we will scrutinize how dilution of the Pt loading, i.e., reduction of the Pt:C ratio, causes a decline of Pt utilization (see Fig 2). This analysis reveals the impact of microstructural features on the overall fuel cell Pt utilization behavior. Model-derived guidelines for the fine-tuning of the CCL design in view of achieving an optimal Pt utilization will be presented and discussed.
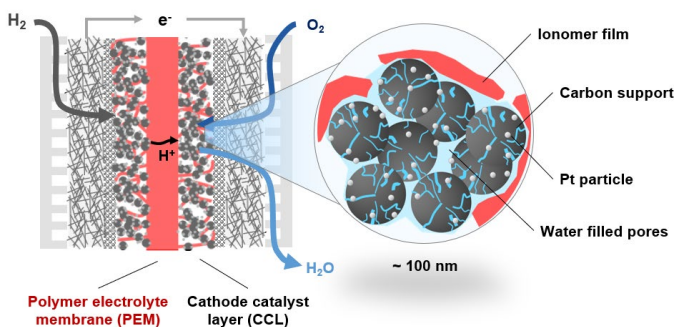
Figure 1: Internal structure of an agglomerate of the cathode catalyst layer and its location in the PEM fuel cell. Pt nanoparticles are either utilized by direct contact with ionomer or via water trapped in the agglomerate's internal pores.
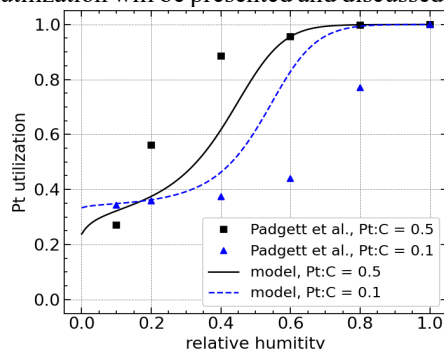
Figure 2: Pt utilization for low and high Pt loadings on a high surface carbon as function of relative humidity. Data from Ref [4].

References:
[1] Eikerling *et al. Physics Today* **59**, 38–44 (2006) doi:10.1063/1.2387087.
[2] Soboleva *et al. ACS Applied Materials & Interfaces* **3**, 1827–1837 (2011) doi:10.1021/am200590w.
[3] Mashio *et al. Electrochimica Acta* **140**, 238–249 (2014) doi:10.1016/j.electacta.2014.07.058.
[4] Padgett *et al. J. Electrochem. Soc.* **165**, F173–F180 (2018) doi:10.1149/2.0541803jes.
[5] Eikerling. *J. Electrochem. Soc.* **153**, E58 (2006) doi:10.1149/1.2160435.
[6] Chowdhury *et al. ECS Transactions* **92**, 247–259 (2019) doi:10.1149/09208.0247ecst.
[7] Harzer *et al. J. Electrochem. Soc.* **165**, F770 (2018) doi:10.1149/2.0311810jes

Structure-Based Modeling to Rationalize the Pt Utilization in Catalyst Layers of PEM Fuel Cells

M.Sc. Wolfgang Olbrich[1,2,3] (presenter), Dr. Thomas Kadyk[1,4], Dr. Ulrich Sauter[2], Prof. Dr. Michael Eikerling[1,3,4].

[1] Theory and Computation of Energy Materials (IEK-13), Institute of Energy and Climate Research, Forschungszentrum Jülich GmbH, 52425 Jülich, Germany
[2] Robert Bosch GmbH, Corporate Research, 71272 Renningen, Germany
[3] Chair of Theory and Computation of Energy Materials, Faculty of Georesources and Materials Engineering, RWTH Aachen University, 52062 Aachen, Germany
[4] Jülich Aachen Research Alliance, JARA Energy, 52425 Jülich, Germany

Nomenclature

Index i indicates the material species (*carb.*, *Pt*, *ion.*, *pores*), or the sum over all species (Σ); and j denotes the location of the species in either primary (index 1) or secondary (index 2) pore size domain, or species from both domains combined (index Σ).

Latin symbols

Symbol	Description	Unit
$A_{carb.,j}$	surface area of carbon support exposed to pore size domain j	m^2
A_{Pt}	surface area of a single Pt nanoparticle	nm^2
A_W	surface area occupied by a single sorption site of water on Pt surfaces	nm^2
b	width parameter of the sigmoid function	-
$c_{i,j}$	concentration of sorption sites of type i in pore size domain j	mol/cm^3
c_{surf}	mass specific concentration of functional groups on carbon support surface	mol/g
$\mathcal{H}$	Heaviside step function	-
EW	equivalent weight, i.e., ionomer mass per amount of sulfonic acid group	g/mol
$K_{L,i}$	Langmuir-type sorption constant	1/Pa
$K_{S,i}$	secondary sorption constant	-
n_i	number of adsorbed layers of water molecules	-
m_{Pt}	mass of a single Pt nanoparticle	g
N_A	Avogadro number	1/mol
p_W	partial pressure of water	Pa
$\mathcal{P}$	sigmoid function mimicking percolation-type behavior	-
r	pore radius	nm
r_{Pt}	radius of Pt nanoparticles	nm
R	universal gas constant	J/(mol K)
RH	relative humidity	-
$S^{(C)}$	critical saturation level for the percolation threshold	-
$S_{i,j}$	liquid saturation level of pore domain j contributed by species i	-
T	temperature	K
$V_{m,W}$	molar volume of water	cm^3/mol
$W_{i,j}$	water uptake per carbon support mass	g/mol
$x_{i,j}$	volume fraction of species i in pore size domain j	-
X_{Pt}	Pt utilization of the catalyst layer	-
Y	water uptake reduction factor of ionomer	-

Greek symbols

Symbol	Description	Unit
γ_W	surface free energy of water	J/m^2
λ_i	number of water molecules adsorbed per sorption site of type i	-
$\phi_{Pt,j}$	fraction of Pt nanoparticles assigned to pore size domain j	-
ρ_i	mass density of material i	g/cm^3
θ	contact angle of pore walls	$\circ$

1 – Introduction

Fuel cells rendered active: the role of water for Pt utilization

Liquid water plays a crucial role in proton exchange membrane fuel cells (PEMFCs). It acts as the proton conductive medium in the catalyst layer (CL) and connects the Platinum catalyst via a spanning network. Thus, it is pivotal for high proton conductivity and optimal catalyst utilization [243]. The Pt utilization, i.e., the ratio of active catalyst particles connected to the proton supply network to the total amount of Platinum in the CL, correlates with the amount of water taken up by the CL material when exposed to a water containing atmosphere [78, 152, 242]. Since the gas phase in operating PEM fuel cells carries high amounts of water vapor generated from the hydrogen fuel conversion, data on water uptake and Pt utilization obtained at varying humidity conditions obtained *ex situ* provide key conclusions on CL behavior for *in operando* conditions. From experimental studies, it is known that the Pt utilization depends strongly on relative humidity (RH), ionomer loading and Pt loading [78, 152, 242]. Especially low-Pt-loaded CLs exhibit a peculiar behavior: Pt utilization drops significantly at moderate RH for such CLs (see Fig. 4.1 (a)). Since current development efforts to reach cost-targets for commercial fuel cells strive to reduce Pt loading, this phenomenon requires special attention.

Water uptake and Pt utilization are determined and shaped by structural features of the CL microstructure [94, 107, 132]. The basic structural unit of a conventional catalyst layer is the primary carbon particle (50...100 nm diameter) that supports Pt nanoparticles (2..10 nm diameter). In the common understanding, Pt/C catalyst particles aggregate as ionomer-free agglomerates, whereas the ionomer forms a thin film on these agglomerates (5...15 nm thickness). Pores within the agglomerates are called *primary pores* (1..10 nm diameter). The inter-agglomerate space contributes a second pore-size domain with a radii length scale similar to the size of Pt/C particles and is referred to as *secondary pores*. An illustration of the CL structure is depicted in Fig. 4.1 (b).

Within this complex structure, Pt utilization is facilitated by contact with liquid water that is absorbed by the ionomer film or condensed in the pore space [94, 107]. Additionally, a recent work of Chowdhury *et al.* suggests that a continuous connection to the proton conductive network might also be established via water films adsorbed onto Pt nanoparticles [119]. This hypothesis was derived from the finding that models for Pt utilization the literature only account for capillary condensation, i.e., Pt nanoparticles only count as utilized if the according pore is fully flooded [119, 132]. However, these models do not consistently describe Pt utilization as observed in experimental works (Fig. 4.1 (a)). As illustrated in Fig. 4.1 (c), the conjectured water film might not be sufficient to span over the distance between individual Pt nanoparticles in low-Pt-loaded CL materials, explaining the observed distinct drop in Pt utilization. The formation of adsorbed water films was already proposed by Mashio *et al.* [94], who deconvoluted water uptake in a model-based analysis by employing a sorption formalism additionally to the capillary condensation. In this work, the approaches of Chowdhury *et al.* and Mashio *et al.* are followed up by extending the parametrization of water uptake to be fully structure-based, i.e., will be derived from ink stage parameters of the CL. Subsequently, the distinct contributions for Pt utilization from different types of water can be deconvoluted and the mechanism of Pt utilization scrutinized further.
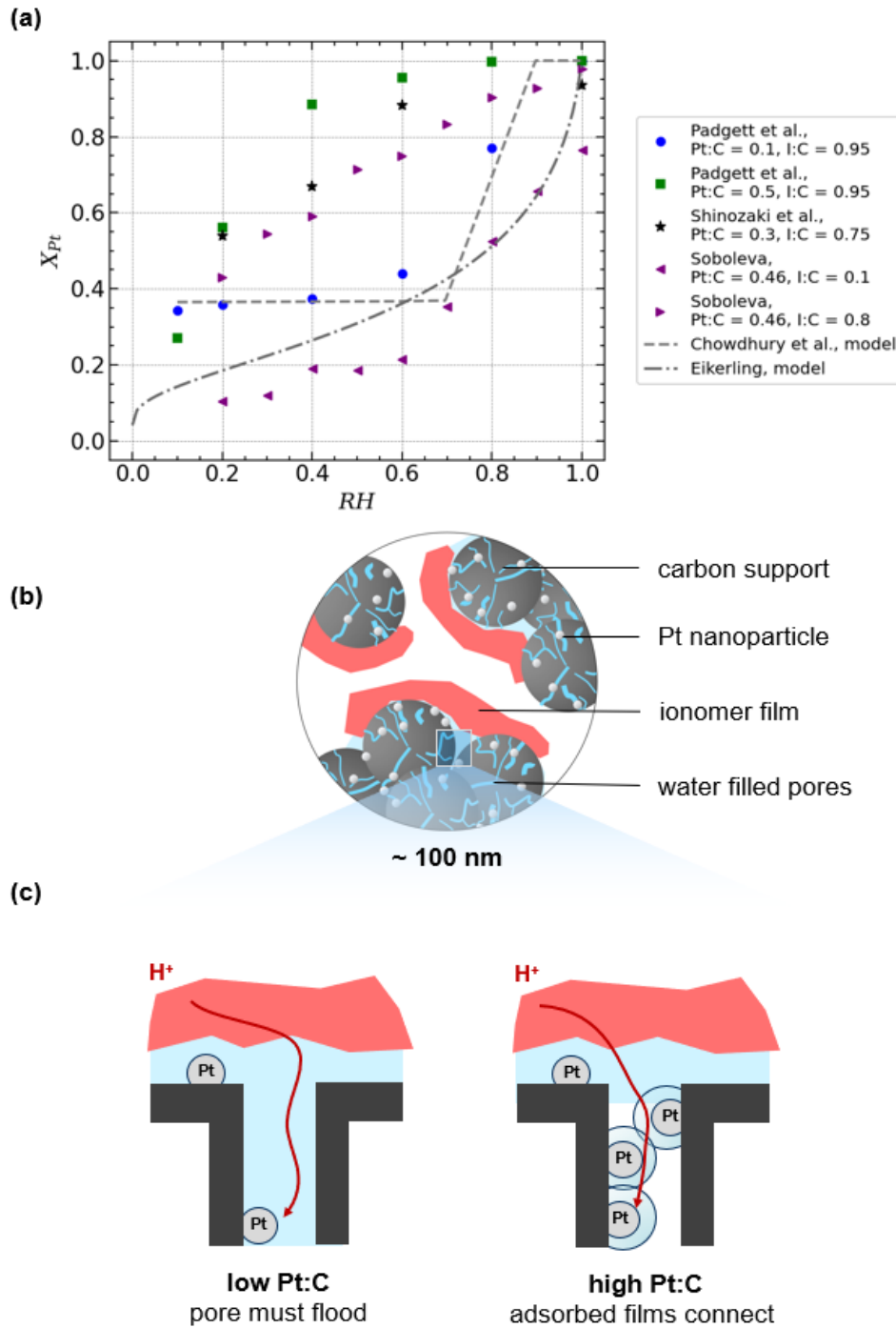
Fig. 4.1: **(a)** Platinum utilization follows different trends for low or high Pt loading as found experimentally by Padgett *et al.* [78], Shinozaki *et al.* [242] and Soboleva [107]. Models from the literature [119, 132] only account for capillary condensation to describe Pt utilization and cannot capture the experimentally observed behavior in all cases. **(b)** The catalyst layer features a complex agglomerated structure with multiple species adsorbing water from a partially saturated atmosphere. **(c)** Water adsorbed in thin films on Pt nanoparticles is conjectured to contribute to Pt utilization and be the root cause for distinct trends for different Pt loading.

2 – Model and methodology

Given the comprehensive picture of CL microstructure and available formalism for water uptake by different species of the CL material, this work proposes a modeling approach to combine both to a structure-based model for water uptake and Pt utilization, as outlined in Fig. 4.2. First, structural parameters and composition of the CL material in dry state as obtained from fabrication must be calculated from ink parameters (Fig. 4.2 (a)). A previously developed composition and wettability model [244] derives the volumetric composition of the layer and statistical metrics of the agglomerated structure, e.g., the pore size distribution, and wetting properties of the pore walls in primary and secondary pores. These parameters provide a complete description of the confinement of water, which adsorbs and condenses on different locations of the CL structure. As illustrated in Fig. 4.2 (b), the model distinguishes three types of water in the CL: liquid water in capillaries, water adsorbed at Pt and carbon surfaces, and water absorbed by ionomer. Applying this distinction, the amount of water present in the CL can be mapped onto the different pore size domains (Fig. 4.2 (c)). From the local saturation of pore space, a description of network strength and connectivity of the liquid water phase can be calculated, which determines Pt utilization. Here, approaches based on percolation theory provide the mathematical foundation to rationalize the probability for the existence of a continuous proton transport pathway in the agglomerated structure. Eikerling and Kornyshev already introduced percolation theory to correlate the composition of a CL with its properties [51, 151]. However, ionomer inside the CL was considered the only percolating agent relevant for Pt utilization. More novel experimental works indicate that water acts as a percolating agent, too [94, 129]. Therefore, the percolation-based approach by Eikerling and Kornyshev will be adapted to account for the saturation of pore space by liquid water.

(a) confinement / dry structure

x

(b) state of water

=

(c) effective Pt utilization network

recipe catalyst layer

H₂O
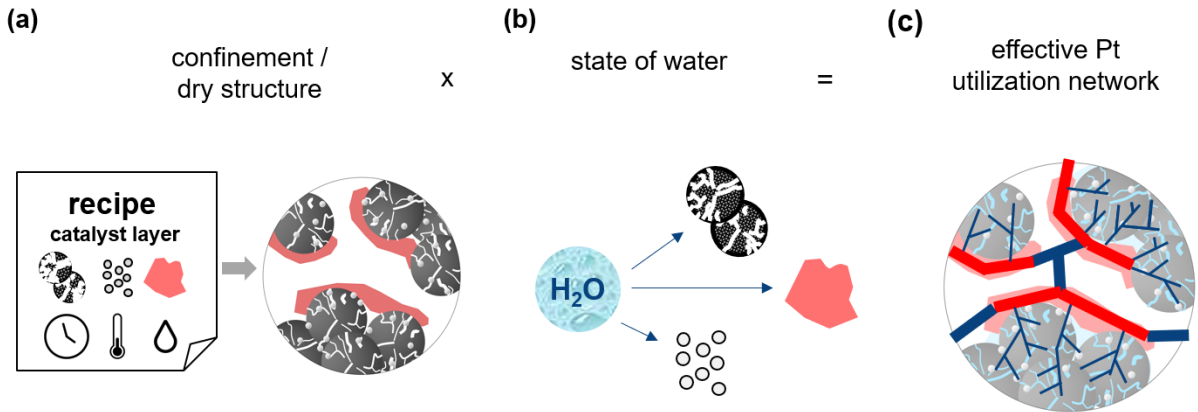
Fig. 4.2: Platinum utilization can be modeled in three steps: **(a)** first, descriptors of the CL microstructure are calculated from ink parameters; **(b)** second, water uptake by sorption and capillary condensation for each materials species is calculated; **(c)** and are finally mapped onto the CL structure to describe effective connecting pathways for proton transport.

Catalyst layer composition and concentration of sorption sites

A previously developed composition model is employed to derive the volume fractions and exposed surface areas of Platinum, carbon support, ionomer, and primary and secondary pores of the CL material in the dry state. The according input parameters characterize the ink composition in terms of Pt:C and I:C mass ratios, the total available pore volume provided by the bare support structure V_0, the ionomer dispersion parameter k_A and t_0, and radii of the pore size distribution. The composition model mimics the agglomeration process of Pt/C particles and film formation of ionomer solvated in the ink. Details of the model have been published in Ref. [244].

As a metric to rationalize the water uptake capacities of each materials species (i.e., Pt, ionomer, carbon) the *concentration of sorption sites*, denoted as $c_{i,j}$ with units mol/cm^3, is adapted from Mashio *et al.* [94]. In the following, variables are specified with two indices: i is indicating the material species (indices *carb.*, *Pt*, *ion.*, *pores*), or the sum over all species (index Σ); and j denotes the location of the species in either primary (index 1) or secondary (index 2) pores, or species from both domains are counted (index Σ). Since ionomer is present in secondary pores only, the second index is dropped there. The volume factions of each materials species $x_{i,j}$ is provided by the composition model and marks the starting point for the calculation of $c_{i,j}$.

For Platinum, the number of sorption sites is proportional to the specific surface area of Pt nanoparticles, which is calculated as

$$[A_{Pt}/m_{Pt}] = \frac{3}{\rho_{Pt} r_{Pt}}, \tag{4.1}$$

assuming spherical particles with a fixed radius r_{Pt}. The surface area of a single sorption site for water A_W and the volume fraction of Platinum $x_{Pt,j}$ determine the effective concentration of sorption sites,

$$c_{Pt,j} = x_{Pt,j} [A_{Pt}/m_{Pt}] \frac{\rho_{Pt}}{A_W N_A}. \tag{4.2}$$

The constants ρ_{Pt} and N_A denote the mass density of metallic Platinum and the Avogadro number. The distribution of Pt nanoparticles over primary and secondary pores is a property of the Pt/C catalyst which can be tuned via the Pt deposition method during synthesis [71] and introduces an additional parameter to the model, $\phi_{Pt,1}$, which splits the total population of Pt nanoparticles accordingly,

$$x_{Pt,1} = \phi_{Pt,1} x_{Pt,\Sigma} \qquad \text{and} \tag{4.3}$$
$$x_{Pt,2} = (1 - \phi_{Pt,1}) x_{Pt,\Sigma}. \tag{4.4}$$

Deviating from the model of Mashio *et al.*, water sorption on graphitic surfaces of the carbon supports is not accounted for since its contribution to water uptake is negligible. In contrast, functional surface groups on the carbon support provide a significant capacity for water uptake. Their concentration $c_{surf.}$ is specific to the carbon support. The resulting concentration of sorption sites in the CL material is calculated as

$$c_{carb.,\Sigma} = x_{carb.,\Sigma} c_{surf.} \rho_{carb.}. \tag{4.5}$$

Assuming functional groups to be uniformly distributed over the carbon surface, the split over the pore size domains follows the ratio of surface areas attributed to primary and secondary pores,

$$c_{carb.,j} = \frac{A_{carb.,j}}{A_{carb.,\Sigma}}. \tag{4.6}$$

The values of the according surface areas $A_{carb.,j}$ are obtained from integration of the pore size distribution, which is facilized by the composition model, too (see Ref. [244]).

For ionomer, the water uptake capabilities directly scales with the number of sulfonic acid groups per ionomer mass, commonly expressed as the inverse ratio called *equivalent weight, EW*. Each sulfonic acid group is assumed to provide three water sorption sites[1]. Thus, $c_{ion.}$ is calculated as

$$c_{ion.} = 3\,x_{ion.}\frac{\rho_{ion.}}{EW}. \tag{4.7}$$

Water sorption isotherms

Following Mashio *et al.*, a multilayer sorption formalism equivalent to a Brunauer-Emmet-Teller theory [245] with a limited number of layers of water molecules adsorbed (n_i) is used to describe the water sorption isotherms of Platinum, carbon, and ionomer. The number of water molecules per sorption site λ_i as function of relative humidity RH is calculated as

$$\lambda_i(RH) = \frac{K_{L,i}\sum_{k=1}^{n_i}k(K_{S,i}RH)^k}{K_{S,i} + K_{L,i}\sum_{k=1}^{n_i}(K_{S,i}RH)^k}. \tag{4.8}$$

Parametrization of the Langmuir-type sorption constants $K_{L,i}$ and secondary sorption constants $K_{S,i}$ are adapted from Mashio *et al.* and are valid for 80℃. Accordingly, relative humidity RH is defined for this temperature by the partial pressure of water p_W,

$$RH = \frac{p_W}{p_{W,80℃}^0}. \tag{4.9}$$

The resulting isotherms for Platinum, carbon support and ionomer are calculated using the parametrization from Tab. 4.3 and are depicted in Fig. 4.3 (a). The volume fraction of water from sorption processes at a given RH is ultimately the product of water molecules per sorption site and the concentration of according sorption sites,

$$x_{W,i,j} = \lambda_i c_{i,j} M_W / \rho_W. \tag{4.10}$$

---

[1] This important information is not provided explicitly in the original manuscript of Mashio *et al.* but can be reconstructed from the reported water uptake data.
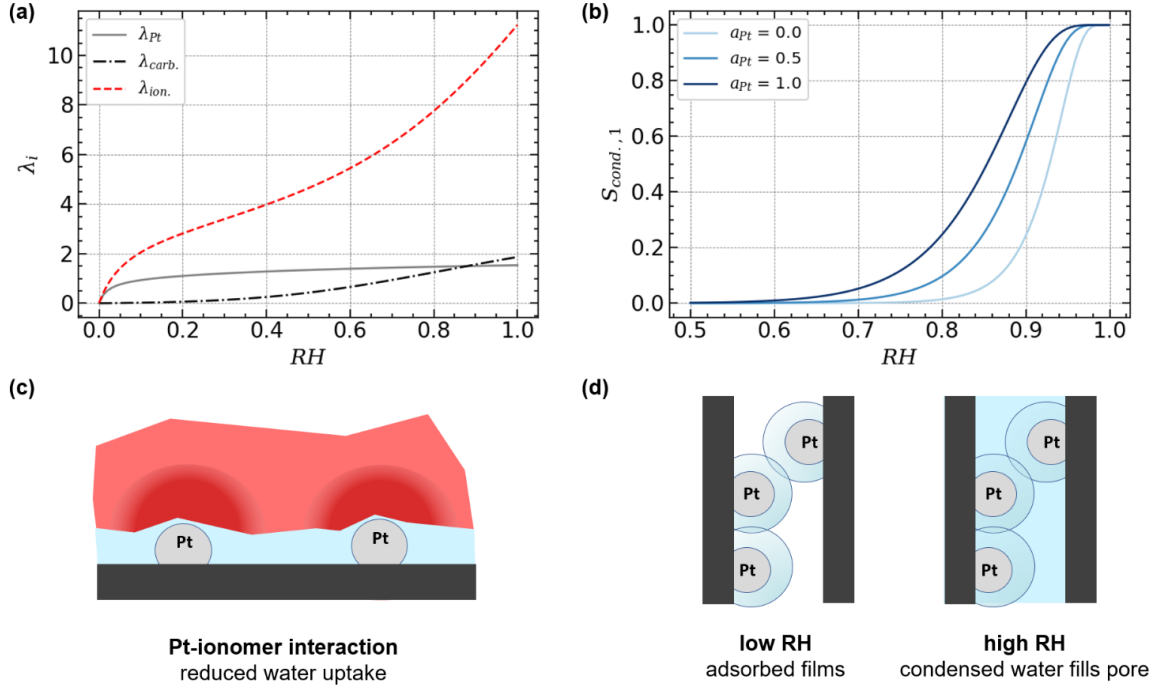
Fig. 4.3: (a) Sorption isotherms as number of water molecules per sorption site for Platinum, carbon support and ionomer. **(b)** Water uptake in terms of liquid saturation of primary pores due to capillary condensation for bare carbon support, half of the pore walls covered with Pt nanoparticles, and fully Pt-covered pore walls. Conditions of 80℃ and 1 bar apply. **(c)** Water uptake of ionomer thin films can be diminished by the strong interaction of ionomer sidechains and Pt nanoparticles. **(d)** When primary pores flood due to capillary condensation, the water from adsorbed films is replaced by bulk liquid water, i.e., must not be accounted for twice in the summation of water uptake.

Tab. 4.3: Constants and sorption parameters adapted from Ref. [94]. Where values were adjusted and deviate from the original values provided by Mashio *et al.*, the original value is written in ( ).

Constants			Sorption parameters				
$\rho_{carb.}$	2.0	g/cm^3	$i =$	carb.	Pt	ion.	
ρ_{Pt}	21.45	g/cm^3	$K_{L,i}$	3E-6	1E-3	3.3E-4	Pa^{-1}
$\rho_{ion.}$	2.1	g/cm^3	$K_{S,i}$	1.7	1.2	0.8	
ρ_W	0.971	g/cm^3	N_i	4 (10)	2	10	
N_A	6.022E23	1/mol					
A_W	0.04	nm^2	$c_{surf.}$	7.3	mmol/g$_{carb.}$		
M_W	18.015	g/mol	EW	1000	g$_{ion.}$ /mol		
$V_{m,W}$	18.74	cm^3/mol					
γ_W	0.062	J/m^2					
$p^0_{W,80°C}$	473	mbar					

Due to strong interaction of ionomer sidechains with Pt/C surface, water uptake was reported to diminish significantly in thin ionomer films [246]. As illustrated in Fig. 4.3 (c), water uptake is constricted at the interface of ionomer and Pt/C surface and the capacity for water uptake lowers significantly. Therefore, a reduction factor Y is used,

$$\lambda'_{ion} = Y \lambda_{ion}. \tag{4.11}$$

Mashio *et al.* [94] reported $Y = 0.8$ on bare carbon support, and $Y = 0.4$ for a catalyst material with Pt:C = 0.46. Experimental data from Kusoglu *et al.* [247] indicates similar values on various substrates ($Y = 0.3...0.5$). In the model, this reduction of water uptake is implemented as a function of Pt coverage of the carbon surface ($a_{Pt,2}$, obtained from composition model), on which the ionomer deposits,

$$Y = \begin{cases} 0.8 - 2\,a_{Pt,2} & 0 \leq a_{Pt,2} \leq 0.3 \\ 0.2 & a_{Pt,2} > 0.3 \end{cases}. \tag{4.12}$$

To provide a comparable measure for different CL materials, water uptake is expressed as liquid saturation of the pore space ($S_{i,j}$). In the experimental literature water uptake is commonly reported in terms of mass of water per mass of carbon support ($W_{i,j}$). Both values can be directly calculated from $x_{W,i,j}$,

$$S_{i,j} = \frac{x_{W,i,j}}{x_{pores,j}} \quad \text{and} \tag{4.13}$$

$$W_{i,j} = x_{W,i,j} \frac{\rho_W}{x_{carb.}\rho_{carb.}}. \tag{4.14}$$

Capillary condensation

Liquid water can condense spontaneously in constrained geometries, such as pores, even at $RH < 1.0$. This phenomenon is referred to as capillary condensation. The critical radius of a pore to be flooded at given RH is determined by the Kelvin equation,

$$r_C = \frac{\gamma_W V_{m,W} \cos\theta}{\ln(RH)RT}. \tag{4.15}$$

The wetting properties in terms of contact angle θ mainly control the onset of flooding since the free surface energy γ_W and molar volume $V_{m,W}$ of water are constants for a given temperature. The partial flooding due to capillary condensation of a set of pores with a continuous range of sizes and wetting properties can be captured analogously to flooding via capillary pressure (see wettability model in Ref. [244]). The combined pore size and contact angle distribution ($\frac{\partial^2 S}{\partial r \partial \theta}$) is integrated to obtain the liquid saturation $S_{cond.,j}$ for a given RH,

$$S_{cond.,j}(RH) = \int_{r_{min}}^{r_{max}} \int_{-1}^{1} \frac{\partial^2 S_j}{\partial r \partial \theta} \mathcal{H} \left(\frac{\gamma_W V_{m,W} \cos\theta}{rRT} - \ln(RH) \right) d\cos(\theta)\,dr. \tag{4.16}$$

The Heaviside step function $\mathcal{H}$ evaluates the Kelvin equation and determines whether a pore is counted as flooded or empty. Here, the model completely relies on the structure-based model developed in Ref. [244] and does not use the correlations proposed by Mashio *et al.*

When calculating the total saturation, i.e., combining water uptake from the distinct materials species, the replacement of water films in a pore by condensed bulk water must be accounted for (see Fig. 4.3 (d)). Otherwise, water uptake would be overestimated and unphysical saturation >1 could be the result. Thus, $S_{\Sigma,1}$ and $S_{\Sigma,2}$ are determined as

$$S_{\Sigma,1} = (1 - S_{cond.,1})(S_{Pt,1} + S_{carb.,1}) + S_{cond.,1} \tag{4.17}$$

$$S_{\Sigma,2} = (1 - S_{cond.,2})(S_{Pt,2} + S_{carb.,2} + S_{ion.}) + S_{cond.,2}. \tag{4.18}$$

The saturation of the CL material S_{CL} is calculated from contributions from primary and secondary pores, using the pore volume fractions $x_{pores,j}$ as weights in the summation,

$$S_{CL} = S_{\Sigma,1}\frac{x_{pores,1}}{x_{pores,\Sigma}} + S_{\Sigma,2}\frac{x_{pores,2}}{x_{pores,\Sigma}} \qquad \text{with} \tag{4.19}$$

$$x_{pores,\Sigma} = x_{pores,1} + x_{pores,2}. \tag{4.20}$$

Literature data of reference materials

The experimental literature was scanned for sources that provide data on water uptake and/or Pt utilization together with essential information on the CL material used, i.e, Pt:C and I:C, the radii of Pt nanoparticles and the fraction of Pt nanoparticles located inside primary pores (see Tab. 4.4). All selected works used Ketjen Black, a high surface area carbon, as support material.

Mashio *et al.* and Soboleva [107] even studied an identical Pt/C material from the same supplier. Also, the ionomer used was identical in all sources. The dataset of Mashio *et al.* is especially valuable for its water uptake data of the single materials (bare carbon, ionomer-free Pt/C catalyst, complete CL with varying I:C), allowing to check whether the model consistently describes catalyst layer materials with varying composition. The work of Soboleva [107] is the only source providing both water uptake and Pt utilization data as a function of RH for the same material but water uptake was measured at room temperature.T Therefore, a cross-comparison with the dataset of Mashio *et al.* is required. The datasets reported by Padgett *et al.* [78] and Shinozaki *et al.* [242] add more points to the parameter space with regard to Pt loading. Especially the properties of the low-Pt-loaded material with Pt:C $= 0.1$ from Padgett *et al.* are of particular interest in this work since it exhibits a distinct correlation between relative humidity and Pt utilization.

The parametrization of the composition model was the same for all materials since it was developed using data from Soboleva, thus apply to all CLs based on Ketjen black and were adapted without changes from Ref. [244].

Tab. 4.4: Catalyst layer properties and available datasets on water uptake and Pt utilization from different sources found in the experimental literature.

Source	Material	Pt:C	I:C	r_{Pt}	$\phi_{Pt,1}$	$W(RH)$ data	$X_{Pt}(RH)$ data
Padgett *et al.* [78]	CCL	0.1	0.95	1.4 nm	0.7	no	yes
	CCL	0.5	0.95	2.0 nm	0.8	no	yes
Mashio *et al.* [94]	Ketjen Black (carbon support)	n.a.	n.a.	n.a.	n.a.	yes	no
	Pt/C catalyst (ionomer free)	0.46	n.a.	2.5 nm	0.6	yes	no
	CCL	0.46	0.7	2.5 nm	0.6	yes	no
	CCL	0.46	0.9	2.5 nm	0.6	yes	no
	CCL	0.46	1.3	2.5 nm	0.6	yes	no
Soboleva [107]	Pt/C catalyst (ionomer free)	0.46	n.a.	2.5 nm	0.6	yes	no
	CCL	0.46	0.1	2.5 nm	0.6	yes	yes
	CCL	0.46	0.78	2.5 nm	0.6	yes	yes
	CCL	0.46	1.5	2.5 nm	0.6	yes	yes
Shinozaki *et al.* [242]	CCL	0.6	0.75	1.5 nm	0.6	no	yes

3 – Results and discussion

Describing water uptake in dependence of CL composition

In order to ensure a consistent parametrization of the model and check its capabilities of handling CL materials with varying composition, experimental water uptake data from Mashio *et al.* [94] and Soboleva [107] are compared with the according model results. The specifications of the materials are listed in Tab. 4.4.

Water uptake data of ionomer-free materials are plotted in Fig. 4.4 (a). The total water uptake follows a monotonous trend, rising from $0\,\mathrm{g_W/g_C}$ to $0.2\,\mathrm{g_W/g_C}$ in the RH range from 0 to 0.8. Beyond $RH > 0.9$ water uptake sharply increases to $\approx 0.5\,\mathrm{g_W/g_C}$, as capillary condensation in the free pore volume sets on. If Platinum is added to the carbon support, additional water uptake of $0.05\,\mathrm{g_W/g_C}$ can be observed, which establishes at already low relative humidity ($RH < 0.2$). The model matches the experimental data for both the bare carbon support material and the Pt/C catalyst powder with Pt:C $= 0.46$. Please note the model results for Mashio *et al.* and Soboleva for Pt/C are identical due to same catalyst used.

If ionomer is included, i.e., assembling an actual functional CL material, water uptake further increases to up to $0.3\,\mathrm{g_W/g_C}$ at $RH = 0.8$. The overall trend persists, only the final raise due to capillary condensation is diminished since a significant fraction of pore volume is occupied by ionomer (see Fig. 4.4 (b) and (c)). The more ionomer is included in the CL material, the larger the overall water uptake. This trend is well captured by the model, although the exact values do not match as accurate as for the ionomer-free materials. The complicated interactions of ionomer with the solid surfaces of Pt and carbon, and thin film effects are suspected to be the cause for the deviation, as they are only covered by the model in a basic manner.

Furthermore, the dataset from Soboleva exhibits a pronounced water uptake, compared to dataset from Mashio *et al.* At $RH = 0.8$ values increase from $0.3...0.4\,\mathrm{g_W/g_C}$ to $0.35...0.6\,\mathrm{g_W/g_C}$. This significant mismatch is attributed to the cold conditions applied by Soboleva. At lower temperature, water uptake of the ionomer increases. The model does not include a temperature dependency, thus, it cannot replicate the dataset measured at 25℃but returns reliable results for 80℃.

Deconvoluting water uptake of PEMFC catalyst layers

Using the proposed model approach, water uptake can be deconvoluted and attributed to the distinct contributions from Platinum, carbon, ionomer and capillary condensation in primary and secondary pores. In the following, a CL made of Ketjen Black carbon support with Pt:C $= 0.5$ and I:C $= 1.0$ serves as reference material.

Figure 4.5 (a) depicts the evolution of saturation as function of relative humidity. At low relative humidity ($RH < 0.2$) only small amounts of water are adsorbed predominately at Platinum nanoparticles and by ionomer. Saturation does not exceed 0.1, i.e., most of the void pore space is not filled with water. Water uptake gradually increases from moderate to high relative humidity ($RH = 0.2...0.8$) and is mainly contributed by functional groups on the carbon supports surface and further increasing absorption
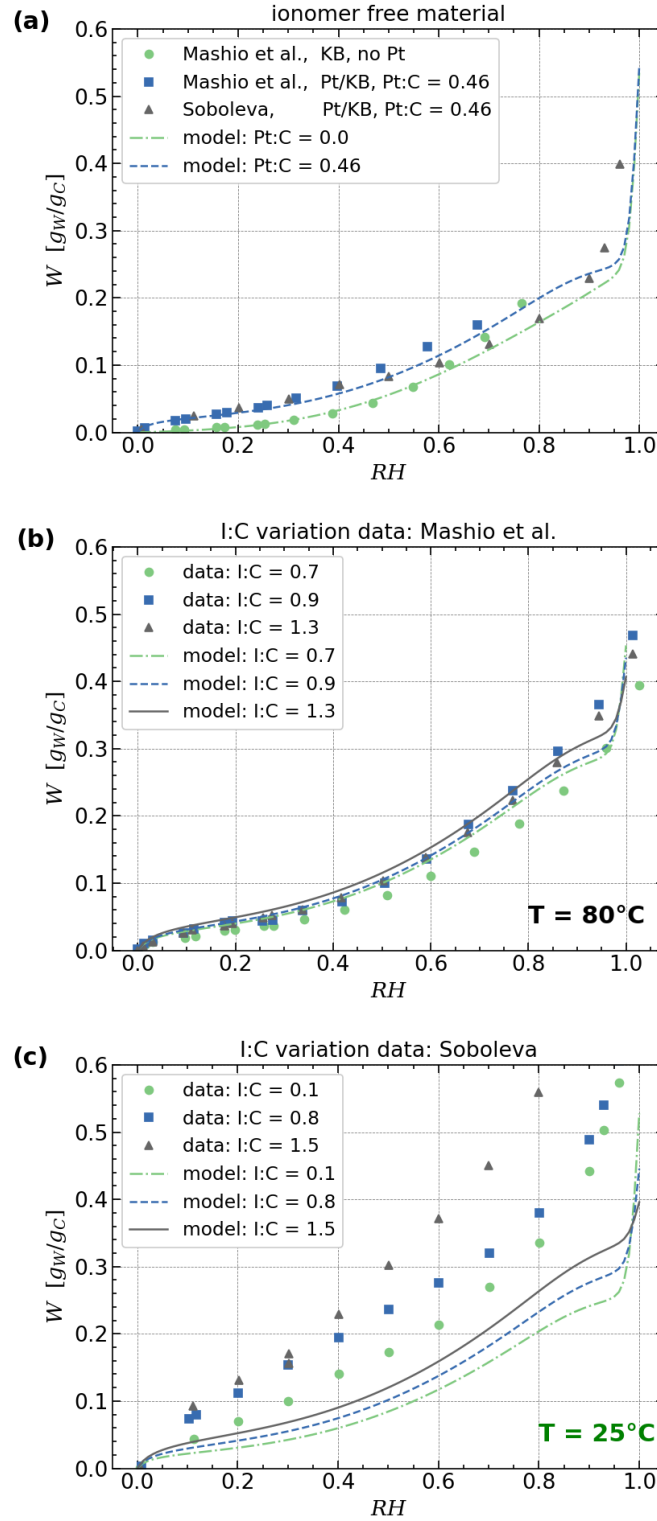
Fig. 4.4: Water uptake data (model and experiment) as a function of relative humidity for: **(a)** ionomer-free Ketjen Black carbon support with and without Pt-loading (Pt:C = 0.46), **(b)** CL material with I:C = {0.7, 0.9, 1.3} measured at 80℃, and **(c)** CL material with I:C = {0.1, 0.8, 1.5} measured at 25℃. Experimental data provided from Mashio *et al.* (Ref. [94]) and Soboleva (Ref. [107]).

of water by ionomer. Capillary condensation sets on at $RH \approx 0.7$ for primary pores, followed by secondary pores at $RH \approx 0.95$. At $RH > 0.8$, capillary condensations poses the predominate contribution to water uptake.

The major fraction of primary pore volume is flooded ($S_{\Sigma,1} > 0.5$) above $RH > 0.6$ and exceeds $S_{\Sigma,1} > 0.9$ for $RH > 0.8$ (see Fig. 4.5 (b)). In operative PEM fuel cells, where water is abundantly generated from fuel conversion and dry conditions, i.e., $RH > 0.5$, are rarely encountered, primary pores can be considered well flooded. Therefore, the Pt catalyst can be considered to be fully utilized for the operative RH range, which is in agreement for most datasets found in the literature (see Fig. 4.1 (a)). It shall be emphasized that capillary condensation is not the only contributor as assumed in the literature [132]. In fact, the picture can be refined in a way that especially at low-to-moderate relative humidity water uptake by the sorption onto the carbon support surface and the Pt nanoparticles is pivotal to accumulate enough water to form a continuous proton supply path.

The liquid saturation in secondary pores stays well below 0.3 for all conditions with $RH < 0.9$ (see Fig. 4.5 (c)). Due to the larger pore radii compared to primary pores, only a minor fraction of carbon support surface is exposed to the secondary pore space. Thus, its contribution is limited to $S_{carb.,2} < 0.2$. Ionomer and Platinum increase the liquid saturation by another 0.1, each. Flooding due to capillary condensation occurs around $RH \approx 1$. Due to the mixed wetting behavior of the ionomer film, only half of the pores flood at $RH = 1$. This behavior is considered favorable for high-performance fuel cells, as enough pore space remains free to ensure effective oxygen supply.

Pt utilization in primary pores at reduced Pt loading

The peculiar behavior of low-Pt-loaded CL materials regarding catalyst utilization at moderate humidity conditions as discussed in the introductory section, will be analyzed in the following. The literature dataset provided by Padgett *et al.* [78] (see Fig. 4.6 (a)) allows first conclusions on the underlying water uptake and its link to Pt utilization. It features two CL material samples with distinct Pt loading and Pt utilization behavior: at Pt:C $= 0.5$, the experimentally observed Pt utilization (X_{Pt}) sharply increases from partial ($X_{Pt} \approx 0.3$) to full utilization ($X_{Pt} \approx 1$) in the RH range from 0 to 0.4; instead, for Pt:C $= 0.1$ the Pt utilization remains almost constant ($X_{Pt} \approx 0.3$) at $RH < 0.5$ and rises to full utilization within the range of $RH = 0.5...1.0$.

Additionally, Padgett *et al.* provided experimental data on the fraction of Pt particles located inside the primary and secondary pore space. Using cryo-tomography in a scanning transmission electron microscope, the fraction of Pt particles exposed to secondary pore space was determined and found to coincide with the catalyst utilization at dry conditions, i.e, $RH \approx 0.1$, [78]. Under such conditions, the primary pores fall dry, thus, only Pt particles exposed to the secondary pore space can be utilized by ionomer, which covers the Pt/C agglomerates surface, thereby providing a connection to the proton supply network. Based on these findings, Pt utilization in secondary pores is assumed to be independent from humidity conditions – which implies that all RH-dependent behavior must have its root cause in the primary pore space.
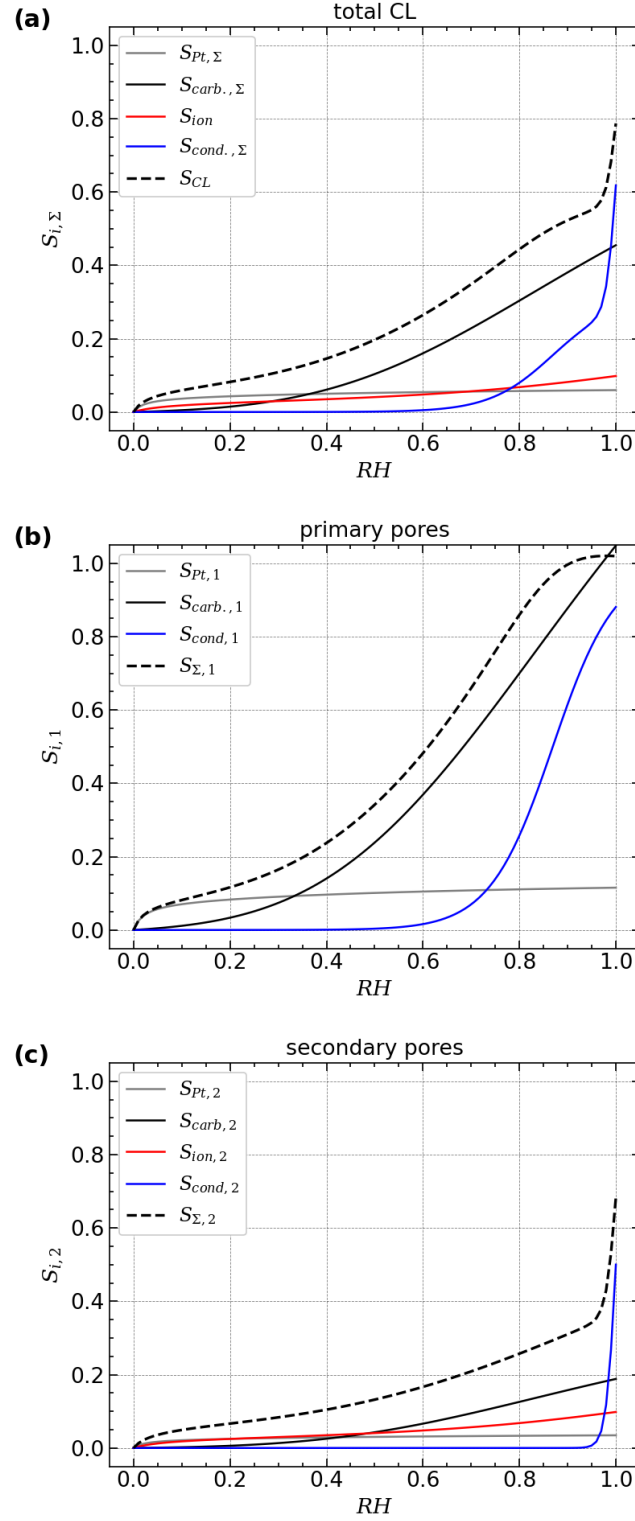
Fig. 4.5: Contributions to water uptake by Platinum, ionomer, carbon support and capillary condensation calculated by the model for a reference material (Ketjen Black high surface carbon, Pt:C = 0.5, and I:C = 1.0) in terms of liquid saturation level of **(a)** the complete catalyst layer, **(b)** in primary pores and **(c)** secondary pores.

To unravel the correlation between liquid saturation levels and resulting Pt utilization inside primary pores, the water uptake model developed in this work can be employed. Model results for the corresponding two CL materials from the Padgett-dataset are plotted in Fig 4.6 (b) and (c). The onset and contributions to water uptake from the different water-adsorbing surface species involved and capillary condensation can be well distinguished for both samples. For Pt:C = 0.1, only minor contributions to water uptake from sorption at Pt nanoparticles is found ($S_{Pt,1} < 0.1$), whereas water sorption on the carbon surface bears the major fraction of water uptake, which raises monotonously from 0 to 1 over the full RH range. Capillary condensation sets on at $RH > 0.8$. However, at this point, the primary pore space is almost fully saturated, i.e., $S_{\Sigma,1} > 0.8$. With higher Pt loading (sample with Pt:C = 0.5), the onset of capillary condensation is shifted to occur at $RH > 0.6$, due to higher surface coverage with hydrophilic Pt nanoparticles, which lower the effective contact angle of primary pores (see wettability model in Ref. [244]). With higher Pt-loading the water sorption at Pt nanoparticles contributes a significant share ($S_{Pt,1} \approx 0.2$) to the liquid saturation level and is established already at dry conditions at $RH = 0...0.1$. Water uptake by the carbon surface remains unchanged by the variation in Pt loading.

In the relevant RH range between 0.3 and 0.7, in which the distinct trends in $X_{Pt}(RH)$ for the two different Pt loading occur, the total liquid saturation level is solely altered by the contribution from sorption at Pt nanoparticles. Furthermore, the sharp rise in X_{Pt} over increasing RH occurs when $S_{\Sigma,1}$ is calculated by the model to increase from 0.2 to 0.5. This threshold behavior resembles percolation phenomena in random media. Thus, water that partially and randomly fills the primary pore space, can be modeled to behave like the percolating phase. Therefore, an approach based on percolation theory is tested for its capabilities to reproduce the experimentally observed behavior, i.e., to describe Pt utilization as a function of relative humidity. The proposed analytical correlation is composed by a RH-independent offset attributed to Pt particles exposed to the secondary pore space and the utilized fraction of Pt particles inside the primary pores as function of $S_{\Sigma,1}$, which, in turn, is a function of RH,

$$X_{Pt}(RH) = (1 - \phi_{Pt,1}) + \phi_{Pt,1} \; \mathcal{P}(S_{\Sigma,1}(RH)). \qquad (4.21)$$

The threshold-behavior is captured by the sigmoid function $\mathcal{P}(S)$, which describes the likelihood of establishing a continuous proton-conductive pathway in the primary pore space occupied by water,

$$\mathcal{P}(S) = \frac{1}{1 + \exp\left(-\frac{S - S^{(C)}}{b}\right)}. \qquad (4.22)$$

The parameter b controls the width of the sigmoids step and was set to 0.1 to match the experimentally observed RH-span for the sharp raise in X_{Pt}. The percolation threshold $S^{(C)}$ was assumed to be 0.3, corresponding to an ideally random percolating medium with three dimensions.

The direct comparison of the percolation model with the experimental data (see Fig. 4.6 (a)) shows not an exact match, but a clear offset, for both the low and high Pt-loaded material. For Pt:C = 0.5 the raise of Pt utilization with increasing relative
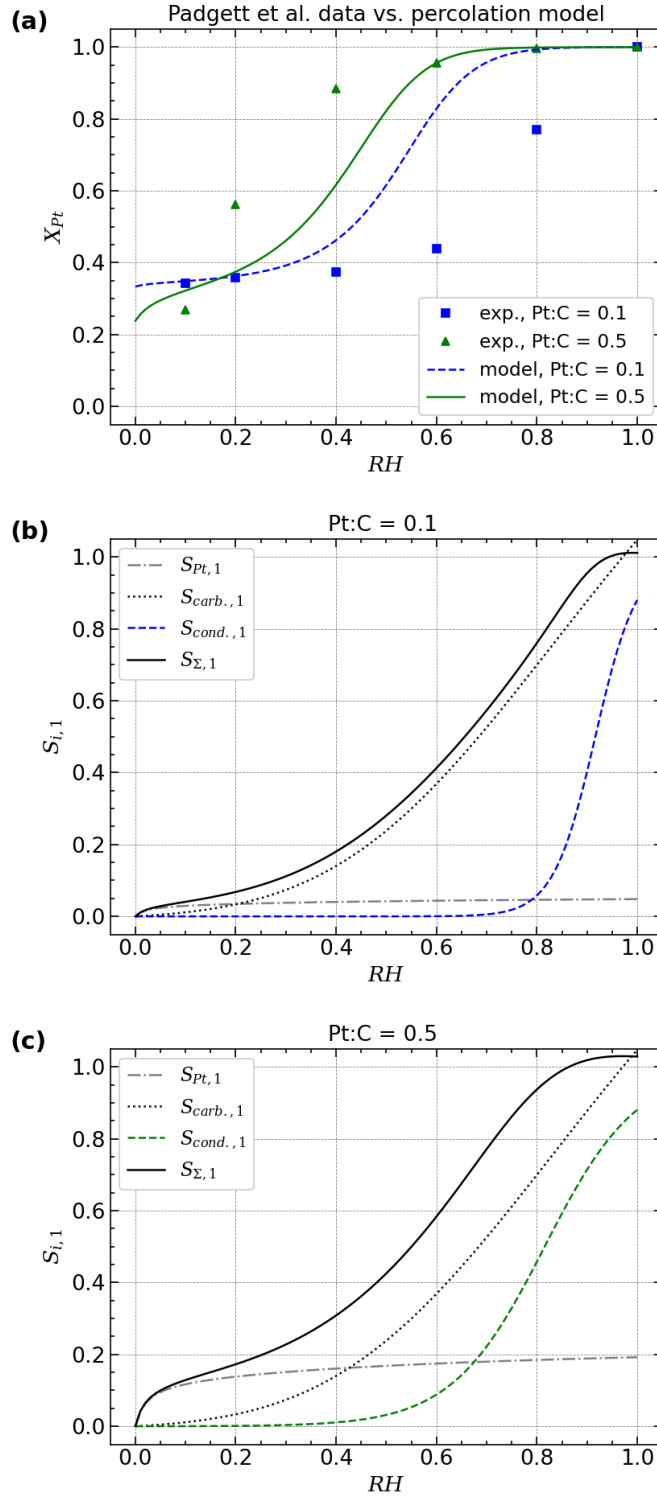
Fig. 4.6: **(a)** Comparison of Pt utilization data provided by Padgett *et al.* in Ref. [78] and the according model results obtained using a percolation-based approach. The water uptake calculated by the model in terms of liquid saturation level in primary pores reveals the distinct contribution of water sorption by Pt nanoparticles for the two material samples with **(b)** Pt:C = 0.1) and **(c)** Pt:C = 0.5.

humidity is predicted to occur at RH values larger by 0.2 than the experimental data. Conversely, for Pt:C = 0.1, the step in Pt utilization is calculated to occur at significantly smaller value than indicated by the experimental data. This result can be interpreted in a way that the percolation-based approach describing a random media might not be sensitive enough to differentiate the essential mechanism of Pt utilization by adsorbing water. Instead, details on the geometry and location of Pt particles and primary pores might be decisive. For instance, if a continuous pathway can be established by overlapping water films, as hypothesized by Chowdhury *et al.* [119], then the effective distance between Pt nanoparticles and their distribution inside the agglomerate might play a crucial role – and might be altered significantly by varying Pt:C ratio. Such details of the CL microstructure fall in the sub-agglomerate scale and cannot be captured by the statistical descriptors developed in this work. Nonetheless, the fundamental trends in $X_{Pt}(RH)$ could be reproduced using a basic percolation-type approach.

Together with the results from the deconvolution of water uptake, it can be concluded that water sorption at Pt nanoparticles located in primary pores is the most plausible origin for the distinct Pt utilization in PEM fuel cell catalyst layers – and not the altered wetting behavior of the pore walls and the thereby shifted onset of capillary condensation. However, further details on how and under which circumstances these changes in water uptake induced by varying Pt:C ratios trigger the distinct trends in Pt utilization cannot be scrutinized and are left for future research.

4 – Conclusion

Liquid water plays a crucial role in proton-exchange membrane fuel cells as it utilizes Platinum nanoparticles in the catalyst layer to partake in the electrochemical fuel conversion. The establishment of a well-connected proton supply pathway was found to correlate with water uptake from a partially vapor-saturated atmosphere. Here, low-Pt-loaded catalyst materials exhibit a peculiar behavior of a significantly lowered Platinum utilization at low-to-moderate humidity conditions, which deserves special attentions with regard to ongoing efforts to reduce Platinum loading for future commercial fuel cell devices.

In order to investigate this relationship, a model has been developed to deconvolute the distribution of water inside the catalyst layer microstructure. A literature model was adapted and generalized by a fully structure-based parametrization. The model approach builds on the distinction of contributions from adsorbed water on Platinum, carbon support and ionomer, and condensed water in the pore space. Experimental data from the literature that correlate water uptake and with relative humidity could be successfully reproduced by the model. The model results allowed to scrutinize the relevant contributors to water uptake for different humidity conditions and catalyst layer compositions.

The analysis of water uptake indicated that Pt utilization inside the primary pores of the agglomerated microstructure of the catalyst layer is facilitated through adsorbed water at Pt nanoparticles. An approach applying percolation theory to the liquid saturation level of primary pore space was proposed to analytically link Pt utilization and relative humidity. The model results could capture the essential trends but exhibited a significantly lower sensitivity regarding the Pt-loading. Therefore, the underlying mechanism and relations of Pt utilization by adsorbed water are conjectured to be controlled by structural details on the sub-agglomerate scale, e.g., the inter-particle distance of Pt nanoparticles, which remain subject to future research.

5   Summary and discussion of results

The results from the publications cumulated in this work are summarized in the following sections, including insights to structure formation during ink stage (5.1), crucial relations between wetting behavior and catalyst layer microstructure (5.2), the impact of ionomer morphology on proton conductivity (5.3), and a model-based analysis of Platinum utilization (5.4). The discussion will contextualize the structure-based models developed and their essential results with regard to requirements of holistic catalyst layer design introduced in section 3.1. Derived guidelines for purposeful catalyst layer design and future research approaches for both experimental and theoretical works are elaborated on in sections 5.5 and 5.6.

5.1   Structure formation during ink stage

A composition model was developed to rationalize the structure formation during ink stage in catalyst layer fabrication. Thereby, the model introduced a common framework of metrics that describe the agglomerated CL microstructure, including pore size distribution, ionomer coverage and ionomer film thickness. The details of the model were documented in publication II. The composition model was used in publication II and publication III to link catalyst layer properties with ink parameters and derive approaches to tune the catalyst layer to desired properties.

The composition model describes the formation of the ionomer structure as an incremental assembly of the composite. Ionomer mobilized in the ink solvent can either attach to uncovered Pt/C surface, or deposit on an existing ionomer film and thereby contribute to film thickness growth. Any ionomer not deposited as part of the ionomer film forms large, dense aggregates embedded in the catalyst layer structure and is therefore considered not to be part of the porous network. The incremental assembly of ionomer films was analytically described by a set of two differential equations. The solution of the model introduces a novel dispersion parameter k_A, which captures the tendency of ionomer to form thin films or to aggregate. The second key parameter is the initial film thickness t_0, which serves as a measure for the length scale of the first layer of ionomer molecules deposited on the Pt/C surface. Additionally, parameters quantifying the pore size distribution of the carbon support and the I:C ratio must be provided as model input. The model output provides the ionomer film geometry, the volumetric composition and pore size distribution of the resulting catalyst layer microstructure.

By analyzing experimental data from the literature using the composition model, three growth stages can be distinguished: initially, the coverage growth of ionomer film dom-

inates and an ionomer film covering most of the agglomerate's surface emerges rapidly; once the film is established, a phase where the film grows mainly in thickness follows; ultimately, thickness and coverage cannot grow further and excess ionomer not incorporated in the ionomer film expands the total catalyst layer volume. For a typical ink formulation extracted from the literature ($k_A = 4.5$ and $t_0 = 6.5\,nm$, using a high surface area carbon support), at increasing I:C ratios (> 0.5), additional ionomer volume expands the catalyst layer volume compared to the ionomer free structure. At small I:C ratio (≈ 0.3), a volume contraction occurs, which is also observed in experimental data. This contraction is conjectured to be caused by ionomer binding the carbon particles closer together. The evolution of microstructure matches the experimentally observed behavior in the literature: ionomer fills the secondary pores but not all ionomer is used to replace pore volume. Literature data for ionomer coverage are found to be in good agreement with the model as well. Also, the calculated ionomer film thickness matches the experimentally observed range of $5...15\,nm$.

Systematic parameter studies conducted in publication II and publication III showed how ionomer coverage and thickness emerge differently for varying ink parameters. If both ionomer dispersion and initial film thickness are reduced ($k_A = 2$ and $t_0 = 4\,nm$), ionomer coverage is established only at rather high I:C ratios ($a_{ion} > 0.5$ at I:C > 0.5) and the resulting film thickness stays low ($< 8\,nm$) for any given I:C ratio. Thus, only little ionomer is deposited as part of the thin film in the secondary pore space and more pore volume remains free. Excess ionomer becomes the major fraction of ionomer that forms a significant amount of larger aggregates. In contrary, for values $k_A = 5$ and $t_0 = 8\,nm$, representing ionomer that adsorbs well on the agglomerate surface, the resulting film is rather thick ($> 15\,nm$ at I:C > 0.6). In this scenario, ionomer coverage increases sharply at low I:C ratios and aggregation outside the ionomer film is suppressed.

A higher degree of complexity of the structure formation process might be implemented in future works. Details on structure formation during ink stage remain subject to ongoing investigation in the experimental literature, too. The common understanding suggests that the solvent used during ink stage alters the balance between polar and dispersion interactions among ionomer molecules and between the ionomer and the Pt/C surface. Accordingly, varying the ink solvent or manipulating the chemical nature of the carbon surface has been found to be very effective in the literature. Ongoing experimental developments suggest that there is great potential for tweaking ionomer dispersion during the fabrication process. By focusing on the interactions between ionomer and catalyst, and also between ionomer and ink solvent, the model provides actual guidance on how to tune the catalyst layer microstructure. In the future, systematic studies are needed to understand how k_A and t_0 are constituted and affected by various processing parameters during catalyst fabrication. Here, the proposed composition model can serve as an analysis tool for experimental research.

5.2 Relations between wetting behavior and catalyst layer microstructure

The development of a modeling approach that captures the heterogeneous and complex wetting behavior of PEM fuel cell catalyst layers required a combination of two sub-models: firstly, a novel analytical approach to link the molecular alignment inside ionomer thin films with the films wetting properties was carved out from a comprehensive review of the literature in publication I; secondly, the distribution of surface species and their respective wetting properties over the catalyst layer's pore network were modeled using a statistical approach that is documented in publication II.

As a key feature, the developed model describes the role of ionomer for catalyst layer wetting properties. The alignment of ionomer molecules at the catalyst-ionomer interface determines the exhibition of hydrophilic or hydrophobic properties. The following mechanism was proposed in the literature: Platinum strongly interacts with the ionomer sidechains, imposing an alignment that leaves the hydrophobic backbone exposed to the outer surface of the ionomer film. In contrary, a hydrophobic carbon surface causes the ionomer sidechains to orient away from the ionomer-carbon interface, rendering the ionomer film hydrophilic. This work collected supporting data from the theoretical and experimental literature in publication I, including molecular dynamics studies, surface probing of CL materials with microdroplets, macroscopic water retention measurements, and microscopic and spectroscopic methods. Based on the literature reviewed, this work proposes a novel descriptor, the ionomer's degree of alignment Δ_{DA} that correlates the orientation of ionomer molecules with the resulting contact angle of the ionomer film exhibited to the secondary pore network. The dimensionless value of Δ_{DA} is defined to be in the range of 0...1 and corresponds to the full scale of ionomer contact angles observed in the literature, reaching from hydrophobic ($\theta = 120°$ for $\Delta_{DA} = 0$) to hydrophilic ($\theta = 30°$ for $\Delta_{DA} = 1$) properties.

By applying a model-based analysis employing the proposed correlations, the boundary conditions for the effective exhibition of hydrophobic properties were estimated in publication I. Platinum nanoparticles should constitute a minimum of around 50% of the surface fraction in secondary pores to render the ionomer film hydrophobic, i.e., $\theta_{eff} > 90°$. Additionally, ionomer coverage must also be high. Given an optimal alignment, i.e., a maximized hydrophobicity of the ionomer thin film, still a minimum of 70% ionomer coverage on the secondary pore space surface area is required to uphold hydrophobic properties. Given this crucial role of the Platinum-ionomer interaction and a high ionomer coverage, an explanation for the occurrence of severe oxygen transport losses when reducing Platinum loading of the catalyst layer can be derived: lowering the Platinum loading while keeping the CCL thickness constant can cause an inversion of the wetting behavior of the Pt/C/ionomer composite due to the reorientation of the ionomer. This hypothesis is consistent with a previous work from the literature where the scenarios of achieving a Platinum loading reduction were considered, corresponding to constant composition or constant thickness. For the constant composition scenario, trimming the platinum loading translates to a reduction in catalyst layer thickness. This consequently reduces the vaporization capability and thereby shifts the tipping point for flooding to lower current densities. This work completes the larger picture of the water balance tipping over when

lowering the platinum loading: in any case, regardless of whether a low Platinum loading is achieved by thickness reduction or by dilution, the water balance of the cell is disrupted and the porous layers will flood. This hurdle is especially critical for current research efforts that aim to further reduce Platinum loading. Publications I and II both discuss altering the carbons chemical nature so ionomer aligns hydrophobically as a suitable mitigation strategy to overcome limitations reducing the Platinum loading. Experimental materials were identified in the literature that might have the potential to employ such an approach, namely Nitrogen doping of the carbon support.

To relate wetting properties to actual performance of cathode catalyst layers, water retention curves have been identified as the most suitable descriptor for this purpose in the literature. In publication II, a complementary model has been developed that resolves the experimental limitations of measuring a large number of water retention curves. The water retention curve is calculated from the statistical distribution of surface species with distinct wetting properties (e.g., Platinum nanoparticles and ionomer) inside the catalyst layers porous network. Employing the metrics established by the composition model from publication II, information on pore network geometry (specifically, the pore size distribution) is utilized as model input parameter. The contact angle distribution and water retention curve of the catalyst layer were simplified to closed-form analytic expressions, fostering the direct implementation of the model in computationally expensive optimization routines for holistic fuel cell design.

Evaluation of the model confirmed that the primary pores never fall dry under any relevant operating conditions. However, the secondary pores instead might turn out hydrophilic or hydrophobic depending on the catalyst layers ink parameters. To scrutinize the impact of material choices on water management a systematic parameter study has been conducted in publication II.

The reference catalyst layer material for the parameter study (Pt:C=0.4 and low surface area carbon) exhibits a maximum in hydrophobicity at an I:C ratio of around 0.5. This trend can be explained by the ionomer film initially growing rapidly in coverage, leading to increasingly hydrophobic wetting properties. With more ionomer added, the ionomer film begins to grow in thickness, which weakens the hydrophobic alignment of the backbone towards the secondary pore space. This maximum in hydrophobicity at an intermediate I:C ratio has also been reported in experimental literature. If the I:C ratio falls below 0.3, the ionomer coverage will not be sufficient to cover significant parts of the pore walls, leaving the intrinsic hydrophilicity of the Pt/C surface exposed, and the catalyst layer remains overall hydrophilic for any Pt:C ratio.

Variation of the dispersion parameter k_A from 1.5 to 6 resulted in a similar trend to the I:C variation. Initially, hydrophobicity increases, followed by a collapse of hydrophobic wetting behavior. The underlying picture is similar to that of I:C variation, with only the morphology of the ionomer film being affected. For low values of k_A ($k_A \leq 2$), a thin ionomer film with poor coverage forms, and a larger amount of ionomer aggregates inside the catalyst layer without contributing to film formation. At $k_A \approx 3$, the ionomer dispersion reaches an optimum of high coverage and film thickness that is not too high to impair wetting properties. Above $k_A > 5$, the ionomer strongly adheres to the Pt/C structure during the ink stage, resulting in coverage of close to 100% and an increasing film thickness.

Based on this understanding, the two main parameters for tuning the ionomer properties, I:C and k_A, were evaluated in combination. A higher value of k_A requires a lower I:C ratio to achieve hydrophobic wetting behavior. Also, the I:C window becomes narrower at higher k_A. For a low-dispersed ionomer ($k_A = 3$), any I:C in the range of 0.5 to 1.5 will result in a mostly hydrophobic catalyst layer. At $k_A = 8$, the range where the hydrophobic condition occurs is lowered to I:C = 0.2...0.7.

With regard to the previously identified tip-over of water balance, the Pt:C ratio was studied in combination with an I:C variation. The window between lowest and highest possible I:C that ensures hydrophobic properties shrinks dramatically when lowering the Pt:C ratio. Whereas the I:C window at Pt:C > 1 reaches from 0.3 to 1.3, a diluted catalyst (Pt:C < 0.1) cannot be turned effectively hydrophobic for any I:C.

In another study in publication II, the model was employed to evaluate durability of wetting properties with regard to goals in current fuel cell research. Carbon corrosion can be addressed by assuming that the carbon support shrinks in mass. Increasing the ionomer content per Pt/C surface by shifting the I:C ratio leads to larger ionomer coverage and thickness, ultimately resulting in a decrease in hydrophobicity. Additionally, if the Pt particles grow due to coangulation and redeposition, the wetting behavior shifts into the hydrophilic regime. These trends over prolonged cell degradation are confirmed by experimental studies in the literature, observing an increased hydrophilic wetting behavior after accelerated stress tests.

In future works, the wettability model proposed in this work, especially the novel approach of the degree of alignment can be refined further by including factors such as Platinum/ionomer interface hydration and the potential dependence of this interaction on electric potential. While these factors contribute to ionomer film wetting properties, their exact mechanisms and extent of influence are speculative. Molecular dynamics simulations in the literature suggest that sidechain alignment dominates molecular structure, while the secondary formation of micelles and layered structures of ionomer molecules depends on humidity conditions. Further experimental and theoretical studies are necessary to better understand the complex interactions between ionomer film and substrate or catalyst in order to improve models for structure-property relations.

5.3 Impact of ionomer morphology on proton conductivity

The structure-property relationship between ionomer morphology and proton conductivity is subject to publication III. The literature provides numerous dataset that correlate proton conductivity with catalyst layer composition. However, available analytical relations are adopted from general theories for random heterogeneous media and ignore essential details of the catalyst layer microstructure, such as film-like structures of ionomer, or the hierarchical porous network inside the agglomerates structure.

To disentangle the underlying dependencies between structural parameters and effective proton conductivity, this work proceeded in two steps. Firstly, synthetic volumetric images of the catalyst layer microstructure were generated in a mesoscopic volume element and proton conductivity via the electrolyte phase was calculated using numerical tools. The algorithm for structure generation utilized the geometric information provided by the composition model previously developed in publication II. Secondly, the model complexity was reduced by coining insights from simulation results to mathematical expressions.

Two limiting cases have been identified in systematic parameter studies varying the geometry of the ionomer thin film covering the catalyst particles. Either a thin film with high coverage on the catalyst agglomerates is formed; or the ionomer aggregates as voluminous chunks that connect across the inter-agglomerate space. Adapting relations from percolation theory, both cases were modeled in closed-from expressions, providing the model with a solid theoretical basis and trimming computational complexity to a minimum.

Regarding the quantitative results of the parameter study of ionomer coverage a_{ion} and film thickness t_{ion}, highest values for proton conductivity g are obtained for morphologies with large ionomer coverage ()$a_{ion} > 0.8$). In this scenario, g scales almost linearly with the ionomer volume fraction x_{ion} in the catalyst layer. Extrapolation towards $x_{ion} = 0$ indicates a vanishing percolation threshold. For scenarios where $a_{ion} < 0.5$, a percolation threshold is evident around $x_{ion} \approx 0.15$. Where the threshold is exceeded, the conductivity scales with a power-law behavior with $\alpha \approx 2$. Further analysis of simulation results revealed that any intermediate cases of moderate ionomer coverage can be interpolated from superposition of the two limiting cases of high and low ionomer coverage.

Since increasing the coverage of ionomer has a greater effect on proton conductivity compared to increasing film thickness, ink formulation or interaction of ionomer with Pt/C catalyst should be tweaked towards well-defined films with high coverage of catalyst agglomerates in order to boost proton conductivity. Linking these requirements to composition model parameters, $k_A > 3$ and $t_0 > 6.0\ nm$ should be chosen.

The various datasets from the experimental literature collected in publication III that correlated ionomer content in the catalyst layer with proton conductivity were analyzed using the proposed analytical correlations. The presented approach was found to be a versatile tool for the interpretation of experimental trends. The comparison of the results from the model with experimental literature data illustrates how distinct ionomer morphologies can explain different trends in proton conductivity. The single datasets are well captured by the model and were linked to different scenarios of ionomer morphology.

Furthermore, the comparison of literature data with the model revealed a discrepancy regarding the intrinsic conductivity of the ionomer film. In fact, it was estimated that the thin film conductivity in polymer electrode catalyst layers is effectively increased by a factor of ≈ 3, whereas the model assumes equal proton conductivity for the ionomer thin films and the bulk ionomer. This assumption might not be true since structural reorganization within the thin films could alter the proton conductivity. Proton mobility has been reported to be impaired or enhanced in PFSA thin films, depending on the solid substrate used. On Platinum substrates, a well-defined water layer forms at the Pt/ionomer interface, increasing the conductivity by an order of magnitude compared to silica substrates. As a result, the thin film conductivity in catalyst layers may differ significantly from the bulk ionomer conductivity. In addition, the roughness and curvature of the agglomerate surface in real catalyst layer materials might be significantly lower than those in the simulations due to water uptake or ionomer swelling, which effectively reduces the tortuosity of the proton conducting pathways. However, both the effects of tortuosity and the pronounced ionomer conductivity could not be reliably quantified in this work and need further research.

5.4 Model-based analysis of Platinum utilization

Focusing on water as a vital component in PEM fuel cell catalyst layers, a model has been developed to deconvolute the distribution of water inside the catalyst layer microstructure, i.e., adsorbed water films on Platinum and carbon surfaces, water absorbed by the ionomer, and condensed liquid water in the volume of the porous network. In order to obtain a comprehensive understanding of Platinum utilization by water present inside the catalyst layer, experimental data from the literature that correlate water uptake and Platinum utilization were analyzed. Details of the modeling approach are documented in section 4.4.

As starting point, a literature model was adapted so that parameters quantifying the concentration of sorption sites inside the catalyst layer could be coupled to the composition model from publication II. For water uptake at Platinum nanoparticles and carbon surfaces, and in the ionomer electrolyte phase, sorption isotherms from the literature were used. The calculation of capillary condensation was modified to employ the Kelvin equation, taking contact angle and pore size distribution provided by the wettability model proposed in publication II as input parameters. In fact, this need for a structure-based parametrization of wetting properties preceded the development of the wettability model in publication II.

In the literature it been assumed that Platinum is rendered active, i.e., utilized for electrochemical conversion, if wetted by liquid water. Another, complementary hypothesis proposed utilization via cross-linking adsorbed water films around sorption sites at Platinum nanoparticles or functional groups on the carbon supports surface. Peculiarly, Platinum utilization follows fundamentally different trends for low or high Pt:C ratios. In this work, it was suspected that the first or second hypothesis applies as a mechanism for Platinum utilization depending on wetting behavior of the catalyst layer and concentration of sorption sites. To test this conjecture, the water uptake model was parameterized using, where possible, parameters from the literature and was corroborated with exper-

imental water uptake data from different sources from the literature for bare carbon support, ionomer-free catalyst material with Pt:C = 0.1 and Pt:C = 0.5, Platinum-free composite material with I:C = 1.0, and a complete catalyst layer composite material.

As a result from this model-based analysis, water uptake from the vapor phase could be successfully deconvoluted and attributed to the distinct contributions from Platinum, carbon, ionomer and capillary condensation. At low relative humidity ($RH < 0.2$) only small amounts of water are adsorbed predominately at Platinum nanoparticles and by ionomer. Water uptake at functional groups on the carbon supports surface contributes a minor fraction of total water uptake gradually from moderate to high relative humidity ($RH = 0.2...1$). At $RH > 0.8$, ionomer and primary capillary condensation bear the major fraction of water uptake, followed by the onset of capillary condensation in the secondary pores at $RH > 0.95$.

A first attempt to scrutinize the details of Platinum utilization applied an analytical expression derived from percolation theory, in which the liquid saturation in primary pores of the catalyst layer was taken as a measure for occupation with proton-conductive phase. The percolation-type approach could reproduce the general trend but displayed a significant mismatch regarding the onset of Platinum utilization with increasing RH. The used analytical approach was found not to be sensitive enough to account for essential details of Platinum particle geometry and distribution on the sub-agglomerate level – which might vary drastically when the Platinum loading is altered. Therefore, the development of a model with higher resolution was subject to student research projects that were supervised during this work. The most promising approach employed a graph-based model and was first tested by participants of the *CAMMP week Pro 2021* seminar at RWTH Aachen University [248] and was followed up by master student Vera Hauser in a seminar project [249]. The students' approach spatially resolved the details of proton pathways inside the catalyst layer on the pore scale and demonstrated that apparently not all relevant mechanisms for Platinum utilization are covered by the current understanding in the literature. Nonetheless, some fundamental trends could be captured and rationalized by the underlying structural features described by the graph-based microstructure model.

Since in operational fuel cells liquid water is abundant, a complete understanding of Platinum utilization is considered only moderately critical for developing commercial fuel cells and is left to future fundamental research.

5.5 Purposeful design of PEMFC catalyst layers

The models for catalyst layer wetting behavior and proton conductivity were evaluated in publication II and III with regard to potential improvements of fuel cell performance to meet the PEM fuel cell development goals introduced in section 1.7. A special focus was put on increasing power density and efficiency while reducing Platinum loading to further reduce the nominal costs per power output. The derived guidelines for future development of catalyst layer materials are summarized in the following – together with implications for future materials research.

Regarding wetting behavior of the catalyst layer, the design principles devised here aim to increase the hydrophobicity of the catalyst layer material to ensure a sufficient resistance against flooding under increasing current densities:

1. A high ionomer coverage on the catalyst agglomerate is pivotal to establish any hydrophobicity at all. Thus, a_{ion} should always be significantly larger than 70%, preferably even close to 100%.

2. Since the magnitude of ionomer alignment quickly decays over ionomer film thickness, it must not be too thick, i.e., it should be adjusted to remain as close as possible to the initial film thickness t_0.

3. Ionomer coverage and film thickness emerge alongside with increasing with I:C ratio. Therefore, the ink parameters k_A, t_0, and I:C must be well adjusted to match each other. The optimal set of ink parameters will also depend on the total surface area ot the Pt/C catalyst to be covered, i.e., is affected by the choice of low or high surface area carbons as support materials. Generally, a higher value of k_A requires a lower I:C ratio to achieve hydrophobic wetting behavior, and vice versa. Furthermore, the I:C window where the hydrophobic condition occurs becomes narrower at higher k_A. For the low surface area carbon reference material discussed in publication II, the tolerated range is I:C = 0.3...1.3 at $k_A = 4.5$.

4. Catalyst layers with a strongly diluted Platinum concentration, i.e., Pt:C < 0.1 require special attention: using state-of-the-art carbon support materials, a hydrophobic wetting behavior can be hardly achieved. Generally, the lower the Pt:C ratio, the less room remains to maneuver with regard to the I:C ratio. This is of particular importance when reducing Platinum loading for cost efficient catalyst layers. This work devised the approach to direct innovation towards chemically modified carbons to counteract the tipping water balance encountered when reducing Platinum loading.

5. Where aging cannot be mitigated, fuel cell developers should include an adequate safety margin in hydrophobicity since degradation of the cell by carbon corrosion or coarsening and dissolution of the Pt nanoparticles can cause the wetting behavior to invert from hydrophobic to hydrophilic properties.

The following design guidelines apply with regard to the objective to enhance proton conductivity for high-power-density PEM fuel cells:

6. A high ionomer coverage close to 100% is the primary lever to maximize proton conductivity. Aggregated ionomer morphologies should be avoided. A well-defined film is the primary objective of an optimized ink formulation. Therefore, for common I:C ratios, $k_A > 3$ should be chosen.

7. Secondly, proton conductivity scales linearly with ionomer film thickness and therefore should be increased as far possible. In order to not fall behind the proton conductivity of state-of-the-art catalyst layers, $t_{ion} > 6.0\,nm$ should be chosen.

Ideally, these guidelines are all realized in a purposefully designed catalyst layer material. Regarding the ionomer coverage and the requirement of a well dispersed films, the objectives for high hydrophobicity and high proton conductivity do not conflict. To provide enough ionomer to establish sufficient ionomer coverage, will result in a minimal ionomer

content for most materials in the range of I:C $= 0.3...0.5$, depending on the exact catalyst material, type of ionomer used, and fabrication parameters. Moderate to high values of the ionomer dispersion parameter ($k_A \geq 4$) can be realized in this window. Adjusting the film thickness will need a compromise between the requirement of a low film thickness from wetting properties requirements, and a high film thickness for proton conductivity. Given the ranges for I:C and k_A, the middle ground will be most likely around $t_{ion} \approx 10\,nm$. This implies values $< 10\,nm$ for t_0. Here, any value between $5\,nm$ and $10\,nm$ will fulfill the above requirements.

At this point, it shall be noted that the above set of parameters is not to be applied universally. In practice, catalyst layer properties must be properly integrated into the transport properties of neighboring layers and the cells operation conditions. Here, the proposed modeling framework of this work provides the toolset to conduct a directed, purposeful choice of materials and ink parameters to obtain a catalyst layer with desired properties.

The approach to tune the ionomer morphology was found to be in line with experimental works in the literature, where the choice and composition of the ink solvent is proven to affect ionomer dispersion and film formation. Additionally, numerous literature works implied that also processing time, agitation and dispersion techniques (e.g., ultra-sonication), stirring, milling, subsequent thermal treatment, etc. all affect the final ionomer morphology obtained. Further tailoring of catalyst layer materials can involve modifying the chemical nature or morphology of the carbon support material. Here, the role of carbon modification is two-fold: an altered interaction with ionomer molecules can possibly enhance dispersion, and strengthen hydrophobic alignment. Among the experimental works reviewed in this work, Nitrogen doping was found to be the most promising approach.

The above stated design principles and practical approaches collected in this work demonstrate how fuel cell developers can customize the catalyst layer structure by intentionally adjusting its microstructural features during fabrication. Being more cost- and time-efficient than empirical screening of materials, the model supports an optimal design of experiment and thereby fosters rapid fulfillment of development goals for commercial fuel cell devices. Furthermore, quantitative modeling can serve to interpret experimental data since it provides a fundamental understanding of observed trends and might suggests directions for future materials improvements. Ultimately, the proposed model contributes to holistic optimization of catalyst layer properties under an integrated perspective within the complete fuel cell device. The provided unified framework to correlate ink parameters with catalyst layer structure, and, subsequently, structure with properties and performance, lays the foundation for future modeling works. Structure-property relationships subject to follow-up research will be discussed in the final section of this chapter.

5.6 Future research to enable holistic PEM fuel cell design

The presented models provided numereos novel insights as discussed in the previous section – and also sparked new questions arising in the realm of structure-based modeling of PEMFC catalayst layers.

The proposed model for incremental self-assembly and ionomer aggregation lumps all details on the solvent properties, ionomer-carbon interactions, etc., in the key parameters k_A and t_0. In order to gain deeper understanding on how to adjust ink parameters, such as the choice of solvent, these parameters could be derived from molecular properties. Effective quantities, e.g., the solvent's dielectric constant [97], that modulate the relevant interactions could link molecular solvent structure and resulting effects for the agglomeration process.

In fact, the experimental database on tested ink parameters and solvents used is already highly extensive – and keeps growing [113]. Systematically collecting different solvent compositions (together with other fabrication parameters) and link them to k_A and t_0 empirically might also contribute to support the choice of solvent for fuel cell developers.

The increased proton conductivity of ionomer thin films hypotized in this work should be further corroborated by both experimental and theoretical works. The experimental literature already provides indications for various substrates but not for catalyst materials as used in real devices. Methodologically, proton mobility in ionomer thin films could be evaluated theoretically by MD studies. In agreement to this work, a past study already indicated increased proton mobility [250] in supported Nafion® films. However, the root cause for this phenomenon requires further investigation.

The mechanism for Platinum utilization is well understood for the flooded condition of the pore space and high Platinum loading. However, this work carved out a gap in the theory for Pt utilization in low-Pt-loaded catalyst layers. As conjectured in this work, the highly RH-sensitive Pt utilization might be explained by an ultra-thin water film and/or changes in the structural details on the sub-agglomerate scale but requires further fundamental theoretical and experimental investigation.

Holistic fuel cell design must not solely address wetting properties, proton conductivity, and Platinum utilization. A fully integrated fuel cell design requires modeling of other essential phenomena and catalyst layer properties that were not in the scope of this work. The following phenomena should also be included to cover all relevant processes and potential sources of voltage losses in high-performance fuel cell devices.

At present, all kind of mass transfer phenomena, including gas diffusion and liquid permeation, and phase transitions of water, can be modeled with satisfying results in MHMs for isothermal conditions [165]. On the mesoscale, comprehensive studies of fluid flow by DNS, LBM and PNMs investigated transport properties of the catalyst layer porous structure [190, 204, 251–253]. Thus, accurate models for mesoscale and macroscale exist. Hence, future efforts should focus on extending and close the cause-effect relation to ink parameters and intensify bridging between the modeling scales. With regard to multiscale modeling, different approaches in the literature discussed the concept of effectiveness fac-

tors [110, 164, 213], i.e., descriptors accounting for the ratio of ideal to effectively realized reaction rate of the catalyst layer. Future works could merge the insights on the varying heterogeneous reactions conditions from pore scale models [69, 254] with statistical descriptors to calculate averaged reaction rates, similar to how this work treated the heterogeneities in wetting properties.

Recent insights from the experimental literature indicate that water transport is significantly controlled by temperature differences across the cell [255], with even minor thermal gradients trigger intense coupled heat-mass-transfer. Therefore, wetting behavior and thermal management could face intensified joint discussion in future modeling works and the role of CL wetting properties might be revised as novel measurement techniques to determine the water balance *in operando* emerge [256].

Once all parameters required for extensive macroscale simulation of the fuel cell device are integrated via structure-based models, the complete modeling chain from ink parameters to device performance can be demonstrated. If successful, this could proof and eventually realize the concept of model-driven holistic cell design. The ultimate proof might deliver an joint experimental and modeling work, in which a material is designed by the model, and experimentally synthesized and characterized. In the past, optimization routines for single aspects, e.g., for graded catalyst layers [257] or optimized flow-field geometry [258], have successfully facilitated such model-driven CCL design. The next stage of optimization might include multiple components, and each with multiple properties, at once, with each property tailored to match the overall-optimal cell design.

On the bigger picture, modeling approaches keep evolving as novel and fundamentally disruptive methods arise. Recently, powerful stochastical algorithms from the field of machine learning and data-driven models gained prominent attention across all scientific disciplines. The ability to analyze large amounts of complex data, identify patterns and relationships, and learn from past experiences to make more accurate predictions and generate insights, renders them intriguing approaches for PEMFC modeling, too. Recent trends discuss a combination of physical theory and learning algorithms to merge the distinct advantages of both [259]. So called *hybrid models* might be the next stage of highly integrated model approaches. From the experimental side, automated labs and self-learning machines might join this trend in the future [260].

6 Conclusion

At present, proton exchange membrane fuel cells provide are a mature technology for compact, robust and durable energy converters with high specific power output. However, the ongoing transition to a decarbonized energy system requires them to make the leap into broad commercialization. Thus, ambitious developments in terms of durability, costs and power efficiency must be met by fuel cell developers. This work strove to guide and accelerate these efforts by providing a structure-based model to enable purposefully tailored materials and holistic cell design, which fosters further improvement and optimization of fuel cell devices. In the scope of this work, physical relations between fabrication procedures, catalyst layer composition, microstructure, effective properties, and performance were established and captured by analytical models, which allowed a thorough traceability of propagation of cause-effect relations from micro- to macroscale.

As a particular challenge, the Platinum loading of the cathode catalyst layer must be brought down significantly since Platinum, and thereby the catalyst layers, remain the major cost driver of proton exchange membrane fuel cells. Since no suitable replacement for Platinum as catalyst material is currently in reach, the necessary reduction is without alternative but faces a severe hurdle: low-Pt-loaded notoriously suffer from unexpected, over-proportional performance losses. In the literature, a distorted water balance has been conjectured to be responsible. However, the root cause of this phenomenon is only partially understood. Therefore, this work directed particular attention to possible explanations provided by the developed models.

Providing the starting point to evaluate the full scope of ink-to-structure-to-property relations, a composition model was developed that describes the formation of the ionomer structure as an incremental assembly of the composite during ink stage. The self-assembly processes of ionomer and Pt/C particles mobilized in the ink solvent were captured by ordinary differential equations. From the model solution, key parameters of the ink process, which are the ionomer dispersion parameter and the initial film thickness, were identified. As a primary outcome, the model calculates the ionomer film geometry, the volumetric composition and pore size distribution of the catalyst layer microstructure. The results were found to be in close agreement with experimental data and revealed three stages of structure formation: initially, the ionomer grows predominately in coverage, establishing a typical thin film on the Pt/C agglomerates' surfaces; successively, more ionomer adds to the film, increasing its thickness; ultimately, when thickness and coverage growth reach their limits, excess ionomer not incorporated in the ionomer film forms dense aggregates and expands the total catalyst layer volume. From these insights, this work devised purposeful measures to alter the balance between polar and dispersion interactions among ionomer molecules and between the ionomer and the Pt/C surface. Here, varying the ink

solvent composition and modifications of the surface chemistry of carbon support were identified to be viable approaches in the experimental literature.

As the next step along the cause-effect chain from microstructure to macroscopic properties, the heterogeneous and complex wetting behavior of the catalyst layer was modeled. This work proceeded by a combination of two sub-models. For the molecular scale, a novel analytical approach was developed to link the molecular alignment inside ionomer thin films with the films' wetting properties. Here, a novel descriptor, the ionomer's degree of alignment, was derived from an extensive literature review of theoretical and experimental works. Its value correlates the orientation of ionomer molecules with the resulting contact angle of the ionomer film exhibited to the secondary pore network. Subsequently, a statistical modeling approach captured the distribution of surface types encountered in the CCL material and their respective wetting properties over the mesoscale pore network, and eventually integrated them to water retention curves. The contact angle distribution and water retention curve of the catalyst layer could be simplified to closed-form analytic expressions, which enable the direct implementation of the model in computationally expensive optimization routines for holistic fuel cell design.

A first study conducted with the wettability model derived an explanation for the occurrence of severe oxygen transport losses when reducing Platinum loading of the catalyst layer. Lowering the Platinum loading while keeping the catalyst layer thickness constant can cause an inversion of the wetting behavior of the catalyst layer caused by a reorientation effect within the ionomer thin films. On highly Pt-loaded carbon surfaces, Platinum strongly interacts with the ionomer sidechains, imposing an alignment that leaves the hydrophobic backbone exposed to the outer surface of the ionomer film. Conversely, a hydrophobic carbon surface carrying only little Platinum causes the ionomer sidechains to orient away from the ionomer-carbon interface, rendering the ionomer film hydrophilic. This mechanism completes the bigger picture on performance losses in low-Pt-loaded cells: regardless of whether a low Platinum loading is achieved by thickness reduction or by dilution, the water balance of the cell will be severely distorted, resulting in the observed flooding phenomena.

A systematic parameter study was conducted to evaluate the impact of material choices on water management and evaluate the boundary conditions for the effective exhibition of hydrophobic properties for the catalyst layer. Two key parameters, which are defined by the ink stage, namely the ionomer dispersion parameter and ionomer-to-carbon ratio, must be adjusted in combination in a way that the dispersion tendency matches the amount of ionomer to ensure well-defined film formation. To overcome the limitations of reducing the Platinum loading, this work proposed altering the carbon's chemical nature to stabilize the hydrophobic alignment condition. Experimental materials were identified in the literature that might have the potential to employ such an approach, namely Nitrogen doping of the carbon support.

Finally, the wettability model was employed to evaluate the durability of wetting properties. For both carbon corrosion and coarsening of Platinum nanoparticles, the model predicts a decay of hydrophobicity over prolonged cell degradation, which was found to be confirmed by experimental studies in the literature.

Including catalyst activation by water to the scope of this work, the calculated wetting properties were used to set up a water uptake model to deconvolute the distribution of water inside the catalyst layer microstructure. Here, models in the literature were found to only cover capillary condensation. This work extended this approach by including adsorbed water films on Platinum and carbon surfaces, and water absorbed by the ionomer. Experimental data from the literature that correlated water uptake and Platinum utilization were analyzed in order to decipher the individual contributions to Platinum utilization by water. As a peculiarity, Platinum utilization follows fundamentally different trends for low or high Platinum concentration. The common understanding in the literature considers a Platinum particle active, thus utilized, if wetted by liquid water. Another, complementary hypothesis proposed that connection to the proton conducting network could also be facilitated by adsorbed water films around sorption sites at Platinum nanoparticles or functional groups on the carbon support's surface. This work conjectured that the first or second scenarios applies depending on wetting behavior of the catalyst layer and concentration of sorption sites, which is primarily determined by the Platinum-to-carbon ratio.

Using the developed model, water uptake from the vapor phase could be successfully deconvoluted and attributed to the distinct contributions from Platinum, carbon, ionomer and capillary condensation. As an attempt to scrutinize the details of Platinum utilization, an analytical approach employing percolation theory was tested but could not be brought to full agreement with experimental data for Platinum utilization in low-Pt-loaded cells. Apparently, not all relevant mechanisms were covered by the model. Nonetheless, the fundamental trends for platinum utilization could be captured and rationalized by the underlying structural features.

Building on the composition model, this work further resolved details of ionomer morphology to study their impact on proton transport. Variations in the spatial distribution and geometry of ionomer thin film have been reported in the recent literature and were suspected to be root cause for diverging properties of different catalyst layer with identical ionomer content. Therefore, this work conducted a direct numerical simulation of proton transport, which employed virtual structure generation to obtain synthetic binary images of the electrolyte phase distribution in the agglomerated catalyst layer structure microstructure. In a systematic study, proton conductivity was calculated over a wide range of structure parameters in terms of ionomer coverage and film thickness.

The simulation results converged into two limiting structural scenarios: ionomer can either form a thin, well-defined and closed film on the catalyst agglomerate surface; or the ionomer forms aggregates with substantial thickness that only partially cover the Pt/C surfaces and connect across the inter-agglomerate space. These two limiting cases were modeled analytically by adapting expressions from percolation theory. The proposed analytical model accurately describes the limiting cases and also reliably interpolates intermediate morphological scenarios.

Literature data from multiple sources were analyzed using the developed model. Distinct trends of ionomer content and proton conductivity were linked to variations of ionomer morphology. Coupling the proton transport model with the composition model, ionomer morphology and proton transport were jointly studied over a range of ink parameters, including the ionomer-to-carbon ratio, initial ionomer film thickness, and the

ionomer dispersion parameter. From this analysis, measures to optimize proton conductivity were derived and found in agreement with current efforts in the experimental literature.

The cumulated insights from the different models and studies conducted in this work were collected and consolidated in design principles that ensure both a high resistance to flooding and high proton connectivity. This covers microstructural features that are essential to obtain the desired properties, together with concrete ink parameter ranges recommended to ensure during fabrication. However, it was also pointed out by this work that the mere combination of conventional base materials encounters certain limitation in upholding a favorable, i.e., predominately hydrophobic, wetting behavior and devised disruptive strategies, which can be implemented in the form of novel carbon support materials.

In conclusion, this work demonstrated how profound quantitative modeling and understanding of the complex relation between the catalyst layer's microstructure and its effective properties can support the interpretation of experimental data and guide the design of experiments. Thereby, it will foster directed modifications and adjustments of the microstructure, eventually enabling the creation of materials with purposefully tailored properties. Further, it defined future directions for both theoretical and experimental research in the realm of molecular-, pore- and agglomerate scale phenomena.

Overall, the structure-based models developed in this work contributed to bridging the gaps between fabrication parameters, details of the microstructure, and macroscopic performance-decisive properties of catalyst layers in proton exchange membrane fuel cell – and thereby provided valuable support for the ongoing development efforts for economically viable, efficient and durable fuel cells.

7 References

All references that were used outside the published articles, which constitute this thesis and have their own individual bibliography, are listed below.

[1] H.-O. Pörtner, D. Roberts, H. Adams, I. Adelekan, C. Adler, R. Adrian, P. Aldunce, E. Ali, R. A. Begum, B. B. Friedl, R. B. Kerr, R. Biesbroek, J. Birkmann, K. Bowen, M. Caretta, J. Carnicer, E. Castellanos, T. Cheong, W. Chow, G. C. G. Cissé, and Z. Z. Ibrahim, editors. *Climate Change 2022: Impacts, Adaptation and Vulnerability.* Technical Summary. Cambridge University Press, Cambridge, UK and New York, USA, 2022. ISBN 978-1-00-932584-4.
https://www.ipcc.ch/report/ar6/wg2/downloads/report/IPCC_AR6_WGII_TechnicalSummary.pdf.

[2] M. Hannah. *Extinctions.* Cambridge University Press, Cambridge, England, Sept. 2021. ISBN 978-1-108-84353-9.
https://doi.org/10.1017/S0030605322000369.

[3] IPCC Core Writing Team, R. Pachauri, and A. Reisinger. *Climate Change 2007: Synthesis Report: Contributions of Working Groups I, II and III to the Fourth Assessment Report of the intergovernmental panel on Climate Change.* IPCC, Geneva, Switzerland, 2007.
https://www.ipcc.ch/site/assets/uploads/2018/02/ar4_syr.pdf.

[4] National Oceanic Atmospheric Administration (NOAA) – Earth System Research Laboratory. Annual Greenhouse Gas Index (AGGI, 2022), 2022.
https://gml.noaa.gov/aggi/.

[5] P. A. Stott, N. Christidis, F. E. L. Otto, Y. Sun, J. Vanderlinden, G. J. van Oldenborgh, R. Vautard, H. von Storch, P. Walton, P. Yiou, and F. W. Zwiers. Attribution of extreme weather and climate-related events. *WIREs Climate Change*, 7(1):23–41, Jan. 2016.
https://doi.org/10.1002/wcc.380.

[6] F. E. Otto. Attribution of Weather and Climate Events. *Annual Review of Environment and Resources*, 42(1):627–646, Oct. 2017.
https://doi.org/10.1146/annurev-environ-102016-060847.

[7] P. Naveau, A. Hannart, and A. Ribes. Statistical Methods for Extreme Event Attribution in Climate Science. *Annual Review of Statistics and Its Application*, 7(1):89–110, Mar. 2020.
https://doi.org/10.1146/annurev-statistics-031219-041314.

[8] Intergovernmental Panel on Climate Change. *Global Warming of 1.5°C: IPCC Special Report on Impacts of Global Warming of 1.5°C above Pre-industrial Levels in Context of Strengthening Response to Climate Change, Sustainable Development, and Efforts to Eradicate Poverty.* Cambridge University Press, 1st edition, June 2022. ISBN 978-1-00-915794-0 978-1-00-915795-7.
https://doi.org/10.1017/9781009157940.

[9] United Nations Framework Convention on Climate Change (UNFCCC). *The Paris Agreement.* United Nations Treaty Collection, Paris Climate Change Conference - November 2015, 2018.
https://unfccc.int/documents/184656.

[10] A. Risquez Martin, G. Grassi, E. Solazzo, J. F. O. Duarte, D. Guizzardi, S. Rossi, J. San-Miguel-Ayanz, F. Pagani, M. Crippa, J. Olivier, E. Vignati, M. Muntean, A. BRANCO, M. Banja, R. Quadrelli, F. Monforti-Ferrario, P. Taghavi-Moharamli, and E. Schaaf. Emissions Database for Global Atmospheric Research, version v7.0_ft_2021, 2022.
https://edgar.jrc.ec.europa.eu.

[11] Umweltbundesamt. Kohlendioxid-Emissionen Deutschlands, 2023.
www.umweltbundesamt.de/daten/klima/treibhausgas-emissionen-in-deutschland/kohlendioxid-emissionen.
Accessed: 24.03.2023.

[12] V. Masson-Delmotte, P. Zhai, A. Pirani, S. L. Connors, C. Péan, S. Berger, N. Caud, Y. Chen, L. Goldfarb, M. Gomis, et al. Climate change 2021: the physical science basis. *Contribution of working group I to the sixth assessment report of the intergovernmental panel on climate change*, 2, 2021. https://report.ipcc.ch/ar6/wg1/IPCC_AR6_WGI_FullReport.pdf.

[13] Umweltbundesamt. Treibhausgasminderungsziele Deutschlands, 2023.
https://www.umweltbundesamt.de/daten/klima/treibhausgasminderungsziele-deutschlands.
Accessed: 24.03.2023.

[14] Umweltbundesamt. Erneuerbare Energien in Zahlen, 2023.
https://www.umweltbundesamt.de/themen/klima-energie/erneuerbare-energien/erneuerbare-energien-in-zahlen. Accessed: 24.03.2023.

[15] V. Quaschning. *Regenerative Energiesysteme*. Carl Hanser Verlag GmbH & Co. KG, München, Nov. 2021. ISBN 978-3-446-47163-4.

[16] O. Ruhnau, S. Bannik, S. Otten, A. Praktiknjo, and M. Robinius. Direct or indirect electrification? A review of heat generation and road transport decarbonisation scenarios for Germany 2050. *Energy*, 166:989–999, Jan. 2019.
https://doi.org/10.1016/j.energy.2018.10.114.

[17] A. M. Oliveira, R. R. Beswick, and Y. Yan. A green hydrogen economy for a renewable energy society. *Current Opinion in Chemical Engineering*, 33:100701, Sept. 2021.
https://doi.org/10.1016/j.coche.2021.100701.

[18] M. Wietschel, L. Zheng, M. Arens, C. Hebling, O. Ranzmeyer, A. Schaadt, C. Hank, A. Sternberg, S. Herkel, and C. Kost. *Metastudie Wasserstoff-Auswertung von Energiesystemstudien*. Studie im Auftrag des Nationalen Wasserstoffrats. Fraunhofer ISI, Fraunhofer ISE, Fraunhofer IEG, Karlsruhe, Freiburg, Cottbus, 2021.
https://www.ise.fraunhofer.de/content/dam/ise/de/documents/publications/studies/Metastudie_Wasserstoff.pdf.

[19] C. Stiller. Nutzung von konventionellem und grünem Wasserstoff in der chemischen Industrie. In J. Töpler and J. Lehmann, editors, *Wasserstoff und Brennstoffzelle*, pages 175–188. Springer Berlin Heidelberg, Berlin, Heidelberg, 2014. ISBN 978-3-642-37414-2 978-3-642-37415-9.
https://doi.org/10.1007/978-3-642-37415-9_10.

[20] A. Otto, M. Robinius, T. Grube, S. Schiebahn, A. Praktiknjo, and D. Stolten. Power-to-Steel: Reducing CO2 through the Integration of Renewable Energy and Hydrogen into the German Steel Industry. *Energies*, 10(4):451, Apr. 2017.
https://doi.org/10.3390/en10040451.

[21] K. H. Chua, H. Lih Bong, Y. S. Lim, J. Wong, and L. Wang. The State-of-the-Arts of Peak Shaving Technologies: A Review. In *2020 International Conference on Smart Grid and Clean Energy Technologies (ICSGCE)*, pages 162–166. IEEE, Oct. 2020. ISBN 978-1-72815-736-8.
https://doi.org/10.1109/ICSGCE49177.2020.9275637.

[22] Bundesministerium für Bildung und Forschung. Nationale Wasserstoffstrategie, June 2020.
https://www.bmbf.de/bmbf/de/forschung/energiewende-und-nachhaltiges-wirtschaften/nationale-wasserstoffstrategie/nationale-wasserstoffstrategie_node.html. Accessed: 23.03.2023.

[23] Bundesministerium für Bildung und Forschung. Greenhouse gas savings and the associated hydrogen demand in Germany, Feb. 2023.
https://www.wasserstoffrat.de/fileadmin/wasserstoffrat/media/Dokumente/EN/2023/2023-02-01_White_Paper_H2-Demand.pdf. Accessed: 25.03.2023.

[24] L. Galvani, G. Aldini, and B. Carminati. *De Viribus Electricitatis In Motu Musculari Commentarius*. Apud Societatem typographicam, 1792.
https://books.google.de/books?id=qYwHJPw_i2YC.

[25] M. Faraday. On electrical decomposition. *Philosophical Transactions of the Royal Society*, 124:77–122, 1834.
https://doi.org/10.1098/rstl.1834.0008.

[26] W. Nernst. Die elektromotorische Wirksamkeit der Jonen. *Zeitschrift für Physikalische Chemie*, 4U(1):129–181, July 1889.
https://doi.org/10.1515/zpch-1889-0412.

[27] J. Tafel. Über die Polarisation bei kathodischer Wasserstoffentwicklung. *Zeitschrift für physikalische Chemie*, 50(1):641–712, 1905.
https://doi.org/10.1515/zpch-1905-5043.

[28] W. Grove. LXXII. On a gaseous voltaic battery. *The London, Edinburgh, and Dublin Philosophical Magazine and Journal of Science*, 21(140):417–420, Dec. 1842.
https://doi.org/10.1080/14786444208621600.

[29] L. Mond and C. Langer. V. a new form of gas battery. *Proceedings of the Royal Society of London*, 46(280-285):296–304, 1890.
https://doi.org/10.1098/rspl.1889.0036.

[30] W. Grove. XXIV. On voltaic series and the combination of gases by platinum. *The London, Edinburgh, and Dublin Philosophical Magazine and Journal of Science*, 14(86-87):127–130, Feb. 1839.
https://doi.org/10.1080/14786443908649684.

[31] C. Schönbein. X. On the voltaic polarization of certain solid and fluid substances: To the editors of the Philosophical Magazine and Journal. *The London, Edinburgh, and Dublin Philosophical Magazine and Journal of Science*, 14(85):43–45, Jan. 1839.
https://doi.org/10.1080/14786443908649658.

[32] Ostwald, Wilhelm. Die Wissenschaftliche Elektrochemie der Gegenwart und die Technische der Zukunft. *Zeitschrift für Elektrotechnik und Elektrochemie*, 1(3):81–84, June 1894.
https://doi.org/10.1002/bbpc.18940010302.

[33] A. Schmid. Die Diffusionsgaselektrode. *Helvetica Chimica Acta*, 7(1):370–373, 1924.
https://doi.org/10.1002/hlca.19240070143.

[34] IEEE History Center - Engineering and Technology History Wiki. Bacon's Fuel Cell, 2019.
https://ethw.org/Bacon%27s_Fuel_Cell. Accessed: 28.03.2023.

[35] W. T. Grubb and L. W. Niedrach. Batteries with Solid Ion-Exchange Membrane Electrolytes. *Journal of The Electrochemical Society*, 107(2):131, 1960.
https://doi.org/10.1149/1.2427622.

[36] W. T. Grubb and L. W. Niedrach. A High Performance Saturated Hydrocarbon Fuel Cell. *Journal of The Electrochemical Society*, 110(10):1086, 1963.
https://doi.org/10.1149/1.2425591.

[37] BBC Archive. The Brits Who Bolstered the Moon Landings, Feb. 1969.
https://www.bbc.co.uk/archive/the-brits-who-bolstered-the-moon-landings/zfcrscw. Accessed: 21.03.2023.

[38] National Aeronautics and Space Administration (NASA). Space Applications of Hydrogen and Fuel Cells, May 2021.
https://www.nasa.gov/content/space-applications-of-hydrogen-and-fuel-cells.
Accessed: 21.03.2023.

[39] Apolllo Service Module Fuel Cell. Fotographed by James Humphrey, 19 Dec. 2009, National Space Centre, Leicester.
https://commons.wikimedia.org/wiki/File:Apollo_SM_fuel_cell.jpg.

[40] Allis-Chalmers Company. Allis-Chalmers Fuel Cell Tractor, *National Museum of American History*, Oct. 1959.
https://americanhistory.si.edu/collections/search/object/nmah_687671.

[41] N. Swinford. *Allis-Chalmers farm equipment, 1914-1985.* American Society of Agricultural Engineers, St. Joseph, Mich, 1994. ISBN 978-0-929355-54-2.

[42] I. D. Raistrick. Modified gas diffusion electrode for proton exchange membrane fuel cells. In *Proceedings of the Symposium on Diaphragms, Separators, and Ion-Exchange Membranes*, volume 86, page 172. Electrochemical Society, 1986.

[43] I. D. Raistrick. Electrode assembly for use in a solid polymer electrolyte fuel cell. *US patent no.* 4876115A., Mar. 1988.
https://www.osti.gov/biblio/6912568.

[44] T. Zawodzinskijr, T. Springer, F. Uribe, and S. Gottesfeld. Characterization of polymer electrolytes for fuel cell applications. *Solid State Ionics*, 60(1-3):199–211, Mar. 1993.
https://doi.org/10.1016/0167-2738(93)90295-E.

[45] T. E. Springer, T. A. Zawodzinski, M. S. Wilson, and S. Gottesfeld. Characterization of Polymer Electrolyte Fuel Cells Using AC Impedance Spectroscopy. *Journal of The Electrochemical Society*, 143(2):587–599, Feb. 1996.
https://doi.org/10.1149/1.1836485.

[46] M. L. Perry and T. F. Fuller. A Historical Perspective of Fuel Cell Technology in the 20th Century. *Journal of The Electrochemical Society*, 149(7):S59, 2002.
https://doi.org/10.1149/1.1488651.

[47] Bundesministerium für Digitales und Verkehr. Elektromobilität mit Wasserstoff Brennstoffzelle, Mar. 2020.
https://bmdv.bund.de/DE/Themen/Mobilitaet/Elektromobilitaet/Elektromobilitaet-mit-wasserstoff/elektromobilitaet-mit-wasserstoff.html.
Accessed: 28.03.2023.

[48] N. Carnot. Reflections on the Motive Power of Heat and on Machines fitted to develop that Power, *translated by H. Thurston. Science*, 16(390):52–53, 1890.
https://doi.org/10.1126/science.ns-16.390.52.d.

[49] A. A. Konnov. Remaining uncertainties in the kinetic mechanism of hydrogen combustion. *Combustion and Flame*, 152(4):507–528, Mar. 2008.
https://doi.org/10.1016/j.combustflame.2007.10.024.

[50] M. Suermann, T. J. Schmidt, and F. N. Büchi. Comparing the kinetic activation energy of the oxygen evolution and reduction reactions. *Electrochimica Acta*, 281:466–471, Aug. 2018.
https://doi.org/10.1016/j.electacta.2018.05.150.

[51] M. Eikerling, A. Ioselevich, and A. Kornyshev. How good are the Electrodes we use in PEFC? *Fuel Cells*, 4(3):131–140, Aug. 2004.
https://doi.org/10.1002/fuce.200400029.

[52] M. Pan, C. Pan, C. Li, and J. Zhao. A review of membranes in proton exchange membrane fuel cells: Transport phenomena, performance and durability. *Renewable and Sustainable Energy Reviews*, 141:110771, May 2021.
https://doi.org/10.1016/j.rser.2021.110771.

[53] N. F. Asri, T. Husaini, A. B. Sulong, E. H. Majlan, and W. R. W. Daud. Coating of stainless steel and titanium bipolar plates for anticorrosion in PEMFC: A review. *International Journal of Hydrogen Energy*, 42(14):9135–9148, Apr. 2017.
https://doi.org/10.1016/j.ijhydene.2016.06.241.

[54] P. Kurzweil. *Brennstoffzellentechnik: Grundlagen, Komponenten, Systeme, Anwendungen.* Springer Fachmedien Wiesbaden, Wiesbaden, 2013. ISBN 978-3-658-00084-4.
https://doi.org/10.1007/978-3-658-00085-1.

[55] R. O'Hayre, S.-W. Cha, W. Colella, and F. B. Prinz. *Fuel Cell Fundamentals: O'Hayre/Fuel Cell Fundamentals.* John Wiley & Sons, Inc, Hoboken, NJ, USA, May 2016. ISBN 978-1-119-19176-6.
https://doi.org/10.1002/9781119191766.

[56] S. Mekhilef, R. Saidur, and A. Safari. Comparative study of different fuel cell technologies. *Renewable and Sustainable Energy Reviews*, 16(1):981–989, Jan. 2012.
https://doi.org/10.1016/j.rser.2011.09.020.

[57] M. Gasik, editor. *Materials for fuel cells.* Woodhead publishing in materials. Woodhead Publ, Cambridge, 2008. ISBN 978-1-84569-483-8.

[58] S. Gottesfeld, D. R. Dekel, M. Page, C. Bae, Y. Yan, P. Zelenay, and Y. S. Kim. Anion exchange membrane fuel cells: Current status and remaining challenges. *Journal of Power Sources*, 375:170–184, Jan. 2018.
https://doi.org/10.1016/j.jpowsour.2017.08.010.

[59] T. Ferriday and P. H. Middleton. Alkaline fuel cell technology - A review. *International Journal of Hydrogen Energy*, 46(35):18489–18510, May 2021.
https://doi.org/10.1016/j.ijhydene.2021.02.203.

[60] S. Simon Araya, V. Liso, X. Cui, N. Li, J. Zhu, S. L. Sahlin, S. H. Jensen, M. P. Nielsen, and S. K. Kær. A Review of The Methanol Economy: The Fuel Cell Route. *Energies*, 13(3):596, Jan. 2020.
https://doi.org/10.3390/en13030596.

[61] United States Department of Energy - Hydrogen and Fuel Cell Technologies Office. DOE Technical Targets for Fuel Cell Systems and Stacks for Transportation Applications, 2015.
https://www.energy.gov/eere/fuelcells/doe-tec

```
hnical-targets-fuel-cell-systems-and-stacks-t
ransportation-applications.
```
Accessed: 20.03.2023.

[62] N. Guerrero Moreno, M. Cisneros Molina, D. Gervasio, and J. F. Pérez Robles. Approaches to polymer electrolyte membrane fuel cells (PEMFCs) and their cost. *Renewable and Sustainable Energy Reviews*, 52: 897–906, Dec. 2015.
```
https://doi.org/10.1016/j.rser.2015.07.157.
```

[63] B. G. Pollet, S. S. Kocha, and I. Staffell. Current status of automotive fuel cells for sustainable transport. *Current Opinion in Electrochemistry*, 16:90–95, Aug. 2019.
```
https://doi.org/10.1016/j.coelec.2019.04.021.
```

[64] X. Ren, Q. Lv, L. Liu, B. Liu, Y. Wang, A. Liu, and G. Wu. Current progress of Pt and Pt-based electrocatalysts used for fuel cells. *Sustainable Energy & Fuels*, 4(1):15–30, 2020.
```
https://doi.org/10.1039/C9SE00460B.
```

[65] G. Ercolano, S. Cavaliere, J. Rozière, and D. J. Jones. Recent developments in electrocatalyst design thrifting noble metals in fuel cells. *Current Opinion in Electrochemistry*, 9:271–277, June 2018.
```
https://doi.org/10.1016/j.coelec.2018.05.019.
```

[66] N. Zamel. The catalyst layer and its dimensionality – A look into its ingredients and how to characterize their effects. *Journal of Power Sources*, 309:141–159, Mar. 2016.
```
https://doi.org/10.1016/j.jpowsour.2016.01.091.
```

[67] F. Ciucci. Modeling electrochemical impedance spectroscopy. *Current Opinion in Electrochemistry*, 13: 132–139, Feb. 2019.
```
https://doi.org/10.1016/j.coelec.2018.12.003.
```

[68] A. Z. Weber, R. L. Borup, R. M. Darling, P. K. Das, T. J. Dursch, W. Gu, D. Harvey, A. Kusoglu, S. Litster, M. M. Mench, R. Mukundan, J. P. Owejan, J. G. Pharoah, M. Secanell, and I. V. Zenyuk. A Critical Review of Modeling Transport Phenomena in Polymer-Electrolyte Fuel Cells. *Journal of The Electrochemical Society*, 161(12):F1254–F1299, 2014.
```
https://doi.org/10.1149/2.0751412jes.
```

[69] K. Chan and M. Eikerling. A Pore-Scale Model of Oxygen Reduction in Ionomer-Free Catalyst Layers of PEFCs. *Journal of The Electrochemical Society*, 158 (1):B18, 2011.
```
https://doi.org/10.1149/1.3505042.
```

[70] J. Huang, J. Zhang, and M. Eikerling. Theory of electrostatic phenomena in water-filled Pt nanopores. *Faraday Discussions*, 193:427–446, 2016.
```
https://doi.org/10.1039/C6FD00094K.
```

[71] G. S. Harzer, A. Orfanidi, H. El-Sayed, P. Madkikar, and H. A. Gasteiger. Tailoring catalyst morphology towards high performance for low Pt loaded PEMFC cathodes. *Journal of The Electrochemical Society*, 165 (10):F770, 2018.
```
https://doi.org/10.1149/2.0311810jes.
```

[72] M. Eikerling and A. Kulikovsky. *Polymer Electrolyte Fuel Cells: Physical Principles of Materials and Operation.* CRC Press, Sept. 2014. ISBN 978-1-4398-5406-8.
```
https://doi.org/10.1201/b17429.
```

[73] D. Banham and S. Ye. Current Status and Future Development of Catalyst Materials and Catalyst Layers for Proton Exchange Membrane Fuel Cells: An Industrial Perspective. *ACS Energy Letters*, 2(3):629–638, Mar. 2017.
```
https://doi.org/10.1021/acsenergylett.6b00644.
```

[74] S. G. Rinaldo, J. Stumper, and M. Eikerling. Physical Theory of Platinum Nanoparticle Dissolution in Polymer Electrolyte Fuel Cells. *The Journal of Physical Chemistry C*, 114(13):5773–5785, Apr. 2010.
```
https://doi.org/10.1021/jp9101509.
```

[75] P. Urchaga, T. Kadyk, S. G. Rinaldo, A. O. Pistono, J. Hu, W. Lee, C. Richards, M. H. Eikerling, and C. A. Rice. Catalyst Degradation in Fuel Cell Electrodes: Accelerated Stress Tests and Model-based Analysis. *Electrochimica Acta*, 176:1500–1510, Sept. 2015.
```
https://doi.org/10.1016/j.electacta.2015.03.15
2.
```

[76] H. A. Baroody, D. B. Stolar, and M. H. Eikerling. Modelling-based data treatment and analytics of catalyst degradation in polymer electrolyte fuel cells. *Electrochimica Acta*, 283:1006–1016, Sept. 2018.
```
https://doi.org/10.1016/j.electacta.2018.06.10
8.
```

[77] J. Zhao and X. Li. A review of polymer electrolyte membrane fuel cell durability for vehicular applications: Degradation modes and experimental techniques. *Energy Conversion and Management*, 199: 112022, Nov. 2019.
```
https://doi.org/10.1016/j.enconman.2019.112022.
```

[78] E. Padgett, N. Andrejevic, Z. Liu, A. Kongkanand, W. Gu, K. Moriyama, Y. Jiang, S. Kumaraguru, T. E. Moylan, R. Kukreja, and D. A. Muller. Connecting Fuel Cell Catalyst Nanostructure and Accessibility Using Quantitative Cryo-STEM Tomography. *Journal of The Electrochemical Society*, 165(3):F173–F180, 2018.
```
https://doi.org/10.1149/2.0541803jes.
```

[79] A. L. Dicks. The role of carbon in fuel cells. *Journal of Power Sources*, 156(2):128–141, June 2006.
```
https://doi.org/10.1016/j.jpowsour.2006.02.054.
```

[80] P. Serp and B. Machado. *Nanostructured carbon materials for catalysis.* Number 23. Royal Society of Chemistry, 2015. ISBN 9781849739092.
```
https://doi.org/10.1039/9781782622567.
```

[81] M. Uchida. PEFC catalyst layers: Effect of support microstructure on both distributions of Pt and ionomer and cell performance and durability. *Current Opinion in Electrochemistry*, 21:209–218, June 2020.
```
https://doi.org/10.1016/j.coelec.2020.02.019.
```

[82] S. J. Hamrock and M. A. Yandrasits. Proton Exchange Membranes for Fuel Cell Applications. *Journal of Macromolecular Science, Part C: Polymer Reviews*, 46(3):219–244, Sept. 2006.
```
https://doi.org/10.1080/15583720600796474.
```

[83] M. Ghelichi, K. Malek, and M. H. Eikerling. Ionomer Self-Assembly in Dilute Solution Studied by Coarse-Grained Molecular Dynamics. *Macromolecules*, 49(4): 1479–1489, Feb. 2016.
https://doi.org/10.1021/acs.macromol.5b02158.

[84] J. A. Elliott and S. J. Paddison. Modelling of morphology and proton transport in PFSA membranes. *Physical Chemistry Chemical Physics*, 9(21):2602, 2007.
https://doi.org/10.1039/b701234a.

[85] R. Fernández, P. Ferreira-Aparicio, and L. Daza. PEMFC electrode preparation: Influence of the solvent composition and evaporation rate on the catalytic layer microstructure. *Journal of Power Sources*, 151: 18 – 24, 2005.
https://doi.org/https://doi.org/10.1016/j.jpowsour.2005.02.048.

[86] P. E. Santangelo, M. Cannio, and M. Romagnoli. Review of catalyst-deposition techniques for PEMFC electrodes. *TECNICA ITALIANA-Italian Journal of Engineering Science*, 63:65 – 72, 2019.
https://doi.org/https://doi.org/10.18280/ti-ijes.630109.

[87] M. Cannio, S. Righi, P. E. Santangelo, M. Romagnoli, R. Pedicini, A. Carbone, and I. Gatto. Smart catalyst deposition by 3d printing for Polymer Electrolyte Membrane Fuel Cell manufacturing. *Renewable Energy*, 163:414 – 422, 2021.
https://doi.org/10.1016/j.renene.2020.08.064.

[88] M. Breitwieser, M. Klingele, B. Britton, S. Holdcroft, R. Zengerle, and S. Thiele. Improved Pt-utilization efficiency of low Pt-loading PEM fuel cell electrodes using direct membrane deposition. *Electrochemistry Communications*, 60:168 – 171, 2015.
https://doi.org/https://doi.org/10.1016/j.elecom.2015.09.006.

[89] A. Strong, C. Thornberry, S. Beattie, R. Chen, and S. R. Coles. Depositing Catalyst Layers in Polymer Electrolyte Membrane Fuel Cells: A Review. *Journal of Fuel Cell Science and Technology*, 12:064001–1 – 064001–11, 2015.
https://doi.org/https://doi.org/10.1115/1.4031961.

[90] Y. V. Yakovlev, Y. V. Lobko, M. Vorokhta, J. Nováková, M. Mazur, I. Matolínová, and V. Matolín. Ionomer content effect on charge and gas transport in the cathode catalyst layer of proton-exchange membrane fuel cells. *Journal of Power Sources*, 490: 229531, Apr. 2021.
https://doi.org/10.1016/j.jpowsour.2021.229531.

[91] M. Lopez-Haro, L. Guétaz, T. Printemps, A. Morin, S. Escribano, P.-H. Jouneau, P. Bayle-Guillemaud, F. Chandezon, and G. Gebel. Three-dimensional analysis of Nafion layers in fuel cell electrodes. *Nature Communications*, 5(1), Dec. 2014.
https://doi.org/10.1038/ncomms6229.

[92] T. Morawietz, M. Handl, C. Oldani, K. A. Friedrich, and R. Hiesgen. Quantitative in Situ Analysis of Ionomer Structure in Fuel Cell Catalytic Layers. *ACS Applied Materials & Interfaces*, 8(40):27044–27054, Oct. 2016.
https://doi.org/10.1021/acsami.6b07188.

[93] R. Girod, T. Lazaridis, H. A. Gasteiger, and V. Tileli. Three-dimensional nanoimaging of fuel cell catalyst layers. *Nature Catalysis*, Apr. 2023.
https://doi.org/10.1038/s41929-023-00947-y.

[94] T. Mashio, K. Sato, and A. Ohma. Analysis of Water Adsorption and Condensation in Catalyst Layers for Polymer Electrolyte Fuel Cells. *Electrochimica Acta*, 140:238–249, Sept. 2014.
https://doi.org/10.1016/j.electacta.2014.07.058.

[95] T. Soboleva, X. Zhao, K. Malek, Z. Xie, T. Navessin, and S. Holdcroft. On the Micro-, Meso-, and Macroporous Structures of Polymer Electrolyte Membrane Fuel Cell Catalyst Layers. *ACS Applied Materials & Interfaces*, 2(2):375–384, Feb. 2010.
https://doi.org/10.1021/am900600y.

[96] Y.-C. Park, H. Tokiwa, K. Kakinuma, M. Watanabe, and M. Uchida. Effects of carbon supports on Pt distribution, ionomer coverage and cathode performance for polymer electrolyte fuel cells. *Journal of Power Sources*, 315:179–191, May 2016.
https://doi.org/10.1016/j.jpowsour.2016.02.091.

[97] K. Malek, M. Eikerling, Q. Wang, T. Navessin, and Z. Liu. Self-Organization in Catalyst Layers of Polymer Electrolyte Fuel Cells. *The Journal of Physical Chemistry C*, 111(36):13627–13634, Sept. 2007.
https://doi.org/10.1021/jp072692k.

[98] T. Suzuki, S. Tsushima, and S. Hirai. Effects of Nafion® ionomer and carbon particles on structure formation in a proton-exchange membrane fuel cell catalyst layer fabricated by the decal-transfer method. *International Journal of Hydrogen Energy*, 36(19): 12361–12369, Sept. 2011.
https://doi.org/10.1016/j.ijhydene.2011.06.090.

[99] M. Uchida, Y. Aoyama, N. Eda, and A. Ohta. Investigation of the Microstructure in the Catalyst Layer and Effects of Both Perfluorosulfonate Ionomer and PTFE-Loaded Carbon on the Catalyst Layer of Polymer Electrolyte Fuel Cells. *Journal of The Electrochemical Society*, 142(12):4143–4149, Dec. 1995.
https://doi.org/10.1149/1.2048477.

[100] K. Malek, T. Mashio, and M. Eikerling. Microstructure of Catalyst Layers in PEM Fuel Cells Redefined: A Computational Approach. *Electrocatalysis*, 2(2): 141–157, June 2011.
https://doi.org/10.1007/s12678-011-0047-0.

[101] T. Suzuki, K. Kudo, and Y. Morimoto. Model for investigation of oxygen transport limitation in a polymer electrolyte fuel cell. *Journal of Power Sources*, 222:379–389, Jan. 2013.
https://doi.org/10.1016/j.jpowsour.2012.08.068.

[102] S. Komini Babu, H. T. Chung, P. Zelenay, and S. Litster. Resolving electrode morphology's impact on platinum group metal-free cathode performance using nano-CT of 3d hierarchical pore and ionomer distribution. *ACS applied materials & interfaces*, 8(48): 32764–32777, 2016.
https://doi.org/10.1021/acsami.6b08844.

[103] C.-N. Sun, K. L. More, and T. A. Zawodzinski. Investigation of Transport Properties, Microstructure, and Thermal Behavior of PEFC Catalyst Layers. *ECS Transactions*, 33(1):1207–1215, Oct. 2010.
https://doi.org/10.1149/1.3484614.

[104] G. Doo, J. H. Lee, S. Yuk, S. Choi, D.-H. Lee, D. W. Lee, H. G. Kim, S. H. Kwon, S. G. Lee, and H.-T. Kim. Tuning the Ionomer Distribution in the Fuel Cell Catalyst Layer with Scaling the Ionomer Aggregate Size in Dispersion. *ACS Applied Materials & Interfaces*, 10(21):17835–17841, May 2018.
https://doi.org/10.1021/acsami.8b01751.

[105] D. Susac, V. Berejnov, A. P. Hitchcock, and J. Stumper. STXM Study of the Ionomer Distribution in the PEM Fuel Cell Catalyst Layers. *ECS Transactions*, 41(1):629–635, Oct. 2011.
https://doi.org/10.1149/1.3635596.

[106] R. Zeng, H. Y. Zhang, S. Z. Liang, L. G. Wang, L. J. Jiang, and X. P. Liu. Possible scenario of forming a catalyst layer for proton exchange membrane fuel cells. *RSC Advances*, 10(9):5502–5506, 2020.
https://doi.org/10.1039/C9RA09864J.

[107] T. Soboleva. *On the microstructure of PEM fuel cell catalyst layers.* PhD thesis, Simon Fraser University, 2010.
https://summit.sfu.ca/item/11450.

[108] Z. Xie, X. Zhao, M. Adachi, Z. Shi, T. Mashio, A. Ohma, K. Shinohara, S. Holdcroft, and T. Navessin. Fuel cell cathode catalyst layers from "green" catalyst inks. *Energy & Environmental Science*, 1(1):184, 2008.
https://doi.org/10.1039/b808613n.

[109] J. Xie, F. Xu, D. L. Wood, K. L. More, T. A. Zawodzinski, and W. H. Smith. Influence of ionomer content on the structure and performance of PEFC membrane electrode assemblies. *Electrochimica Acta*, 55(24):7404–7412, Oct. 2010.
https://doi.org/10.1016/j.electacta.2010.06.067.

[110] M. Lee, M. Uchida, H. Yano, D. A. Tryk, H. Uchida, and M. Watanabe. New evaluation method for the effectiveness of platinum/carbon electrocatalysts under operating conditions. *Electrochimica Acta*, 55(28):8504–8512, Dec. 2010.
https://doi.org/10.1016/j.electacta.2010.07.071.

[111] T. A. M. Suter, K. Smith, J. Hack, L. Rasha, Z. Rana, G. M. A. Angel, P. R. Shearing, T. S. Miller, and D. J. L. Brett. Engineering Catalyst Layers for Next-Generation Polymer Electrolyte Fuel Cells: A Review of Design, Materials, and Methods. *Advanced Energy Materials*, 11(37):2101025, Oct. 2021.
https://doi.org/10.1002/aenm.202101025.

[112] S. Holdcroft. Fuel Cell Catalyst Layers: A Polymer Science Perspective. *Chemistry of Materials*, 26(1):381–393, Jan. 2014.
https://doi.org/10.1021/cm401445h.

[113] S. A. Berlinger, S. Garg, and A. Z. Weber. Multicomponent, multiphase interactions in fuel-cell inks. *Current Opinion in Electrochemistry*, 29:100744, Oct. 2021.
https://doi.org/10.1016/j.coelec.2021.100744.

[114] R. Sharma and S. M. Andersen. Zoom in Catalyst/Ionomer Interface in Polymer Electrolyte Membrane Fuel Cell Electrodes: Impact of Catalyst/Ionomer Dispersion Media/Solvent. *ACS Applied Materials & Interfaces*, 10(44):38125–38133, Nov. 2018.
https://doi.org/10.1021/acsami.8b14622.

[115] T. Van Cleve, S. Khandavalli, A. Chowdhury, S. Medina, S. Pylypenko, M. Wang, K. L. More, N. Kariuki, D. J. Myers, A. Z. Weber, S. A. Mauger, M. Ulsh, and K. C. Neyerlin. Dictating Pt-Based Electrocatalyst Performance in Polymer Electrolyte Fuel Cells, from Formulation to Application. *ACS Applied Materials & Interfaces*, 11(50):46953–46964, Dec. 2019.
https://doi.org/10.1021/acsami.9b17614.

[116] A. Orfanidi, P. J. Rheinländer, N. Schulte, and H. A. Gasteiger. Ink solvent dependence of the ionomer distribution in the catalyst layer of a PEMFC. *Journal of The Electrochemical Society*, 165(14):F1254, 2018.
https://doi.org/10.1149/2.1251814jes.

[117] S. Ott, A. Orfanidi, H. Schmies, B. Anke, H. N. Nong, J. Hübner, U. Gernert, M. Gliech, M. Lerch, and P. Strasser. Ionomer distribution control in porous carbon-supported catalyst layers for high-power and low Pt-loaded proton exchange membrane fuel cells. *Nature Materials*, 19(1):77–85, Jan. 2020.
https://doi.org/10.1038/s41563-019-0487-0.

[118] T. Muzaffar, T. Kadyk, and M. Eikerling. Physical Modeling of the Proton Density in Nanopores of PEM Fuel Cell Catalyst Layers. *Electrochimica Acta*, 245: 1048–1058, Aug. 2017.
https://doi.org/10.1016/j.electacta.2017.05.052.

[119] A. Chowdhury, R. M. Darling, C. J. Radke, and A. Z. Weber. Modeling Water Uptake and Pt Utilization in High Surface Area Carbon. *ECS Transactions*, 92(8): 247–259, July 2019.
https://doi.org/10.1149/09208.0247ecst.

[120] M. K. Debe. Tutorial on the Fundamental Characteristics and Practical Properties of Nanostructured Thin Film (NSTF) Catalysts. *Journal of The Electrochemical Society*, 160(6):F522–F534, 2013.
https://doi.org/10.1149/2.049306jes.

[121] A. Steinbach. Final Technical Report for project entitled Highly Active, Durable, and Ultra-Low PGM NSTF Thin Film ORR Catalysts and Support. Technical Report DOE-3M–0007270, 1608958, Mar. 2020.
https://www.osti.gov/servlets/purl/1608958/.

[122] S. Du. Recent Advances in Electrode Design Based on One-Dimensional Nanostructure Arrays for Proton Exchange Membrane Fuel Cell Applications. *Engineering*, 7(1):33–49, Jan. 2021.
https://doi.org/10.1016/j.eng.2020.09.014.

[123] A. Nouri-Khorasani, K. Malek, A. Malek, T. Mashio, D. P. Wilkinson, and M. H. Eikerling. Molecular modeling of the proton density distribution in a water-filled slab-like nanopore bounded by Pt oxide and ionomer. *Catalysis Today*, 262:133–140, Mar. 2016.
https://doi.org/10.1016/j.cattod.2015.10.020.

[124] K. Kodama, A. Shinohara, N. Hasegawa, K. Shinozaki, R. Jinnouchi, T. Suzuki, T. Hatanaka, and Y. Morimoto. Catalyst Poisoning Property of Sulfonimide Acid Ionomer on Pt (111) Surface. *Journal of The Electrochemical Society*, 161(5):F649–F652, 2014. `https://doi.org/10.1149/2.051405jes`.

[125] R. Subbaraman, D. Strmcnik, V. Stamenkovic, and N. M. Markovic. Three Phase Interfaces at Electrified Metal-Solid Electrolyte Systems 1. Study of the Pt(*hkl*)-Nafion Interface. *The Journal of Physical Chemistry C*, 114(18):8414–8422, May 2010. `https://doi.org/10.1021/jp100814x`.

[126] K. Shinozaki, Y. Morimoto, B. S. Pivovar, and S. S. Kocha. Suppression of oxygen reduction reaction activity on Pt-based electrocatalysts from ionomer incorporation. *Journal of Power Sources*, 325:745–751, Sept. 2016. `https://doi.org/10.1016/j.jpowsour.2016.06.062`.

[127] T. Mashio, K. Malek, M. Eikerling, A. Ohma, H. Kanesaka, and K. Shinohara. Molecular Dynamics Study of Ionomer and Water Adsorption at Carbon Support Materials. *The Journal of Physical Chemistry C*, 114(32):13739–13745, Aug. 2010. `https://doi.org/10.1021/jp1034135`.

[128] J. A. Spooner, M. J. Eslamibidgoli, K. Malek, and M. H. Eikerling. Molecular Dynamics Study of the Nanoscale Proton Density Distribution at the Ionomer-Catalyst Interface. *ECS Meeting Abstracts*, MA2020-02(33):2101–2101, Nov. 2020. `https://doi.org/10.1149/MA2020-02332101mtgabs`.

[129] Y. Qi, J. Liu, D. C. Sabarirajan, Y. Huang, A. Perego, A. T. Haug, and I. V. Zenyuk. Interpreting Ionic Conductivity for Polymer Electrolyte Fuel Cell Catalyst Layers with Electrochemical Impedance Spectroscopy and Transmission Line Modeling. *Journal of The Electrochemical Society*, 168(5):054502, May 2021. `https://doi.org/10.1149/1945-7111/abf96d`.

[130] R. De Levie. On impedance measurements: The determination of the double layer capacitance in the presence of an electrode reaction. *Electrochimica Acta*, 10 (4):395–402, Apr. 1965. `https://doi.org/10.1016/0013-4686(65)80055-X`.

[131] S. Touhami, J. Mainka, J. Dillet, S. A. H. Taleb, and O. Lottin. Transmission Line Impedance Models Considering Oxygen Transport Limitations in Polymer Electrolyte Membrane Fuel Cells. *Journal of The Electrochemical Society*, 166(15):F1209–F1217, 2019. `https://doi.org/10.1149/2.0891915jes`.

[132] M. Eikerling. Water Management in Cathode Catalyst Layers of PEM Fuel Cells. *Journal of The Electrochemical Society*, 153(3):E58, 2006. `https://doi.org/10.1149/1.2160435`.

[133] Y. M. Volfkovich, V. Sosenkin, and V. Bagotsky. Structural and wetting properties of fuel cell components. *Journal of Power Sources*, 195(17):5429–5441, Sept. 2010. `https://doi.org/10.1016/j.jpowsour.2010.03.002`.

[134] X. Li, F. Feng, K. Zhang, S. Ye, D. Y. Kwok, and V. Birss. Wettability of Nafion and Nafion/Vulcan Carbon Composite Films. *Langmuir*, 28(16):6698–6705, Apr. 2012. `https://doi.org/10.1021/la300388x`.

[135] Y. M. Vol'fkovich, V. E. Sosenkin, and N. F. Nikol'skaya. Hydrophilic-hydrophobic and sorption properties of the catalyst layers of electrodes in a proton-exchange membrane fuel cell: A stage-by-stage study. *Russian Journal of Electrochemistry*, 46(4): 438–449, Apr. 2010. `https://doi.org/10.1134/S1023193510040099`.

[136] T. Muzaffar, T. Kadyk, and M. Eikerling. Tipping water balance and the Pt loading effect in polymer electrolyte fuel cells: a model-based analysis. *Sustainable Energy & Fuels*, 2(6):1189–1196, 2018. `https://doi.org/10.1039/C8SE00026C`.

[137] K. Sakai, K. Sato, T. Mashio, A. Ohma, K. Yamaguchi, and K. Shinohara. Analysis of Reactant Gas Transport in Catalyst Layers; Effect of Pt-loadings. *ECS Transactions*, 25(1):1193–1201, Dec. 2019. `https://doi.org/10.1149/1.3210674`.

[138] Y. Ono, A. Ohma, K. Shinohara, and K. Fushinobu. Influence of Equivalent Weight of Ionomer on Local Oxygen Transport Resistance in Cathode Catalyst Layers. *Journal of The Electrochemical Society*, 160 (8):F779–F787, 2013. `https://doi.org/10.1149/2.040308jes`.

[139] K. Kudo, R. Jinnouchi, and Y. Morimoto. Humidity and Temperature Dependences of Oxygen Transport Resistance of Nafion Thin Film on Platinum Electrode. *Electrochimica Acta*, 209:682–690, Aug. 2016. `https://doi.org/10.1016/j.electacta.2016.04.023`.

[140] R. Jinnouchi, K. Kudo, N. Kitano, and Y. Morimoto. Molecular Dynamics Simulations on O 2 Permeation through Nafion Ionomer on Platinum Surface. *Electrochimica Acta*, 188:767–776, Jan. 2016. `https://doi.org/10.1016/j.electacta.2015.12.031`.

[141] H. Liu, W. K. Epting, and S. Litster. Gas Transport Resistance in Polymer Electrolyte Thin Films on Oxygen Reduction Reaction Catalysts. *Langmuir*, 31(36): 9853–9858, Sept. 2015. `https://doi.org/10.1021/acs.langmuir.5b02487`.

[142] A. Z. Weber and A. Kusoglu. Unexplained transport resistances for low-loaded fuel-cell catalyst layers. *J. Mater. Chem. A*, 2(41):17207–17211, 2014. `https://doi.org/10.1039/C4TA02952F`.

[143] E. W. Thiele. Relation between Catalytic Activity and Size of Particle. *Industrial & Engineering Chemistry*, 31(7):916–920, July 1939. `https://doi.org/10.1021/ie50355a027`.

[144] J. Giner and C. Hunter. The Mechanism of Operation of the Teflon-Bonded Gas Diffusion Electrode: A Mathematical Model. *Journal of The Electrochemical Society*, 116(8):1124, 1969. `https://doi.org/10.1149/1.2412232`.

[145] R. Iczkowski and M. Cutlip. Voltage Losses in Fuel Cell Cathodes. *Journal of The Electrochemical Society*, 127(7):1433–1440, July 1980. `https://doi.org/10.1149/1.2129925`.

[146] P. Björnbom. Modelling of a double-layered PTFE-bonded oxygen electrode. *Electrochimica Acta*, 32(1): 115–119, Jan. 1987.
https://doi.org/10.1016/0013-4686(87)87018-4.

[147] K. Broka and P. Ekdunge. Oxygen and hydrogen permeation properties and water uptake of Nafion® 117 membrane and recast film for PEM fuel cell. *Journal of applied electrochemistry*, 27(2):117–123, 1997.
https://doi.org/10.1023/A:1018469520562.

[148] Y. Bultel, P. Ozil, and R. Dura nd. Modified thin film and agglomerate models for active layers of P.E. fuel cells. *Electrochimica Acta*, 43(9):1077–1087, Apr. 1998.
https://doi.org/10.1016/S0013-4686(97)00269-7.

[149] M. L. Perry. Mass Transport in Gas-Diffusion Electrodes: A Diagnostic Tool for Fuel-Cell Cathodes. *Journal of The Electrochemical Society*, 145(1):5, 1998.
https://doi.org/10.1149/1.1838202.

[150] T. E. Springer, T. A. Zawodzinski, and S. Gottesfeld. Polymer Electrolyte Fuel Cell Model. *Journal of The Electrochemical Society*, 138(8):2334–2342, Aug. 1991.
https://doi.org/10.1149/1.2085971.

[151] M. Eikerling and A. Kornyshev. Modelling the performance of the cathode catalyst layer of polymer electrolyte fuel cells. *Journal of Electroanalytical Chemistry*, 453(1-2):89–106, Aug. 1998.
https://doi.org/10.1016/S0022-0728(98)00214-9.

[152] T. Soboleva, K. Malek, Z. Xie, T. Navessin, and S. Holdcroft. PEMFC Catalyst Layers: The Role of Micropores and Mesopores on Water Sorption and Fuel Cell Activity. *ACS Applied Materials & Interfaces*, 3(6):1827–1837, June 2011.
https://doi.org/10.1021/am200590w.

[153] Q. Wang, M. Eikerling, D. Song, and Z. Liu. Structure and performance of different types of agglomerates in cathode catalyst layers of PEM fuel cells. *Journal of Electroanalytical Chemistry*, 573(1):61–69, Nov. 2004.
https://doi.org/10.1016/j.jelechem.2004.06.022.

[154] E. Sadeghi, A. Putz, and M. Eikerling. Effects of ionomer coverage on agglomerate effectiveness in catalyst layers of polymer electrolyte fuel cells. *Journal of Solid State Electrochemistry*, 18(5):1271–1279, May 2014.
https://doi.org/10.1007/s10008-013-2268-z.

[155] J. Huang, A. Malek, J. Zhang, and M. H. Eikerling. Non-monotonic Surface Charging Behavior of Platinum: A Paradigm Change. *The Journal of Physical Chemistry C*, 120(25):13587–13595, June 2016.
https://doi.org/10.1021/acs.jpcc.6b03930.

[156] J. Huang, J. Zhang, and M. H. Eikerling. Particle Proximity Effect in Nanoparticle Electrocatalysis: Surface Charging and Electrostatic Interactions. *The Journal of Physical Chemistry C*, 121(9):4806–4815, Mar. 2017.
https://doi.org/10.1021/acs.jpcc.6b10842.

[157] J. Liu and I. V. Zenyuk. Proton transport in ionomer-free regions of polymer electrolyte fuel cells and implications for oxygen reduction reaction. *Current Opinion in Electrochemistry*, 12:202–208, Dec. 2018.
https://doi.org/10.1016/j.coelec.2018.11.015.

[158] M. Secanell, A. Putz, P. Wardlaw, V. Zingan, M. Bhaiya, M. Moore, J. Zhou, C. Balen, and K. Domican. OpenFCST: An Open-Source Mathematical Modelling Software for Polymer Electrolyte Fuel Cells. *ECS Transactions*, 64(3):655–680, Aug. 2014.
https://doi.org/10.1149/06403.0655ecst.

[159] L. M. Pant and A. Z. Weber. Communication—Modeling Polymer-Electrolyte Fuel-Cell Agglomerates with Double-Trap Kinetics. *Journal of The Electrochemical Society*, 164(11):E3102–E3104, 2017.
https://doi.org/10.1149/2.0111711jes.

[160] W. Yoon and A. Z. Weber. Modeling low-platinum-loading effects in fuel-cell catalyst layers. *Journal of The Electrochemical Society*, 158(8):B1007, 2011.
https://doi.org/10.1149/1.3597644.

[161] M. Moore, P. Wardlaw, P. Dobson, J. J. Boisvert, A. Putz, R. J. Spiteri, and M. Secanell. Understanding the effect of kinetic and mass transport processes in cathode agglomerates. *Journal of the Electrochemical Society*, 161(8):E3125, 2014.
https://doi.org/10.1149/2.010408jes.

[162] F. C. Cetinbas, S. G. Advani, and A. K. Prasad. Three dimensional proton exchange membrane fuel cell cathode model using a modified agglomerate approach based on discrete catalyst particles. *Journal of Power Sources*, 250:110–119, Mar. 2014.
https://doi.org/10.1016/j.jpowsour.2013.10.138.

[163] L. M. Pant, M. R. Gerhardt, N. Macauley, R. Mukundan, R. L. Borup, and A. Z. Weber. Along-the-channel modeling and analysis of PEFCs at low stoichiometry: Development of a 1+2d model. *Electrochimica Acta*, 326:134963, Dec. 2019.
https://doi.org/10.1016/j.electacta.2019.134963.

[164] E. Sadeghi, A. Putz, and M. Eikerling. Hierarchical Model of Reaction Rate Distributions and Effectiveness Factors in Catalyst Layers of Polymer Electrolyte Fuel Cells. *Journal of The Electrochemical Society*, 160(10):F1159–F1169, 2013.
https://doi.org/10.1149/2.090310jes.

[165] P.-C. Sui, X. Zhu, and N. Djilali. Modeling PEM Fuel Cell Catalyst Layers: Status and Outlook. *Electrochemical Energy Reviews*, 2(3):428–466, Sept. 2019.
https://doi.org/10.1007/s41918-019-00043-5.

[166] S. Tzelepis, K. A. Kavadias, G. E. Marnellos, and G. Xydis. A review study on proton exchange membrane fuel cell electrochemical performance focusing on anode and cathode catalyst layer modelling at macroscopic level. *Renewable and Sustainable Energy Reviews*, 151:111543, 2021.
https://doi.org/10.1016/j.rser.2021.111543.

[167] J. Jankovic and J. Stumper, editors. *Pem fuel cells: characterization and modeling*. De Gruyter Stem. De Gruyter, Boston, 2023. ISBN 978-3-11-062262-1.
https://doi.org/10.1515/9783110622720.

[168] S. J. Paddison, K. S. Promislow, and C. E. Ascheron, editors. *Device and Materials Modeling in PEM Fuel Cells*, volume 113 of *Topics in Applied Physics*. Springer New York, New York, NY, 2009. ISBN 978-0-387-78690-2 978-0-387-78691-9.
https://doi.org/10.1007/978-0-387-78691-9.

[169] E. Engel and R. M. Dreizler. *Density Functional Theory: An Advanced Course*. Theoretical and Mathematical Physics. Springer Berlin Heidelberg, Berlin, Heidelberg, 2011. ISBN 978-3-642-14089-1 978-3-642-14090-7.
https://doi.org/10.1007/978-3-642-14090-7.

[170] A. Kulkarni, S. Siahrostami, A. Patel, and J. K. Nørskov. Understanding Catalytic Activity Trends in the Oxygen Reduction Reaction. *Chemical Reviews*, 118(5):2302–2312, Mar. 2018.
https://doi.org/10.1021/acs.chemrev.7b00488.

[171] M. J. Eslamibidgoli, J. Huang, T. Kadyk, A. Malek, and M. Eikerling. How theory and simulation can drive fuel cell electrocatalysis. *Nano Energy*, 29:334–361, Nov. 2016.
https://doi.org/10.1016/j.nanoen.2016.06.004.

[172] M. J. Eslamibidgoli and M. H. Eikerling. Electrochemical Formation of Reactive Oxygen Species at Pt (111)—A Density Functional Theory Study. *ACS Catalysis*, 5(10):6090–6098, Oct. 2015.
https://doi.org/10.1021/acscatal.5b01154.

[173] E. Skúlason, G. S. Karlberg, J. Rossmeisl, T. Bligaard, J. Greeley, H. Jónsson, and J. K. Nørskov. Density functional theory calculations for the hydrogen evolution reaction in an electrochemical double layer on the Pt(111) electrode. *Phys. Chem. Chem. Phys.*, 9(25):3241–3250, 2007.
https://doi.org/10.1039/B700099E.

[174] J. Huang, J. Zhang, and M. Eikerling. Unifying theoretical framework for deciphering the oxygen reduction reaction on platinum. *Physical Chemistry Chemical Physics*, 20(17):11776–11786, 2018.
https://doi.org/10.1039/C8CP01315B.

[175] J. Huang and M. Eikerling. Modeling the oxygen reduction reaction at platinum-based catalysts: A brief review of recent developments. *Current Opinion in Electrochemistry*, 13:157–165, Feb. 2019.
https://doi.org/10.1016/j.coelec.2019.01.004.

[176] B. Leimkuhler and C. Matthews. *Molecular Dynamics: With Deterministic and Stochastic Numerical Methods*, volume 39 of *Interdisciplinary Applied Mathematics*. Springer International Publishing, Cham, 2015. ISBN 978-3-319-16374-1.
https://doi.org/10.1007/978-3-319-16375-8.

[177] J. H. Lee, G. Doo, S. H. Kwon, H. Kang, S. Choi, S.-D. Yim, H.-T. Kim, and S. G. Lee. Controlling Ionomer Film Morphology through Altering Pt Catalyst Surface Properties for Polymer Electrolyte Membrane Fuel Cells. *ACS Applied Polymer Materials*, 2 (5):1807–1818, May 2020.
https://doi.org/10.1021/acsapm.0c00042.

[178] E. J. Lamas and P. B. Balbuena. Molecular dynamics studies of a model polymer–catalyst–carbon interface. *Electrochimica Acta*, 51(26):5904–5911, Aug. 2006.

https://doi.org/10.1016/j.electacta.2006.03.033.

[179] Y. Kurihara, T. Mabuchi, and T. Tokumasu. Molecular dynamics study of oxygen transport resistance through ionomer thin film on Pt surface. *Journal of Power Sources*, 414:263–271, Feb. 2019.
https://doi.org/10.1016/j.jpowsour.2019.01.011.

[180] T. Mashio, A. Ohma, and T. Tokumasu. Molecular Dynamics Study of Ionomer Adsorption at a Carbon Surface in Catalyst Ink. *Electrochimica Acta*, 202:14–23, June 2016.
https://doi.org/10.1016/j.electacta.2016.04.004.

[181] R. M. Darling. A hierarchical model for oxygen transport in agglomerates in the cathode catalyst layer of a polymer-electrolyte fuel cell. *Journal of The Electrochemical Society*, 165(9):F571, 2018.
https://doi.org/10.1149/2.1231807jes.

[182] S. Kamarajugadda and S. Mazumder. Generalized flooded agglomerate model for the cathode catalyst layer of a polymer electrolyte membrane fuel cell. *Journal of Power Sources*, 208:328–339, June 2012.
https://doi.org/10.1016/j.jpowsour.2012.02.063.

[183] S. Li, J. Yuan, G. Xie, and B. Sundén. Effects of agglomerate model parameters on transport characterization and performance of PEM fuel cells. *International Journal of Hydrogen Energy*, 43(17):8451–8463, Apr. 2018.
https://doi.org/10.1016/j.ijhydene.2018.03.106.

[184] Q. Xiong, T. G. Baychev, and A. P. Jivkov. Review of pore network modelling of porous media: Experimental characterisations, network constructions and applications to reactive transport. *Journal of Contaminant Hydrology*, 192:101–117, Sept. 2016.
https://doi.org/10.1016/j.jconhyd.2016.07.002.

[185] J. Gostick, M. Aghighi, J. Hinebaugh, T. Tranter, M. A. Hoeh, H. Day, B. Spellacy, M. H. Sharqawy, A. Bazylak, A. Burns, W. Lehnert, and A. Putz. OpenPNM: A Pore Network Modeling Package. *Computing in Science & Engineering*, 18(4):60–74, July 2016.
https://doi.org/10.1109/MCSE.2016.49.

[186] J. Gostick, Z. Khan, T. Tranter, M. Kok, M. Agnaou, M. Sadeghi, and R. Jervis. PoreSpy: A Python Toolkit for Quantitative Analysis of Porous Media Images. *Journal of Open Source Software*, 4(37):1296, May 2019.
https://doi.org/10.21105/joss.01296.

[187] M. A. Sadeghi, Z. A. Khan, M. Agnaou, S. Litster, J. Barralet, T. Friscic, and J. T. Gostick. Nanoscale pore network reconstruction and simulation of the fuel cell catalyst layer. *in submission*, 2022.

[188] S. Jung, M. Sabharwal, A. Jarauta, F. Wei, M. Gingras, J. Gostick, and M. Secanell. Estimation of Relative Transport Properties in Porous Transport Layers Using Pore-Scale and Pore-Network Simulations. *Journal of The Electrochemical Society*, 168(6):064501, June 2021.
https://doi.org/10.1149/1945-7111/ac03f2.

[189] R. Wu, Q. Liao, X. Zhu, and H. Wang. Pore network modeling of cathode catalyst layer of proton exchange membrane fuel cell. *International Journal of Hydrogen Energy*, 37(15):11255–11267, 2012. https://doi.org/10.1016/j.ijhydene.2012.04.036.

[190] M. El Hannach, M. Prat, and J. Pauchet. Pore network model of the cathode catalyst layer of proton exchange membrane fuel cells: Analysis of water management and electrical performance. *International Journal of Hydrogen Energy*, 37(24):18996–19006, Dec. 2012. https://doi.org/10.1016/j.ijhydene.2012.09.139.

[191] K. J. Lange, H. Carlsson, I. Stewart, P.-C. Sui, R. Herring, and N. Djilali. PEM fuel cell CL characterization using a standalone FIB and SEM: Experiments and simulation. *Electrochimica Acta*, 85:322–331, Dec. 2012. https://doi.org/10.1016/j.electacta.2012.08.082.

[192] W. K. Epting and S. Litster. Effects of an agglomerate size distribution on the PEFC agglomerate model. *International Journal of Hydrogen Energy*, 37(10):8505–8511, May 2012. https://doi.org/10.1016/j.ijhydene.2012.02.099.

[193] S. H. Kim and H. Pitsch. Reconstruction and Effective Transport Properties of the Catalyst Layer in PEM Fuel Cells. *Journal of The Electrochemical Society*, 156(6):B673, 2009. https://doi.org/10.1149/1.3106136.

[194] P.-C. Sui, L.-D. Chen, J. P. Seaba, and Y. Wariishi. Modeling and optimization of a PEMFC catalyst layer. *SAE transactions*, pages 729–737, 1999. https://doi.org/10.4271/1999-01-0539.

[195] G. Inoue, T. Ohnishi, M. So, K. Park, M. Ono, and Y. Tsuge. Simulation of carbon black aggregate and evaluation of ionomer structure on carbon in catalyst layer of polymer electrolyte fuel cell. *Journal of Power Sources*, 439:227060, Nov. 2019. https://doi.org/10.1016/j.jpowsour.2019.227060.

[196] P. P. Mukherjee, C.-Y. Wang, and Q. Kang. Mesoscopic modeling of two-phase behavior and flooding phenomena in polymer electrolyte fuel cells. *Electrochimica Acta*, 54(27):6861–6875, Nov. 2009. https://doi.org/10.1016/j.electacta.2009.06.066.

[197] N. Siddique and F. Liu. Process based reconstruction and simulation of a three-dimensional fuel cell catalyst layer. *Electrochimica Acta*, 55(19):5357–5366, July 2010. https://doi.org/10.1016/j.electacta.2010.04.059.

[198] T. Hutzenlaub, J. Becker, R. Zengerle, and S. Thiele. Modelling the water distribution within a hydrophilic and hydrophobic 3d reconstructed cathode catalyst layer of a proton exchange membrane fuel cell. *Journal of Power Sources*, 227:260–266, Apr. 2013. https://doi.org/10.1016/j.jpowsour.2012.11.065.

[199] H. Liu, Q. Kang, C. R. Leonardi, S. Schmieschek, A. Narváez, B. D. Jones, J. R. Williams, A. J. Valocchi, and J. Harting. Multiphase lattice Boltzmann simulations for porous media applications: A review. *Computational Geosciences*, 20(4):777–805, Aug. 2016. https://doi.org/10.1007/s10596-015-9542-3.

[200] G. Molaeimanesh and M. Akbari. Agglomerate modeling of cathode catalyst layer of a PEM fuel cell by the lattice Boltzmann method. *International Journal of Hydrogen Energy*, 40(15):5169–5185, Apr. 2015. https://doi.org/10.1016/j.ijhydene.2015.02.097.

[201] H. Deng, Y. Hou, W. Chen, F. Pan, and K. Jiao. Lattice Boltzmann simulation of oxygen diffusion and electrochemical reaction inside catalyst layer of PEM fuel cells. *International Journal of Heat and Mass Transfer*, 143:118538, Nov. 2019. https://doi.org/10.1016/j.ijheatmasstransfer.2019.118538.

[202] S. Thiele, T. Fürstenhaupt, D. Banham, T. Hutzenlaub, V. Birss, C. Ziegler, and R. Zengerle. Multiscale tomography of nanoporous carbon-supported noble metal catalyst layers. *Journal of Power Sources*, 228:185–192, Apr. 2013. https://doi.org/10.1016/j.jpowsour.2012.11.106.

[203] F. C. Cetinbas, R. K. Ahluwalia, N. N. Kariuki, and D. J. Myers. Agglomerates in polymer electrolyte fuel cell electrodes: Part i. structural characterization. *Journal of The Electrochemical Society*, 165(13):F1051, 2018.

[204] F. C. Cetinbas, R. K. Ahluwalia, N. N. Kariuki, V. De Andrade, and D. J. Myers. Effects of Porous Carbon Morphology, Agglomerate Structure and Relative Humidity on Local Oxygen Transport Resistance. *Journal of The Electrochemical Society*, 167(1):013508, 2020. https://doi.org/10.1149/2.0082001JES.

[205] A. A. Kulikovsky. A Physically–Based Analytical Polarization Curve of a PEM Fuel Cell. *Journal of The Electrochemical Society*, 161(3):F263–F270, 2014. https://doi.org/10.1149/2.028403jes.

[206] I. V. Zenyuk, P. K. Das, and A. Z. Weber. Understanding impacts of catalyst-layer thickness on fuel-cell performance via mathematical modeling. *Journal of the Electrochemical Society*, 163(7):F691, 2016. https://doi.org/10.1149/2.1161607jes.

[207] N. Goswami, A. N. Mistry, J. B. Grunewald, T. F. Fuller, and P. P. Mukherjee. Corrosion-Induced Microstructural Variability Affects Transport-Kinetics Interaction in PEM Fuel Cell Catalyst Layers. *Journal of The Electrochemical Society*, 167(8):084519, May 2020. https://doi.org/10.1149/1945-7111/ab927c.

[208] M. Uchida, Y.-C. Park, K. Kakinuma, H. Yano, D. A. Tryk, T. Kamino, H. Uchida, and M. Watanabe. Effect of the state of distribution of supported Pt nanoparticles on effective Pt utilization in polymer electrolyte fuel cells. *Physical Chemistry Chemical Physics*, 15(27):11236, 2013. https://doi.org/10.1039/c3cp51801a.

[209] S. Torquato and H. Haslach. Random Heterogeneous Materials: Microstructure and Macroscopic Properties. *Applied Mechanics Reviews*, 55(4):B62–B63, July 2002. https://doi.org/10.1115/1.1483342.

[210] D. Stauffer and A. Aharony. *Introduction To Percolation Theory*. Taylor & Francis, 2018. ISBN 97813152743860.
https://doi.org/doi.org/10.1201/9781315274386.

[211] D. Song, Q. Wang, Z. Liu, M. Eikerling, Z. Xie, T. Navessin, and S. Holdcroft. A method for optimizing distributions of Nafion and Pt in cathode catalyst layers of PEM fuel cells. *Electrochimica Acta*, 50(16-17):3347–3358, May 2005.
https://doi.org/10.1016/j.electacta.2004.12.008.

[212] M. Secanell, B. Carnes, A. Suleman, and N. Djilali. Numerical optimization of proton exchange membrane fuel cell cathodes. *Electrochimica Acta*, 52(7):2668–2682, Feb. 2007.
https://doi.org/10.1016/j.electacta.2006.09.049.

[213] F. Gloaguen and R. Durand. Simulations of PEFC cathodes: an effectiveness factor approach. *Journal of Applied Electrochemistry*, 27(9):1029–1035, 1997.
https://doi.org/10.1023/A:1018478324564.

[214] Q. Wang, M. Eikerling, D. Song, Z. Liu, T. Navessin, Z. Xie, and S. Holdcroft. Functionally Graded Cathode Catalyst Layers for Polymer Electrolyte Fuel Cells. *Journal of The Electrochemical Society*, 151(7):A950, 2004.
https://doi.org/10.1149/1.1753580.

[215] J. Leszczynski and M. K. Shukla, editors. *Practical Aspects of Computational Chemistry: Methods, Concepts and Applications*. Springer Netherlands, Dordrecht, 2010. ISBN 978-90-481-2686-6 978-90-481-2687-3.
https://link.springer.com/10.1007/978-90-481-2687-3.

[216] M. G. D. Geers, V. G. Kouznetsova, K. Matouš, and J. Yvonnet. Homogenization Methods and Multiscale Modeling: Nonlinear Problems. In E. Stein, R. de Borst, and T. J. R. Hughes, editors, *Encyclopedia of Computational Mechanics Second Edition*, pages 1–34. John Wiley & Sons, Ltd, Chichester, UK, Dec. 2017. ISBN 978-1-119-00379-3 978-1-119-17681-7.
https://doi.org/10.1002/9781119176817.ecm2107.

[217] L. Guetaz, M. Lopez-Haro, S. Escribano, A. Morin, G. Gebel, D. A. Cullen, K. L. More, and R. L. Borup. Catalyst-Layer Ionomer Imaging of Fuel Cells. *ECS Transactions*, 69(17):455–464, Oct. 2015.
https://doi.org/10.1149/06917.0455ecst.

[218] M. So, K. Park, Y. Tsuge, and G. Inoue. A Particle Based Ionomer Attachment Model for a Fuel Cell Catalyst Layer. *Journal of The Electrochemical Society*, 167(1):013544, 2020.
https://doi.org/10.1149/1945-7111/ab68d4.

[219] H. Li, Y. Tang, Z. Wang, Z. Shi, S. Wu, D. Song, J. Zhang, K. Fatih, J. Zhang, H. Wang, Z. Liu, R. Abouatallah, and A. Mazza. A review of water flooding issues in the proton exchange membrane fuel cell. *Journal of Power Sources*, 178(1):103–117, Mar. 2008.
https://doi.org/10.1016/j.jpowsour.2007.12.068.

[220] H. P. F. Gunterman. *Characterization of Fuel-Cell Diffusion Media*. PhD thesis, UC Berkeley, 2011.
https://escholarship.org/uc/item/2hd8f4wp.

[221] J. T. Gostick, M. W. Fowler, M. A. Ioannidis, M. D. Pritzker, Y. Volfkovich, and A. Sakars. Capillary pressure and hydrophilic porosity in gas diffusion layers for polymer electrolyte fuel cells. *Journal of Power Sources*, 156(2):375–387, June 2006.
https://doi.org/10.1016/j.jpowsour.2005.05.086.

[222] H. Yu, C. Ziegler, M. Oszcipok, M. Zobel, and C. Hebling. Hydrophilicity and hydrophobicity study of catalyst layers in proton exchange membrane fuel cells. *Electrochimica Acta*, 51(7):1199–1207, Jan. 2006.
https://doi.org/10.1016/j.electacta.2005.06.036.

[223] D. L. Wood, J. Chlistunoff, J. Majewski, and R. L. Borup. Nafion Structural Phenomena at Platinum and Carbon Interfaces. *Journal of the American Chemical Society*, 131(50):18096–18104, Dec. 2009.
https://doi.org/10.1021/ja9033928.

[224] V. Mulone and K. Karan. Analysis of capillary flow driven model for water transport in PEFC cathode catalyst layer: Consideration of mixed wettability and pore size distribution. *International Journal of Hydrogen Energy*, 38(1):558–569, Jan. 2013.
https://doi.org/10.1016/j.ijhydene.2012.07.107.

[225] P. A. Mateo Villanueva. *A mixed wettability pore size distribution model for the analysis of water transport in PEMFC materials*. Master Thesis, University of Alberta, 2013.
https://era.library.ualberta.ca/items/e96ae1d9-450e-467b-9f82-4d5fddc7f839.

[226] J. Zhou, A. Putz, and M. Secanell. A Mixed Wettability Pore Size Distribution Based Mathematical Model for Analyzing Two-Phase Flow in Porous Electrodes: I. Mathematical Model. *Journal of The Electrochemical Society*, 164(6):F530–F539, 2017.
https://doi.org/10.1149/2.0381706jes.

[227] A. Goshtasbi, P. García-Salaberri, J. Chen, K. Talukdar, D. G. Sanchez, and T. Ersal. Through-the-Membrane Transient Phenomena in PEM Fuel Cells: A Modeling Study. *Journal of The Electrochemical Society*, 166(7):F3154–F3179, 2019.
https://doi.org/10.1149/2.0181907jes.

[228] A. Z. Weber. Improved modeling and understanding of diffusion-media wettability on polymer-electrolyte-fuel-cell performance. *Journal of Power Sources*, 195(16):5292–5304, Aug. 2010.
https://doi.org/10.1016/j.jpowsour.2010.03.011.

[229] J. Huang, Z. Li, and J. Zhang. Review of characterization and modeling of polymer electrolyte fuel cell catalyst layer: The blessing and curse of ionomer. *Frontiers in Energy*, 11(3):334–364, Sept. 2017.
https://doi.org/10.1007/s11708-017-0490-6.

[230] A. Kobayashi, T. Fujii, C. Harada, E. Yasumoto, K. Takeda, K. Kakinuma, and M. Uchida. Effect of Pt and Ionomer Distribution on Polymer Electrolyte Fuel Cell Performance and Durability. *ACS Applied Energy Materials*, 4(3):2307–2317, Mar. 2021.
https://doi.org/10.1021/acsaem.0c02841.

[231] R. Alink, R. Singh, P. Schneider, K. Christmann, J. Schall, R. Keding, and N. Zamel. Full Parametric Study of the Influence of Ionomer Content, Catalyst Loading and Catalyst Type on Oxygen and Ion Transport in PEM Fuel Cell Catalyst Layers. *Molecules*, 25 (7):1523, Mar. 2020.
https://doi.org/10.3390/molecules25071523.

[232] L. Xing, W. Shi, H. Su, Q. Xu, P. K. Das, B. Mao, and K. Scott. Membrane electrode assemblies for PEM fuel cells: A review of functional graded design and optimization. *Energy*, 177:445–464, June 2019.
https://doi.org/10.1016/j.energy.2019.04.084.

[233] Y. Wang, D. F. Ruiz Diaz, K. S. Chen, Z. Wang, and X. C. Adroher. Materials, technological status, and fundamentals of PEM fuel cells – A review. *Materials Today*, 32:178–203, Jan. 2020.
https://doi.org/10.1016/j.mattod.2019.06.005.

[234] C. Boyer, S. Gamburzev, O. Velev, S. Srinivasan, and A. Appleby. Measurements of proton conductivity in the active layer of PEM fuel cell gas diffusion electrodes. *Electrochimica Acta*, 43(24):3703–3709, Aug. 1998.
https://doi.org/10.1016/S0013-4686(98)00128-5.

[235] T. Suzuki, H. Murata, T. Hatanaka, and Y. Morimoto. Analysis of the catalyst layer of polymer electrolyte fuel cells. *R&D Review of Toyota CRDL*, 39(3), 2003.
https://www.tytlabs.co.jp/en/english/review/rev393epdf/e393_033suzuki.pdf.

[236] C. Du, P. Shi, X. Cheng, and G. Yin. Effective protonic and electronic conductivity of the catalyst layers in proton exchange membrane fuel cells. *Electrochemistry Communications*, 6(5):435–440, May 2004.
https://doi.org/10.1016/j.elecom.2004.02.006.

[237] A. D. Modestov, A. V. Kapustin, V. B. Avakov, I. K. Landgraf, and M. R. Tarasevich. Cathode catalyst layers with ionomer to carbon mass ratios in the range 0–2 studied by electrochemical impedance spectroscopy, cyclic voltammetry, and performance measurements. *Journal of Power Sources*, 272:735–742, Dec. 2014.
https://doi.org/10.1016/j.jpowsour.2014.08.113.

[238] A. Havránek and K. Wippermann. Determination of proton conductivity in anode catalyst layers of the direct methanol fuel cell (DMFC). *Journal of Electroanalytical Chemistry*, 567(2):305–315, June 2004.
https://doi.org/10.1016/j.jelechem.2003.12.047.

[239] Y. Liu, J. Jorne, and W. Gu. Thin Shell Model for Proton Conduction in PEM Fuel Cell Cathodes. *Journal of The Electrochemical Society*, 157(7):B1068, 2010.
https://doi.org/10.1149/1.3429885.

[240] K. J. Lange, P.-C. Sui, and N. Djilali. Pore Scale Simulation of Transport and Electrochemical Reactions in Reconstructed PEMFC Catalyst Layers. *Journal of The Electrochemical Society*, 157(10):B1434, 2010.
https://doi.org/10.1149/1.3478207.

[241] T. Hattori, A. Suzuki, R. Sahnoun, M. Koyama, H. Tsuboi, N. Hatakeyama, A. Endou, H. Takaba, M. Kubo, C. A. Del Carpio, and A. Miyamoto. Development of the overpotential simulator for polymer electrolyte fuel cells and application for optimization of cathode structure. *Applied Surface Science*, 254

(23):7929–7932, Sept. 2008.
https://doi.org/10.1016/j.apsusc.2008.03.165.

[242] K. Shinozaki, H. Yamada, and Y. Morimoto. Relative humidity dependence of Pt utilization in polymer electrolyte fuel cell electrodes: effects of electrode thickness, ionomer-to-carbon ratio, ionomer equivalent weight, and carbon support. *Journal of the electrochemical society*, 158(5):B467, 2011.
https://doi.org/10.1149/1.3556906.

[243] M. Eikerling, A. A. Kornyshev, and A. R. Kucernak. Water in polymer electrolyte fuel cells: Friend or foe? *Physics Today*, 59(10):38–44, Oct. 2006.
https://doi.org/10.1063/1.2387087.

[244] W. Olbrich, T. Kadyk, U. Sauter, and M. Eikerling. Modeling of wetting phenomena in cathode catalyst layers for PEM fuel cells. *Electrochimica Acta*, 431: 140850, Nov. 2022.
https://doi.org/10.1016/j.electacta.2022.140850.

[245] S. Brunauer, P. H. Emmett, and E. Teller. Adsorption of gases in multimolecular layers. *Journal of the American chemical society*, 60(2):309–319, 1938.
https://doi.org/10.1021/ja01269a023.

[246] A. Kusoglu. Ionomer Thin Films in PEM Fuel Cells. In R. A. Meyers, editor, *Encyclopedia of Sustainability Science and Technology*, pages 1–23. Springer New York, New York, NY, 2018. ISBN 978-1-4939-2493-6.
http://link.springer.com/10.1007/978-1-4939-2493-6_1021-2.

[247] A. Kusoglu, A. Kwong, K. T. Clark, H. P. Gunterman, and A. Z. Weber. Water uptake of fuel-cell catalyst layers. *Journal of the Electrochemical Society*, 159(9): F530, 2012.
https://doi.org/10.1149/2.031209jes.

[248] S. Bahman, Y.-C. Han, V. Hauser, M. I. Mohammadadabi, F. Engelhardt, T. Kadyk, and W. Olbrich. *CAMMP week Pro Report: It's all connected! Percolation theory applied to fuel cell catalyst layers.* Seminar Report, RWTH, Aaachen, Aug. 2021. Available on request.

[249] V. Hauser. *Applying a graph-based model to proton-related properties of PEM fuel cell catalyst layers.* Seminar Thesis, RWTH, Aaachen, June 2022. Available on request.

[250] J. Aochi, T. Mabuchi, and T. Tokumasu. Molecular Dynamics Study on Proton Transport in Supported Nafion Ionomer Thin Films on Lennard-Jones Walls. *ECS Transactions*, 75(14):607–614, Aug. 2016.
https://doi.org/10.1149/07514.0607ecst.

[251] W. Zheng and S. H. Kim. The effects of catalyst layer microstructure and water saturation on the effective diffusivity in PEMFC. *Journal of The Electrochemical Society*, 165(7):F468, 2018.
https://doi.org/10.1149/2.0711807je.

[252] M. Khakbazbaboli. *Development of a Micro-scale Cathode Catalyst Layer Model of Polymer Electrolyte Membrane Fuel Cell.* PhD thesis, 2013.
https://qspace.library.queensu.ca/bitstream/handle/1974/7846/Khakbazbaboli_Mobin_201303_PhD.pdf?sequence=1.

[253] M. Barreiros Salvado, P. Schott, L. Guétaz, M. Gerard, T. David, and Y. Bultel. Towards the understanding of transport limitations in a proton-exchange membrane fuel cell catalyst layer: Performing agglomerate scale direct numerical simulations on electron-microscopy-based geometries. *Journal of Power Sources*, 482:228893, Jan. 2021. `https://doi.org/10.1016/j.jpowsour.2020.228893`.

[254] T. Muzaffar. *Physical modeling of local reaction conditions inside of cathode catalyst layer of polymer electrolyte fuel cells*. PhD thesis, Simon Fraser University, Vancouver, Canada, Nov. 2018. `http://summit.sfu.ca/item/18738`.

[255] R. Bligny, T. Schmitt, J. Dillet, F. Xu, S. Didierjean, M. Hanauer, U. Sauter, and G. Maranzana. In-situ estimation of water transfer parameters in a proton exchange membrane fuel cell. *Journal of Power Sources*, 560:232719, Mar. 2023. `https://doi.org/10.1016/j.jpowsour.2023.232719`.

[256] L. Lübben, S. Kirsch, T. Kadyk, and M. Eikerling. Test procedure for the prediction of water transport in polymer electrolyte fuel cells. *Journal of Power Sources*, 556:232504, Feb. 2023. `https://doi.org/10.1016/j.jpowsour.2022.232504`.

[257] L. Xing, X. Song, K. Scott, V. Pickert, and W. Cao. Multi-variable optimisation of PEMFC cathodes based on surrogate modelling. *International Journal of Hydrogen Energy*, 38(33):14295–14313, Nov. 2013. `https://doi.org/10.1016/j.ijhydene.2013.08.104`.

[258] A. Aiyejina and M. K. S. Sastry. PEMFC Flow Channel Geometry Optimization: A Review. *Journal of Fuel Cell Science and Technology*, 9(1), Feb. 2012. `https://doi.org/10.1115/1.4005393`.

[259] J. Sansana, M. N. Joswiak, I. Castillo, Z. Wang, R. Rendall, L. H. Chiang, and M. S. Reis. Recent trends on hybrid modeling for Industry 4.0. *Computers & Chemical Engineering*, 151:107365, Aug. 2021. `https://doi.org/10.1016/j.compchemeng.2021.107365`.

[260] A. Malek, M. J. Eslamibidgoli, M. Mokhtari, Q. Wang, M. H. Eikerling, and K. Malek. Virtual Materials Intelligence for Design and Discovery of Advanced Electrocatalysts. *ChemPhysChem*, 20(22):2946–2955, Nov. 2019. `https://doi.org/10.1002/cphc.201900570`.

8 Appendix

In the following, all tables and figures are listed that are not part of one of the published articles constituting this thesis.

8.1 List of tables

8.2 List of figures